Modelisation of the multiwavelength emission of compact objects : from X-ray binaries to Active Galactic Nuclei

Samuel Barnier

THÈSE

Pour obtenir le grade de

DOCTEUR DE L'UNIVERSITÉ GRENOBLE ALPES

École doctorale : PHYS - Physique
Spécialité : Astrophysique et Milieux Dilués
Unité de recherche : Institut de Planetologie et dAstrophysique de Grenoble

Modélisation de l'émission multi-longueur d'onde des objets compacts : des binaires X aux Noyaux Actifs de Galaxies

Modelisation of the multiwavelength emission of compact objects: from X-ray binaries to Active Galactic Nuclei

Présentée par :

Samuel BARNIER

Direction de thèse :

Pierre-Olivier PETRUCCI CHARGE DE RECHERCHE, Université Grenoble Alpes	Directeur de thèse

Rapporteurs :

GUIDO RISALITI
Professeur, Università degli studi di Firenze
CHRISTINE DONE
Professeur, Durham University

Thèse soutenue publiquement le **14 octobre 2022**, devant le jury composé de :

GUIDO RISALITI Professeur, Università degli studi di Firenze	Rapporteur
CHRISTINE DONE Professeur, Durham University	Rapporteure
JIRÍ SVOBODA Docteur en sciences, Akademie ved Ceské republiky	Examinateur
STEPHANE CORBEL Professeur des Universités, UNIVERSITE DE PARIS-CITE	Examinateur
JEAN-LOUIS MONIN Professeur des Universités, UNIVERSITE GRENOBLE ALPES	Président

UNIVERSITÉ GRENOBLE ALPES

Abstract

Institut de Planétologie et d'Astrophysique de Grenoble

Doctor of Philosophy

Modelisation of multi-wavelength emission of compact objects: From X-ray binaries to Active Galactic Nuclei

by Samuel BARNIER

English

Accreting black holes are powered by the gravitational potential energy from the matter falling down on the black hole. They emit from the UV to the hard X-ray energy range and can produce relativistic jets. Stellar mass black hole found in galactic X-ray Binaries (XrB), can undergo powerful outbursts, lasting a few months and during which their luminosity rises to a fraction of their Eddington limit. These outbursts present multiple accretion states with a spectral dichotomy correlated with a jet dichotomy. During the hard states, the X-ray spectrum is dominated by a power-law emission originating from a hot corona, whose characteristics and geometry are still highly debated. At the same time, steady radio jets can be observed. During the soft states, the spectrum is dominated by the thermal emission from the disk and the absence of radio emission suggests the quenching of the jets. Outbursts cannot be observed in supermassive black holes present in Active Galactic Nuclei (AGN) as the timescales are so much longer. Instead, we can associate the time dependent sequence of accretion-ejection seen in a single XrB to the stationary snapshots seen in multiple different AGN. Similar to XrB, AGN show a strong correlation between the X-ray and the radio emission, showing that the accretion-ejection process is quite universal across the entire black hole mass scale.

The Jet Emitting Disk – Standard Accretion Disk (JED-SAD, Ferreira et al. 2006, Marcel et al. 2018a, 2018b) model is a hybrid disk configuration composed of an inner highly magnetized JED (Ferreira, 1997) and an outer SAD (Shakura Sunyaev, 1973). Jets are launched from the magnetized JED, extracting angular momentum, increasing the accretion speed and thus allowing the low-density accretion flow to play the role of the X-ray emitting hot corona. The JED-SAD model naturally explains the spectral and jet dichotomy observed in accreting black hole accretion states. Following the thesis of Gregoire Marcel (2018), who computed the thermal equilibrium and spectral output of any given JED-SAD configuration, with my thesis we take the next step and produce direct fits with the model.

I developed spectral tables of the JED-SAD model that I use to fit UV and X-ray spectra from both XrB and AGN. I apply the model to the hard state's observations of the XrB GX 339-4, constraining the evolution of the accretion flow. I then discover two different functional behavior of the jets' radio emission with the accretion flow parameters, suggesting a possible change of the jet emitting processes and/or emission properties between the beginning and the end of the outburst. In a second part of the thesis, I applied the JED-SAD model to the non-linear correlation observed between the UV (coming from the standard disk) and X-ray (from the hot corona) emissions in AGN samples. I focus on the Lusso et al. (2020) sample and constrain the relevant JED-SAD parameter space. I then produce simulated samples of AGN with the same density distribution in the UV–X-ray plane and presenting similar black hole mass and X-ray spectral index distributions as the Lusso et al. sample. The results suggest that the higher the black hole mass is, the lower the Eddington rate becomes. I interpret this as a lack of material around the most massive black holes, preventing them to reach high Eddington rates.

Français

Les trous noirs accrétant sont alimentés par l'énergie potentielle gravitationnelle de la matière tombant sur le trou noir. Ils émettent dans les UV jusqu'au rayons X dures et sont capable de lancer des jets relativistes. Les trous noirs de masses stellaires, observés dans les binaires X de notre galaxie, présentent des éruptions pouvant durer quelques mois et durant lesquelles leur luminosité atteint une fraction de leur limite d'Eddington. Ces éruptions présentent plusieurs états d'accrétion avec une dichotomie spectrale corrélée à une dichotomie dynamique du jet. Pendant les états dures, le spectre X est dominé par une émission en loi de puissance émise par une couronne chaude dont les caractéristiques et la géométrie sont encore en question. Simultanément, des jets stables sont observés. Pendant les états mous, le spectre est dominé par l'émission thermique du disque et l'absence d'émission radio suggère la disparition des jets. Ces éruptions ne sont pas observables pour les trous noirs supermassifs présents aux centres des Noyaux Actifs de Galaxies (NAG) en raison de leur temps caractéristique bien plus long (millions d'années). On peut cependant associer la séquence d'états d'accrétion-éjection observés dans une binaire X aux images statiques associés à une séquence de NAG. Comme les binaires X, les NAG présentent une corrélation entre leur émission X dure et radio, montrant que le processus d'accrétion-éjection est universel.

Le modèle de disque éjectant – disque standard (JED-SAD pour Jet Emitting Disk – Standard Accretion Disk, Ferreira et al. 2006, Marcel et al. 2018a, 2018b) est une configuration hybride composée dans les régions internes d'un disque éjectant hautement magnétisé (JED, Ferreira 1997) et dans les régions externes d'un disque standard (SAD, Shakura Sunyaev, 1973). Des jets sont lancés depuis le disque magnétisé, extrayant le moment angulaire verticalement, augmentant la vitesse d'accrétion et produisant un flot d'accrétion à faible densité capable de reproduire le rayonnement X dure attendue de la couronne chaude. Le modèle JED-SAD explique naturellement le comportement spectral et dynamique observé dans les trous noirs accrétant. Succédant la thèse de Grégoire Marcel (2018), qui calcula l'équilibre thermique et le spectre de n'importe quelle configuration JED-SAD, ma thèse constitue la prochaine étape logique avec des ajustements directs du modèle aux observations.

J'ai développé des tables spectrales du modèle JED-SAD que j'utilise pour ajuster les spectres UV et X des binaires X et des NAG. En premier lieu, j'applique le modèle aux observations dures de la binaire X GX 339-4, me permettant de contraindre l'évolution du flot d'accrétion. Je découvre deux comportements différents du flux radio avec l'évolution du flot d'accrétion, suggérant un possible changement de processus de lancement et/ou des propriétés d'émission du jet entre le début et la fin des éruptions. Dans une seconde partie de la thèse, j'applique le modèle JED-SAD à la corrélation non linéaire entre l'émission UV (provenant du disque standard) et l'émission X dure (provenant de la couronne chaude) observée dans les échantillons de NAG. Je me focalise sur l'échantillon de Lusso et al. (2020) et contrains l'espace des paramètres JED-SAD permettant de le reproduire. Je produis des échantillons simulés de NAG respectant la distribution dans le plan UV–X et présentant des distributions de masses de trous noirs et d'indice spectral X similaires à l'échantillon de Lusso et al. (2020). Les résultats montrent que plus les trous noirs sont massifs, plus bas est leur taux d'accrétion en unité Eddington. J'interprète cela comme un manque de matériel dans les NAG les plus massifs, empêchant d'alimenter le trou noir à un fort taux d'Eddington.

Acknowledgements

Three years. Three years was both a short and a long time. Looking back, these three years were hard. No doubt about it. Not even 6 months after the start of my Ph.D., the global health crisis of Covid started. I probably worked about a year from my home in lockdown. And even after the lock-downs were over, not many colleagues came back regularly to the office (including me). These three years of Ph.D. seemed to fly by, as with every Ph.D., with highs and lows both in work and in life. But these were also three years of growth with many new experiences, my first talk in conferences (hey, the first time is not always easy), the first missions abroad, first time teaching a class (with sometimes students older than me), the death of both my French grand-parents Maurice and Andrée, the birth of my third nephew and first niece.

Honestly, I think my choice of the Sherpas team for this Ph.D. was the best one. The good relationship both at work and outside in the team is incredible and provides such a comforting work environment for the Ph.D. students. That's why I would like to sincerely thank the entire Sherpas team, Pop, Jon, Maïca, Benoit, Geoffroy, Guillaume, Gilles and Didier. I would also like to thank all of my Ph.D. colleagues with whom we shared great moments while also supporting each other in our work, Etienne, Aurélia, Thomas, Jo, Maxime, Julien, Adrien, Marc (Sorry if I forgot someone). Of course, I have to mention and thank my predecessor Greg, without whom my Ph.D. subject would not have been possible. I think I need to mention Jon a second time and thank him for all the great scientific conversations on MHD who helped me a lot as well as generally supporting me all the way even though I was not his student. Finally, I have to thank my Ph.D advisor, Pop, you are the kindest ice-cream lover and showman one can ask for a mentor!

Now it is time to move on to the next page of my life. But this one will always remain a time I look to with fond memory. (You should seriously turn the page though, enough of this sentimental words written by a non native English speaker)

Contents

Abstract iv

Acknowledgements vii

I Introduction and Model 1

1 Astrophysical context 3
1.1 Accreting black holes and astrophysical jets . . . 9
1.1.1 X-ray binaries . . . 11
1.1.2 Active Galactic Nuclei . . . 13
1.2 Spectral composition . . . 15
1.3 Outbursts dynamics . . . 18
1.3.1 X-ray Binaries outbursts . . . 18
1.3.2 AGN snapshots . . . 19
1.4 Multi-wavelength behavior . . . 21
1.4.1 The radio–X-ray correlation . . . 21
1.4.2 The AGN UV–X-ray correlation . . . 22
1.4.3 Other correlations . . . 23
1.5 Modeling the accretion-ejection process . . . 23
1.5.1 The Standard Disk . . . 23
1.5.2 Corona models . . . 24
1.5.3 Jets . . . 26

2 The JED-SAD model 27
2.1 The Dyplodocus code . . . 32
2.1.1 Motivation . . . 32
2.1.2 Equation and Parametrization . . . 32
2.1.3 Hybrid structure . . . 38
2.1.4 HID and JED-SAD dynamic . . . 40
2.2 Solutions . . . 41
2.2.1 Structure and spectra . . . 41
2.2.2 Power budget . . . 46
2.3 Parameter space . . . 48
2.3.1 Black hole Mass – m . . . 48
2.3.2 Mass accretion rate – $\dot{m}$ . . . 51
2.3.3 Transition radius – r_J . . . 52
2.3.4 Inner radius – r_{isco} . . . 53

2.3.5 Dilution factor – ω . . . 53
2.3.6 Accretion speed – m_s . . . 54
2.3.7 Jet power – b . . . 54
2.3.8 Ejection Index – p . . . 54
2.4 Tables and Reflection . . . 60
2.4.1 JED-SAD tables . . . 60
2.4.2 Reflection computation . . . 60
2.5 General strategy . . . 61
2.6 Caveats and prospects . . . 62

II X-ray binaries **65**

3 First application: GX 339-4 **67**
3.1 Object and data selection . . . 72
3.1.1 Characteristics . . . 72
3.1.2 Data selection . . . 72
3.2 Greg's past results . . . 75
3.3 X-ray Fitting . . . 76
3.3.1 Methodology . . . 76
3.3.2 Examples . . . 77
3.3.3 Evolution of the parameters . . . 79
3.4 Outbursts dynamic . . . 87
3.4.1 Magnetic flux evolution . . . 87
3.4.2 Evolution of the JED regime . . . 89
3.4.3 Evolution of the temperature . . . 90
3.5 Radio emission . . . 92
3.5.1 Radio and X-ray emission . . . 92
3.5.2 Generalization of Greg's radio function . . . 93
3.5.3 New radio function . . . 94
3.6 Discussion and interpretation . . . 100
3.6.1 Indications of different radiative behaviors between the rising and decaying phases . . . 100
3.6.2 Changes in the dynamical ejection properties . . . 102
3.6.3 The radio X-ray correlation . . . 108

4 Other XrB applications and prospects **111**
4.1 MAXI J1820+070 . . . 113
4.1.1 Characteristics and bibliography . . . 113
4.1.2 X-ray Fits . . . 113
4.1.3 Interpretations . . . 114
4.2 Outliers . . . 117
4.2.1 Motivations . . . 117
4.2.2 H 1743-322 . . . 117
4.2.3 MAXI J1348-630 . . . 119
4.3 Comparison to Monte Carlo simulation – The MONK code . . . 121
4.3.1 Collaboration goal and methodology . . . 121
4.3.2 Spectral components . . . 122
4.3.3 Estimation of ω . . . 123
4.3.4 Prospects – Cyg-X1 and polarisation . . . 123

III Active Galactic Nuclei **125**

5 The UV–X-ray correlation **127**
5.1 Motivations and Bibliography . . . 131
5.1.1 Motivations and goals . . . 131
5.1.2 Existing models . . . 131
5.1.3 Strategy, tables and spectra . . . 133
5.2 Sample . . . 134
5.2.1 Description of the samples . . . 134
5.2.2 Black hole mass distribution . . . 135
5.2.3 X-ray spectral index Γ distribution . . . 138
5.3 Breaking down the UV–X-ray correlation . . . 139
5.3.1 The UV emission . . . 140
5.3.2 The X-ray emission . . . 142
5.4 JED-SAD UV–X-ray correlation coverage . . . 143
5.4.1 Grid r_J–$\dot{m}$ . . . 143
5.4.2 Relation r_J–$\dot{m}$ . . . 146
5.5 MC draw . . . 149
5.5.1 Drawing statistically equivalent sample . . . 150
5.5.2 Stratification . . . 153
5.5.3 Equivalent sample? . . . 155
5.5.4 Other samples . . . 158
5.6 AGN outbursts . . . 162
5.7 Discussion . . . 163
5.7.1 Radio-quiet AGN and JED-SAD . . . 163
5.7.2 Clues from spectral shape . . . 164
5.7.3 Inefficient or starved massive AGN? . . . 165
5.7.4 Toy model for an AGN outburst . . . 169
5.7.5 Conclusion and prospects . . . 169

6 Other AGN applications and Prospects **173**
6.1 Soft X-ray excess . . . 175
6.1.1 Context . . . 175
6.1.2 TITAN-NOAR tables . . . 176
6.1.3 XMM–HST survey of RX J1355+5612 . . . 177
6.2 Linking AGN population to outburst accretion states . . . 179
6.2.1 Context and sample . . . 179
6.2.2 Collaboration plan . . . 179
6.2.3 First results . . . 179
6.3 Other prospects . . . 182
6.3.1 Other AGN correlation . . . 182
6.3.2 Origin of the radio emission in radio-quiet AGN . . . 182

7 Conclusion **183**
7.1 Summary of the work . . . 184
7.2 Testing the JED-SAD model . . . 185
7.2.1 Spectral energy distribution . . . 185
7.2.2 Power density spectra, QPOs and timing . . . 185
7.2.3 X-ray polarization . . . 187
7.3 Future development and applications . . . 187

A Opacity in the JED-SAD model **189**
A.1 Kramer opacity 190
A.2 Other sources of opacity 190

B GX 339-4 – Interpolation of the radio flux **193**

C Grid (r_J;$\dot{m}$) **195**

D Nested Sampling **201**
D.1 Bibliography and methodology 201
D.2 Application to the L&R sample 203
D.3 Effects of the soft excess 204

List of Figures

1.1 XrB artist view . . . 11
1.2 Faranoff-Riley classification examples . . . 13
1.3 AGN classification . . . 14
1.4 X-ray binary spectrum . . . 16
1.5 AGN spectrum . . . 17
1.6 Outbursts HID . . . 19
1.7 Radio–X-ray correlation in X-ray binaries . . . 22
1.8 Different corona geometries . . . 24

2.1 Scheme of the JED-SAD model . . . 38
2.2 Example – JED-SAD solution . . . 42
2.3 Example – spectral composition of a JED-SAD solution . . . 43
2.4 Example – JED-SAD solution-2 . . . 44
2.5 Power budget map . . . 46
2.6 READ, RERD and SLIM JED . . . 47
2.7 Influence of the black hole mass . . . 49
2.8 Spectral composition of the JED – dependence with the mass. . . . 50
2.9 Influence of $\dot{m}$ . . . 51
2.10 Influence of r_J . . . 52
2.11 Influence of r_{isco} . . . 55
2.12 Influence of ω . . . 56
2.13 Influence of m_s . . . 57
2.14 Influence of b . . . 58
2.15 Influence of p . . . 59

3.1 GX339-4 – HID and radio–X-ray correlation . . . 73
3.2 GX339-4 – X-ray light-curve . . . 74
3.3 GX 339-4 – Examples of best fits . . . 78
3.4 GX 339-4 – Evolution of $\dot{m}$ . . . 80
3.5 GX 339-4 – Evolution of r_J . . . 81
3.6 GX 339-4 – Parameter light-curve during the 2010-2011 decaying phase. 81
3.7 GX 339-4 – χ^2 parameter space of r_J in the 2010-2011 decaying phase. . 82
3.8 GX 339-4 – MCMC for r_J. . . . 83
3.9 GX 339-4 – log(ξ) light-curve . . . 84
3.10 GX 339-4 – log(ξ) radial profile . . . 85
3.11 GX 339-4 – Influence of m_s . . . 86
3.12 GX 339-4 – Influence of b . . . 86
3.13 GX 339-4 – r_J-$\dot{m}$ . . . 88

3.14 GX 339-4 – Power budget during an outburst . . . 89
3.15 GX 339-4 – Disk maximum temperature . . . 90
3.16 GX 339-4 – Corona temperature . . . 91
3.17 Evolution of the radio and X-ray Luminosity . . . 93
3.18 GX 339-4 – Rejection of Greg's function . . . 94
3.19 GX 339-4: Radio fit (rising 2010-2011) . . . 94
3.20 GX 339-4: Observed to simulated radio flux ratios (rising 2010-2011) . 95
3.21 GX 339-4: Rejection of the rising solution in decaying observations . . 96
3.22 GX 339-4: α-β contours . . . 97
3.23 GX 339-4: Observed to simulated radio flux ratios . . . 98
3.24 GX 339-4: Influence of the systematic errors on α-β contours . . . 99
3.25 GX 339-4: Influence of m_s on α-β contours . . . 100
3.26 GX 339-4: Spectral index evolution . . . 101
3.27 GX 339-4: Radiative efficiency . . . 103
3.28 Jets in the JED-SAD paradigm . . . 106
3.29 GX 339-4: 2010-2011 radio–X-ray correlation . . . 108
3.30 GX 339-4: 3D visualisation of an outburst . . . 109

4.1 MAXI J1820+070 – Geometrical interpretation . . . 114
4.2 H 1743-322 – HID . . . 118
4.3 H 1743-322 – JED-SAD parameters . . . 119
4.4 MAXI J1348-630 – X-ray fits . . . 120
4.5 MAXI J1348-630 – α-β contours . . . 120
4.6 MONK – Observation selection . . . 121
4.7 MONK – Spectral comparison JED-SAD vs MONK . . . 122
4.8 MONK – Cyg X-1 fit . . . 124

5.1 Model from Kubota et al. . . . 131
5.2 Model from Arcodia et al. . . . 132
5.3 Example of AGN spectra and soft excess . . . 134
5.4 UV–X-ray correlation: Samples . . . 135
5.5 Samples: black hole masses . . . 136
5.6 Samples: Eddington ratios . . . 137
5.7 Samples: X-ray spectral index . . . 138
5.8 Spectrum: UV and X-ray luminosities . . . 139
5.9 Evolution of L_{UV} in the JED-SAD parameter space . . . 141
5.10 Evolution of L_X in the JED-SAD parameter space . . . 142
5.11 Grid (r_J;$\dot{m}$) – reading guide . . . 143
5.12 Grid (r_J;$\dot{m}$) – all masses . . . 145
5.13 Grid (r_J;$\dot{m}$) – Soft X-ray excess . . . 146
5.14 Relation $r_J(\dot{m})$ – δ . . . 147
5.15 Relation $r_J(\dot{m})$ – κ . . . 148
5.16 Relation $r_J(\dot{m})$ – κ – Soft X-ray . . . 149
5.17 Reproducing the L&R sample – 10k spectra . . . 151
5.18 Reproducing the L&R sample – 500 spectra . . . 152
5.19 Reproducing the L&R sample – Stratification: m, r_J and $\dot{m}$ . . . 153
5.20 Reproducing the L&R sample – Stratification: r_{isco}, ω, m_s and b . . . 154
5.21 Reproducing the L&R sample – Stratification: r_J/r_{isco} . . . 154
5.22 Reproducing the L&R sample – Mass distribution comparison . . . 155
5.23 Reproducing the L&R sample – X-ray spectral index Γ distribution comparison – 1 . . . 156

5.24 Reproducing the L&R sample – X-ray spectral index Γ distribution comparison – 2 . . . 157
5.25 Reproducing the Zhu+ sample – corner plot . . . 159
5.26 Reproducing the Zhu+ sample – Mass distribution comparison . . . 160
5.27 Reproducing the Liu+ sample – corner plot . . . 161
5.28 AGN outburst – No soft X . . . 162
5.29 Power in the JED versus black hole mass . . . 166
5.30 Cooling power in the JED versus black hole mass and mass accretion rate . . . 167
5.31 Black hole mass distribution vs redshift . . . 167
5.32 Starved AGN interpretation . . . 168

6.1 Warm Corona – sketch of the two coronae scenario . . . 175
6.2 Warm Corona – Fits with TITAN-NOAR . . . 177
6.3 Warm Corona – τ-$log(q_h)$ contours . . . 178
6.4 Jiri's sample . . . 180
6.5 Interpolation of the complete sample . . . 181

A.1 Kramer opacity in JED-SAD . . . 191
A.2 Temperature in JED-SAD . . . 192

B.1 GX 339-4 – Radio interpolation . . . 193

C.1 Grid $(r_J;\dot{m})$ – r_{isco} . . . 196
C.2 Grid $(r_J;\dot{m})$ – m_s . . . 197
C.3 Grid $(r_J;\dot{m})$ – ω . . . 198
C.4 Grid $(r_J;\dot{m})$ – b . . . 199

D.1 Nested sampling – Presentation 1 . . . 202
D.2 Nested sampling applied to the L&R sample – Convergence . . . 203
D.3 Nested sampling applied to the L&R sample – Parameter space . . . 205
D.4 Nested sampling applied to the L&R sample – Soft X-ray added– Parameter space . . . 206

List of Tables

2.1 Model: JED-SAD parameters 40

3.1 GX339-4: Definition of the Hard state 75
3.2 Fitting parameters of the five observations presented in Fig. 3.3. 79
3.3 GX 339-4: Values of $\tilde{f}^*$ 98

4.1 H 1743-322 – Data selection 117
4.2 MONK – JED-SAD parameters used 121
4.3 MONK – Cyg X-1 best fit 124

5.1 Parameters of the AGN JED-SAD table. 133

6.1 MONK – Cyg X-1 best fit 177

List of Abbreviations

ADAF	**A**dvection **D**ominated **A**ccretion **F**low
AGN	**A**citve **G**alactic **N**uclei
ATCA	**A**ustralia **T**elescope **C**ompact **A**rray
BP	**B**landford and **P**ayne
BLR	**B**road **L**ine **R**egion
BZ	**B**landford and **Z**najek
DFLD	**D**isk **F**raction **L**uminosity **D**iagram
DR	**D**ata **R**elease
EHT	**E**vent **H**orizon **T**elescope
FR	**F**aranoff-**R**iley
HERG	**H**igh-**E**xcitation **R**adio **G**alaxies
HEXTE	**H**igh-**E**nergy **X**-ray **T**iming **E**xperiment
HID	**H**ardness **I**ntensity **D**iagram
HMXrB	**H**igh **M**ass **X**-**r**ay **B**inary
HWMT	**H**ard **X**-ray **M**odulation **T**elescope
IXPE	**I**maging **X**-ray **P**olarimetry **E**xplorer
JED	**J**et **E**mitting **D**isk
LED	**L**uminosity–**E**xcitation **D**iagram
LERG	**L**ow-**E**xcitation **R**adio **G**alaxies
LMXrB	**L**ow **M**ass **X**-**r**ay **B**inary
MHD	**M**agneto**H**ydro**D**ynamics
MRI	**M**agneto **R**otational **I**nstability
NICER	**N**eutron star **I**nterior **C**omposition **E**xplore**R**
NuSTAR	**Nu**clear **S**pectroscopic **T**elescope **AR**ray
NLR	**N**arrow **L**ine **R**egion
PCA	**P**roportional **C**ounter **A**rray
READ	**R**adiatively **E**fficient and **A**dvection **D**ominated
RERD	**R**adiatively **E**fficient and **R**adiatively **D**ominated
RXTE	**R**ossi **X**-ray **T**iming **E**xplorer
SAD	**S**tandard **A**ccretion **D**isk
SED	**S**pectral **E**nergy **D**istribution
SDSS	**S**loan **D**igital **S**ky **S**urvey
SNR	**S**ignal to **N**oise **R**atio
VLA	**V**ery **L**arge **A**rray
VLBI	**V**ery-**L**ong-**B**aseline **I**nterferometry
WED	**W**ind **E**mitting **D**isk
XrB	**X**-ray **B**inaries

XMM **X**-ray **M**ulti-Mirror **M**ission

List of Symbols

Free JED-SAD parameters		
m (M)	Black hole mass	Dimensionless ($M_\odot$)
$\dot{m}$ ($\dot{M}$)	Mass accretion rate	Dimensionless ($\dot{M}_{Edd}$)
r_J (R_J)	Transition radius	Dimensionless (R_G)
r_{ISCO} (R_{ISCO})	Radius of the ISCO	Dimensionless (R_G)
ω	Dilution factor	Dimensionless
m_s	Sonic mach number	Dimensionless
b	Power fraction in the jets	Dimensionless

Fixed JED-SAD parameters		
μ	Mid-plane magnetization	Dimensionless
p	Ejection index	Dimensionless

Other Symbols		
B (B_z, B_r, B_Φ)	Magnetic fields strength	T (CGS: G)
L_{Edd}	Eddington luminosity	W
$\dot{M}_{Edd}$	Eddington mass accretion rate (L_{Edd}/c^2)	$kg \cdot s^{-1}$
R (r)	Radius	R_G (dimensionless)
R_G	Gravitational Radius	m
P_{acc} (q_{acc})	Accretion power (volumetric)	W
P_{adv} (q_{adv})	Advection power (volumetric)	W
P_{cool} (q_{cool})	Radiative cooling power (volumetric)	W
P_{jets} (q_{jets})	Power injected in the jets (volumetric)	W
P_{JED}	Accretion power in the JED	W
P_{tot}	Total pressure	Pa (CGS: Ba)
P_{rad}	Radiative pressure	Pa (CGS: Ba)
P_{gas}	Gas pressure	Pa (CGS: Ba)
η_R	Radiative efficiency (radio)	Dimensionless
η_X	Radiative efficiency (X-ray)	Dimensionless
λ_{Edd}	Eddington ratio ($\lambda_{Edd} = L/L_{Edd}$)	Dimensionless
Ξ	compacity ($\Xi = GM/Rc^2$)	Dimensionless
τ (τ_{tot}, τ_T, τ_*)	Optical depth	Dimensionless

Part I

Introduction and Model

Chapter 1

Astrophysical context

Contents

1.1 Accreting black holes and astrophysical jets 9
1.1.1 X-ray binaries 11
1.1.2 Active Galactic Nuclei 13
1.2 Spectral composition 15
1.3 Outbursts dynamics 18
1.3.1 X-ray Binaries outbursts 18
1.3.2 AGN snapshots 19
1.4 Multi-wavelength behavior 21
1.4.1 The radio–X-ray correlation 21
1.4.2 The AGN UV–X-ray correlation 22
1.4.3 Other correlations 23
1.5 Modeling the accretion-ejection process 23
1.5.1 The Standard Disk 23
1.5.2 Corona models 24
1.5.3 Jets 26

Introduction générale

La notion d'objet compact dépend du paramètre de compacité d'un astre astrophysique. Ce paramètre $\Xi = GM/Rc^2$ dépend du rapport entre la masse M et le rayon R d'un astre. Il est utile pour estimer la force gravitationelle d'un astre comparé à sa taille et permet ainsi d'identifier facilement quelle force fondamentale contre-balance la gravité et lui permet de maintenir sa forme. Un astre est identifé comme compact dès lors qu'il possède une compacité supérieure à 10^{-4}. Pour ordre de comparaison, on peut citer les valeurs de compacité de la Terre (7×10^{-10}) ou bien du Soleil (10^{-6}). Il existe trois types d'objets compacts, les naines blanches ($\Xi \sim 10^{-4} \rightarrow 10^{-3}$) où la force de contre-balancement sont les interactions électromagnétiques, les étoiles à neutrons ($\Xi \sim 0.3$) où la force de contre-balancement provient de la pression de dégénérescence des électrons, et enfin les trous noirs où il n'existe pas de force de contre-balancement et l'astre s'est effondré en une singularité, par convention, sa compacité Ξ est fixée à 1. Au cours de cette thèse, je vais principalement m'intéresser à ce dernier type d'objet, les trous noirs.

Historiquement, les trous noirs n'étaient qu'une fascination théorique qui remonte jusqu' au XVIII^{me} siècle. En physique Newtonienne, on est capable de définir la vitesse de libération $v_l = \sqrt{2GM/r}$ qui permet, à un objet se situant à une distance r d'un astre de masse M, d'échapper à l'attraction gravitationnelle de l'astre. Au dessus de cette vitesse, l'objet pourra s'échapper à l'infini, en dessous, il restera à jamais piégé dans l'influence gravitationnelle de l'astre. John Michell (1784) puis Pierre-Simon Laplace (1796) ont considéré cette formule pour un objet ayant une vitesse égale à la célérité de la lumière c. Cette particule ne peut s'échapper uniquement si elle se situe à une distance $r > R_G = 2GM/c^2$ de l'astre. En dessous de ce rayon, même la lumière (considéré comme une particule ans cette exercice) ne peut s'échapper de l'astre. Ces objets dont même la lumière ne s'échappe pas sont appelés trous noirs (la première mention de ce nom n'interviendra que dans les années 1960).

Peu après la publication des la théorie de la relativité générale d'Albert Einstein (1915), Karl Schwarzschild résout l'équation dans le cas d'une symétrie sphérique dans le vide. Cela donnera lieu à la métrique de Schwarzschild, dépendant uniquement de la masse M de l'astre, utilisé pour décrire l'espace-temps autour de trous noirs non chargés et statiques (signifiant sans rotation sur lui même). Dans les années 60 et 70, Werner et Carter montrent qu'il existe au plus 3 paramètres classiques pour décrire un trou noir: sa masse M, son moment angulaire J et sa charge Q (bien qu'il est difficile d'imaginer qu'un trou noir soit chargé électriquement puisque que cela impliquerait une force électrique attirant des charges opposées et qui finiraient par rendre le trou noir neutre électriquement). En 1963, Kerr étend les solutions de Schwarzschild au cas plus général d'un trou noir en rotation, c'est la métrique de Kerr (Kerr 1963).

L'astronomie est historiquement une science d'observations dont le messager principal est la lumière. C'est pourquoi les trous noirs, d'où ne s'échappent aucun photon, sont restés pendant longtemps une fascination théorique sans grand intérêt pour les astronomes. Ce n'est qu'avec la découverte de la première source compacte nommée Cyg-X1 émettant des rayons X en 1962, à l'aide de télescope embarqué dans des fusées pour échapper à l'absorption de l'atmosphère, que la science des objets compacts est mise en avant. Il faudra attendre le premier satellite d'observation X Uhuru (NASA) dans les années 70 pour mesurer la masse de la source et identifier sa nature comme le premier candidat trou noir. En effet le système est identifié comme binaire, composé d'une super-géante bleue et d'un objet compact d'une masse au moins supérieure à 6 $M_\odot$. Cette valeur est significative car les modèles d'étoiles à neutrons prédisent une masse maximale de ces objets entre 1.6 et 3.1 $M_\odot$ (Salgado et al. 1994). Cette source ne peut donc pas être une étoile à neutrons. Cependant, par définition un trou noir n'émet pas de lumière, quelle est donc l'origine des photons X observés ? Cette émission haute énergie provient de la conversion de l'énergie potentielle gravitationnelle de

la matière qui tombe sur le trou noir. Ces photons sont donc émis à l'extérieur du trou noir alors que la matière devient de plus en plus rapide et chaude à mesure qu'elle s'approche du trou noir durant le processus d'accrétion.

L'exemple de Cyg-X1 révèle comment les astronomes et astrophysiciens sont capables d'observer et d'étudier les trous noirs. On détecte les effets de son fort champ gravitationelle sur la matière environnante qui elle est capable d'émettre des photons. Grâce à cette méthode, des dizaines de trous noirs de masses stellaires (5 à 30 $M_\odot$ généralement) ont été identifiés au coeur de systèmes binaires X et des milliers de trous noirs super-massifs (avec des masses pouvant atteindre des millions voir de milliards de masse stellaire) ont été découvert au centre des galaxies. En 2020, Reinhard Genzel and Andrea Ghez ont reçu le prix Nobel pour leur découverte de Sgr A, le trou noir super-massif de notre galaxie (Ghez et al. 1998, 2005, 2008; Genzel et al. 2003, 2010). Celui ci a été identifié uniquement à partir de son influence gravitationnelle sur les orbites des plusieurs étoiles du cnetre de notre galaxie. Très récemment, en 2021, les premières images résolues spacialement de l'évènement des horizons de 2 trous noirs super-massifs, M87 et Sgr A* (voir Event Horizon Telescope Collaboration et al. 2019, 2022), ont été obtenues par la collaboration Event Horizon Telescope (EHT). Enfin, avec la découverte en 2015 des premières ondes gravitationelles par la collaboration LIGO-VIRGO (Abbott et al. 2016), une nouvelle fenêtre d'observations, ne dépendant pas de photons mais de la déformation même de l'espace-temps alors que deux objets compacts coalescent, s'ouvrent vers les trous noirs. Cette découverte fut elle aussi récompensée par un prix Nobel pour Rainer Weiss, Kip Thorne and Barry Barish en 2017. depuis plus d'une centaine d'évènements de coalescence d'objets compacts ont été observés. Au cours de cette thèse, je vais principalement me concentrer sur la première méthode d'observation, utilisant l'émission haute énergie de la matière environnante des trous noirs.*

Les binaires X

Les binaires X son des systèmes composées d'un objet compact (dans mon cas un trou noir de masse stellaire) et d'une étoile 'compagnon' (Voir Fig. 1.1 pour une image d'artiste). Elles sont principalement observées dans notre galaxie. Sous l'influence gravitationelle de l'objet compact, le compagnon va se déformer et remplir son lobe de Roche. Le lobe de Roche est la région où la matière reste gravitationellement lié à un astre. La matière en surface du compagnon va subir une attraction gravitationelle supérieur à sa cohésion gravitationelle. Elle est alors tirée et transférée vers l'objet compact. Le gaz, conservant un haut moment angulaire comparer à l'objet compact, va former un disque autour du trou noir. Dans le disque, la matière est en rotation différentielle, c'est à dire que sa vitesse de rotation dépend de sa distance au trou noir. Ainsi pour que la matière accrète et tombe sur le trou noir, celle ci doit perdre son moment angulaire. Ce transport du moment angulaire est une étape clé et nécessaire au processus d'accrétion. Alors que le gaz s'approche du trou noir, son énergie potentielle gravitationelle est libérée en rayonnement. La luminsoité maximale L_{acc} du flot d'accrétion peut être estimée à partir de la formule $L_{acc} = \eta \dot{M} c^2$, où $\dot{m}$ est le taux d'accrétion de la matière et η l'efficacité de la conversion de l'énergie cinétique en rayonnement (pour un trou noir, elle est de l'ordre de 10%). De même on peut définir une luminosité maximale que le flot ne peut dépasser: la luminosité d'Eddington L_{Edd} (voir Eq. 1.1). Celle ci ne dépend que de la masse du trou noir. En effet au dessus de cette valeur, la pression de radiation dans le flot d'accrétion sera suffisante pour contre-balancer l'attraction gravitationelle du trou noir et le gaz sera repoussé. Il est important de noter que cette limite définie par l'Eq. 1.1 repose sur des hypothèses, notamment une symétrie sphérique de l'accrétion, ce qui n'est pas le cas puisque celle ci se fait sous forme de disque. Cette limite peut donc parfois être dépassée.

La plupart du temps, les binaires X sont dans un état quiescent, de faible accrétion, et ne sont pas détectables. Les binaires X sont principalement découvertes et observées au cours

d'éruptions, pendant lesquelles elles sont bien plus brillantes et leur luminosité X atteint une fraction de leur limite d'Eddington, elles sont alors dans un état de forte accrétion. Ces éruptions peuvent durer de quelques mois à une année. L'origine physique de ces éruptions n'est pas encore complètement comprise, Une possibilité est le modèle de disque Instable (DIM, Dubus et al. 2001; Coriat et al. 2012; Hameury et al. 2017).

Les binaires X présentent aussi des jets de matières très grands devant la taille de leur système. Ces jets, habituellement observés dans les fréquences radio montrent un spectre plat cohérent avec une émission synchrotron. Les jets présentent des vitesses relativsites et transportent une grande partie d'énergie cinétique. Le processus de formation et d'accélération des jets n'est pas encore compris. Mais les meilleurs modèles à ce jour supposent tous la présence de fort champ magnétique autour du trou noir. Ces jets peuvent aussi servir comme un mécanisme de l'évacuation du moment angulaire permettant l'accrétion.

Les Noyaux Actifs de Galaxies

Les trous noirs super massifs sont présents au centre de toutes les galaxies (comme le suggère la présence du trou noir dormant Sgr A au centre de notre galaxie). Cependant, on ne peut détecter uniquement les plus actifs, d'où le nom Noyaux Actifs de Galaxies (NAG). Dans les NAG, le flot d'accrétion n'est pas alimenté par une étoile compagnon, mais par la grande quantité de gaz entourant le centre de la galaxie. La formation et croissance de ces trous noirs super-massifs n'est pas claires. Mais les études suggèrent une connections directe entre la formation stellaire des galaxies et la puissance d'accrétion des trous noirs en leur centre (Harrison 2017). Comme leur cousins de masse stellaire, les NAG présentent aussi des jets astrophysiques (voir Fig. 1.2). Ces jets permettent de transporter l'énergie au travers d'échelles de taille très différentes, procurant une rétroaction dans la galaxie et liant l'évolution du trou noir super-massif et sa galaxie hôte. Les NAG peuvent avoir des masses entre* 10^5 *et* 10^10 $M_\odot$. *La plupart des quantités d'un trou noir grandissent linéairement avec la masse, y compris sa taille et son temps caractéristique d'évolution. De ce fait, on ne peut pas observer l'éruption d'un NAG comme on le fait pour les binaires X. Ces éruptions dureraient des milliards d'années. A la place, on utilise des études statistiques sur des échantillons de NAG.*

Les NAG montrent un très grand nombre de comportements et forment alors une zoologie complexe, influencée par son environnement, l'angle d'observation ou encore son état d'accrétion. Selon l'intérêt scientifique, il existe plusieurs façons de les classifier. On peut résumer ces classifications à 3 principaux composants: la présence d'une émission radio forte (identifiée comme la présence d'un jet), la variabilité et polarisation de la source, ou encore la taille de raies d'émissions de la source. Une manière de résumer cela à été proposée dans la Fig. 1.3 produite dans la thèse de (Biteau 2013).

Composition spectrale

La composition spectrale large-bande des trous noirs est complexe et présente plusieurs composantes s'étendant de la radio jusqu'au rayon γ. *Certaines composantes proviennent du flot d'accrétion lui même, d'autre de la matière environnante. Je vais ici formuler les principales composantes.*

Qu'ils soient présents dans une binaires X ou un NAG, les trous noirs accrétant possèdent une émission de corps noir d'un disque froid (voir ligne bleue sur les Figs. 1.4 et 1.5). Alors que la matière approche du trou noir, elle chauffe et émet une émission de corps noir à différentes températures (Shakura & Sunyaev 1973; Mitsuda et al. 1984). Le spectre résultant est alors la somme de tout ces corps noirs. On peut montrer que la température dans le disque est inversement proportionnelle avec la masse du trou noir. De ce fait les binaires X

piquent à haute énergie autour de 1 ou 2 keV, alors que les NAG piquent dans les UV autour de 1 et 20 eV.

La plupart des trous noirs présentent une émission en loi de puissance X dure (ligne rouge dans la Fig. 1.4 et cyan dans la Fig. 1.5). L'indice spectrale de la loi de puissance Γ *est autour de 1.8 (c'est à dire que le flux de photons* F_{ph} *est proportionnel à la fréquence des photons avec un indice 1.8,* $F_{ph} \propto \nu^{-1.8}$*). Cette composante présente une coupure exponentielle à haute énergie à des températures variables, suggérant une origine thermique. Elle est supposée provenir de la diffusion compton des photons émis par le disque froid sur des électrons chauds à l'intérieur d'une couronne chaude quelque part proche du trou noir. La température de cette coupure nous informe directement sur la température des électrons dans la couronne puisque ceux ci ne peuvent pas fournir plus d'énergie aux photons que ceux qu'ils possèdent. Les caractéristiques et la géométrie de la couronne chaude restent à ce jour sans consensus dans la communauté scientifique.*

Une partie de l'émission en loi de puissance peut être réfléchie sur le disque froid. Cela produit la composante de réflection (en vert sur les Figs. 1.4 et 1.5). Celle ci est notamment caractérisé par la présence d'une raie du fer autour de 6.4 keV. Enfin comme déjà mentionné, des jets sont observés comme un spectre plat dans les bandes radios.

Dynamique d'éruption

Les éruptions de binaires X suivent habituellement la même évolution. On la représente dans un diagramme d'intensité-dureté (HID, voir Fig. 1.6), où on trace la luminosité (parfois divisée par la luminosité d'Eddington des trous noirs pour comparer différentes sources) d'une observation en fonction de la dureté du spectre. La dureté peut être comprise comme une couleur, il s'agit du rapport de flux entre 2 bandes d'énergies dans les X. Lorsque le spectre est 'mou', celui ci est dominé par la composante à basse énergie provenant du disque froid. Lorsque le spectre est 'dur', celui ci est dominé par l'émission en loi de puissance provenant de la couronne chaude.

Dans un HID, une éruption suit habituellement une forme en 'q' et présente à la fois une dichotomie spectrale et dichotomie dynamique. Une éruption commence dans un état quiescent dur. La luminosité va augmenter tout en restant dans un état dur, dominé apr l'émission de la couronne chaude. La présence de jets est alors observés en radio. Au bout d'un moment, le spectra transite vers les états mous. C'est au cours de cette transition que le jet semble disparaître alors que le disque devient de plus en plus chaud et lumineux. Cette transition se fait habituellement à luminosité constante. Une fois dans l'état mou, l'émission radio et X dure a disparu. Seule l'émission de corps noir du disque subsiste. La luminosité de la source va alors commencer à diminuer. Le système finit par retourner vers les états durs (une fois de plus à luminosité constante). Au cours de cette seconde transition, les jets semblent apparaître de nouveau. Curieusement, cette transition mou $\rightarrow$ *dur se fait habituellement toujours au même taux d'Eddington (rapport de luminosité sur la luminosité Eddington des sources). Finalement, la source retourne en quiescence. Pour une revue complète, on peut se référer à Dunn et al. (2010).*

Les temps caractéristiques des NAG étant bien plus élevés que celui des binaires X, on ne peut observer l'éruption d'un NAG. A la place, on peut associer la séquence temporelle d'état d'accrétion-éjection observée dans une binaire X aux images stationnaires observés dans différents NAG. Chaque NAG représenterait alors un état d'accrétion-éjection dans le diagramme en 'q' du HID. Malheureusement, cela n'est pas si facile, puisque chaque NAG est différent d'un autre (masse, environnement, angle d'observation...). De plus tout les processus physiques ne grandissent pas avec la masse de trou noir (diffusion compton par exemple), et de ce fait, un même état dynamique peut avoir différents états spectraux selon la masse du NAG.

Des corrélations entre les émissions provenant de différentes composantes sont observées. Par exemple, au cours des états durs des binaires X, où l'émission est dominée par la couronne chaude et où des jets radio sont observés, l'émission radio et l'émission X dure sont corrélées (voir Fig. 1.7 ainsi que Corbel et al. 2000, 2013; Gallo et al. 2003; Coriat et al. 2011). Cela suggère un fort lien entre ces deux composantes. C'est pourquoi on parle de processus d'accrétion-éjection. Quel est donc le lien entre le jet et la couronne chaude ? Cette corrélation n'est cependant pas seulement limité au binaire X, mais s'étend aussi au trous noirs super-massifs. C'est ce qu'on appelle le plan fondamental d'activité des trous noirs (Merloni et al. 2003). Ce dernier point suggère que ces processus d'accrétion-éjection sont commun quelque soit la taille du trou noir. Une autre corrélation est observée uniquement dans les NAG entre l'émission UV, provenant du disque froid, et de l'émission X dure, provenant de la couronne chaude. Cependant la non linéarité de cette corrélation UV-X est intéressante car elle cache une physique non comprise. Pourquoi les trous noirs plus massifs seraient moins lumineux dans les rayons X ?

Dans cette thèse, je vais principalement travailler avec un modèle d'avant garde d'accrétion-éjection développé dans mon laboratoire. Je vais le présenter dans le chapitre 2. Je vais tout d'abord chercher à l'appliquer pour la première fois à de observations de binaires X, me concentrant notamment sur la source GX 339-4 dans le chapitre 3. Dans le chapitre 4, je vais mentionner d'autres applications aux binaires X que j'ai été amené à faire en collaborations avec des collègues. Dans une seconde partie de ma thèse, je me suis focalisé sur l'application aux NAG, et notamment à la reproduction de la corrélation UV-X dans le chapitre 5. Enfin, je mentionnerai d'autres projets et pistes de recherches concernant les NAG dans le chapitre 6.

1.1 Accreting black holes and astrophysical jets

The notion of compact objects encompass three categories of objects. To identify them, we can use the dimensionless compacity parameter $\Xi = GM/Rc^2$, depending on the mass M and radius R of the object. The compacity parameter is useful to estimate the gravitational pull of an object compared to its size and can then indicate which force is used as a counterbalance to gravity to maintain the object's size. An object is defined as compact when its compacity is superior to 10^{-4}. For comparison sake, the compacity of a planet like Earth, where the counterbalance force comes from electromagnetic interactions, is of the order of 7×10^{-10}, as for the Sun, where the thermal gas pressure acts as counterbalance, it is of the order of 10^{-6}. In order of increasing compacity, the three categories of compact objects are: white dwarfs where the counterbalance is ensured by the degeneracy pressure from electrons, with masses $M \sim 0.1 \rightarrow 1.4\,M_\odot$, a typical radius $R \sim 10\,000$ km, resulting in a density $\rho \sim 10^6 \rightarrow 10^7$ g.cm^{-3} and a compacity $\Xi \sim 10^{-4} \rightarrow 10^{-3}$. ; neutron stars, dominated by the Strong interaction, with masses $M \sim 1 \rightarrow 3\,M_\odot$, a typical radius $R \sim 10$ km, resulting in a density $\rho \sim 10^{15}$ g.cm^{-3} and a compacity $\Xi \sim 0.3$; and finally black holes, where no force is able to counterbalance the gravitational pull resulting in the collapse of the object into a singularity, by convention, its compacity Ξ is fixed to 1. In this thesis, the subject of interest will mostly lie with this last category, black holes. So what is a black hole?

Going back in time, the first consideration of these objects is purely theoretical and date back to the late 18^{th} century. In Newtonian physics, one can define the speed required to escape a spherical gravitational field, this speed is defined as the escape velocity $v_e = \sqrt{2GM/r}$ at a given distance r of the gravitational source of mass M. A particle with a speed above this critical value will be able to escape to infinity, below this value, the particle will forever be stuck in the gravitational field. John Michell (1784) and Pierre-Simon Laplace (1796) considered this formula for a particle of light of velocity c[1]. They found that the light emitted at the surface of a gravitational source could only escape to infinity if the object possessed a radius $r > R_G = 2GM/c^2$. Below this value, the escape velocity at the object's surface would be higher then c, and thus not even light can escape the gravitational pull. These objects, from which not even light can escape, are named black holes[2].

Not long after the publication of the general relativity theory in 1915 by Albert Einstein, Karl Schwarzschild solved the exact solution of Einstein's spherical symmetric equation in the void. This solution, depending only on the mass M of the object, can be used to define the space-time around any given spherical gravitational source. In the case of black holes, it is used to define the Schwarzschild metric and to describe space-time around a static relativistic black hole. In the 60s and 70s, Werner and Carter showed that a black hole requires at-most 3 classical parameters to be described, a mass M, and angular momentum J and an electrical charge Q. This was summarized by Wheeler in the sentence "black holes have no hair", meaning that beside these three parameters, there is not a single supplementary hidden parameter. However, it seems unlikely that a black hole is charged as this would imply an electrical force pulling opposed charges on the black hole, soon resulting in a neutral black hole. The space-time around a spinning neutral black hole is described by the Kerr metric (Kerr 1963).

[1] This velocity, first measured by Huygens and Romer in 1675 and later by Bradley in 1729 was then known to be around 220 000 and 301 000 km.s^{-1}.

[2] The first actual mention of this name only appears in the 1960s.

Astronomy is a fundamentally observational science and the main messenger of information are photons. As such, black holes, from which no light can be emitted, remained for a long time objects of purely theoretical consideration, without great interest for astronomers and astrophysicists. It is only in 1962 with the discovery of the first compact sources emitting X-rays that the physics of compact objects is put under the spotlight. To observe these X-ray compact sources, astronomers had to send instruments in space to circumvent the atmospheric absorption, first by sending them on board of rockets and latter placing them on satellites. In 1964, one source was found in the Cygnus constellation but no optical counterpart was identified, leaving its nature as a mystery. It was then named Cyg-X1. The launch of the first X-ray satellite *Uhuru* by NASA allowed to shed some light on its nature as the first black hole *candidate*. In 1970, this source was observed, narrowing the uncertainty of its location, and showing variability on short time scale, shorter than the second[3]. Such short time scale suggests a high energy emission from a compact source. The identification of an optical counterpart and the measure of its Doppler shift showed an orbital motion, revealing this source to be a binary system. A blue super-giant star emitting in the optical and UV range of the spectrum is orbiting a compact high energy emitting source. The mass of the compact object was estimated from orbital motion at around 6 $M_\odot$. This value is significant as all neutron star equation states imply a maximum mass between 1.6 and 3.1 $M_\odot$ (Salgado et al. 1994), as such, this compact source can not be a neutron star and thus is the first black hole *candidate* discovered. But, by definition, a black hole does not emit light, so where does the X-ray emission come from? These high energy emitting sources are powered by the conversion of the gravitational potential energy from the matter falling down on the black hole. Meaning that the light we see is emitted outside the black hole as the matter becomes hotter and faster when it falls down on the black hole during the process of accretion.

The example of Cyg-X1 reveals how astronomers and astrophysicists are able to observe and study black holes: one can observe the gravitational effects of its strong gravitational field on the light-emitting matter surrounding it. Using this method, dozens of stellar mass black holes have been identified in X-ray binary systems within our galaxy, and thousands supermassive black holes, with masses as high as tens of billions of solar masses have been identified at the center of other galaxies. In 2020, Reinhard Genzel and Andrea Ghez were awarded the Nobel prize for the discovery of Sgr A*, a supermassive black hole at the center of our own galaxy (see for instance Ghez et al. 1998, 2005, 2008; Genzel et al. 2003, 2010). Sgr A* was identified only thanks to its influence on the orbits of multiple stars in the center of our galaxy. Very recently, in 2021, the Event Horizon Telescope (EHT) collaboration was able to spatially resolve the inner region of two supermassive black holes, M87 (see Event Horizon Telescope Collaboration et al. 2019 and subsequent papers) and Sgr A* (Event Horizon Telescope Collaboration et al. 2022), and for the first time observe the event horizon of a black hole. Using a large number of radio telescopes around the globe, they virtually obtained an Earth-sized radio interferometer. Finally, with the recent discovery of the first gravitational wave event in 2015 by the LIGO-VIRGO observatories (Abbott et al. 2016), another window of observation has been opened to study black holes. Gravitational waves are ripples in the curvature of space-time and propagating in the universe. They result from the acceleration of compact objects, particularly during coalescence events of two black

[3]The limit of detection at that time, this source is now known to possess even shorter time scale variability.

holes. They were predicted a century before their first observation by the theory of general relativity. In 2017 Rainer Weiss, Kip Thorne and Barry Barish were awarded the Nobel prize for the first direct detection of gravitational waves. Since then, more then a hundred of events were detected, allowing the study of black holes mergers as well as neutron star mergers. The future gravitational waves observatories like the LISA project will allow to explore a new region of gravitational wave frequency, allowing the study of mergers involving supermassive black holes. These examples show that, most observations are consistent to the theoretical expectations from general relativity and that the current interest for black hole observation is growing with new powerful methods to study. In this thesis, I will mostly tackle the first observational method of detection, based on the high energy emission coming from the in-falling matter.

1.1.1 X-ray binaries

X-ray binaries (XrB) are binary systems composed of a stellar mass black hole, and an orbiting companion or donor star (see Fig. 1.1 for an artist view). They are mostly observed within our own galaxy. Under the extreme gravitational influence of the compact object, the companion star can be deformed during its orbit and will fill its Roche lobe. The Roche lobe is defined as the region where the material is gravitationally bound to the star. In binary systems, the Roche lobe will have a teardrop shape extending toward the companion object, the black hole. When this happen, the gravitational pull from the compact object on the surface of the companion star becomes stronger than the gravitational cohesion of the star itself and gas in the external region of the star is transferred toward the compact object. Some companion stars can be massive, resulting in the presence of stellar winds that can feed the compact object accretion disk continuously. We can distinguish two type of XrB depending on the mass of the companion star. If the companion star is more massive

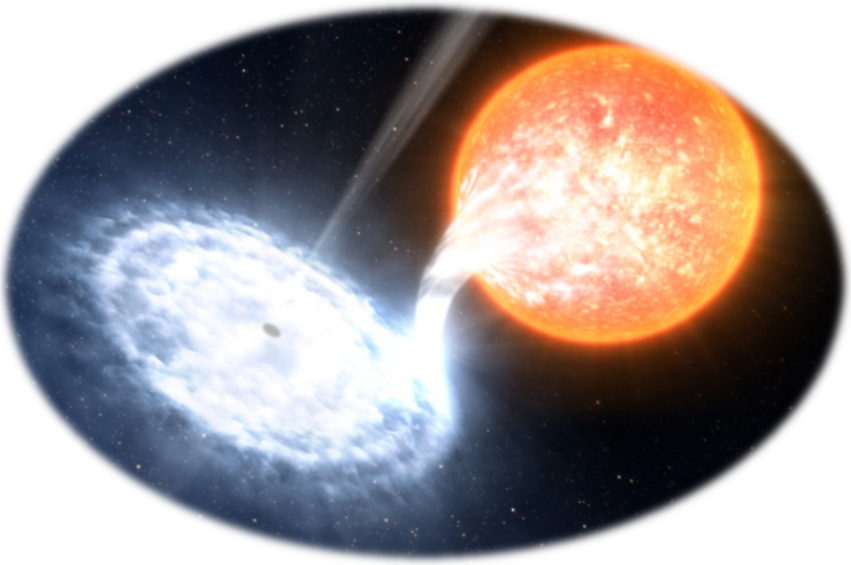

FIGURE 1.1: Artist view of an X-ray binary system. The companion or *donor* star is losing matter through Roche lobe overflow. The gas is pulled toward the black hole and forms an accretion disk around it. The accretion flow will radiate high energy X-ray emission, giving its name to X-ray binaries. Some matter is accelerated and ejected, forming jets, when getting close to the black hole.

than 10 $M_\odot$, and thus sometime more massive than the compact object, the system is called a High Mass X-ray binary (HMXrB). HMXrB are more likely to have main sequence stars with spectral class O or B or in a more advanced state of stellar evolution: blue super-giants. The companion star is then easily detected and stronger constrains on the compact object mass can be inferred. HMXrB are also more likely to present thermal or line driven winds from the companion star which will feed the compact object. If the mass of the companion star is lower, the system is called a Low Mass X-ray binary (LMXrB). In this case, the companion star is most likely to be a main sequence star that will not present any winds. The black hole will then only be fed by Roche lobe overflow.

The material transferred from the donor star to the compact object maintains a given amount of angular momentum compared to the smaller compact object. Due to friction, the gas will flatten in the direction of the total angular momentum and form an accretion disk around the black hole. In the disk, the material is in a differential rotation, meaning that the gas orbital velocity depends on the radius. As such, the gas must lose angular momentum in order to move inwards and be accreted on the black hole. The transport of angular momentum appears as a unavoidable requirement for accretion to occur. As it is accreted toward the black hole, the matter's gravitational energy will be converted and released as high energy emission in the X-ray energy band. One can define the maximum luminosity L_{acc} of the accretion flow by assuming the conversion of accreted mass energy into radiation: $L_{acc} = \eta \dot{M} c^2$, where $\dot{m}$ is the mass accretion rate and η is the radiative efficiency of conversion from the kinetic energy to radiation of the gas. The value of η can be inferred from the kinetic energy at the surface R of the compact object for a particle of mass m, initially at rest at infinity: $E = GMm/R$. The total energy deposited on the object is then $L_{acc} = GM\dot{M}/R = R_G/R\dot{M}c^2$, where $R_G = GM/c^2$ is the gravitational radius. Thus $\eta = R_G/R$. In the case of black holes, the compact object does not possess a surface and the energy must be released before reaching the event horizon. Similarly, one can identify an upper limit of luminosity. The mass accretion rate can not be arbitrarily large, at some point, the radiation pressure created by the inner region of the accretion flow will overcome the gravitational force and push back the in-falling gas. This limit, called the Eddington luminosity L_{Edd}, is then obtained from the equilibrium of the radiation pressure and gravitational force. Assuming that Thomson scattering dominates radiation pressure, we get:

$$L_{Edd} = \frac{4\pi GMm_p c}{\sigma_T} = 1.3 \times 10^{38} \left(\frac{M}{M_\odot} \right) \text{ erg} \cdot \text{s}^{-1} \tag{1.1}$$

This luminosity constitutes a theoretical upper limit for accreting systems and provides an idea of their typical luminosity. It should however be noted that some rare systems reach super-Eddington luminosity $L_{acc} > L_{Edd}$, possibly due to the simplification behind the displayed computation of the luminosity limit (spherical accretion, Thomson scattering domination).

Most of the time XrB remain in a quiescent state and are not detectable. In this state, the flow of gas in the disk is very shallow. XrB are mainly discovered when they enter outbursts during which their X-ray luminosity becomes much brighter, reaching a fraction of their Eddington luminosity, they are then in a state of high accretion. These outbursts can last from a few months long up to a year. During the outburst, the luminosity and thus the mass accretion rate increases by multiple orders of magnitude. The physical process at the origin of these outbursts is not yet

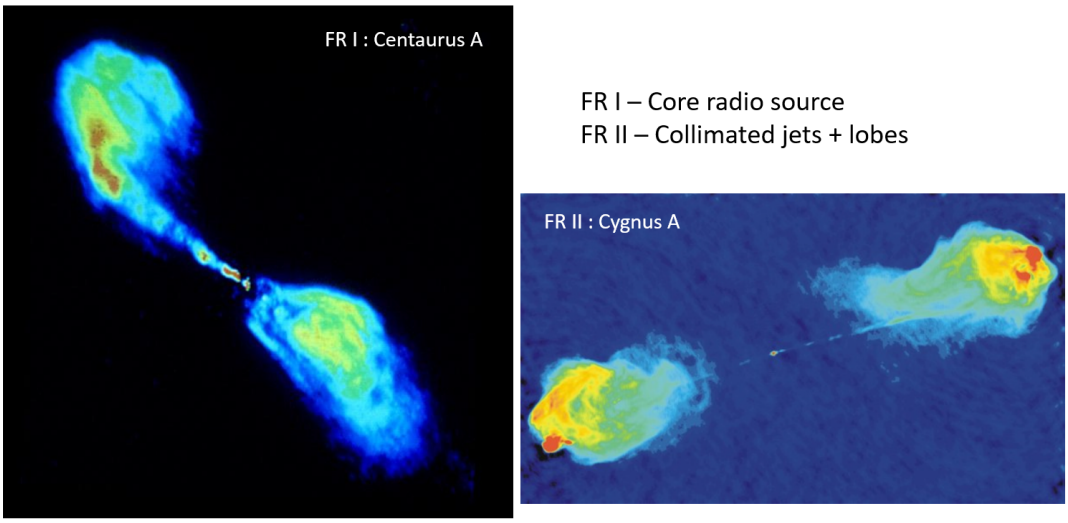

FIGURE 1.2: *Left*: Example of FR I class AGN, Centaurus A observed by the Very Large Array (VLA). Core emission are observed in the radio jets. *Right*:Example of FR II class AGN, Cygnus A observed by VLA. The radio jets are collimated and almost invisible, two strong radio lobes are observed at the terminal points of the jets.

known. One possibility is a modified version of the Disk Instability Model (DIM). In the DIM, the accretion flow remains stable as long as hydrogen is neutral everywhere in the accretion flow, usually in a cold and low density disk. But if either the temperature or the mass accretion rate from the companion star becomes high enough for hydrogen to be ionised, the disk becomes thermally and viscously unstable. The disk than oscillates between a hot, ionized state (outburst) and a cold, neutral state (quiescence). Illumination from the inner region of the disk heating the external regions and ionizing hydrogen, combined with disk evaporation have been shown to reproduce the typical timescale of the outbursts (Dubus et al. 2001; Coriat et al. 2012; Hameury et al. 2017).

XrB also show the presence of large scale jets that can stretch for millions of gravitational radii from the sources. These jets are usually observed in the radio frequency range and have flat radio spectra consistent with synchrotron emission. They exhibit relativistic velocities, transporting a lot of kinetic energy. The physical processes behind the formation and acceleration of the jets is still unknown, but currently, the best guess involve strong magnetic fields and possible pair creation in the black hole magnetosphere. The jets might also be one of the possible mechanisms allowing the extraction of angular momentum from the accretion flow.

1.1.2 Active Galactic Nuclei

Supermassive black holes are most certainly present at the center of all galaxies (as shown by the presence of the quiescent supermassive black hole Sgr A* in our galaxy). Yet we only detect them in the most Active Galactic Nuclei (AGN). In AGN, the accretion flow is not fed by a companion star but rather by the large quantities of gas present in the center region of the host galaxies. Most AGN are thus surrounded by a large dust and gas torus. It is expected that a quiescent supermassive black hole would look like Sgr A*, the supermassive black hole at the center of our galaxy. The formation and growth of these supermassive black hole is unclear. However, studies show a direct connection between the star formation powered growth of a

galaxy and the accretion powered growth of the black hole at its centre Harrison (2017). Like their smaller stellar mass cousins, AGN show the presence of strong relativistic jets larger than their host galaxies (see Fig. 1.2). The jet gives a physical mechanism to transport energy across very different scales, procuring a feedback in the galactic environment and linking the black hole and its host galaxy together across cosmic time. AGN span a large range of mass, from $10^5\,M_\odot$ to $10^{10}\,M_\odot$. In black holes, most quantities scale linearly with the mass, including their size. Consequently, supermassive black holes are much larger and thus have much longer time scales compared to XrB. As such, one does not expect to observe an AGN outburst within a lifetime. This also implies that any study of supermassive black hole evolution calls for a statistical approach and one should be mindful of the possible selection biases they introduce in their study.

AGN exhibit a large range of behaviour, forming a complex zoology that can be influenced by the AGN environment, angle of observation (relativistic boosting effects of the jets and possible obscuration of the inner regions by the dust torus, Urry & Padovani 1995) and their accretion states. Depending on the scientific interest (line science, jets, X-ray astronomy...), there are many ways to classify AGN. One can summarize most classification using three main characteristics of AGN: the radio loudness defined as the ratio between the fluxes in a radio and optical band, marking whether the radio jet dominates in the Spectral Energy Distribution (SED) or not; variability and polarization, mainly depending on the alignment of the jets and procuring a relativistic boosting effect toward the observer; and the width of the emission line, which informs us on the disk illumination and obscuration. I find this to be well resumed in Fig. 1.3 that I shamelessly adapted from the PhD. Thesis of Biteau (2013). Below, I will try to list some of the possible classifications:

Radio galaxies and the The Faranoff-Riley classification

Radio galaxies are AGN with a radio loudness superior to 10. They can be classified depending on the properties of their jets in the Faranoff-Riley (FR) classification. FR

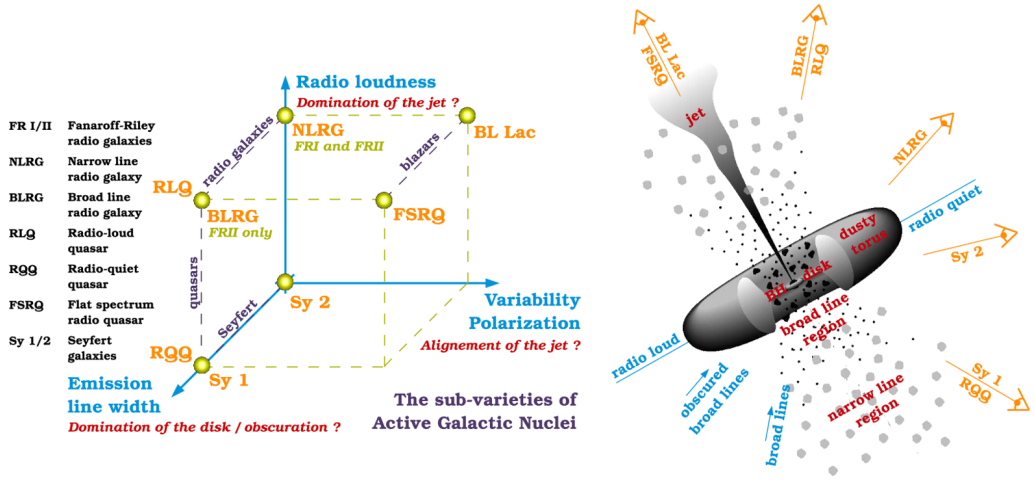

FIGURE 1.3: *Left*: How to classify AGN based on three main parameters, radio loudness, emission line width and polarisation properties. *Right*: AGN structure and how the observational inclination might impact the AGN classification. At the top: the radio loud case; at the bottom: the radio quiet case. *Credits: PhD. Thesis of Biteau (2013).*

I sources possess strong visible radio cores and the jets extends in lobes. FR II AGN show two very luminous radio lobes where the jets decelerate as they interact with the surrounding interstellar material, the jet appear strongly collimated and is not always visible (See Fig. 1.2). Radio galaxies can also be classified depending ont the broadness of their emission line.

Seyfert galaxies

Seyfert galaxies are radio quiet AGN that can be classified depending on the broadness of their optical emission lines. These emission lines are the result of the reprocess of the inner region ionizing emission in gas clouds, possibly resulting from disk winds. Seyfert 2 galaxies (Sy 2) only present narrow emission line that are interpreted with the presence of gas clouds only in a region far away from the black hole, the Narrow Line Region (NLR). Seyfert 1 galaxies (Sy 1) present both broad lines and narrow lines, the lines are suffering from general relativistic broadening due to the close proximity of the gas clouds to the black hole, the Broad Line Region (BLR). One possibility is that AGN always present both a broad line and narrow line region, but depending on the observation angle, we might only see the NLR, the BLR being hidden by the dust torus.

Quasars

Quasar is the historical term used to describe objects that looked like point-like sources, and so appears as stars, yet do not present a stellar spectra. They are very distant galaxies from which we can not separate the nucleus, host galaxy and extended jets emission. Both radio loud and radio quiet quasars exist.

Other classifications

Depending on the excitation class, line scientists can separate radio loud AGN between the LERGs (Low Excitation Radio Galaxies) and HERGs (High Excitation Radio Galaxies).

1.2 Spectral composition

Spectrally, accreting black holes present a complex broad band shape presenting multiple components from the radio to the γ-rays. Some components originating from the accretion flow itself, others from their surrounding environment. In this section, I will describe the main spectral components and what we know about their nature and physical origin.

Cold disk emission

Whether they be XrB or AGN, accreting black hole present a disk blackbody emission (see the blue line in Figs. 1.4 and 1.5). This optically thick and thermal emission originates from the cold region of the accretion flow. As the matter approach the black hole, its temperature increases. Each annulus of the disk is then emitting a blackbody with different temperature. The resulting spectrum is then the sum over all radii of these different temperature components, forming a multi-colour disk blackbody (e.g. Shakura & Sunyaev 1973; Mitsuda et al. 1984). One can show that the temperature of the disk depends inversely with the black hole mass. As

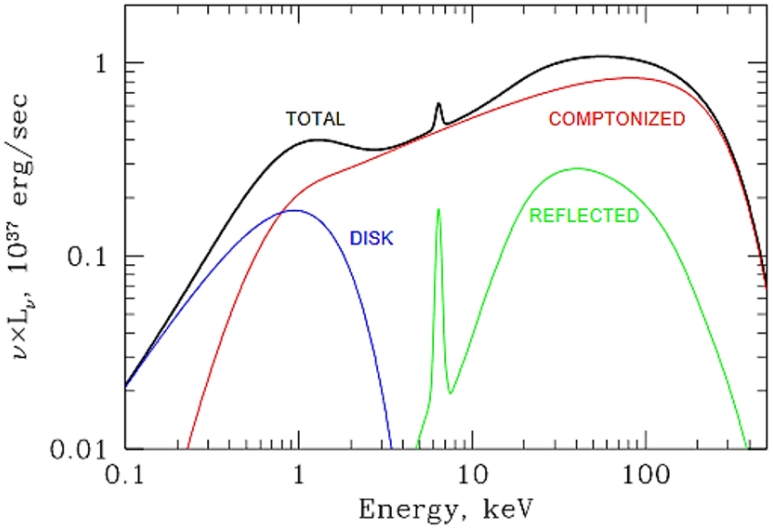

FIGURE 1.4: Typical spectrum of a *hard* X-ray binary. There are three main spectral components: the disk blackbody emission (blue), the comptonized emission coming from the hot corona (red) and the reflection of the hot corona emission on the cold disk (green).

such a stellar mass black hole disk blackbody will peak at a higher energy compared to a supermassive black hole. In fact, XrB disk usually peak in the Soft X-ray band (below 2 keV), whereas AGN disk usually peak in the UV range (between 1 and 20 eV depending on the black hole mass).

Corona emission

Most stellar mass and supermassive black holes show the presence of a hard X-ray power law (see the red line in Fig. 1.4 and cyan line in Fig. 1.5) of spectral index Γ around 1.8, meaning that the photon flux F_{ph} is proportional to $\nu^{-1.8}$. This component presents a high energy cutoff of variable temperature, suggesting a thermal origin. It is believed to originate from the Compton up-scattering of disk seed photons interacting and gaining energy from the hot electrons within a hot corona somewhere close to the black hole. The high-energy cutoff then gives information about the electronic temperature within the corona, as the electrons can not give more energy to the photons than what they have. The characteristics, geometry and general nature of this hot corona are still highly debated within the scientific community.

Reflection

The high energy photons produced by the hot corona irradiates the disk, producing what we call a reflection component (see green line in Figs. 1.4 and 1.5). In fact, all the flux that goes into the disk is eventually reprocessed and comes back out again with a different spectrum. As such, the physical process is not really reflection but reprocessing. The reflection is characterized by the presence of the Compton Hump, around 20 to 30 keV, which is produced by the inelastic Compton down-scattering of the high energy photons. However, this component is also characterized by the presence of multiple fluorescence lines in the X-ray energy range. The most important ones being the Iron Kα and Kβ lines around 6.4 keV. In the disk rest frame, these emission lines critically depends on the ionization ξ of the disk. The higher the

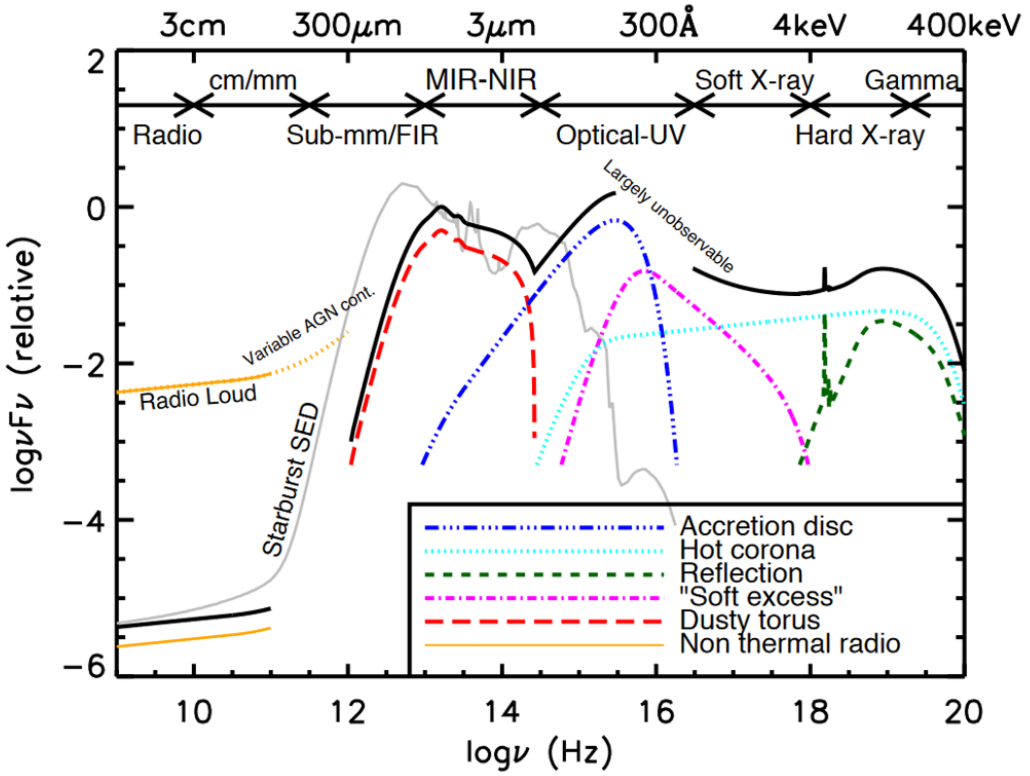

FIGURE 1.5: Schematic view of an AGN spectrum. *Credits: PhD. Thesis from Harrison (2014).*

ionization, the more ionic species and free electrons will be present within the disk, resulting in less lines and a stronger down-scattering component of the irradiating spectrum. When the disk is fully ionized, it acts as a mirror and reflects the irradiating spectra through Compton down-scattering. For the observer, the fluorescent lines can appear blurred either by the gravitational redshift due to the close proximity to the black hole, by the rapidly orbiting disk producing Doppler shifts and boosting or by the scattering of the lines within a thin atmospheric corona above the disk.

Soft X-ray excess

Most AGN present a soft X-ray excess component below 2 keV compared to the hard power-law extrapolation (see the magenta line in Fig. 1.5). This component does not seem to have any counterpart in XrB, even though this point is still heavily debated. It is characterized by a steep spectral index ($F_{ph} \propto \nu^{-2.5}$) and a high energy cutoff around $0.5 \rightarrow 1$ keV. Some claim that this components extends down in the UV and connects with the cold disk emission. Multiple propositions have been advanced to explain this component. The main two being the presence of a warm corona above the disk and comptonizing part of the disk seed photons (e.g. Magdziarz et al. 1998; Jin et al. 2012; Petrucci et al. 2013; Jin et al. 2017a,b; Petrucci et al. 2018; Petrucci et al. 2020), or the presence of a highly ionized blurred reflection (Crummy et al. 2006; Walton et al. 2013; Jiang et al. 2020).

Jets

The jets are usually observed as a flat or inverted radio spectrum breaking somewhere in the infrared (see the yellow line in Fig. 1.5). Their emission is mostly consistent with partially self absorbed synchrotron emitted along the jet due to the strong magnetic fields required to launch the jets.

Hard tail

Accreting black holes sometimes present a high energy X-ray power-law with a rather steep spectral index and reaching the γ-ray energy range. This component is usually called the hard tail. The physical origin of this component is still unclear, however, it is expected to be produced by synchrotron emission from non-thermal particle, either at the base of the jets or within the accretion flow.

Dust torus

There is evidence that some AGN are surrounded by a large dust torus far away from the black hole and producing infrared emission (see the red line in Fig. 1.5).

All the emission resulting from the accreted and ejected matter should somehow be connected. The energy range, number and sheer physical complexity of the spectral components in accreting black holes show the necessity to study these objects using a multi-wavelength approach. Without it, one might miss the complete picture of accretion-ejection around black holes.

1.3 Outbursts dynamics

1.3.1 X-ray Binaries outbursts

X-ray binaries outbursts usually follow the same evolution. To represent them, the community usually use the Hardness Intensity Diagram (HID), where we represent the X-ray luminosity, sometimes scaled to the black hole mass by dividing it by the black hole Eddington luminosity (this is called the Eddington ratio $\lambda_{Edd} = L/L_{Edd}$)[4], in function of the hardness of the spectrum. The hardness is defined as the ratio between a soft X-ray and a hard X-ray energy bands and helps determine whether the X-ray spectrum is dominated by the disk blackbody or the hard X-ray power-law emission coming from the hot corona. When the Hardness is close to 1, the spectrum is dominated by the hard X-ray power-law emission and we call the spectrum ***hard***. When the Hardness is small (< 0.1), the disk is rather dominated by the disk blackbody and we call the spectrum ***soft***.

Typically XrB outbursts follow a 'q' shaped path in the HID (see Fig. 1.6), presenting both a spectral and dynamical dichotomy: an outburst starts in a quiescent, low luminosity, hard state. The luminosity increases with a hard spectrum, dominated by the hard X-ray corona component. While being in the hard states, steady radio jets can be observed. At some point, the system transit rapidly from the hard to the soft state, the hard X-ray power-law seemingly disappearing while the disk blackbody becomes hotter and more luminous. Simultaneously to this transition, the

[4]The Eddington ratio λ_{Edd} can be useful when one wants to compare the track in the HID of XrB with different black hole masses.

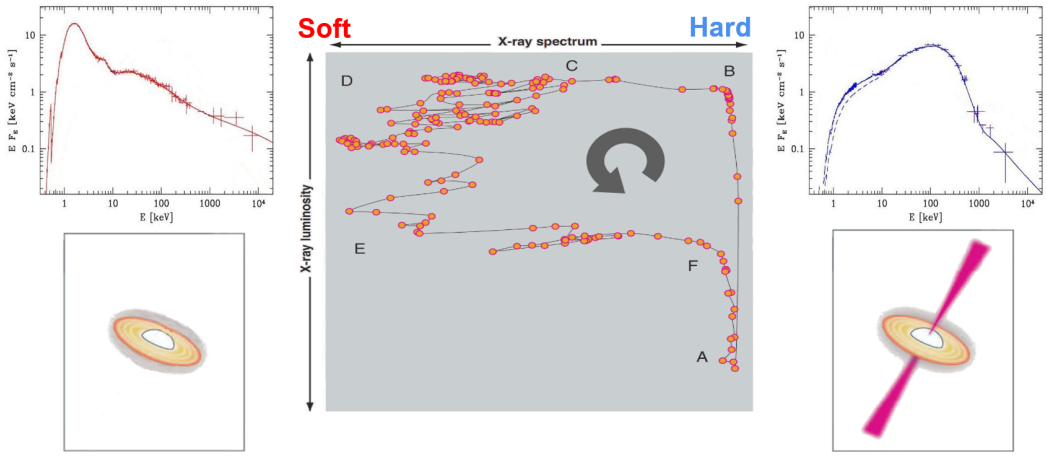

FIGURE 1.6: Spectral and dynamical schematic evolution seen in XrB outbursts. Adapted from Fender & Belloni 2012. Left: Soft spectral state, the X-ray spectrum is dominated by the disk blackbody emission. No jets are observed. Right: Hard spectral state, the X-ray spectrum is dominated by the high energy power-law emitted by the hot corona. Steady jets are observed.

steady jets disappear and the system shows radio flare coming from the ejection of relativistic ejecta that can be followed with Very-long-baseline interferometry (VLBI) images (e.g. Carotenuto et al. 2021a). This transition usually happen at a constant level of luminosity. During the transition, the hard tail component appear in the spectrum. In the soft state, the hot corona emission is not present, the spectrum is only composed of the disk blackbody emission and the hard tail. The radio emission coming from the jets seem to have completely disappeared, whether they have been quenched and no longer exist, are not luminous enough to be visible or have been replaced by the massive winds that are observed in a few sources, is however unclear. The total X-ray luminosity will slowly decrease. At some point, the hard X-ray hot corona reappears in the spectrum and the system transits towards the hard state in the matter of a few days. At the same time the steady radio jets reappear in the spectrum. Interestingly, this transition from soft $\rightarrow$ hard usually happens around the same Eddington ratio for all outbursts. And finally, the binary go back to quiescence while remaining in the hard spectral state.

There are a few objects behaving differently and presenting special states (Cyg X-1 being one of them), however the general picture stays the same. It should be noted, that some sources show a rising phase of the outburst with a slowly softening spectrum (e.g. MAXI J1820-70, H 1743-322), creating a slope in the HID. Some outbursts never reach the soft state. In this case, the system rises and then decrease in luminosity while staying in the hard state. They are called 'failed' outbursts. The success or failure of an outburst does not depend on the XrB as some sources have shown both complete and failed outbursts (H 1743-322, GX 339-4). For a full review on this subject, one can consult Dunn et al. (2010).

1.3.2 AGN snapshots

As the black hole mass are millions of times larger in AGN compared to XrB, the expected timescale of an AGN outburst would be millions of times larger, meaning millions to billions of years long. As such, it is impossible to follow the outburst

evolution of a single supermassive black hole. We can instead use the Ergodic theorem to associate the time dependent sequence of accretion-ejection seen in a single XrB to the stationary snapshots seen in multiple different AGN. This mean that each AGN would represent a single accretion state and looking at all AGN simultaneously would reveal an AGN outburst. There are some caveat to this method as each AGN is different, whether due to the mass, its environment, its spin. For instance due to the large range of mass in AGN, using Eddington ratio instead of the total luminosity in the HID becomes a necessity to compare the different objects, inducing stronger uncertainties due to the mass measurement. Furthermore, not all physical processes scale with the mass, Compton scattering and electron-positron interactions being a few examples. As such, a similar dynamical state can have different spectral output. Thus, associating the different AGN classes with outburst accretion state is far from being a trivial endeavour.

Fifteen years ago, Kording et al. (2006) studied a sample of 4963 quasars observed by the Sloan Digital Sky Survey (SDSS) and constructed a disk fraction luminosity diagram (DFLD) as an analogous to the HID of XrB outbursts. In the DFLD, the spectrum hardness is replaced with the ratio of the hard X-ray power-law luminosity to the total luminosity. They showed that the AGN with the highest radio loudness were analogous to the bright luminous hard state of XrB where their radio jets are the strongest. In a very recent study, Moravec et al. (2022) studied the AGN population position within the HID of an AGN sample from Jiri Svoboda's team in Prague. They were able to separate the position of FRI and FRII radio galaxies, with FRII showing in average a higher luminosities and hardness compared to the FRI. Similarly, the HERGs presented larger luminosities and higher hardness compared to the LERGs.

With a different approach, Fernández-Ontiveros & Muñoz-Darias (2021) used forbidden infrared lines to study the UV to X-ray spectral shape of the accretion flow of a sample of 167 nearby AGN. These lines are sensitive to ionizing radiation above given energy threshold in the UV to X-ray. Using the flux from two lines $[\mathrm{NeII}]_{12.8\mu m}$ and $[\mathrm{OIV}]_{25.9\mu m}$, respectively sensitive to the ionizing radiation above 21.6 and 54.9 eV, they were able to estimate both the total luminosity from the sources and a spectral hardness called the infrared Lyman hardness LyH_{IR} as it is measured from Lyman infrared lines. These two lines are interesting as they are sensitive to area of the spectrum exactly were the disk blackbody should exponentially decay. As such, depending on the disk temperature, the ratio between these two lines can have very different values. When the disk is cold, [NeII] can be strong while [OIV] will be weak. The system is then in a low excitation state, and the accretion flow spectrum is dominated by the hard X-ray power-law component. Whereas when the disk is hotter, the [OIV] will be excited and possibly stronger than the [NeII] line. The system is then in a high excitation state, and the accretion flow spectrum is dominated by the disk blackbody component. They then produced luminosity–excitation diagram (LED), where they represent the Eddington ratio as a function of their Lyman hardness, as an analogue to the HID and studied the AGN population within this diagram. Similarly to Kording et al. (2006), the radio loud AGN were identified as harder than other sources (with respect of LyH_{IR}). Low-ionization nuclear emission-line regions (LINERs) AGN, which usually present low X-ray luminosity, appear as the hardest sources due to their low excitation state, they are thus analogous to the hard accretion state of XrB where the X-ray luminosity is not the strongest either. Seyfert 1 and Seyfert 2 AGN are separated in two distinct region of the LED, with the Seyfert 2 appearing as transition state between the harder LINERs and the softer Seyfert 1 galaxies. This method produced very interesting results and used only two

infrared lines. The recent launch of the James Webb Space Telescope (JWST) and its infrared instruments will allow to use this method on a larger sample of AGN with even more infrared forbidden lines.

1.4 Multi-wavelength behavior

The spectrum of accreting black holes presented multiple components appearing at very different wavelength, from the radio of the jets to the hard X-ray of the hot corona. As such, to understand the complete picture of accretion and ejection around these compact objects, one need to approach these objects with a multi-wavelength point of view.

1.4.1 The radio–X-ray correlation

During the X-ray binary hard spectral state, the spectrum is dominated by the hot corona hard X-ray power-law component. Concurrently, steady jets are observed in the radio. Interestingly, a strong correlation between the hard X-ray flux from the hot corona and the radio flux from the jets is observed. This correlation was first reported at the beginning of the millennium by Corbel et al. (2000, 2013) for the XrB GX 339-4. They showed that the radio flux F_R is proportional to the hard X-ray flux F_X to the power ~ 0.6 ($F_R \propto F_X^{0.6}$). During the transition states and the soft state, such correlation become meaningless and non existent as both the hard X-ray corona emission and the jets both disappear from the spectrum. However, the historical correlation observed for GX 339-4 and later for V404 Cyg (Gallo et al. 2003) could be special cases among XrB. Indeed the discovery of H 1743-322 and its radio–X-ray correlation Coriat et al. (2011) following a different behavior, introduced a second population of objects that were then called 'outliers'. The outliers follow a correlation with at least one and possibly two breaks within the radio–X-ray correlation. At very low X-ray luminosity, the system seems to follow a relation close to the historical one, however, at such low radio and X-ray fluxes, the uncertainty are larger. Then, the system follows a different, almost flat, slope, with almost no increase in the radio flux while the X-ray flux increases by 2 order of magnitude. Finally at high X-ray luminosity, the slope suddenly break and appear with a very steep power-law index: $F_R \propto F_X^{1.4}$ (see Fig. 1.7), close to the one observed in neutron stars. Interestingly, since the discovery of this outlier population, it seems that almost all newly observed XrB follows the outlier trend rather then the historical one, possibly making GX 339-4 and V404 Cyg the exceptions. For those interested in looking at the XrB radio–X-ray data collected over the years, a large sample of XrB radio X-ray observations, updated every couple of years, can be found in an open repository[5] (Bahramian et al. 2018). However, it should be noted that inconsistencies exist between the different studies from which the collected data originates. Most objects and study use different X-ray band or different radio bands. Uncertainties remain in the distance and mass estimation of most objects, propagating errors in the reported luminosities. Finally, when comparing multiple objects, one should remember to scale the luminosities depending on their black hole mass (use the Eddington ratio λ_{Edd}), else the comparison could become meaningless.

Multiple interpretations to the existence of these two different radio–X-ray correlation branches were advanced. One possibility stands in the existence of a radiatively efficient flow within the outlier population as they appear as X-ray loud

[5] https://github.com/bersavosh/XRB-LrLx_pub

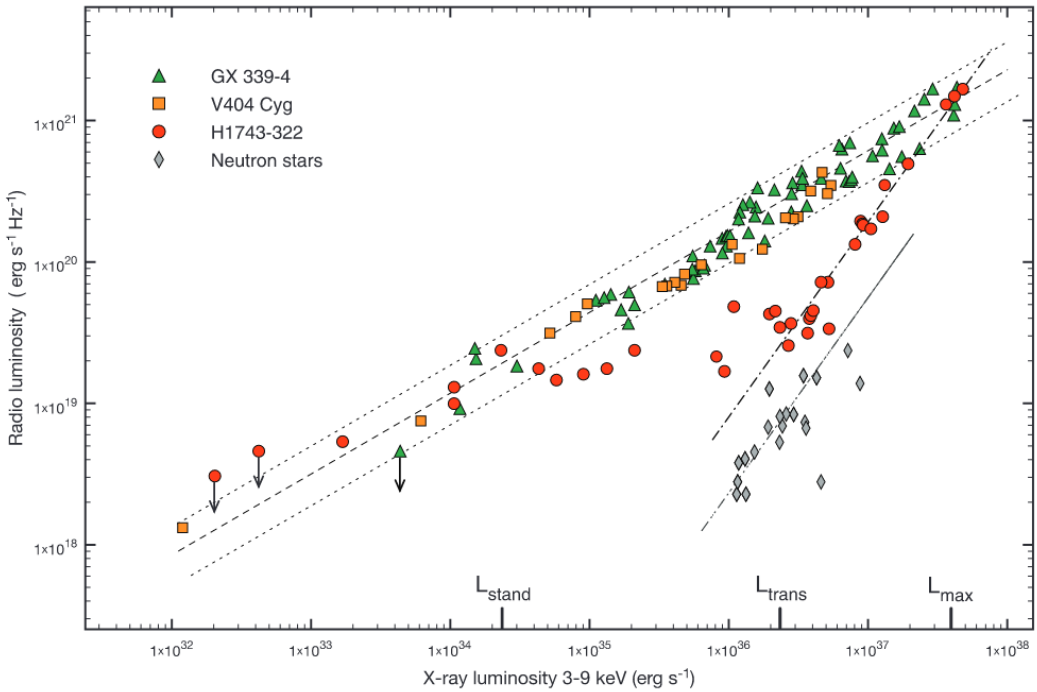

FIGURE 1.7: The radio–X-ray correlation of GX 339-4 (green triangles, Corbel et al. 2000, 2003, 2013), V404 Cyg (orange squares, Gallo et al. 2003) and H 1743-322 (red circles, Coriat et al. 2011). The neutron stars radio–X-ray correlation has been added as a mean of comparison. H 1743-322 follows a different trend, with multiple breaks, compared to the 'historical' radio–X-ray correlation observed in GX 339-4 and V404 Cyg. The population of XrB following this different trend has been named 'outliers'. *Credit: Coriat et al. (2011).*

sources compared to the historical branch. In radiatively efficient flows, the X-ray luminosity is expected to be proportional to the mass accretion rate ($L_X \propto \dot{M}$), comparatively, in radiatively inefficient flows the luminosity is expected to be $L_X \propto \dot{M}^{2-3}$ and most of the energy is either advected on the black hole or given to the jets (Coriat et al. 2011). A second possibility stands in the existence of a radio quiet branch. The outliers would then be radio quiet XrB and the historical branch would be the radio loud XrB, thus creating a possible analogous classification as the radio quiet and radio loud quasars in AGN.

This non-linear correlation is however not only limited to the XrB and actually extends all the way to the AGN, 10 orders of magnitude of luminosity away. This extension is famously known as the fundamental plane of black hole activity (Merloni et al. 2003) and shows a consistency between the accretion systems in stellar mass black hole binaries and the supermassive black holes. This suggest strong links between the accretion and ejection processes whatever the accreting systems is.

1.4.2 The AGN UV–X-ray correlation

Samples of accreting supermassive black holes within AGN present a correlation between the UV emission, coming from the disk blackbody, and the hard X-ray emission, coming from the hot corona. I will cite here below a few studies that have been

recognized for their exceptional data selection, avoiding as much observational biases as possible. The group of Lusso and Risaliti and collaborators studied this correlation in-depth (see Lusso et al. 2010; Risaliti & Lusso 2015; Lusso & Risaliti 2016; Lusso et al. 2020). Over the years, they collected a sample of radio quiet bright luminous quasars for which they put extra attention to discard any selection biases. They report a non-linear correlation between the monochromatic luminosity[6] measured at 2 keV and the monochromatic luminosity at 2500Å, with power index ~ 0.6 ($L_{2\,keV} \propto L^{0.6}_{2500\,\text{Å}}$). They also studied the evolution of this correlation depending on the redshift of the quasars. With the assumptions that quasars accretion can act as standard candles to estimate the luminosity distance of the objects, they have been using this correlation as a way to study cosmology and test the standard model. Other studies have looked at this correlation for other types of objects, for instance, it was reported that radio loud quasars could have a correlation with a larger power-index compared to the Lusso & Risaliti sample (Zhu et al. 2020), or that both AGN accreting at low mass accretion rate and close to Eddington rate showed the same correlation (Liu et al. 2021).

The physical explanation behind the non-linearity of the correlation linking the hard X-ray power-law and the disk luminosity is not yet understood. Why more UV luminous AGN would be less X-ray bright ? Multiple attempts to modelize AGN accretion flow emission and reproduce the correlation have been made (see Sect. 5 as well as Kubota & Done 2018, 2019; Arcodia et al. 2019, 2020). But no consensus on the physical origin for this power index has been reached.

1.4.3 Other correlations

Given the complexity and number of spectral components in the AGN broadband SED, it is difficult to coordinate the different instruments required to get the complete shape of the SED with good precision. Instead, the community relies on a number of spectral parameters to describe the broad-band SED. Correlations between the parameters are observed in AGN samples. One might refer to Jin et al. (2012) for an analysis of an AGN sample and an exhaustive list of spectral parameters correlations.

1.5 Modeling the accretion-ejection process

1.5.1 The Standard Disk

A global consensus in the community as to the nature of the cold accretion flow has been reached. In a binary system, the material transferred from the donor star to the compact object maintains a given amount of angular momentum. Due to friction, the gas will flatten in the direction of the total angular momentum and form an accretion disk around the black hole (Lynden-Bell 1969). As such, the gas must lose angular momentum in order to move inwards and be accreted on the black hole. The transport of angular momentum appears as a unavoidable requirement for accretion to occur. Shakura & Sunyaev (1973) showed that such an accretion disk would be formed of two regions, one dominated by radiative pressure (hotter, inner regions) where the Thomson opacity dominates and a second region dominated by the gas

[6] Meaning, the non-integrated *spectral luminosity density* L_ν taken at a given frequency ν in units of erg/s/Hz.

pressure and the free-free opacity. Both region do not have the same thermal equilibrium and spectral output. For the matter to accrete, they introduced a turbulence term α that allow the transport of angular momentum outwards. The higher α is, the stronger the friction are and thus the factor the angular momentum is transported, increasing the accretion speed. Another important parameter is the mass accretion rate $\dot{M}$, which controls the quantity of accreted matter crossing the accretion flow with time. The higher the mass accretion rate, the larger the density of the accretion flow. These two parameters (α and $\dot{M}$) are the two main parameters controlling the extension of the two regions of the disk and thus the spectral output. This is the so called α-disk or standard disk.

The model of Shakura & Sunyaev (1973) is non magnetized. It is only once the idea of magnetic fields were introduced to the model that the nature of the turbulent parameter α was understood. In the presence of a weak axial magnetic field, Balbus & Hawley (1991) showed that two adjacent particle will behave as if they were connected by a mass-less spring. Yet inside of the disk in Keplerian rotation, the two particles will not rotate at the same speed. This induces a magnetic tension slowing the rotation of the inner particle, decreasing its angular momentum and thus pushing it inwards. The particle is accreted. The outer particle will instead accelerate and thus move toward a larger orbit. The angular momentum is thus transported radially outwards. This process is called the Magneto rotational instability (MRI, see also Balbus & Hawley 1998).

1.5.2 Corona models

The modelization of the hot corona is still highly debated. Multiple ideas, geometries, and processes are proposed but none have yet found consensus within the community.

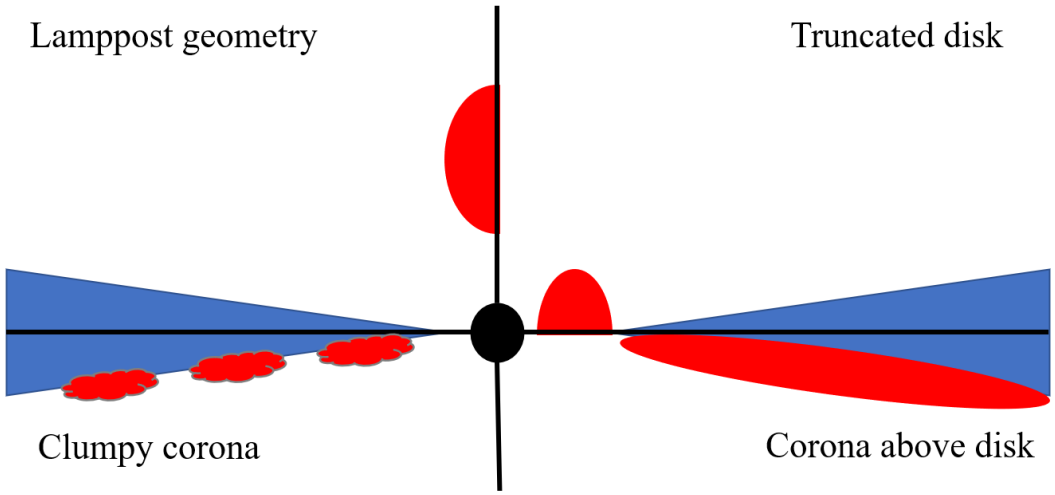

FIGURE 1.8: Different geometries proposed for the hot corona. In blue: the cold Standard disk, in red the hot corona. Top left: the lamppost geometry, the hot corona is situated at the base of the jets. Top right: truncated disk geometry. The corona is part of the accretion flow. Bottom left: patchy corona geometry. Bottom right: The corona covers the accretion flow.

Geometry

In the last 50 years, multiple geometries have been proposed for the hot corona. In Fig. 1.8, I present some of these geometries. The truncated disk geometry proposes a hybrid disk configuration and is composed of an outer standard disk (Shakura & Sunyaev 1973) and an inner hot accretion flow playing the role of the hot corona (see for instance Thorne & Price 1975; Shapiro et al. 1976; Abramowicz et al. 1980). This hot accretion flow is characterized by a thick geometry. By playing with the transition radius between the part of the accretion flow, Thorne & Price (1975) showed that one could qualitatively reproduce the spectral state variation observed in Cyg-X1. Different approaches are then proposed to drive the spectral variation of the accretion flow: the mass accretion rate (Esin et al. 1997), of the turbulent viscosity α (Lasota et al. 1996) or the magnetic field strength (Ferreira et al. 2006). In another geometry, the corona is produced by a electron atmosphere above the standard disk and the corona covers the disk (see for instance Hameury et al. 1986). Inside of the corona, the hot electrons up-scatter the photons produced by the cold standard disk to higher energy and the hard X-rays. However it has been shown that the spectral output of such corona would be too steep compared to what is usually observed in X-ray binaries. This idea is however used to explain the presence of the soft X-ray excess observed in AGN (e.g. Petrucci et al. 2018). Another version of this geometry proposes that this atmosphere is only produced locally above certain region of the accretion flow (patchy corona). Other studies proposed that the base of the jets, where the particles are created and accelerated could play the role of the hot corona (see for instance Nayakshin & Kallman 2001; Różańska et al. 2002; Dauser et al. 2014).

Modeling hot accretion flow

The α disk is characterised by a weak turbulence $\alpha \ll 1$ and is limited to geometrically thin and optically thick solutions. The standard disk can not produce an optically thin corona. To produce a geometrically thick and optically thin accretion flow, new solutions are explored, Abramowicz et al. (1980) developed the *slim* solution which is however only accessible at very high luminosity and mass accretion rate, and thus can not explain the observed hard spectral state in XrB. However this solution is characterised by the presence of strong advection term. The radiation cooling is not sufficient to cool down the disk and the addition of an important advection term in the thermal equilibrium is necessary. Later, Narayan & Yi (1994) explored a turbulent solution ($\alpha > 0$) of the standard disk (Shakura & Sunyaev 1973) characterized by a strong advection term. This solution is not radiatively efficient and geometrically thin and hot and is usually called the Advection Dominated Accretion Flow (ADAF, see also Narayan & Yi 1995a,b).

The only way to explain the jets involves the presence of strong magnetic field around the black hole and thus these magnetic field lines would most certainly have an impact on the accretion flow and the hot corona. Multiple scenario have been proposed to explain the presence of these strong magnetic fields within the inner regions. The cosmic battery scenario (Contopoulos & Kazanas 1998; **?**) proposes that magnetic field are generated through the Poynting-Robertson effect. Similarly, the proposition of a dynamo effect at the interface of the accretion disk with the hot corona could produce magnetic fields (see for instance Begelman & Armitage 2014; Kylafis & Belloni 2015). These two propositions however adopt the ADAF

model, now magnetized, for the hot corona but do not take into account any magnetic torque. A corona model taking into account the magnetic torque and simultaneously explaining teh presence of jets is the Jet Emittign Disk (JED, Ferreira & Pelletier 1993, 1995). This consideration lead to the development of a hybrid disk model composed of an outer standard accretion disk (SAD, Shakura & Sunyaev 1973) and an inner JED (Ferreira et al. 2006). This model called the JED-SAD, is the model that I will be using in this thesis.

With the development of computational power, a new approach to the modelization of the accretion flow appeared. Simulating the evolution of an accretion flow from initial conditions, different type of MHD solutions appeared. Narayan et al. (2003) showed that accreting gas could drag a poloidal magnetic field in the inner region of the accretion flow. The inner region is saturated by the magnetic field strength and the accretion only proceeds as discrete blobs or streams. This is the Magentically Arrested Disk (MAD) regime (see also McKinney et al. 2012; Narayan et al. 2012). Over the years, 3D MHD simulations have evolved and the model also. Most recent simulations show the presence of winds extracting angular momentum from the inner region and the flow is no longer as arrested as initially thought (Liska et al. 2018; Liska et al. 2020).

1.5.3 Jets

Multiple models to explain the launch of the jets have been proposed. As a general consensus in the community, the presence of strong magnetic fields is required in all of these models. In the Blandford-Znajek (BZ, Blandford & Znajek 1977) process, the jets is powered with energy extracted from a rotating black hole. Magnetic fields line threading the black hole ergosphere are twisted on each side of the black hole rotational pole. Charged particles (electron-positron), created by pair cascade within the strong radiation and electric field, within the twisted line will be accelerated away within jets. The outgoing flow extracts angular momentum from the black hole. This process requires the presence of a strong poloidal magnetic field around the spinning black hole. The power extrcated can be estimated:

$$P_{BZ} \approx P_0 \, B^2 \, (\Omega_{BH}^2 / c) \, R_g^4 \tag{1.2}$$

Where, B is the magnetic field strength, R_g the gravitational radius $R_g = GM/c^2$ and Ω_{BH} is the rotation frequency of the spinning black hole. $P_0 = 0.01 - 0.1$ is a parameter which uncertainty originates as the magnetic field strength is not self-consistently determined (McKinney 2005).

In the Blandford-Payne (BP, Blandford & Payne 1982) process, the jets is instead powered from the accretion flow because of rotating magnetic fields lines threading the accretion flow. In the BP process, for a jet to be launched, the magnetic field lines must be inclined at the surface of the accretion flow. Launching the outflow will lead to a laminar magnetic torque exerted on the accretion flow, this will transport angular momentum vertically away from the system (see also Ferreira 1997). Some consider the power of the BP process insufficient to launch the powerful jets observed within XrB or AGN but agree that it can produce slower less collimated wind-like outflows.

Chapter 2

The JED-SAD model

Contents

2.1 The Dyplodocus code . . . 32
2.1.1 Motivation . . . 32
2.1.2 Equation and Parametrization . . . 32
2.1.3 Hybrid structure . . . 38
2.1.4 HID and JED-SAD dynamic . . . 40
2.2 Solutions . . . 41
2.2.1 Structure and spectra . . . 41
2.2.2 Power budget . . . 46
2.3 Parameter space . . . 48
2.3.1 Black hole Mass – m . . . 48
2.3.2 Mass accretion rate – $\dot{m}$ . . . 51
2.3.3 Transition radius – r_J . . . 52
2.3.4 Inner radius – r_{isco} . . . 53
2.3.5 Dilution factor – ω . . . 53
2.3.6 Accretion speed – m_s . . . 54
2.3.7 Jet power – b . . . 54
2.3.8 Ejection Index – p . . . 54
2.4 Tables and Reflection . . . 60
2.4.1 JED-SAD tables . . . 60
2.4.2 Reflection computation . . . 60
2.5 General strategy . . . 61
2.6 Caveats and prospects . . . 62

Dans ce chapitre, je présente le modèle de disque éjectant - disque standard (Jet Emitting Disk Standard Accretion Disk, JED-SAD) que j'utilise dans cette thèse. Ce modèle est en développement depuis plus de 20 ans, commençant avec l'article présentant les disque éjectant (JED, Ferreira 1997). Cependant ce n'ets que récemment que ce modèle a pris de l'ampleur avec la thèse de Grégoire Marcel (soutenue en 2018, Marcel 2018) et le développement du code Dyplodocus. Pour plus de détails sur le modèles, on pourra se référer aux articles suivants: Ferreira (1997); Ferreira et al. (2006); Petrucci et al. (2008, 2010); Marcel et al. (2018a,b); Marcel (2018); Marcel et al. (2020, 2022); Barnier et al. (2022); Marino et al. (2021).

Motivation

Dans les états durs des éruptions de binaires X, l'émission provenant de la loi de la couronne chaude et l'émission des jets sont corrélées. De plus, ils disparaissent simultanément lors des transitions vers les états mous. Cela suggère un fort lien entre ces deux composantes dynamiques. Puisque de si grands liens entre ces deux composantes existent, pourquoi ne pas supposer que ces jets soient lancés depuis la couronne chaude ? Le lancement des jets a besoin de la présence de forts champs magnétiques, de ce fait, le flot d'accrétion doit lui aussi être fortement magnétisé. Ce sont donc les équations de la magnétohydrodynamique (MHD) que l'on doit résoudre. Assumant un flot d'accrétion traversé par un fort champ magnétique vertical $\vec{B} = B_z$ au plan médian, Ferreira (1997) a montré 1) qu'un jet pouvait être lancé depuis le flot d'accrétion, résultant dans un couple extrayant le moment angulaire et accélérant l'accrétion de la matière, celle ci atteint des vitesses supersonique. 2) que le flot d'accrétion résultant est un disque épais et chaud capable d'émettre des rayons X. Le détail de la résolution et de la paramétrisation des équations MHD du disque éjectant ayant déjà été détaillées dans la thèse de Grégoire Marcel (Marcel 2018), je ne vais pas les répéter ici. Grégoire Marcel, en paramétrisant ces équations, arrive à un système pour l'équation d'énergie à 3 équations avec 3 inconnues, il s'agit de résoudre l'équilibre thermique du disque: l'épaisseur du disque $\epsilon = H/R$ (avec H, la hauteur du disque, et R la distance radiale au trou noir), la température des électrons T_e et la température des ions T_i. La résolution de ce système fait cependant appel au calcul de l'émission optiquement mince émise permettant de refroidir le disque et n'est donc pas trivial.

Structure hybride

Marcel et al. (2018b) a montré qu'un simple disque éjectant (JED) n'était pas suffisant pour reproduire le comportement entier observé dans les éruptions de binaires X. En effet les états mous sont caractérisés par l'absence d'émission X dure et de jets radio. Le modèle repose alors sur une structure hybride (Ferreira et al. 2006) composée d'un disque interne éjectant (JED) et d'un disque externe standard (SAD, voir le schéma dans la Fig. 2.1). Dans cette vision, la couronne chaude est représenté par le JED. Le disque interne est hautement magnétisé et lance des jets (Blandford & Payne 1982). Ces jets extraient le moment angulaire du flot d'accrétion de manière efficace et accélèrent l'accrétion à des vitesses super-soniques. De ce fait, le JED devient optiquement mince et chaud. Le disque externe, froid et optiquement épais, est responsable pour l'émission de corps noir du disque. Cette structure JED-SAD résulterait naturellement d'une stratification radiale du champ magnétique. Dans les régions internes, les lignes de champs ont été advectés et accumulés, résultant dans une région hautement magnétisé, le JED. Les régions externes du disques seraient alors peu magnétisé, résultant dans un SAD. Cette stratification radiale du champ magnétique a été observé dans les récentes simulations de pointes MHD (Liska et al. 2020; Scepi et al. 2020; Jacquemin-Ide et al. 2021), validant notre approche commencé 20 plus tôt.

Dans le code Dyplodocus, développé par Grégoire (Marcel et al. 2018a, 2019; Marcel

2018) et résolvant l'équilibre thermique et l'émission du flot d'accrétion pour n'importe quelle configuration JED-SAD, le rayon de transition entre les régions JED et SAD est un paramètre nommé R_J. Dans le JED, on peut mesurer le taux d'accrétion à n'importe quel rayon R: $\dot{M}(R) = \dot{M}_{ISCO}(R/R_{isco})^p$, où $\dot{M}_{ISCO}$ est le taux d'accrétion mesuré au rayon interne de dernière orbite stable (ISCO, ne dépendant uniquement de la rotation du trou noir) R_{isco} et p est le paramètre d'éjection mesurant la quantité de matière provenant du JED éjectée dans les jets. Cela introduit 3 nouveaux paramètres dans la résolution: $\dot{M}_{ISCO}$, R_{isco} et p. Pour simplification, je noterai à présent $\dot{M}$ le taux d'accrétion mesuré à l'ISCO $\dot{M}_{ISCO}$. Dans le SAD, il n'est supposé aucune éjection, et de ce fait on a: $\dot{M}(R) = \dot{M}(R_J) = \dot{M}_{ISCO}(R_J/R_{isco})^p$ Bien entendu la masse du trou noir intervient aussi comme un des paramètres du modèle. Les prochains paramètres sont supposés constants radialement dans le JED: La vitesse d'accrétion dans le JED est supersonique et mesuré à l'aide du paramètre m_s mesuré en nombre de MAch sonique. Une partie de la puissance disponible dans la couronne chaude est utilisé pour le lancement des jets, pour mesurer cela, on introduit le paramètre $b = P_{jets}/P_{JED}$ où P_{jets} est la puissance des jets et P_{JED} est la puissance d'accrétion disponible dans le JED. Un autre paramètre nécessaire est la magnétisation du disque éjectant au plan médian $\mu = B_z^2/(\mu_0 P_{tot})$ qui peut être compris comme le rapport entre la pression magnétique et la pression totale P_{tot}. Enfin, le dernier paramètre est utilisé pour prendre en compte la proportion des photons froid émis par le SAD qui vont rentrer dans la couronne chaude pour la refroidir par effet Compton. Ce paramètre est dénoté ω et ne dépend que de la géométrie de la solution JED-SAD. La plupart de ces paramètres peuvent être exprimés avec des grandeurs adimensionnées que l'on notera en minuscule. Par exemple, les rayons peuvent être exprimé en unité de rayon gravitationel $R_G = GM/c^2$. On notera alors le rayon de transition adimensionné $r_J = R_J/R_G$. Le taux d'accrétion est lui mesuré en unité du taux d'accrétion Eddington: $\dot{m} = \dot{M}/\dot{M}_{Edd} = \dot{M}/(L_{Edd}/c^2)$. L'ensemble des paramètres du modèle et leur domaines d'existences ont été résumé dans le Tab. 2.1. Dans cette thèse, la magnétisation μ n'est pas étudiée et fixée à 0.5.

Afin de résoudre l'équilibre thermique, le code Dyplodocus a besoin de calculer l'émission optiquement mince qui sert à refroidir la couronne chaude. Pour cela il fait appel aux solutions de Renaud Belmont (Belmont et al. 2008; Belmont 2009) et prenant en compte les émissions Bremsstrahlung (rayonnement de freinage), synchrotron, leur comptonisation, la comptonisation de photons externes et la production de paire électron-positron. Le code Dyplodocus fait quelques hypothèses et approximations, dont l'hypothèse d'une symétrie axiale ou l'approximation de l'absence de stratification verticale. Le point le plus marquant est peut être l'absence de relativité générale dans les calculs. En effet, l'ensemble des solutions JED-SAD est calculé dans un espace purement Newtonien. Le calcul de la solution JED-SAD se fait anneau par anneau du disque en commençant par les régions externes.

Comment peut on comprendre les éruptions de binaires X avec le modèle JED-SAD ? Dans les états durs, caractérisé par la présence d'une émission en loi de puissance dure et la présence de jets, le rayon de transition r_J serait large. Cela signifie que l'on aurait un grand JED capable de lancer les jets et de produire l'émission X dure observés. Dans les états mous, caractérisés par la présence d'un corps noir de disque et l'absence d'émission radio, le rayon de transition serait petit et proche de l'ISCO $r_J \sim r_{ISCO}$. Cela signifie que le JED serait quasiment inexistant, expliquant de ce fiat, l'absence d'émission X dure ou des jets radio. Donc en jouant avec le rayon de transition r_J, nous sommes capables de changer d'état spectral. Pour augmenter en luminosité, on peut augmenter le taux d'accrétion $\dot{m}$, afin d'augmenter la puissance d'accrétion disponible dans le flot d'accrétion. Ces deux paramètres peuvent alors être considérés comme les principaux paramètres du modèle.

Solutions

Puisque le modèle JED-SAD n'est pas un modèle phénoménologique mais provient de la résolution des équations MHD du flot d'accrétion, nous sommes capables de d'obtenir le profil radial de l'ensemble des quantités physiques du disque d'accrétion. Ce paragraphe sert d'exemple de ce qui peut être obtenu pour une solution JED-SAD donnée. Les paramètres utilisés ici sont: $m = 10$; $r_J = 30$; $\dot{m} = 0.5$; $r_{isco} = 2$; $\omega = 0.1$; $m_s = 1.5$; $b = 0.3$; $p = 0.01$.

Dans la Fig. 2.2, je montre en haut le spectre total en unité ν *obtenu dans les rayons X en noir. Je montre aussi l'émission provenant des différents anneaux du disques, en rouge quand l'anneau est dans le JED, en bleu quand il est dans le SAD. L'émission de chaque anneau dans le JED est une émission similaire à une loi de puissance. Chaque rayon du JED a une température et une épaisseur optique différente, résultant dans des index de loi de puissance un peu différent. Le spectre total du JED est alors une émission ressemblant à une loi de puissance avec une faible courbure. La composition spectrale est montré dans la Fig. 2.3.*

Dans les panels du milieu et du bas de la Fig. 2.2, je montre la géométrie, la hauteur verticale ainsi que les températures des électrons et l'épaisseur optique. Tout à gauche de la figure, on retrouve le trou noir, dans les régions proches du trou noirs, on trouve le disque éjectant épais, et plus loin, après r_J*, le disque standard. Le JED est chaud (*$kT_e > 10^9$ *keV), optiquement mince (*$\tau_T \sim 1$*) et géométriquement épais (*$\epsilon \sim 0.3$*). Le SAD est lui, froid (*$kT_e < 10^7$ *keV), optiquement épais (*$\tau_T \gg 1$*) and géométriquement mince (*$\epsilon \ll 0.1$*). La température et l'épaisseur optique peuvent aussi être observé dans la Fig. 2.4.*

Nous pouvons aussi regarder le bilan de puissance à l'intérieur du JED. La puissance d'accrétion dans le JED peut être libérée en 3 formes différentes: l'advection, le rayonnement et les jets. Dans le panel en bas à droite de la Fig. 2.4, je montre le profil radial de ces quantités normalisées à la puissance total disponible pour chaque anneau du flot d'accrétion. Dans le SAD ($r > r_J = 30$*), quasiment toute la puissance est libérée sous forme de rayonnement. Dans le JED, 30 % de la puissance part dans les jets (c'est le paramètre b), le reste est libéré sous forme de radiation ou alors advecté. Le rapport entre les puissances d'advection* P_{adv} *et de rayonnement* P_{cool} *est important car il permet de caractérisé différents types de solutions JED-SAD (voir les Figs. 2.5 et 2.6, montrant respectivement le rapport* P_{adv}/P_{cool} *dans l'espace des paramètres* $r_J - \dot{m}$ *du JED-SAD. et les solutions physiques de 3 configurations mise en avant).*

Une étude complète de l'espace des paramètres et leur influence sur le spectre et différentes grandeurs physiques sont présentés dans les Figs. 2.7 (influence de la masse du trou noir m), 2.9 (influence du taux d'accrétion $\dot{m}$*), 2.10 (influence du rayon de transition* r_J*), 2.11 (influence du rayon de dernière orbite stable* r_{isco}*), 2.12 (influence du facteur de dilution* ω*), 2.13 (influence de la vitesse d'accrétion* m_s*), 2.14 (influence de la puissance donnée au jets b) et 2.15 (influence de la matière éjectée dans les jets p).*

Tables et stratégie

Une de mes premières contribution a été le calcul et la construction de tables du modèle permettant l'ajustement direct de données X observées dans le logiciel Xspec de la NASA. J'ai par ailleurs aussi calculé les tables de la composante en réflection associé à l'émission du JED. Pour cela je me suis basé sur le code Xillver de J. Garcia

(Garcia et al. 2013; García et al. 2015). J'ai, pour tout les spectres JED-SAD de ma table, mesuré l'indice spectral Γ et la coupure à haute énergie kT_e de l'émission du JED et utilisé ses valeurs pour associer à chaque spectre JED-SAD un spectre de réflection. Grâce à ces outils, nous pouvons maintenant réaliser les premiers ajustements de données avec le modèle JED-SAD.

Mais avant cela, je souhaite faire un point sur la stratégie employée dans notre équipe. Le modèle JED-SAD provient de motivation physique. De ce fait, les solutions spectrales sont contraintes et limités à des situations physiquement viables. Nous nous attendons à ce que certains de nos paramètres soient liés, corrélés entre eux, cependant, récupérer théoriquement ces liens est loin d'être trivial. Notre objectif est alors de récupérer l'évolution physique du flot d'accrétion en confrontant notre modèle aux données. Chaque observation X du diagramme HID nous donnera un état physique de l'accrétion-éjection. Nous pourrons alors étudier l'évolution temporelle du flot au cours d'une éruption et comment chaque paramètre évolue.

In this chapter, I will present the Jet Emitting Disk Standard Accretion Disk (JED-SAD) model that I will use in this thesis. This model has been in development for more than 20 years, starting with the paper of Jonathan Ferreira introducing Jet Emitting Disks (Ferreira 1997). However it is only recently that the model spread its wings with the development of the Dyplodocus code by Gregoire Marcel (Greg) during his thesis (Marcel 2018). Certain part of this chapter have thus already been covered in published papers and in Greg's thesis (in French), as such I will introduce but not enter the details of the MHD equations. For more information on the JED-SAD, one might take a look at the following papers: Ferreira (1997); Ferreira et al. (2006); Petrucci et al. (2008, 2010); Marcel et al. (2018a,b); Marcel (2018); Marcel et al. (2020, 2022); Barnier et al. (2022); Marino et al. (2021).

2.1 The Dyplodocus code

2.1.1 Motivation

During the hard states of an XrB outbursts, the hard X-ray emitting hot corona and the steady radio jets are observed, moreover, a correlation between their luminosities suggests a connection between the jet and the corona. Similarly, the absence of radio emission when the system enters the soft state suggests that both the jets and hot corona disappear simultaneously. Since such strong links between the jet and the hot corona seem to exist, why not launch the jets from the hard X-ray emitting part of the accretion flow? The jets require the presence of large scale strong magnetic fields, the accretion flow must be magnetized. As such we must solve MHD equations which can have strong impacts on the thermal structure of the accretion flow. Given an accretion flow threaded by a large scale vertical magnetic field $\vec{B} = B_z$ at the mid-plane, Ferreira (1997) showed that 1) a jet can be launched from the accretion flow, inferring a magnetic torque on the accretion flow and thus extracting angular momentum and accelerating the accretion. 2) The resulting accretion flow is a hot and puffy disk that is able to emit hard X-ray photons.

2.1.2 Equation and Parametrization

As much as the next five pages are not the result of any of my personal research, I believe their presence to be important in this thesis to emphasize the physical aspect of the model. Like most magnetized accretion flow, the main equations are the same, conservation of mass, conservation of impulsion, conservation of energy, equation state, conservation of electric charge and the Maxwell equations. These equations were detailed in Greg's thesis (in French, Marcel 2018). Before presenting the equations and their parametrization, I should however mention a few assumptions that are made.

Assumptions

The dynamical timescale of the inner part of the accretion flow is of the order of the millisecond, while observations usually require more than thousands of seconds to get enough photons for the spectra, as such what we observe is the mean spectrum emitted. We can thus assume that the possible asymmetries of the accretion flow (due for instance to Lense-Thirring precession) is averaged out. We thus assume axisymmetry for the accretion flow.

We assume that the disk is plunged in a **Newtonian** potential, introducing strong caveats about the emission of the inner most regions where relativistic effects are the most important. Furthermore, we assume Keplerian rotation around the black hole $\Omega_K = \sqrt{GM/R^3}$.

The Dyplodocus code do not treat the vertical stratification of the accretion flow. This strong assumption simplifies the thermal equilibrium computation of the accretion flow.

Mass conservation

The conservation of the mass within the accretion flow can be written as:

$$\frac{\partial \rho}{\partial t} + \vec{\nabla} \cdot (\rho \vec{u}) = 0 \tag{2.1}$$

Where $\rho(r,z)$ and $\vec{u}(r,z)$ are the disk density and its speed. Assuming axisymetry $\frac{\partial}{\partial \Phi}(u_\Phi) = 0$ results in the equation:

$$\frac{1}{r}\frac{\partial}{\partial r}(r\rho u_r) = -\frac{\partial}{\partial z}(\rho u_z) \tag{2.2}$$

Two different cases can be identified depending whether we have mass ejection in the disk ($u_z \neq 0$) or not ($u_z = 0$). Let us start with the second case. By integrating vertically the disk and not taking into account the vertical stratification of the disk, we obtain:

$$\frac{\partial}{\partial r}(2\Sigma r u_r) = 0 \tag{2.3}$$

Where we define the surface density of the disk Σ:

$$\Sigma(r) = \frac{1}{2}\int_{-H}^{H} \rho dz.$$

Usually, the height scale H of the accretion disk is defined from the isothermal height scale:

$$\rho(r,z) = \rho_0(r)\, exp\left(-\frac{z^2}{2H^2}\right) \tag{2.4}$$

where $H = c_s/\Omega_K$, with c_s the local sound speed and Ω_K the Keplerian rotation. Deviations due to the strong magnetization is minimal (refer to Sec. II.1.2 in Greg's thesis Marcel (2018)) and we use this definition. Note that even if we use this definition, we assume no vertical stratification in the JED computation.
From 2.3, we can define the mass accretion rate $\dot{M}$ in a case without ejection:

$$\dot{M}(r) = \dot{M} = -4\pi\Sigma r u_r \tag{2.5}$$

However, if there is ejection from the disk ($u_z \neq 0$), we get the following equation instead:

$$\frac{\partial \dot{M}}{\partial r} = 4\pi r \rho(r, z = H) u_z(r, z = H) = 2\frac{\partial \dot{M}_J}{\partial r} \tag{2.6}$$

where $\dot{M}_J$ is the ejected mass on each side of the disk. As such, the mass accretion rate is no longer a radial constant. Assuming a constant ejection rate in the flow, we

introduce the ejection parameter p[1]:

$$p = \frac{\partial \log(\dot{M})}{\partial \log(r)} \tag{2.7}$$

Within the Jet Emitting Disk, the mass accretion rate is a function of the radius and is written as $\dot{M}(r) = \dot{M}(r_{isco})(R/r_{isco})^p$, where r_{isco} is the inner most stable circular orbit.

Equation of state

The equation of state is written as:

$$P_{tot} = n_e k_B T_e + n_i k_B T_i + P_{rad} = \rho c_s^2 \tag{2.8}$$

Where P_{tot} is the total pressure, P_{rad} the pressure due to the radiation. $n_{(e,i)}$ and $T_{(e,i)}$ are the density and temperature of the electrons ($_e$) and ions ($_i$). ρ is the total density, $\rho = n_i m_i + n_e m_e$. And c_s is the sound speed $c_s = \Omega_K H = \sqrt{GM/R^3} \cdot H$.

Conservation of the impulsion

The conservation of the impulsion writes as:

$$\frac{\partial \rho \vec{u}}{\partial t} + \rho(\vec{u} \cdot \vec{\nabla})\vec{u} = -\rho \vec{\nabla} \Phi_G - \vec{\nabla} P_{tot} + \vec{\nabla} \cdot \vec{T} + \vec{J} \times \vec{B} \tag{2.9}$$

Where, Φ_G is the gravitational potential of the compact object, P_{tot} is the total pressure and $\vec{T}$ is the local stress tensor of the fluid. The final term results from the presence of magnetic fields and depends on the current density $\vec{J}$ and the magnetic field $\vec{B}$.

Let us first look at the projection on the toroidal vector $\vec{e}_\Phi$. Assuming that the Keplerian speed depends weakly on the height of the disk, we obtain the following equation:

$$\rho \left(u_r \frac{\partial u_\Phi}{\partial r} + \frac{u_r u_\Phi}{r} \right) = \rho u_r \frac{\partial r u_r}{\partial r} = \frac{1}{r} \frac{\partial}{\partial r}(r^2 T_{r,\Phi}) - \frac{r}{\mu_0} B_z \frac{\partial B_\Phi}{\partial z} \tag{2.10}$$

The stress tensor $T_{r,\Phi}$ can be obtained from the viscous deformation and the kinematic viscosity ν_v of the viscosity ($\eta_v = \rho \nu_v$). It can also be expressed with the alpha parameter (Shakura & Sunyaev 1973):

$$\alpha_v = \frac{\nu_v}{c_s H} = \frac{\eta_v}{\rho c_s H} \tag{2.11}$$

By integrating vertically Eq. 2.10 and assuming Keplerian rotation $u_\phi = r^2 \Omega_K$, we get:

$$u_r = -\frac{3}{r^2 \Omega_K \Sigma} \frac{\partial}{\partial r}(\nu_v r^2 \Omega_K \Sigma) - \frac{1}{\mu_0 \Sigma \Omega_K} 2 B_z B_\Phi (z = H) \tag{2.12}$$

[1]It should be noted that in earlier paper, this parameter was called ξ. But due to the confusion with the disk ionisation parameter also usually called ξ, it was later decided to rename this parameter p instead.

Where $B_\Phi(z = H)$ is the toroidal magnetic field on the disk surface (z=H). The first term results from the hydrodynamic while the second results from the disk magnetization. We can then define another parameter: the sonic mach number of the accretion $m_s = -u_r/c_s$:

$$m_s = 3\alpha_v\epsilon\frac{\partial \log(\Sigma r^{1/2})}{\partial \log(r)} + 2q\mu = m_{s,turb} + m_{s,jets} \tag{2.13}$$

with ϵ the aspect ratio defined as $\epsilon = H/r$, $q = -B_\Phi(z = H)/B_z$ characterizing the curvature of the magnetic field lines and μ the disk mid-plane magnetization defined as:

$$\mu = \frac{B^2}{\mu_0 Ptot} \tag{2.14}$$

From this equation, it appears that inside the JED, the accretion velocity, or equivalently the sonic mach number m_s, is influenced by both a turbulent torque and the magnetic torque. In the case of a non-magnetized disk, $\mu \ll 1$, the magnetic torque is negligible, and $m_s = m_{s,turb} \sim \alpha_v\epsilon \ll 1$. However in a magnetized disk $\mu \sim 1$, the magnetic torque $2q\mu$ dominates and the m_s can be close or superior to 1, resulting in super sonic accretion speed.

If we look at the conservation of the radial impulsion, by projection of Eq. 2.10 on $\vec{e}_r$, one can obtain the deviation of the orbital rotation compared to the Keplerian rotation:

$$\frac{\Omega}{\Omega_K} \sim 1 - \frac{5m_s^2 + 1}{4}\epsilon^2 - \mu\epsilon\frac{B_r(z = H)}{B_z} \tag{2.15}$$

In a weakly magnetized disk ($\mu \ll 1$), the magnetic term is not important and the Keplerian deviation is of the order of ϵ^2. In a magnetized disk ($\mu \sim 1$), the Keplerian deviation is of the order of $\mu\epsilon$.

The conservation of the vertical impulsion leads to the magnetic correction of the height scale. One can look at section ii.1.2 of Greg's thesis for more details (in French, Marcel 2018).

Conservation of energy

The conservation of energy is written as:

$$\frac{\partial U}{\partial t} + \vec{\nabla}\cdot\left(U\vec{u} + \vec{F}_{rad}\right) + P_{tot}\vec{\nabla}\cdot\vec{u} = \left(\vec{T}\cdot\vec{\nabla}\right)\vec{u} + \eta_m\vec{J}^2 \tag{2.16}$$

Where $U = U_{gas} + U_{rad}$ is the total internal energy, $\vec{F}_{rad}$ is the bolometric radiative flux, $P_{tot} = P_{gas} + P_{rad}$ is the total pressure, $\vec{T}$ is the local stress tensor of the fluid, η_m is the Ohmique resistivity and $\vec{J}$ is the current density. One can summarize this equation as the equilibrium between the advected energy, the energy radiated away and the available energy:

$$q_{adv} + q_{rad} = q_+ \tag{2.17}$$

Where $q_{adv} = \vec{\nabla}\cdot(U\vec{u}) + P_{tot}\vec{\nabla}\cdot\vec{u}$ is the advection volumetric power, $q_{rad} = \vec{\nabla}\cdot\vec{F}_{rad}$ is the volumetric radiative cooling term and $q_+ = \left(\vec{T}\cdot\vec{\nabla}\right)\vec{u} + \eta_m\vec{J}^2$ is the heating. The heating is composed of two viscous term, η_v trough the stress tensor $\vec{T}$ and η_m, it is difficult to estimate. Instead let us define the heating as the available energy inside the disk, meaning the volumetric accretion energy q_{acc}. In the JED however, part of the matter is ejected, as such we lose part of the available energy. To quantify this energy loss, we use the parameter b defined as the fraction of the accretion energy

lost in the jets.

$$b = \frac{P_{jets}}{P_{acc}} = \frac{2P_{jet}}{P_{acc}} \tag{2.18}$$

Where $P_{jets} = 2P_{jet}$ is the energy lost in the jets on both side of the accretion flow. b is thus limited to a range of value between 0 and 1. This allow to simplify the energy equation as:

$$q_{adv} + q_{rad} = (1 - b)q_{acc} \tag{2.19}$$

As the temperature of electrons and ions can be different in the accretion flow, we get a set of two energy equations, one for electrons and one for the ions. We do not know a priori the distribution of energy between the electrons and ions, as such we introduce the parameter δ controlling the proportion of energy given to the electrons (δ) and ions ($1 - \delta$). Furthermore, as the temperature between the two species is different, one must add the coulomb interaction term q_{ie} between ions and electrons.

$$\begin{aligned}(1 - \delta)(1 - b) \cdot q_{acc} &= q_{adv,i} + q_{ie} \\ \delta(1 - b) \cdot q_{acc} &= q_{adv,e} - q_{ie} + q_{rad}\end{aligned}$$

With $q_{adv,(e,i)}$ the advection term for the electrons ($_e$) and ions ($_i$), and q_{rad} applying only to the radiating electrons. The parameter δ is a free parameter of the model. However, protons and electrons are expected to be heated in the same way and suggesting $\delta = 0.1 \rightarrow 0.5$ (Yuan & Narayan 2014). In this thesis (and in all the currently published results of the JED-SAD model), we assume $\delta = 0.5$.

Solving the energy equation

The Dyplodocus code solve the energy equation and thermal equilibrium for each ring [R ; R + dR] of scale height H and volume $2\pi R dR\, 2H$ from the outer edge of the disk to the inner edge of the disk in a single iteration. The caveat introduced by this last aspect will be discussed in Sec. 2.6. The accretion power within one ring can be obtained from:

$$dP_{acc}(R) = P_{acc}(R) - P_{acc}(R + dR) = \left(\frac{GM\dot{M}(R)}{2R} - \frac{GM\dot{M}(R + dR)}{2(R + dR)} \right) \tag{2.20}$$

As $\dot{M}(R) = \dot{M}_{ISCO}(R/r_{isco})^p$ due to ejection, we get:

$$\frac{dP_{acc}(R)}{dR} = (1 - p)\frac{GM\dot{M}_{ISCO}}{2R}\left(\frac{R}{r_{isco}}\right)^p \tag{2.21}$$

This gives: $q_{acc} = \frac{dP_{acc}(R)}{dR}\frac{1}{2\pi R \cdot 2H}$.

The coulomb interaction can be inferred from the work of Stepney & Guilbert (1983). For a two temperature plasma, the general fromula is then:

$$q_{ie} = \frac{3}{2}\frac{m_e}{m_i} n_e n_i \sigma_T c \ln\Lambda (k_B T_i - k_B T_e)\Delta_{ie} \tag{2.22}$$

with $\ln\Lambda = 15$ the coulomb logarithm for XrB and Δ_{ie} a function of temperature and mass of the species (see ii.2.2 from Greg's thesis for the details Marcel 2018).

The advection term $q_{adv,(e,i)} = \vec{\nabla} \cdot (U\vec{u}) + P_{tot}$ for a given species is analytical but requires radial derivative. The Dyplodocus code assumes that each species

behave as a fluid, which entails that the total internal energy can be written as $U_{(e,i)} = P_{(e,i)}/(\gamma_{(e,i)} - 1)$ with $\gamma_{(e,i)}$ the adiabatic index of the given species. For relativistic electrons, $\gamma_e = \gamma_{rad} = 4/3$. For the non-relativistic ions $\gamma_i = 5/3$. Finally, the code assumes that both species have the same accretion speed $\vec{u}_r = -m_s c_s \vec{e}_r$, resulting in the following equation:

$$q_{adv,(e,i)} = q_{adv,0} \frac{P_{(e,i)}}{P_{tot}} \Delta_{(e,i)} \tag{2.23}$$

with $P_{tot} = P_{gas} + P_{rad} = P_i + P_e + P_{rad}$ the total pressure, $q_{adv,0} = -m_s \epsilon \Omega_K P_{tot}$ and the radial term $\Delta_{(e,i)} = \frac{\gamma_{(e,i)}}{\gamma_{(e,i)}-1}\left(\frac{1}{2} + \frac{\partial \log(m_s \epsilon)}{\partial \log r}\right) + \frac{1}{\gamma_{(e,i)}-1}\frac{\partial \log P_{(e,i)}}{\partial \log r}$. This last term is analytical and the species pressure can be obtained from their density $P_{(e,i)} = n_{(e,i)} k_B T_{(e,i)}$. However, the radiative pressure must be computed from the radiation.

As the accretion flow can be either optically thin, optically thick or in-between depending on the parameters, the Dyplodocus code takes into account both possibilities as well as a *bridge* function between the two emissions. As such, the radiative power q_{rad} of a given ring [R; R+dR] is a function of the optically thick emission q_{thick} and optically thin emission q_{thin}. The code uses the half-height vertical Rosseland optical depth $\tau_{tot} = \kappa_R \rho_0 H$, with $\kappa_R = \kappa_T + \kappa_K$ the sum of the Thomson and Kramer opacity which dominate within black hole accretion disks. It should be noted that in AGN, the temperature and density can be low enough, Hydrogen can recombine and other sources of opacity appear. This is discussed in Appendix. A.

For the optically thick emission, the emission comes from black body radiation and can simply be obtained from the Stefan-Boltzmann law:

$$q_{thick} = \frac{1}{H}\sigma_B T_{eff}^4 = \frac{1}{H}\frac{4\sigma_B T_e^4}{3\tau_{tot}} \tag{2.24}$$

with σ_B the Stefan-Boltzmann constant.

The optically thin emission can come from multiple radiative processes, bremsstrahlung, synchrotron and their comptonization. To compute the optically thin emission we use the Belm code (Belmont et al. 2008; Belmont 2009). The Belm code solves the thermal equilibrium within a homogeneous sphere of radius R_s with a unique temperature T_e, density n_e and magnetization. To get the spectrum emitted by a ring, we must use the same density and optical depth, meaning ideally we have $R_s = H$. As such, to get the full solution, the code solves a system of three equations: the energy equation for each species and the vertically integrated equilibrium of the disk.

$$\begin{aligned} 0.5(1-b)\cdot q_{acc} &= q_{adv,i} + q_{ie} \\ 0.5(1-b)\cdot q_{acc} &= q_{adv,e} - q_{ie} + q_{rad} \\ \frac{\rho_0 GM}{R}\epsilon^2 &= P_{rad} + P_{gas} \end{aligned}$$

for which we have three unknown physical parameters to determine : ϵ, T_e, T_i.

When the optical depth is neither optically thin nor optically thick, the code uses a *bridge* function between the two, which depends on an effective optical depth $\tau_* =$

$\sqrt{q_{thin}/q_{thick}}$ and is based on the work of Hubeny (1990). The bridge formula must be able to recover both optically thick and thin regime:

$$q_{rad} \simeq q_{thick} \text{ when} \tau_* \gg 1$$
$$q_{rad} \simeq q_{thin} \text{ when} \tau_* \ll 1$$

We will use the estimation of the transition between the two regimes obtained by Artemova et al. (1996):

$$q_{rad} = \frac{q_{thick}}{1 + \frac{4}{3\tau_{Tot}} + \frac{q_{thick}}{q_{thin}} e^{-\tau_{Tot}/\tau_{lim}}} \tag{2.25}$$

where $\tau_{lim} = \tau_{T,max}/5$ has been introduced due to the use of external tables to compute the optically thin emission. Indeed, these tables have by construction an upper limit to the optical depth $\tau_{T,max}$. When the optical depth exceed this limit, we have $q_{thin}(\tau_T) = q_{thin}(\tau_{T,max})$. If the optical depth is even more important, we can reach $q_{thin} \sim q_{thick}$ even though $\tau_{Tot} \geq \tau_T \gg 1$ and the bridge formula doesn't work anymore. To alleviate this problem, an empirical limit $\tau_{lim} = \tau_{T,max}/5$ has been fixed, above which the radiative solution is forced as optically thick.

Once the radiation is computed, we can extract the radiative pressure (Artemova et al. 1996):

$$P_{rad} = \frac{q_{rad} H}{c} \left(\tau_{tot} + \frac{4}{3} \right) \tag{2.26}$$

2.1.3 Hybrid structure

Marcel et al. (2018a) have shown that a JED is not sufficient to explain the observed behaviour within XrB outbursts, indeed the soft states are characterized by a disk black body emission and the absence of radio jets. We thus assume a hybrid structure (Ferreira et al. 2006) composed of an inner Jet Emitting Disk and an outer Standard Accretion Disk (see Fig. 2.1) based on the solution of Shakura & Sunyaev (1973). As

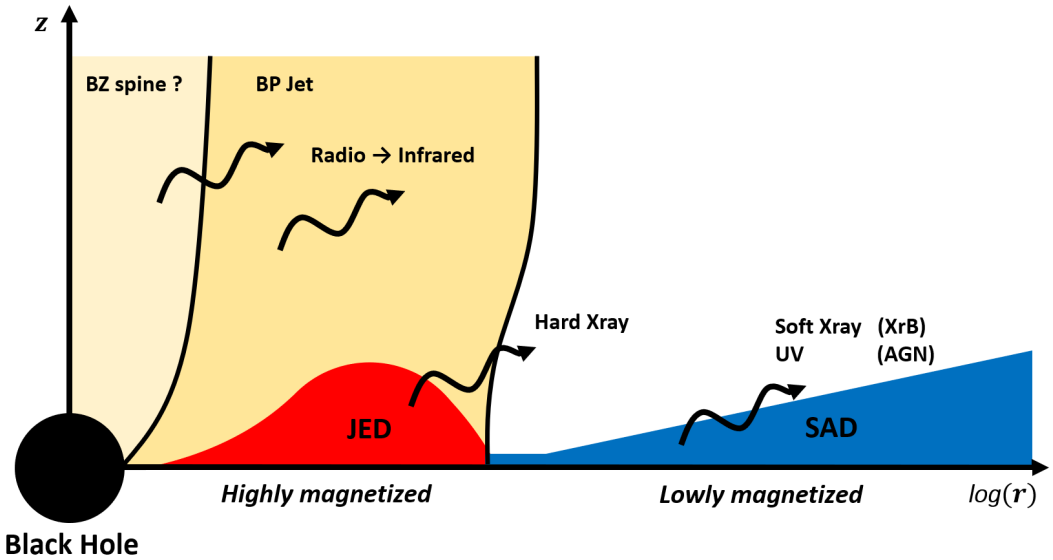

FIGURE 2.1: Schematic view of the section of the inner region of the JED-SAD model. The inner region is highly magnetized and launches a jet, resulting in Jet Emitting Disk. The outer region is lowly magnetized and is a Standard Accretion Disk.

such the JED-SAD model belongs to the inner corona - truncated disk geometry class of accretion model. The inner JED, due to the launching of BP jets, plays the role of the hot corona emitting hard X-ray photons. The colder and optically thick SAD radiates a disk blackbody emission which is observed in the soft X-ray for XrB and in the UV for AGN. In our view this JED-SAD structure would naturally result from a radial stratification of the magnetic field strength. In the inner region, to get a JED, strong magnetic field have been accumulated due to advection. In the outer region, the accretion flow remains weakly magnetized. Such radial stratification of the magnetization have since been observed in a few recent MHD simulations (Liska et al. 2020; Scepi et al. 2020; Jacquemin-Ide et al. 2021), confirming the approach started 20 years ago. The jets could be composed of two components, the BP jet launched from the JED in the accretion flow and acting as a sheat around a spine, possibly fueled through the BZ mechanism.

In the code, the radius of the transition between the JED and the SAD regions is fixed by the parameter R_J. As in the JED, all the extracted angular momentum is diffused vertically thanks to the jets, there is no deposit of angular momentum (thanks to MRI) in the inner region of the SAD (Marcel et al. 2018b). This entails the presence of a no-torque condition at this interface, introducing a factor $f_0(r) = (1 - \sqrt{R_J/R})$ to the available accretion energy inside of the SAD region. The accretion rate within the JED depends on the radius due to ejection: $\dot{M}(R) = \dot{M}_{ISCO}(R/r_{isco})^p$. However, within the SAD, we assume no ejection and thus $\dot{M}(R) = \dot{M}(R_J) = \dot{M}_{ISCO}(R_J/r_{isco})^p$. To characterize a solution we thus need two more parameters, $\dot{M}_{ISCO}$ and r_{isco}, the mass accretion rate measured at the ISCO and the radius of the ISCO. For simplification, we will write the mass accretion rate measured at the ISCO $\dot{M}_{ISCO}$ as $\dot{M}$ and $\dot{M}(R)$ the mass accretion rate at radius R. As the accretion speed is super-sonic within the JED and sub-sonic in the SAD, we thus expect an acceleration region and a trans-sonic point at the interface between the two regions. The complete physics of this interface is not yet well understood and is still part of a work in progress.

The cold photons emitted within the SAD can enter the JED and interact with the hotter electrons. They thus provide a cooling term due to external inverse comptonization. This cooling is prescribed by a dilution factor ω representing the number of SAD photons entering the JED region, ω mostly depends on the geometry of the solution and is comprised between 0 and 50%. If we write $L_{SAD} = GM\dot{M}/2R_J = 4\pi R_*^2 \sigma T_s^4$ the total SAD luminosity, where $T_s = T_{eff}(R_*)$ is the effective temperature at the radius R_* where the SAD reaches its maximum temperature (Frank et al. 2002). The radiation field inside the sphere $r = r_J$ can be approximated by $U_{rad} = \omega\, L_{SAD}/(4\pi R_J^2 c)$. The number of seed photons reaching each JED ring of height scale H and its Belm sphere of radius H is then:

$$L_s = U_{rad} 4\pi H^2 c = \omega (H/R_J)^2 L_{SAD} \tag{2.27}$$

As a mean of simplification, ω is the same for all JED ring, meaning that we assume an homogeneous SAD photon field within the JED region. However, the code allows the consideration of a radial stratification of ω. This aspect is part of a work in progress and is discussed in Sec. 2.6 and Chapter 4.

For simplification in the notation, the JED-SAD parameters are normalised based on usual quantities and are noted with lower case. We express the mass of the black hole M as $m = M/M_\odot$, with $M_\odot$ the mass of the sun. The radii are expressed in units

of gravitational radius $R_G = \frac{GM}{c^2}$: $r_J = R_J/R_G$; $r_{isco} = R_{isco}/R_G$. The mass accretion rate is expressed in units of Eddington mass accretion rate $\dot{M}_{Edd}$, the mass accretion rate corresponding to the Eddington luminosity: $\dot{m} = \dot{M}/\dot{M}_{Edd} = \dot{M}/(L_{Edd}/c^2)$. This definition of the mass accretion rate ignores the radiative efficiency η and represent the actual physical mass accretion rate present inside of the accretion flow, as such a value of $\dot{m}$ above 1 does not mean super-Eddington luminosity. In Tab. 2.1 I summarised the parameters of the JED-SAD models, the value assumed for some parameters that have not been studied yet and the existing regime where the JED is thermally stable as identified by Greg (Marcel et al. 2018b; Marcel 2018).

TABLE 2.1: Summary of the parameters characterizing a JED-SAD solution. Value between parentheses are assumed fixed and are not studied. There are 8 free parameters that we study: m, r_{isco}, r_J, $\dot{m}$, b, m_s, p, ω.

Parameter	Definition	Domain of existence
Global		
m	Mass of the black hole	$5 \rightarrow 20$ (XrB) $10^5 \rightarrow 10^{10}$ (AGN)
r_{isco}	Radius of the ISCO	$1 \rightarrow 6$
r_{out}	Outer edge of accretion flow	(10^5)
r_J	transition radius between JED and SAD	$r_{isco} \rightarrow r_{out}$
$\dot{m}$	Mass accretion rate at ISCO	$10^{-3} \rightarrow 10^2$
δ	Fraction of energy in electrons	(0.5)
Jet Emitting Disk		
μ	Magnetization in JED	(0.5)
b	Power going in the jets	$0.1 \rightarrow 0.99$
m_s	Sonic Mach number of the accretion	$0.5 \rightarrow 3.0$
p[2]	Index of the ejected matter	$10^{-3} \rightarrow 10^{-1}$
Standard Accretion Disk		
α_v	Alpha parameter of the viscosity	(10^{-1})
μ_{SAD}	Magnetization in SAD	(10^{-3})
Transition		
ω	Dilution factor	$0 \rightarrow 0.5$
f_0	No-torque condition at transition	$(1 - \sqrt{r_J/r})$

2.1.4 HID and JED-SAD dynamic

How can we understand an XrB outburst using this hybrid disk scenario? The hard state, characterized by a hard X-ray power-law and the presence of jets can be explained with the presence of a large Jet Emitting Disk that extends radially. The soft states, characterized by the strong disk blackbody emission and the absence of the jets, can be explained with the absence of a Jet Emitting Disk and the nearing of the Standard Accretion Disk to the black hole, possibly extending all the way down to the ISCO. So by playing with two parameters, we expect to be able to reproduce qualitatively the behaviour of an XrB outburst: to increase the luminosity, we can

[2]This parameter was called ξ in earlier publications but to avoid confusion with disk ionisation, we change the name to p.

increase the mass accretion rate $\dot{m}$ which increases the total available energy in the accretion flow ; and to transit between the hard and soft states, we can play with the radial extension of the JED r_J, controlling the proportion of accretion power released in the corona or in the cold disk. This image is simplified as the flux and temperature of the standard disk but also the flux, spectral index and high energy cutoff of the hard X-ray power-law are all impacted by both of these parameters. Then, Compared to a usual DISKBB + CUTOFF POWER-LAW model, the JED-SAD spectra rely only on two parameter, influencing the geometry, thermal structure and its spectral output.

These two parameters can thus be considered as the two main parameters of the model. r_J and $\dot{m}$ are expected to be physically linked through the evolution the magnetization across the accretion flow. This link is however far from being trivial to estimate and requires global 3D MHD simulations. In the absence of any physical law that could be used as an input, these two parameters are considered independent from one another. We hope to constrain the relation between r_J and $\dot{m}$ from the observations, allowing us to get a glimpse into the process of magnetic field advection.

2.2 Solutions

2.2.1 Structure and spectra

Since the JED-SAD model is not a phenomenological spectral model but based on the accretion flow equations, we get the complete solution and are able to compute any physical quantities inside of the accretion flow. This paragraph serves as an example of what we can obtain for any given JED-SAD configuration. The parameters used for the showcased simulation are: $m = 10$; $r_J = 30$; $\dot{m} = 0.5$; $r_{isco} = 2$; $\omega = 0.1$; $m_s = 1.5$; $b = 0.3$; $p = 0.01$.

Spectrum

Let us first take a look at the spectral solution from the JED-SAD model. In the top panel of Fig. 2.2, I plot the spectrum in νF_ν of a given JED-SAD solution. In black I plot the total spectrum of the accretion flow, I also plot the spectrum emitted by each ring, in blue if it is emitted from the SAD, and in red if it is emitted from the JED region. The emission of each SAD ring is a blackbody emission with different temperature, the total SAD region emission is then a disk blackbody. The emission from each JED ring is a power-law like emission coming from the comptonization of the local bremsstrahlung, the local synchrotron and the external photons coming from the SAD. Each JED ring has a different temperature and optical depth, resulting in different power-law like spectral index and high energy cutoff for each ring. The total hot corona emission is then a cut-off power-law like emission with a slight curvature due to radial stratification of the temperature. This is a major feature of the JED-SAD model that is not present in most accretion model used to fit data, the hot corona is a multi-temperature region.

Spectral composition

With the JED-SAD model, we are able to recover the composition of the spectrum in term of physical process. In Fig. 2.3, I plot the spectral components for the same solution. The total JED spectrum (in dashed black line) results from the sum of the

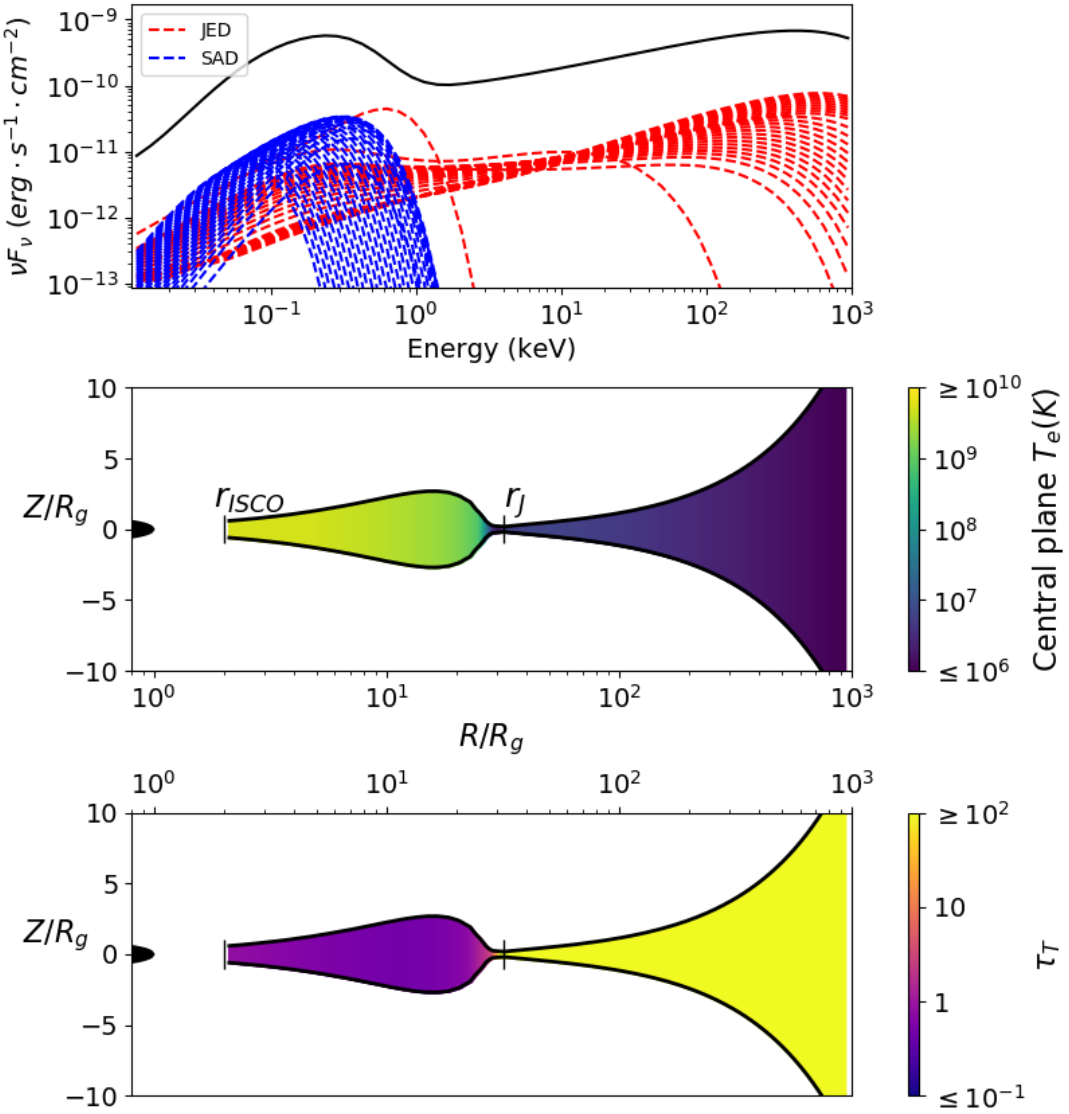

FIGURE 2.2: Example of JED-SAD solution. Parameters used: $m = 10$; $r_J = 30$; $\dot{m} = 0.5$; $r_{isco} = 2$; $\omega = 0.1$; $m_s = 1.5$; $b = 0.3$; $p = 0.01$. **Top**: Spectrum in νF_ν. The red dashed lines are the spectra emitted by each ring inside the JED region, the blue dashed lines are the spectra emitted by each ring inside the SAD region. The total spectrum results from the addition of each ring's emission and is plotted in black full line. **Middle**: Section of the inner region of the JED-SAD model. The color represent the temperature of the electrons in each ring. The JED-SAD model assume no vertical stratification. **Bottom**: The color represent the Thomson vertical optical depth in each ring.

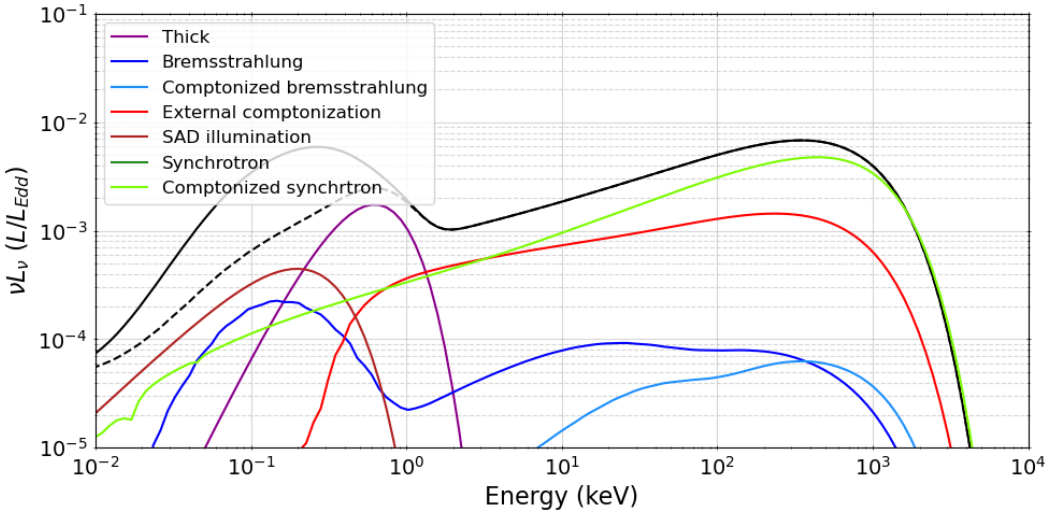

FIGURE 2.3: Example of the spectral composition of a JED-SAD solution. Parameters used: $m = 10$; $r_J = 30$; $\dot{m} = 0.5$; $r_{isco} = 2$; $\omega = 0.1$; $m_s = 1.5$; $b = 0.3$; $p = 0.01$.

optically thick emission and the optically thin components: bremsstrahlung, synchrotron, their comptonization and the comptonization of external photons. For this solution, the spectrum is dominated by the comptonization of the local synchrotron emitted by the JED. The details of the spectral composition is still part of a work in progress that will be discussed in Chapter 4.

Geometry

In the middle and lower panel of Fig. 2.2, I plot the geometry of a given JED-SAD solution, showing the section of the inner regions. A word of caution on the observed shape, on this figure, the x-axis is in logarithmic scale while the y-axis is linear. The middle panel is color-codded by the temperature while the lower one by the vertical optical depth of each ring. Once again, I should remind the reader that the JED-SAD model does not possess any vertical stratification. On the far left, we find the black hole. In the inner most region of the accretion flow, we find the hot ($kT_e > 10^9$ keV), optically thin ($\tau_T \sim 1$) and geometrically thick ($\epsilon \sim 0.3$) Jet Emitting Disk. On the right, we find the cold ($kT_e < 10^7$ keV), optically thick ($\tau_T \gg 1$) and geometrically thin ($\epsilon \ll 0.1$) Standard Accretion Disk.

Temperature

The temperature is plotted in both Figs. 2.2 (middle panel) and 2.4 (upper left panel). Inside the SAD region ($r > r_J = 30$), the accretion flow is cold ($kT_e < 10^7$ keV). At $r \gtrsim r_J$, the SAD temperature deviates from the Shakura & Sunyaev (1973) solution due to the no-torque condition at the transition between the SAD and the JED. This results in a small drop in temperature. Inside the JED, the temperature are much higher ($kT_e > 10^9$ keV) and electrons and ions have a different temperature. The JED is not a one temperature corona model, we obtain a radial stratification of the temperature inside of the accretion flow.

Density and optical depth

The Thomson optical depth is plotted in both Figs. 2.2 (lower panel) and 2.4 (lower left panel). In Fig. 2.4, I add the density of electrons (in green), total optical depth, sum of the Thomson and free-free optical depth and the effective optical depth used in the bridge formula linking optically thick and thin emission (see Sec. 2.1.2). In the JED region ($r < r_J = 30$), the optical depth is of the order of unity. In the SAD region ($r > r_J = 30$), the optical depth is much larger and the accretion flow is optically thick. The Thomson optical depth seem to provide the largest proportion to the total optical depth, except in the outer, colder, region ($r > 300$). Both the electron density and optical depth drop at $r = r_J$ due to the sudden acceleration to supersonic accretion.

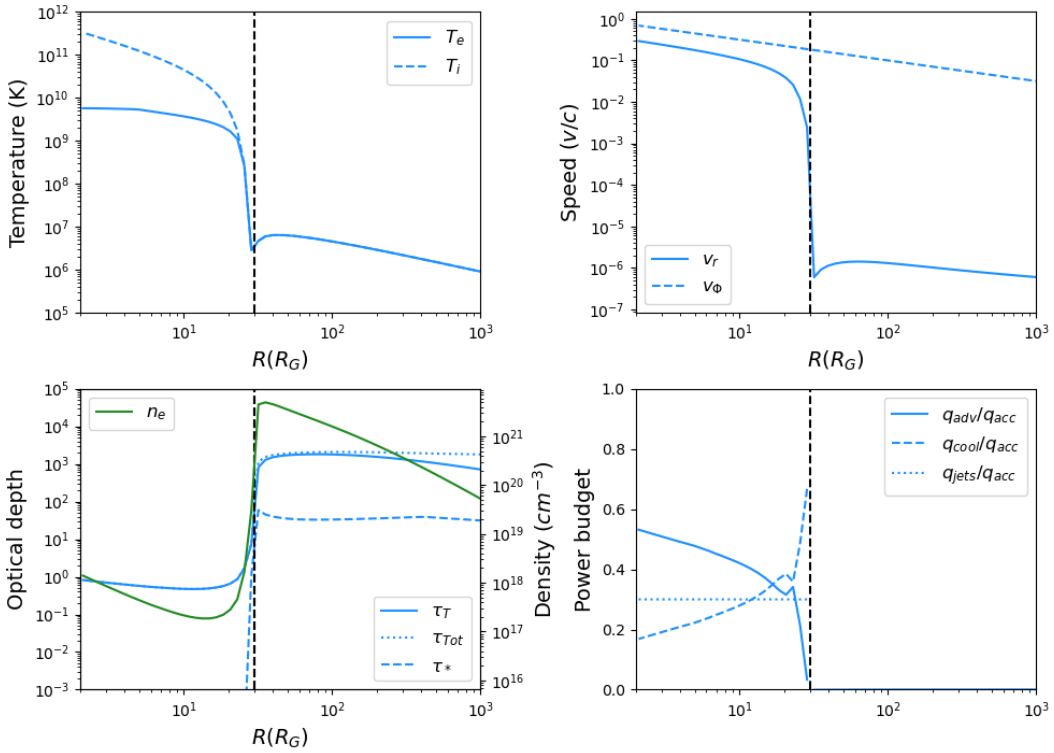

FIGURE 2.4: Example of JED-SAD solution. Parameters used: $m = 10$; $r_J = 30$; $\dot{m} = 0.5$; $r_{isco} = 2$; $\omega = 0.1$; $m_s = 1.5$; $b = 0.3$; $p = 0.01$. In each panel, the black vertical dashed line mark the separation between the JED and SAD at $r = r_J = 30$. **Upper left**: temperature of each ring. The blue solid line are for the electrons. The blue dashed line for ions. **Upper right**: velocities inside of each ring, measured in unit of c. The blue solid line is the accretion speed, the blue dashed line is the orbital velocity. **Lower left**: Vertical optical depth (blue) and electron density (green). The blue solid line represent the Thomson optical depth, the dotted line the total optical depth (sum of Thomson and free-free) and the dashed line is the effective optical depth used in the bridge formula (see Sec. 2.1.2). **Lower right**: Power budget. The blue solid line is the proportion of accretion power spent in the advection, the blue dashed line, the proportion in the cooling power and the dotted line, the proportion powering the jets.

Accretion and orbital speed

In Fig. 2.4 (upper right panel), I represent the accretion and orbital velocities in unit of c. The orbital velocity is quasi-Keplerian and almost reaches c when approaching the ISCO. The accretion or radial velocity is very low in the SAD and suddenly accelerates when entering the JED at $r = r_J$. Inside of the JED, the accretion is supersonic, the sonic mach number for this solution is $m_s = 1.5$. This value is supposed constant inside the JED. However, this does not entail that the radial velocity is also constant. Here, we see that the radial velocity increases inside of the JED and reaches a fraction of c at the ISCO.

Power budget

In Fig. 2.4 (lower right panel), I plot the power budget, meaning the proportion of accretion energy spend in advection, cooling and powering the jets, computed for each ring. Inside of the SAD ($r > r_J = 30$), almost all the accretion q_{acc} power is spent in radiative cooling ($q_{adv}/q_{acc} \ll 1$ and $q_{cool}/q_{acc} \sim 1$) which is expected for the optically thick region emitting blackbody spectra. In the JED, 30% of the accretion power is given to the jets, this is controlled by the parameter b of the model, supposed constant inside of the JED. Here, the rest of the accretion power (70%) is divided much more evenly between advection and cooling.

Magnetic field

One can extract the vertical magnetic field strength in any given ring from the expression of the magnetization $\mu = B_z^2/(\mu_0 P_{tot})$. The total pressure P_{tot} can be written (see Eq. 2.8):

$$P_{tot} = \rho c_s^2 = \rho \frac{GM}{R} \epsilon^2$$

Using the dimensionless parameters we introduced, we obtain the following expression:

$$P_{tot} = P_* \frac{\dot{m}(r) r^{-5/2}}{m_s} \tag{2.28}$$

where $P_* = m_i n_* c^2$ and $n_* = 1/(\sigma_T R_G) \backsimeq 1.02 \times 10^{18} \cdot (10/m)$ cm^{-3}, where we assumed a black hole mass m=10. We thus obtain the following equation for the vertical magnetic field:

$$B_z = \sqrt{\mu_0 P_*} \left(\frac{\mu}{m_s}\right)^{1/2} \dot{m}(r)^{1/2}\, r^{-5/4} \tag{2.29}$$

where $\sqrt{\mu_0 P_*}$ is a constant, μ and m_s are supposed constant within the JED and the radial dependence is limited to the term $\dot{m}(r)^{1/2}\, r^{-5/4}$. Thus, inside the JED we have:

$$B_z = 1.1 \times 10^8 \cdot \left(\frac{10}{m}\right)^{1/2} \left(\frac{\mu}{1}\right)^{1/2} \left(\frac{1.5}{m_s}\right)^{1/2} \left(\frac{\dot{m}}{1}\right)^{1/2} \left(\frac{r_{isco}}{1}\right)^{p/2} r^{-5/4-p/2} \text{ G} \tag{2.30}$$

As such, in the JED, we have $B_z(r) \propto r^{-5/4-p/2}$. In the SAD, $\dot{m}(r) = \dot{m}(r_J)$ as we assume no ejection in this region and thus $B_z(r) \propto r^{-5/4}$.

2.2.2 Power budget

In the Jet Emitting Disk region, the accretion heating power available in the accretion flow P_{acc} is written as:

$$P_{acc} = \frac{GM\dot{M}}{2R_{isco}} \left[1 - \left(\frac{r_{isco}}{r_J} \right)^{1-p} \right] \tag{2.31}$$

P_{acc} is balanced in three different types of cooling: advection, radiation and ejection. The ejection power is released in the jets and is controlled by one of the model parameter b, as $P_{jets} = b\, P_{acc}$. The other two occurs inside the accretion flow and their sum is equal to $(1-b)\, P_{acc}$. In Fig. 2.4 (lower right panel), I present the radial profile of the power budget of a given solution. At high mass accretion rate, the JED can always be considered as a radiatively efficient flow (compared to an ADAF), with the radiative cooling power of the same order as the advection power. At low mass accretion rate ($\dot{m} < 10^{-2}$), the JED-SAD behaves like an ADAF.

One can thus characterize a JED solution with the proportion of power released in radiative cooling and in advection. This is actually relevant as three different JED regimes can be observed. In Fig. 2.5, I present the ratio between the advected and cooling power inside of the JED region in the plane $[r_J; \dot{m}]$. The top left region is characterized by a larger advection $P_{adv} \gtrsim P_{cool}$ and can thus be called the radiatively efficient and advection dominated (READ) JED (see simulation (a) in Fig. 2.6). Below a threshold in r_J (around 10) and above a threshold in $\dot{m}$ (around 0.5-1), the JED becomes dominated by the radiative cooling power $P_{adv} \lesssim P_{cool}$ and transits towards the radiatively efficient and radiatively dominated (RERD) JED (simulation

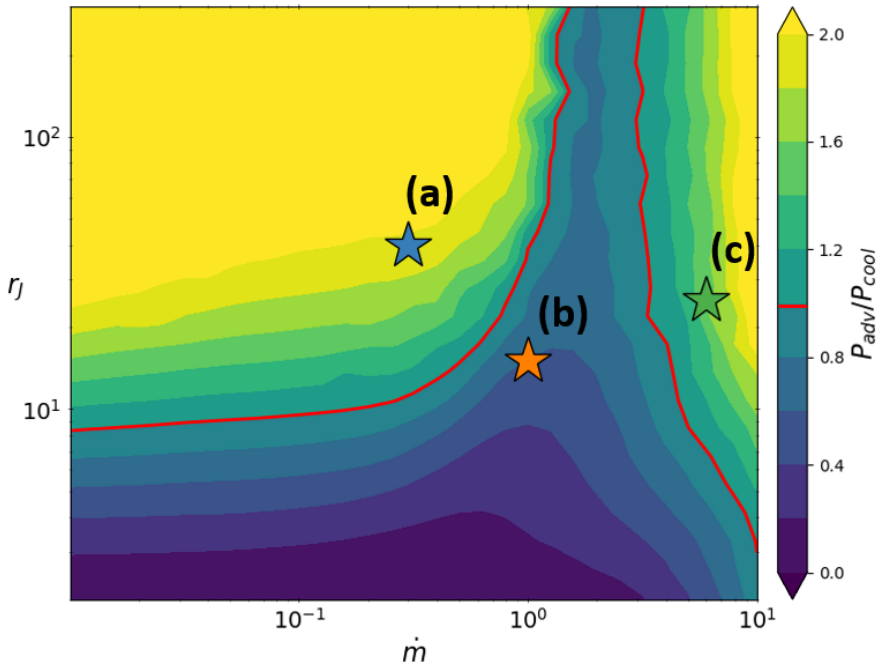

FIGURE 2.5: Ratio between the advection and radiative cooling power in the 2D parameter space $[r_J; \dot{m}]$. The other parameters are fixed to: $m = 10$; $r_{isco} = 2$; $\omega = 0.1$; $m_s = 1.5$; $b = 0.3$; $p = 0.01$. The red line show the equipartition $P_{adv} = P_{cool}$. Three stars, ($r_J = 40$, $\dot{m} = 0.3$), ($r_J = 15$, $\dot{m} = 1$) and ($r_J = 25$, $\dot{m} = 6$), highlight the simulations plotted in Fig. 2.6.

(b) in Fig. 2.6; see Marcel et al. 2022 for more details). Finally, above a high value of $\dot{m}$ (above 3-5) the JED reaches a SLIM state regardless of r_J reminding what is obtained by Abramowicz et al. (1980, 1988) (simulation (c) in Fig. 2.6).

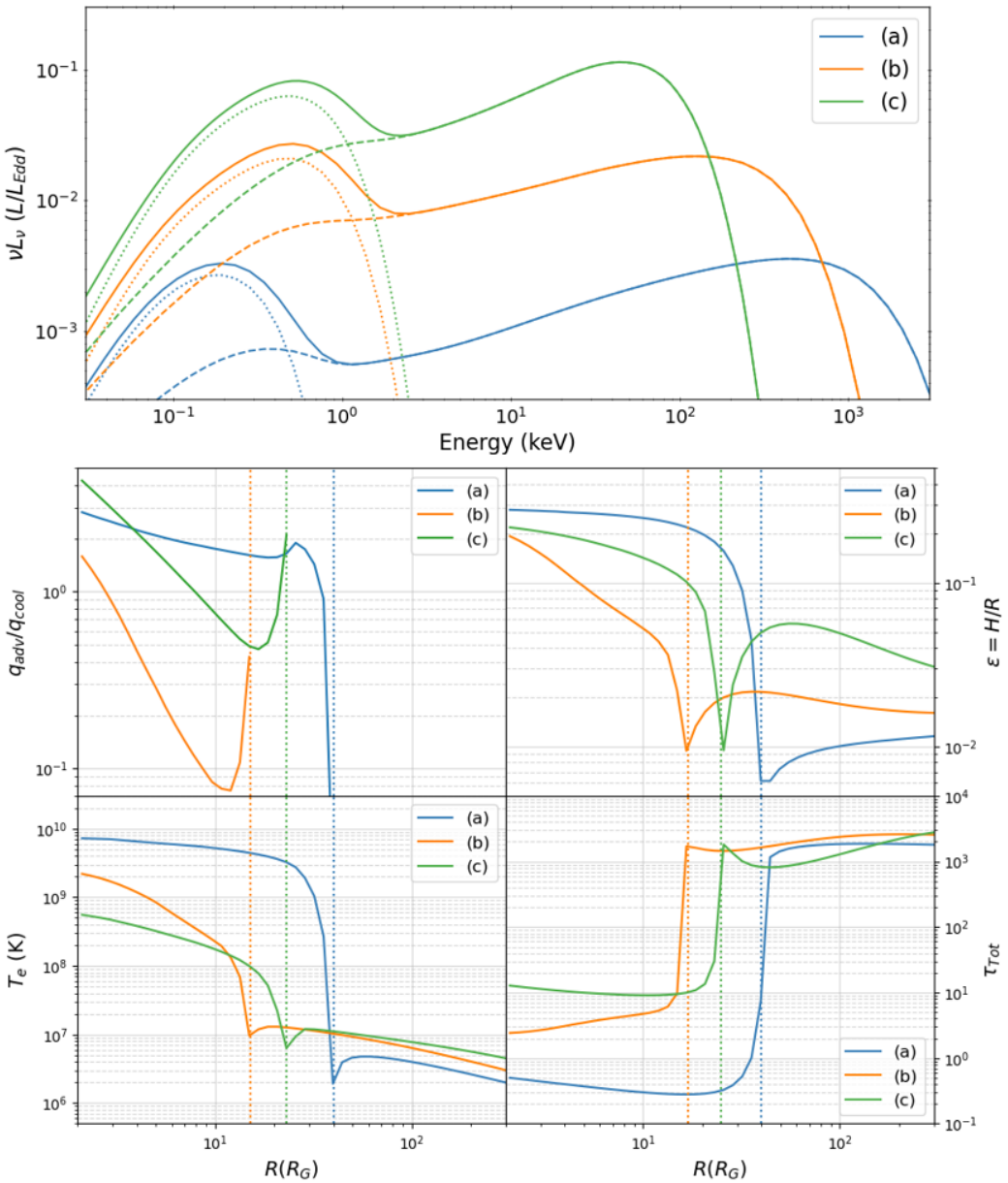

FIGURE 2.6: Difference between a radiatively efficient and advection dominated (READ) JED, a radiatively efficient and radiatively dominated (RERD) JED and a SLIM JED. The three simulations (a, b and c) have been highlighted in Fig. 2.5. Their parameters are ($r_J = 40$, $\dot{m} = 0.3$), ($r_J = 15$, $\dot{m} = 1$) and ($r_J = 25$, $\dot{m} = 6$) respectively. The other parameters are fixed to: $m = 10$; $r_{isco} = 2$; $\omega = 0.1$; $m_s = 1.5$; $b = 0.3$; $p = 0.01$. They are plotted in blue, orange and green respectively. **Top**: Spectral shape in $\nu L\nu$. The solid line represent the total spectrum, the dashed line the emission coming from the JED and the dotted line from the SAD. **Bottom**: Radial profile of the advection to radiative cooling power ratio q_{adv}/q_{cool} (top left), aspect ratio ϵ (top right), electron temperature T_e (bottom left) and total optical depth τ_{Tot} (bottom right). The transition radius between the JED and the SAD is highlighted with a dotted vertical line using the same color as the corresponding simulations.

The three simulations (a: $r_J = 40$, $\dot{m} = 0.3$), (b: $r_J = 15$, $\dot{m} = 1$) and (c: $r_J = 25$, $\dot{m} = 6$) highlighted in Fig. 2.5 are respectively examples of the READ, RERD and SLIM regime. Their spectra, power budget, geometry, temperature and vertical total optical depth are presented in Fig. 2.6. Simulation (a) representative of the radiatively efficient and advection dominated (READ) JED regime still possesses a radiative cooling power of the same order of the advection power (contrarily to an ADAF where $q_{adv} \gg q_{cool}$). In this case, the JED appear geometrically thick ($\epsilon \sim 0.2 \rightarrow 0.3$) and optically thin ($\tau_{Tot} \sim 1$). Almost all the JED rings present the same temperature (within a factor of $3 \rightarrow 5$). Simulation (b) representative of the radiatively efficient and radiatively dominated (RERD) JED regime shows a aspect ratio anti-correlated with the radius ($\epsilon \sim 0.01 \rightarrow 0.1$) and a medium optical depth ($\tau_{Tot} \sim 1 \rightarrow 10$). The JED is also comparatively colder and present a larger radial stratification of the temperature (within a factor of $10 \rightarrow 20$) compared to the READ regime. As such, the X-ray power-law indexes of the emission from the different JED rings show a larger range and the total spectrum is a bit softer. Finally, Simulation (c) representative of the SLIM JED regime shows a SLIM geometry ($\epsilon \sim 0.1$), a rather high optical depth ($\tau_{Tot} \sim 10$) and lower temperatures.

2.3 Parameter space

In this section, I will study the effect of the different JED-SAD parameters on both the power budget and the spectra.

2.3.1 Black hole Mass – m

The black hole mass can be multiple order of magnitude apart depending whether we look at XrB or at AGN. Here I present three different cases for three different masses: $m = 10$, $m = 10^7$ and $m = 10^{10}$. In the top panel of Fig. 2.7, I plot the ratio of the advection to radiative cooling power in the 2D parameter space $[r_J; \dot{m}]$ for the three different black hole masses. The red line marks the transition between the READ, RERD and SLIM JED regimes. From this figure, we can conclude that this transition does not depend on the black hole mass. In the middle and bottom panel of Fig. 2.7, I plot the total spectrum, temperature and total optical depth for three given JED-SAD solution, assuming three different black hole masses. As I am comparing spectra with very different luminosities, I rescaled the luminosity to their Eddington luminosity. The other parameters are fixed to: $r_J = 30$; $\dot{m} = 0.5$; $r_{isco} = 2$; $\omega = 0.1$; $m_s = 1.5$; $b = 0.3$; $p = 0.01$. Two points can be raised: The peak emission of the standard disk is shifting toward lower energy the higher the mass, consistent with the decrease of the standard disk temperature with the mass. And secondly, whatever the mass, the JED present the same radial profile of temperature and optical depth, and show a similar spectral shape with approximately the same high energy cutoff and spectral index.

The implications of this paragraph are quite surprising as some physical processes do not scale with the mass, Compton scattering and electron-positron interactions being a few examples. Furthermore, the electron density inside of the accretion flow scales with the mass and so there is 9 order of magnitude of difference between the $10M_\odot$ XrB and the $10^{10}M_\odot$ AGN. The fact that the JED-SAD reaches the same thermal equilibrium, given the same geometry and accretion speed is puzzling. To explain why this the chosen solution would require the study of the thermal solution, which I leave for later study. However, I can already explain why the same solution would work. One can show (see Eq. 4 in Marcel & Neilsen 2021):

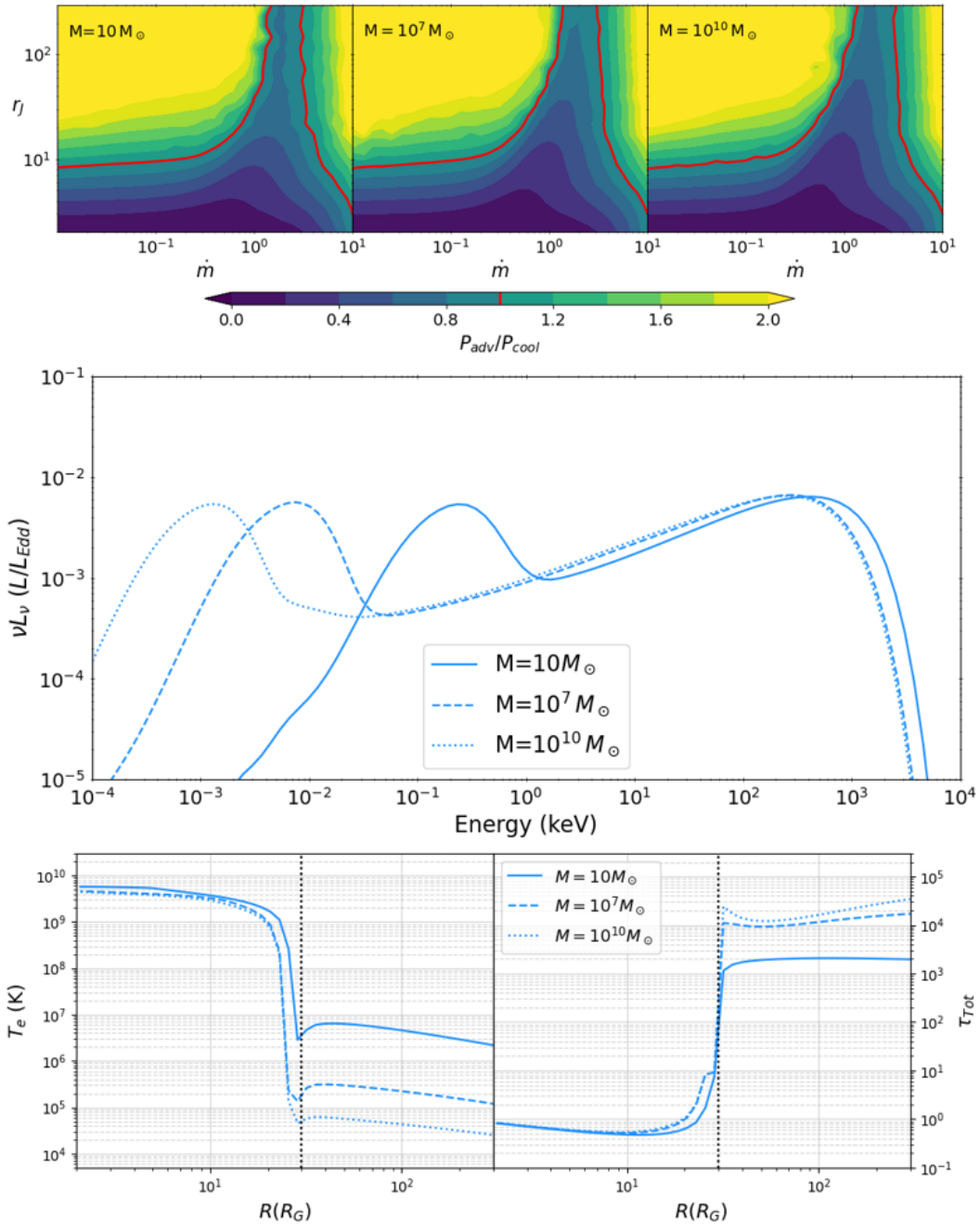

FIGURE 2.7: Influence of the black hole mass. **Top:** Ratio of the advected power to the radiative cooling power in a 2D parameter space map $[r_J;\dot{m}]$ for three different values of the black hole mass $m = 10$ (left), $m = 10^7$ (middle) and $m = 10^{10}$ (right). The red line represent the equipartition $P_{adv} = P_{cool}$. **Middle:** Total JED-SAD spectrum obtained for three different values of the black hole mass $m = 10$ (solid line), m=10^7 (dashed line) and m=10^{10} (dotted line). The other parameters are fixed to $r_J = 30$; $\dot{m} = 0.5$; $r_{isco} = 2$; $\omega = 0.1$; $m_s = 1.5$; $b = 0.3$; $p = 0.01$. **Bottom:** Radial profile of the electron temperature (left), and total optical depth (right) for the same three simulations. The dotted vertical line marks the transition (r_J) between the JED and SAD.

$$\epsilon\tau = \frac{H}{R}\tau = 5\left(\frac{\dot{m}}{1}\right)\left(\frac{1.6}{m_s}\right)\left(\frac{10}{r}\right)^{1/2} \tag{2.32}$$

Thus the product $\epsilon\tau$, for a given mass accretion rate $\dot{m}$ and sonic mach number m_s, is a constant and does not depend on the black hole mass. Assuming that we have the same aspect ratio ϵ for solutions with different black hole masses, the optical depth will be the same. And the same thermal equilibrium will be solution of the energy equation. Furthermore, in a comptonized spectrum, what matters is not the electron density but the Thomson optical depth. So as long as the the comptonization (of any emitting physical process) dominates the spectrum, similar JED spectral output should be expected regardless of the black hole mass. This point will be relevant for the AGN study in Chapter 5.

Even though the total JED spectral output does not depend on the mass, its composition can vary as the physical process responsible for the emission (bremsstrahlung, synchrotron...) depends on the accretion flow density. In Fig. 2.8, I plot the different spectral components of the JED emission for the three different simulations presented in Fig. 2.7 using the same line-style code: $m = 10$ in solid line, m=10^7 in dashed line and m=10^{10} in dotted line. AGN spectra are dominated by the comptonization of external photons while the XrB spectrum is rather dominated by the comptonized synchroton. This can be understood as the AGN disk is much colder and peaks at lower energy but with roughly the same power fraction (in Eddington units). As such, the AGN standard disk emission provides a lot more cold photons to the JED compared to the XrB standard disk. In Fig. 2.8, the comptonization of external photons appears above the total JED emission around $10^{-2} \rightarrow 1$ keV, this is explained as part of these photons are possibly deducted by photon-photon interactions. The details of the spectral composition is still part of a work in progress that

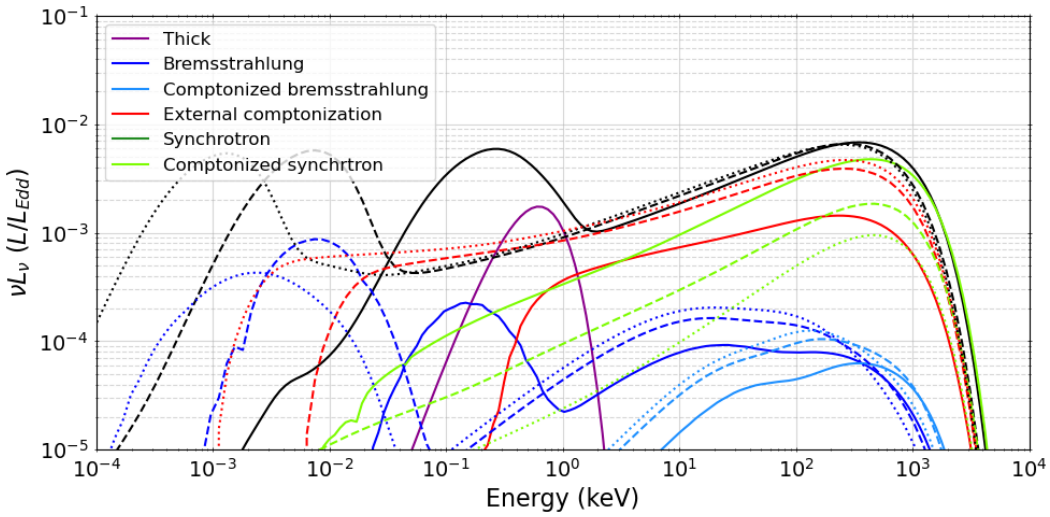

FIGURE 2.8: Influence of the black hole mass on the spectral composition. Spectral composition for three different values of the black hole mass $m = 10$ (solid line), m=10^7 (dashed line) and m=10^{10} (dotted line). The other parameters are fixed to $r_J = 30$; $\dot{m} = 0.5$; $r_{isco} = 2$; $\omega = 0.1$; $m_s = 1.5$; $b = 0.3$; $p = 0.01$. In purple, the optically thick emission from the JED. In red, the comptonization of external photons (coming from the SAD). In black, the total spectrum. In blue and light blue, the bremsstrahlung and comptonized bremsstrahlung respectively. In green and light green, the synchrotron and comptonized synchrotron respectively.

will be discussed in Chapter 4.

2.3.2 Mass accretion rate – $\dot{m}$

In Fig. 2.5, we have seen the power budget of the JED in the 2D parameter space $[r_J; \dot{m}]$. Let us take a closer look at the influence of the mass accretion rate on this figure: The red lines, marking the transition between the READ, RERD and SLIM JED regime present two critical values of $\dot{m}$. One of which is almost always crossed in XrB outbursts $\dot{m} \sim 0.5 \rightarrow 1$. This line is curved and at lower $r_J \sim 20 \rightarrow 10$, the critical value is closer to $\dot{m} \sim 0.5$. In this thesis, we will see that this transition is important to understand the spectral behaviour during an outburst as the JED transits from the READ to RERD regime. The second transition happens at $\dot{m} \sim 3 \rightarrow 5$ where the JED transits to the SLIM regime.

In Fig. 2.9, I plot the SED and radial profile of the temperature and optical depth for three different JED-SAD solution for $\dot{m} = 0.05$, $\dot{m} = 0.5$ and $\dot{m} = 5$. All other parameters are fixed to $m = 10$; $r_J = 30$; $r_{isco} = 2$; $\omega = 0.1$; $m_s = 1.5$; $b = 0.3$; $p = 0.01$. The higher the mass accretion rate, the higher the total available accretion

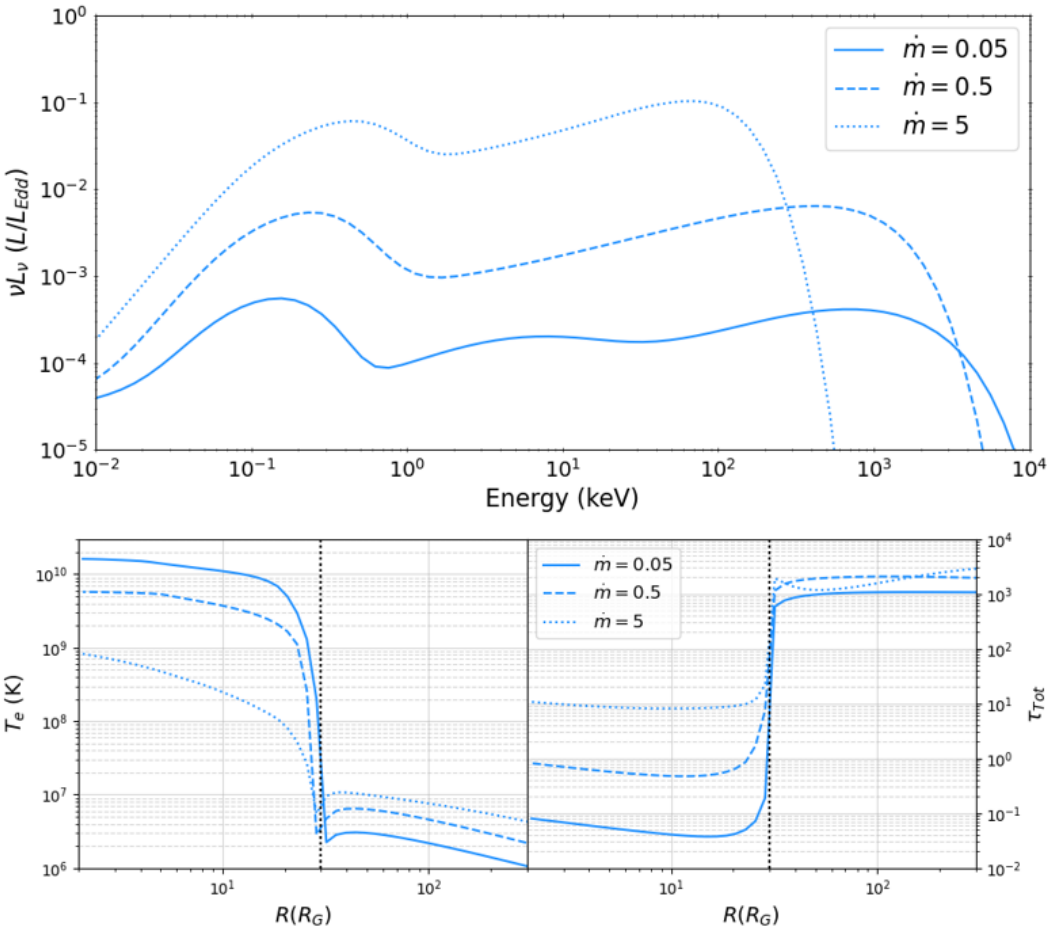

FIGURE 2.9: Influence of the mass accretion rate. **Top:** Total JED-SAD spectrum obtained for three different values of the mass accretion rate $\dot{m} = 0.05$ (solid line), $\dot{m} = 0.5$ (dashed line) and $\dot{m} = 5$ (dotted line). The other parameters are fixed to $m = 10$; $r_J = 30$; $r_{isco} = 2$; $\omega = 0.1$; $m_s = 1.5$; $b = 0.3$; $p = 0.01$. **Bottom:** Radial profile of the electron temperature (left), and total optical depth (right) for the same three simulations. The dotted vertical line marks the transition (r_J) between the JED and SAD.

power in the JED. This entails that we get higher luminosity with $\dot{m}$. The SAD disk blackbody (low energy part of the SED) becomes hotter with $\dot{m}$. The high-energy cutoff of the JED power-law like emission decreases with $\dot{m}$. This is explained as the density and total optical depth increases the higher $\dot{m}$ is, inferring lower maximal temperature inside the JED. The spectral shape of the $\dot{m} = 0.05$ JED spectrum present multiple Compton orders due to the low optical depth ($\tau_{Tot} \sim 10^{-1}$).

2.3.3 Transition radius – r_J

In Fig. 2.5, we have seen the power budget of the JED in the 2D parameter space $[r_J; \dot{m}]$. Let us now take a closer look at the influence of the transition radius on this figure: The red lines, marking the transition between the READ, RERD and SLIM JED regime present a critical value of r_J. Below $r_J \sim 10$, the JED transits toward a RERD regime. This critical line is however curved and closer to $\dot{m} \sim 0.5 \rightarrow 1$, the critical value of the transition radius ranges $r_J \sim 10 \rightarrow 30$. Above $\dot{m} \sim 1$, the JED is in a RERD regime regardless of r_J. The second transition between the RERD and SLIM regimes depends poorly on r_J.

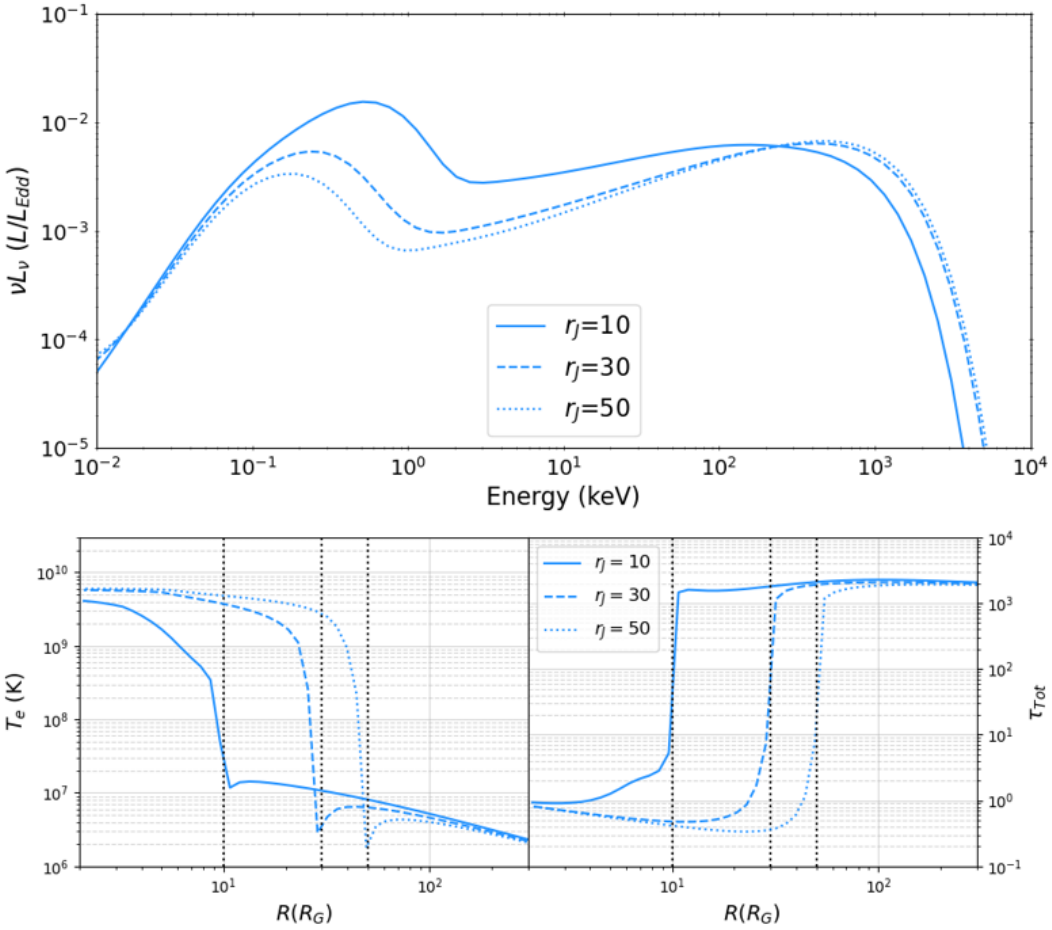

FIGURE 2.10: Influence of the transition radius. **Top:** Total JED-SAD spectrum obtained for three different values of the transition radius $r_J = 10$ (solid line), $r_J = 30$ (dashed line) and $r_J = 50$ (dotted line). The other parameters are fixed to $m = 10$; $\dot{m} = 0.5$; $r_{isco} = 2$; $\omega = 0.1$; $m_s = 1.5$; $b = 0.3$; $p = 0.01$. **Bottom:** Radial profile of the electron temperature (left), and total optical depth (right) for the same three simulations. The dotted vertical lines mark the transition (r_J) between the JED and SAD.

In Fig. 2.10, I plot the SED and radial profile of the temperature and optical depth for three different JED-SAD solution with for $r_J = 10$, $r_J = 30$ and $r_J = 50$. All other parameters are fixed to $m = 10$; $\dot{m} = 0.5$; $r_{isco} = 2$; $\omega = 0.1$; $m_s = 1.5$; $b = 0.3$; $p = 0.01$. The lower r_J is, the closer the standard disk is to the black hole and the smaller the corona is. As such, the SAD disk blackbody maximum temperature (low energy part of the SED) becomes hotter the smaller r_J is. Furthermore, as more energy is released within the cold and optically thick part of the accretion flow, the SAD total luminosity increases. The high-energy cutoff of the JED power-law like emission and the maximum temperature of the JED decreases by a small amount when r_J decreases. The biggest difference in the JED emission is observed for the spectral index of the power-law like emission due to changes in the radial stratification of the temperature. The rings ($r \sim 4 \rightarrow 10$) that were hot for large r_J are colder but still release an important part of the radiative energy. As such, the relative importance of the colder, softer X-ray increases the smaller r_J becomes. And thus the softer the spectral index becomes. When r_J decreases, the relative importance of the SAD increases compared to the JED. When r_J reaches the ISCO, the JED disappears and there is no longer any hard power-law emission, only the SAD disk blackbody remains. This is a soft spectral state.

2.3.4 Inner radius – r_{isco}

In the top panel of Fig. 2.11, I plot the power budget in the 2D parameter space [r_J;$\dot{m}$] for three different values of the ISCO. The larger the ISCO is and the higher the critical value of r_J for the READ→RERD regime becomes. Furthermore, the SLIM regime is reached for higher mass accretion rate. From the spectral point of view (middle panel of Fig. 2.11, the value of the ISCO mostly impacts the high energy cutoff and spectral index of the power-law. Indeed, the smaller the ISCO, the closer the JED gets to the black hole and the hotter it can be as shown by the radial profile of temperature in the bottom panel of Fig. 2.11. A larger ISCO also reduces by a small amount the total accretion power released within the JED region (see Eq. 2.31), as such the total luminosity is also smaller.

2.3.5 Dilution factor – ω

The dilution factor ω controls the number of seed photons emitted by the cold disk blackbody entering the JED region. The larger omega and the larger the external Compton cooling. In the top panel of Fig. 2.12, I plot the power budget in the [r_J;$\dot{m}$] parameter space for three different values of ω. The impact on the power budget is negligible, the transition $P_{adv} = P_{cool}$ is slightly affected, its curvature increasing between the horizontal critical value for r_J and the vertical critical value for $\dot{m}$. In the middle and bottom panel of Fig. 2.12, I plot the SED and radial profile of the temperature and optical depth for three different values of ω. The other parameters are fixed to $m = 10$; $r_J = 30$; $\dot{m} = 0.5$; $r_{isco} = 2$; $m_s = 1.5$; $b = 0.3$; $p = 0.01$. It should be noted that this solution is dominated by comptonized synchrotron. Thus ω has a small spectral impact. Its effect is mostly on the X-ray spectral index for which a higher ω means a softer JED. This is explained as ω increases the cooling inside the JED and thus changes the radial stratification of the temperature, cooling down the external ring of the JED. The high energy cutoff of the JED spectrum is not impacted. The range of value and importance of this parameter are further discussed in Chapter 4.

2.3.6 Accretion speed – m_s

In the top panel of Fig. 2.13, I plot the power budget of the JED in the [r_J;$\dot{m}$] parameter space for three different values of m_s. Here major difference are observed. When the accretion speed is sub-sonic ($m_s = 0.5$), the JED is much denser than when the accretion is supersonic. As such, the optical depth is generally higher and the RERD JED regime takes a large region of the parameter space. The critical value for $\dot{m}$ is close to 0.1. Whereas, when the accretion speed is very high ($m_s = 3$), the accretion flow density is smaller and the optical depth much lower, as such it is harder to reach the RERD JED regime. In fact the RERD regime can no longer be reached for $r_J \gg 10$, and a transition directly between the READ and SLIM JED exist. This has major impact on the spectral output we get for the different values of m_s. For a given set of JED-SAD parameters, changing m_s can result in the transition from a READ to a RERD or even SLIM JED.

In the middle and bottom panel of Fig. 2.13, we see the spectral implications. In the case of $m_s = 0.5$, optically thick emission from the JED is important and the usual disk blackbody shape seen at low energy is deformed. As the density is much higher and the radiative cooling processes much more efficient, the JED temperature is lower by orders of magnitude at the ISCO and the resulting high-energy cutoff is smaller by an order of magnitude. The luminosity of the JED is also higher in the hard X-ray energy band and the spectral index softer, this is due to the large range of temperature observed in the profile. In the supersonic case, the higher m_s, the lower the density is, and the hotter the JED can be. The spectral index of the JED also decreases with m_s. The difference in luminosity between the two supersonic case is however much smaller compared to the difference with the subsonic case.

2.3.7 Jet power – b

In the top panel of Fig. 2.14, I plot the power budget of the JED in the [r_J;$\dot{m}$] parameter space for three different values of the power given to the jets b. Once again major difference are observed. For low value of b ($b = 0.1$), the RERD JED state does not exist above $r_J = 40$, the vertical critical value of $\dot{m}$ having almost disappeared. Whereas with a lot of power in the jets ($b = 0.7$), the RERD JED state takes a large portion of the parameter space and the critical value of $\dot{m}$ is close to 0.2. In the middle and bottom panel of Fig. 2.14, we see the spectral implications. The two solutions with low value of b are extremely similar and are both optically thin and hot JED. Where as the solution for $b = 0.7$ presents a much colder JED. The luminosity in the soft and hard X-ray spectral region is a factor 3 to 4 higher. The SAD bump is also not well visible in the SED due to the large optically thick emission coming from the JED rings.

2.3.8 Ejection Index – p

The ejection index p has a very small impact on both the power budget of the JED and the total SED (see Fig. 2.15) within the range of existence of the JED ($p \leq 0.1$). Only with very high value of the ejection index ($p \sim 0.1$) do we see a difference in the SAD emission as the mass accretion rate within the SAD $\dot{m}(r_{SAD}) = \dot{m}(r_J) = \dot{m}\,(r_J/r_{isco})^p$ is more important and thus the standard disk is hotter and more luminous.

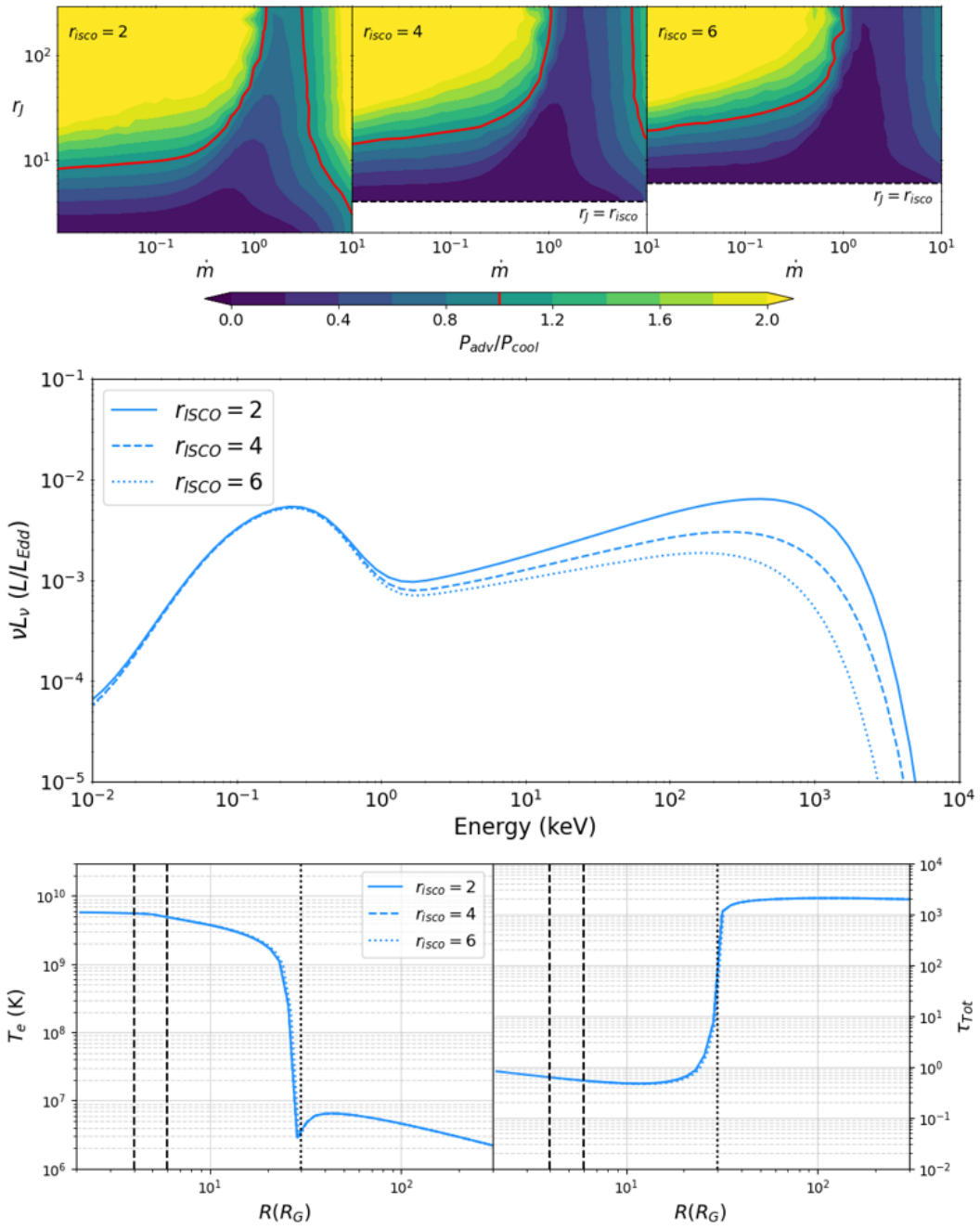

FIGURE 2.11: Influence of the ISCO. **Top:** Ratio of the advected power to the radiative cooling power in a 2D parameter space map $[r_J;\dot{m}]$ for three different values of the ISCO $r_{isco} = 2$ (left), $r_{isco} = 4$ (middle) and $r_{isco} = 6$ (right). The red line represent the equipartition $P_{adv} = P_{cool}$. The black dashed line represent teh soft state $r_J = r_{isco}$. **Middle:** Total JED-SAD spectrum obtained for three different values of the ISCO $r_{isco} = 2$ (solid line), $r_{isco} = 4$ (dashed line) and $r_{isco} = 6$ (dotted line). The other parameters are fixed to $m = 10$; $r_J = 30$; $\dot{m} = 0.5$; $\omega = 0.1$; $m_s = 1.5$; $b = 0.3$; $p = 0.01$. **Bottom:** Radial profile of the electron temperature (left), and total optical depth (right) for the same three simulations. The dotted vertical line marks the transition (r_J) between the JED and SAD. The dashed vertical lines mark the position of the ISCO below which there is no JED.

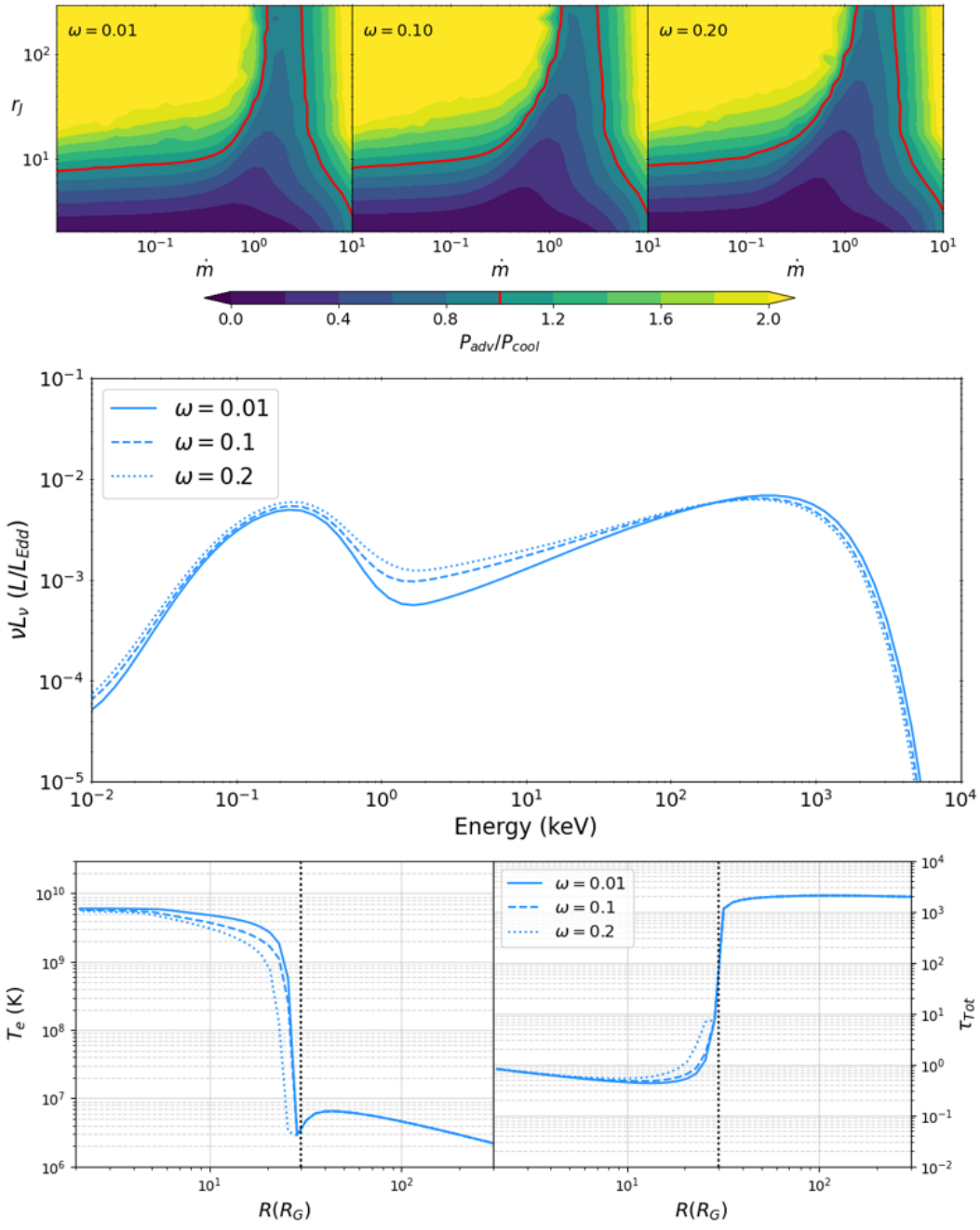

FIGURE 2.12: Influence of the dilution factor ω. **Top:** Ratio of the advected power to the radiative cooling power in a 2D parameter space map [r_J;$\dot{m}$] for three different values of the dilution factor $\omega = 0.01$ (left), $\omega = 0.1$ (middle) and $\omega = 0.2$ (right). The red line represent the equipartition $P_{adv} = P_{cool}$. **Middle:** Total JED-SAD spectrum obtained for three different values of the dilution factor $\omega = 0.01$ (solid line), $\omega = 0.1$ (dashed line) and $\omega = 0.2$ (dotted line). The other parameters are fixed to $m = 10$; $r_J = 30$; $\dot{m} = 0.5$; $r_{isco} = 2$; $m_s = 1.5$; $b = 0.3$; $p = 0.01$. **Bottom:** Radial profile of the electron temperature (left), and total optical depth (right) for the same three simulations. The dotted vertical line marks the transition (r_J) between the JED and SAD.

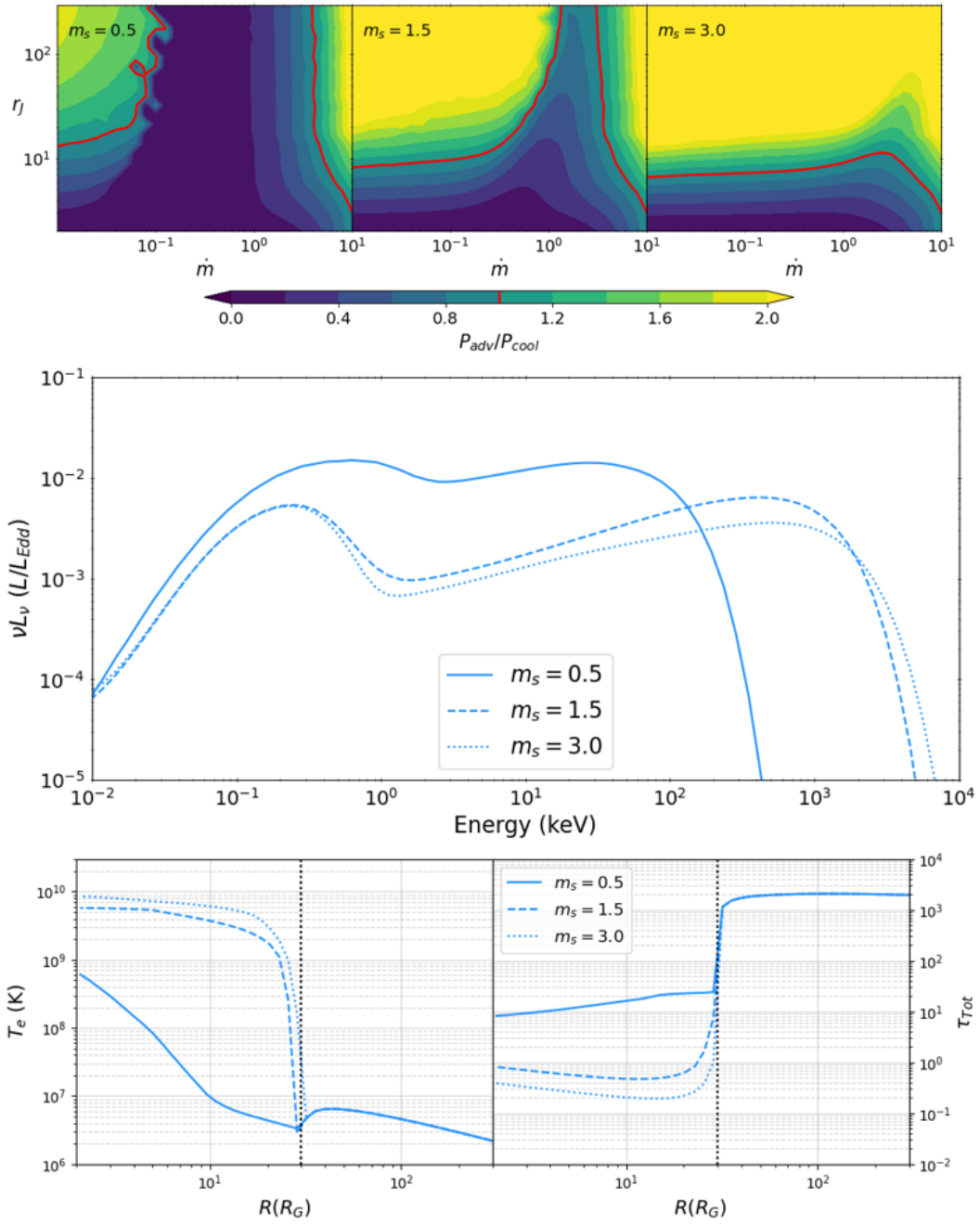

FIGURE 2.13: Influence of the sonic mach number m_s. **Top:** Ratio of the advected power to the radiative cooling power in a 2D parameter space map $[r_J;\dot{m}]$ for three different values of the sonic mach number $m_s = 0.5$ (left), $m_s = 1.5$ (middle) and $m_s = 3.0$ (right). The red line represent the equipartition $P_{adv} = P_{cool}$. **Middle:** Total JED-SAD spectrum obtained for three different values of the sonic mach number $m_s = 0.5$ (solid line), $m_s = 1.5$ (dashed line) and $m_s = 3.0$ (dotted line). The other parameters are fixed to $m = 10$; $r_J = 30$; $\dot{m} = 0.5$; $r_{isco} = 2$; $\omega = 0.1$; $b = 0.3$; $p = 0.01$. **Bottom:** Radial profile of the electron temperature (left), and total optical depth (right) for the same three simulations. The dotted vertical line marks the transition (r_J) between the JED and SAD.

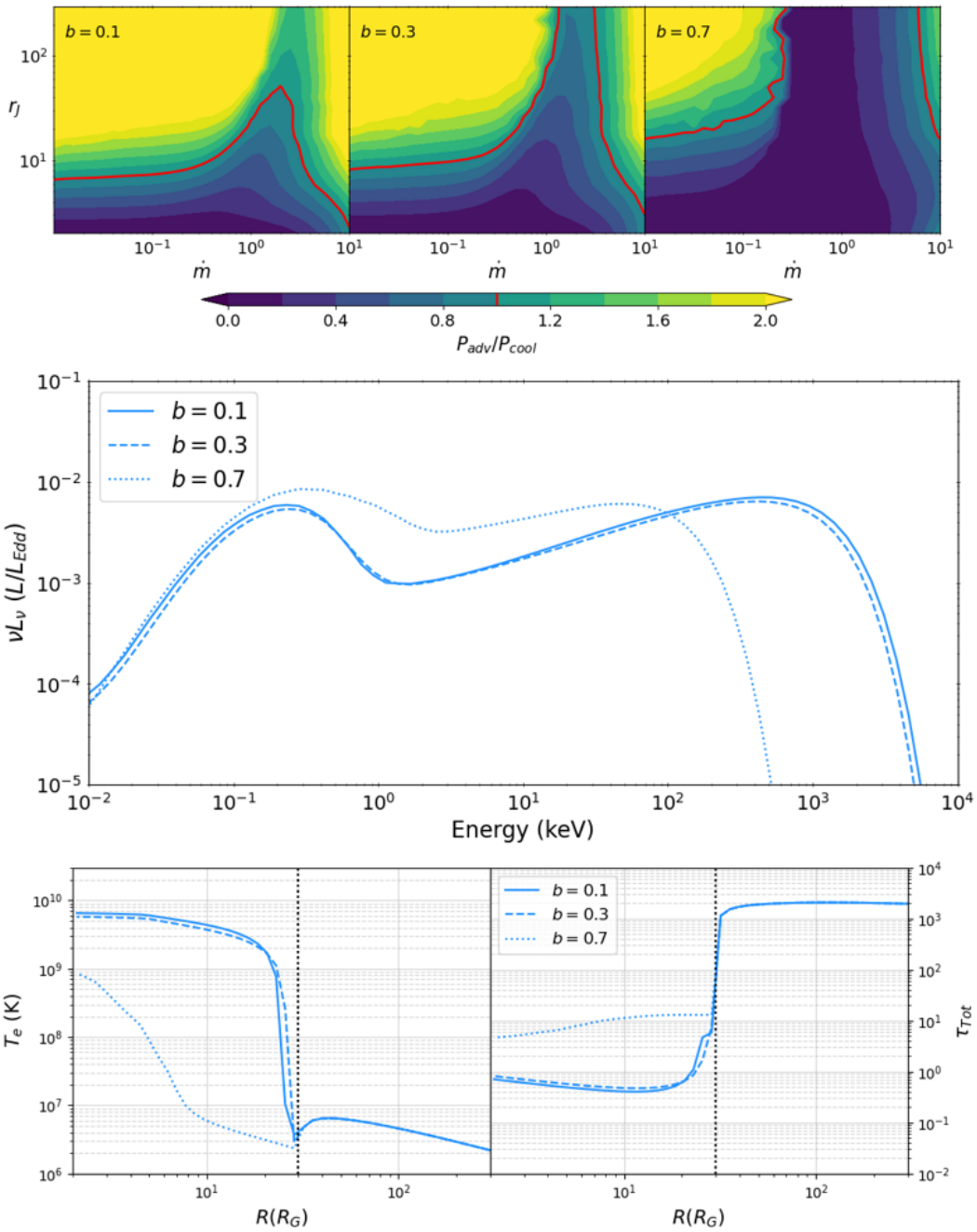

FIGURE 2.14: Influence of the power released in the jets b. **Top:** Ratio of the advected power to the radiative cooling power in a 2D parameter space map $[r_J;\dot{m}]$ for three different values of the power lost in the jets $b = 0.1$ (left), $b = 0.3$ (middle) and $b = 0.7$ (right). The red line represent the equipartition $P_{adv} = P_{cool}$. **Middle:** Total JED-SAD spectrum obtained for three different values of the power lost in the jets $b = 0.1$ (solid line), $b = 0.3$ (dashed line) and $b = 0.7$ (dotted line). The other parameters are fixed to $m = 10$; $r_J = 30$; $\dot{m} = 0.5$; $r_{isco} = 2$; $\omega = 0.1$; $m_s = 1.5$; $p = 0.01$. **Bottom:** Radial profile of the electron temperature (left), and total optical depth (right) for the same three simulations. The dotted vertical line marks the transition (r_J) between the JED and SAD.

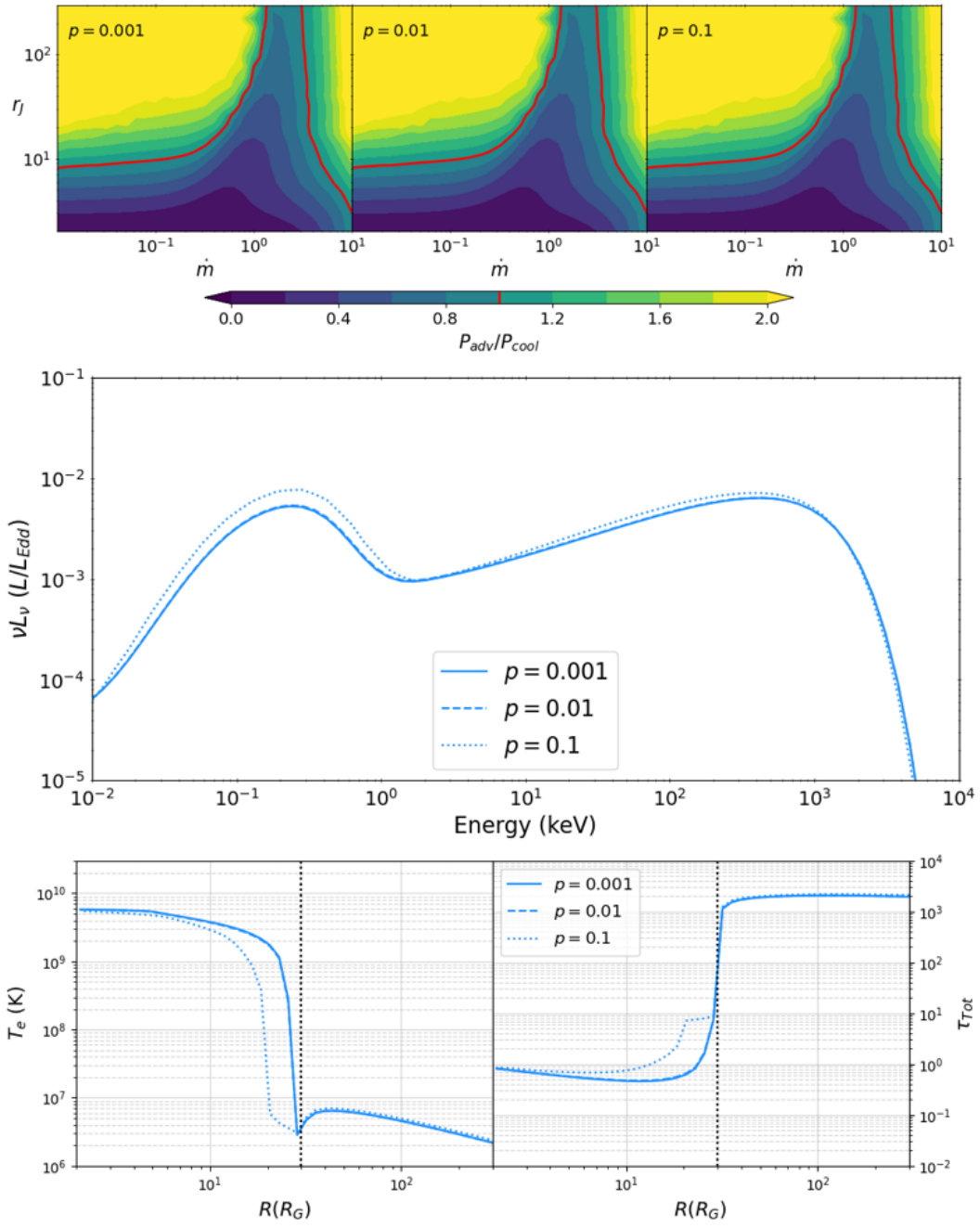

FIGURE 2.15: Influence of the ejection index p. **Top:** Ratio of the advected power to the radiative cooling power in a 2D parameter space map $[r_J;\dot{m}]$ for three different values of the ejection index $p = 0.001$ (left), $p = 0.01$ (middle) and $p = 0.1$ (right). The red line represent the equipartition $P_{adv} = P_{cool}$. **Middle:** Total JED-SAD spectrum obtained for three different values of the ejection index $p = 0.001$ (solid line), $p = 0.01$ (dashed line) and $p = 0.1$ (dotted line). The other parameters are fixed to $m = 10$; $r_J = 30$; $\dot{m} = 0.5$; $r_{isco} = 2$; $\omega = 0.1$; $m_s = 1.5$; $b = 0.3$. **Bottom:** Radial profile of the electron temperature (left), and total optical depth (right) for the same three simulations. The dotted vertical line marks the transition (r_J) between the JED and SAD.

2.4 Tables and Reflection

The beginning of this thesis marked the start of the exploitation phase of the JED-SAD model. Here I describe how I computed the JED-SAD table and the reflection component for direct spectral application within the XSPEC software.

2.4.1 JED-SAD tables

Using the Dyplodocus code, I compute spectra for a large set of JED-SAD parameters. These spectra are defined with bins of energy $[E_i;E_{i+1}]$. XSPEC tables must be defined in units of ph/s/cm^2. If the flux array contains N bins, then the corresponding table must be specified with an energy array of length N+1, containing the energy range of each bins ($[E_1; E_2; ...; E_N; E_{N+1}]$). As such, one can directly implement the JED-SAD spectra within a Xspec table using the pyxspec python module where functions are provided for this effect[3]. Xspec works in units of ph/s/cm^2, as such when plotting in νL_ν, the model are multiplied twice by the Xspec energy array. However, if the Xspec energy array is not the same as the energy array used for the model, then the spectra can appear dented. This is a purely cosmetic issue. One might want to increase the number of bins to produce nice looking spectra for presentations and papers, even though, this does not change anything when fitting data.

I produce JED-SAD table that are separated in two different tables. Indeed, since the Dyplodocus code computes the spectra emitted by each ring, we are able to separate the emission coming from the JED and the one coming from the SAD regions. As such, I create two tables for each set of JED-SAD parameters. One containing the JED emission, and the other containing the SAD emission. This is useful as the SAD is an optically thick emission and thus should suffer from the viewing angle in inclined systems. By separating the two tables, one can apply to the JED-SAD table a cosine factor to take this effect into account. This does not apply to the optically thin emission from the JED. Since the total spectrum of a given JED-SAD configuration is separated between two tables, one must make sure to link the parameters of both tables when fitting data.

2.4.2 Reflection computation

The JED-SAD model does not compute the reflection spectrum associated with the JED-SAD geometry and thermal solution. Instead we hijack the Xillver model from J. Garcia (Garcia et al. 2013; García et al. 2015). In the Xillver model, an optically thick 1-dimensional slab with constant density is illuminated by a cut-off power-law spectrum (emitted by the hot corona). The code solves both ionization and energy balance producing the reflection spectrum. Compton scattering is included using a Gaussian redistribution kernel. The main parameters of the Xillver models are:

- Γ, the spectral index of the illuminating power-law. $\Gamma \in [1.2; 3.4]$.
- E_{cut} or kT_e, the high energy cutoff in keV of the illuminating power-law, related to the electron temperature inside of the hot corona. $E_{cut} \in [20; 300]$.
- ξ, the ionization parameter of the optically thick accretion flow. $\xi = 4\pi F_{inc}/n_e$, with F_{inc} the incident ionizing flux and n_e the electron density of the gas. $log(\xi) \in [0; 4.7]$.

[3]One can follow the steps presented in the example on the Heasarc webpage: https://heasarc.gsfc.nasa.gov/docs/software/lheasoft/headas/heasp/node39.html

- AF_e, the iron abundance of the gas, in units of solar abundance. $AF_e \in [0.5; 10]$.
- i, the viewing angle compared to the disk normal. $i \in [5°; 85°]$.

To compute a reflection spectrum consistent with the JED-SAD model, I fit the JED emission using a high energy cutoff power-law to get approximate values of the spectral index Γ and high energy cutoff kT_e of the each JED spectrum in my JED-SAD tables. I then build a new reflection table with 1) the same JED-SAD parameters as my JED-SAD tables, 2) the ionization parameter ξ, 3) the iron abundance AF_e, 4) the viewing inclination. In another word, I replace the spectral index and high energy cutoff of the Xillver table with sets of JED-SAD parameters.

As the JED-SAD model present degeneracies, multiple set of parameters produce the same Γ and E_{cut}, this means that the substitution is not a bijection and the JED-SAD reflection table contains redundancies. The new table is thus much larger compared to the Xillver table. This approach allows to reduce computation time during the actual fit of a data set by a large amount compared to proceeding with the computation of the reflection spectrum while fitting. To limit the reflection table size, I first identify the relevant JED-SAD parameter space for the observations, usually by fitting the continuum with the JED-SAD table. If the inclination angle of the source is known or at least limited to a range of value, I limit the viewing angle parameter of the Xillver table to a given value. But even with this precaution, JED-SAD table can be as heavy as 10 Go. This however never posed problems to fit data in Xspec.

This procedure is not perfect, there are multiple improvements to be made. The choice of the Xillver model over the more recent and complete Relxill (Dauser et al. 2014; García et al. 2014) which includes relativistic effects from the relline ray tracing code, is justified by the addition of the large number of parameters this would entail. To include relativistic effects, we instead use the multiplicative model kdblur[4] (Laor 1991) from the Xspec library, allowing us to keep the relativistic effects parameters within Xspec and not within the reflection table. There are more parameters in Xillver than the few I mentioned above. For instance, in early version of the table the density of the electrons inside the disk was fixed to $n_e = 10^{15}$ cm^{-3}. This value is closer to what is usually expected for AGN compared to XrB (the density of the disk being inversely proportional to the mass). In a more recent version of the code, they produced new tables adding the density n_e as a free parameters and observed significant changes in the spectrum. New tables can always be produced with more parameters (increasing their size) and can be tested, but this is not the purpose of my thesis. The tables that I use in this thesis were computed based on the first Xillver model, where the density was fixed to $n_e = 10^{15}$ cm^{-3}.

2.5 General strategy

The JED-SAD spectral model is physically motivated. As such the spectral solutions are constrained and limited to physically viable solution. The evolution of the spectral parameters are connected together through the JED-SAD parameter space. For instance, increasing the mass accretion rate $\dot{m}$ will increase the JED luminosity, but this will also increase the SAD luminosity and the SAD temperature, while decreasing the high energy cutoff and softening the JED spectrum. Similarly, reducing the transition radius r_J will not only soften the spectrum, the SAD will get hotter and more luminous as it approaches the black hole. These examples show how the

[4] https://heasarc.gsfc.nasa.gov/xanadu/xspec/manual/node289.html

JED-SAD spectral model is physically constrained and one can not do whatever one wants. This render the fitting of data harder, but also give much more information about the physics happening inside of the disk.

The JED-SAD model has several parameters, some possibly physically correlated to each other, however as we do not know à priori how, we consider them independent from each other in the code. Our strategy is to constrain the evolution of the parameters, by fitting spectra, and determine how these parameters evolve together to reproduce what the observed XrB behavior. This informs us on the relations between the parameters and how the physical process behind these relations works (magnetic field advection, etc...).

2.6 Caveats and prospects

The JED-SAD model has some caveats that can be improved. Some of them have already been mentioned, but let me comment them and introduce others in this paragraph.

Newtonian computation

As mentioned, the Dyplodocus assumes a purely Newtonian gravitational potential. It is clear that relativistic effects should apply close to the inner regions, close to the black hole, and as such the emission of these region would probably be different. There is currently no plan to compute a general relativistic version of the model. However, one can start with a first order approximation of the spectral relativistic effects. The KYN code allows to compute GR spectral effects assuming that we have the spectra emitted at each radius and the gas velocities (private communication with Michal Dovciak).

Degeneracies

The effect of each parameters have been discussed in Sec. 2.3. As we have seen, the JED-SAD parameters can have different spectral effects (luminosity, spectral index, high energy cutoff, disk temperature...), some have similar effects. In the absence of the complete broadband spectrum to better constrain the parameters, the JED-SAD model present degeneracies. To avoid them, we limit the parameter space of the JED-SAD tables to the main parameters r_J, $\dot{m}$ and fix most of the other parameters. Letting other parameter free would certainly allow better fits, but it has to be done with care since as the 2 space is more complicated, with probably several local minima and multiple degeneracies.

The ω approximation

The dilution factor ω controls the number of SAD photons cooling the JED and thus available for comptonization. It assumes a uniform photon density within the sphere of radius R_J: $U_{rad} = \omega\, L_{SAD}/(4\pi R_J^2 c)$. Each JED radius then receive seed photons detailed by Eq. 2.27. However, ideally, ω should reflect the true geometry of the JED-SAD. Moreover the inner JED radii should receive less SAD seed photons due to the radial optical depth of the JED which can be important enough to stop the seed photons after a few R_G. The exact computation of the external comptonization is part of a work in progress developed in collaboration with Wenda Zhang and his Monte Carlo code MONK (see Sec. 4.3.3).

Spectral components

The contribution of each physical process to the spectrum can be computed using the Belm table (see Figs. 2.3 and 2.8). Comparison with much more precise Monte Carlo simulation done by Wenda Zhang using the MONK code shows general agreement in the physical process spectral composition. A few discrepancies still exist. MONK is however time consuming and not able to fit spectra. This is also part of the work discussed in Sec. 4.3.3.

Jet model

The JED-SAD model is an accretion flow model that takes into account the presence of jets and the consequence of its magnetic feedback torque on the accretion flow. It also predicts the power and density of particle ejected in the jets. However the model does not include any spectral prediction for the jet yet. This is part of a work in progress with Julien Malzac and his jet SED models. In the ISHEM model (e.g. Malzac et al. 2018; Marino et al. 2020) for instance, shells of matter are ejected at time intervals roughly similar to the dynamical time. Each shell possess a random Lorentz factor (ejection speed). Thus faster shells will collides with slower shells, forming shocks that produce particle acceleration and synchrotron emission.

Part II

X-ray binaries

Chapter 3

First application: GX 339-4

Contents

3.1 Object and data selection 72
3.1.1 Characteristics 72
3.1.2 Data selection 72
3.2 Greg's past results 75
3.3 X-ray Fitting 76
3.3.1 Methodology 76
3.3.2 Examples 77
3.3.3 Evolution of the parameters 79
3.4 Outbursts dynamic 87
3.4.1 Magnetic flux evolution 87
3.4.2 Evolution of the JED regime 89
3.4.3 Evolution of the temperature 90
3.5 Radio emission 92
3.5.1 Radio and X-ray emission 92
3.5.2 Generalization of Greg's radio function 93
3.5.3 New radio function 94
3.6 Discussion and interpretation 100
3.6.1 Indications of different radiative behaviors between the rising and decaying phases 100
3.6.2 Changes in the dynamical ejection properties 102
3.6.3 The radio X-ray correlation 108

Objet et données

Pour tester le modèle, je vais me concentrer sur la binaire X GX 339-4. Cette source est estimée à une distance de 8 à 12 kpc (Zdziarski et al. 2004; Parker et al. 2016; Zdziarski et al. 2019). Elle est composée d'une étoile compagnon de masse entre 0.5 et 1.4 $M_\odot$ et d'un trou noir de masse entre 4 et 11 $M_\odot$ (Parker et al. 2016; Zdziarski et al. 2019). La détermination du spin (rotation sur lui même) du trou noir est hautement dépendant de la méthode employée. GX 339-4 est une source bien connue car elle a présenté un grand nombre d'éruptions au cours du fonctionnement du satellite Rossi X-Ray Timing Explorer (RXTE, observant dans les rayons X) entre Décembre 1995 et Janvier 2012. Durant cette période, GX 339-4 présente 5 éruptions, en 1999, 2002, 2004, 2007 et 2010. A l'exception de la première éruption en 1999, elles ont toutes faits le sujet d'une étude multi-longueur d'onde approfondie (voir par exemple Corbel et al. 2003; Homan et al. 2005; Belloni et al. 2006; Cadolle Bel et al. 2011; Motta et al. 2011; Stiele et al. 2011; Corbel et al. 2013) et donnant la possibilité de suivre l'évolution du flot d'accrétion (dans les rayons X avec RXTE) et des jets (dans la radio avec l'Australia Telescope Compact Array, ATCA) au quotidien. C'est aussi une des premières sources où la corrélation entre l'émission X dure et l'émission radio a été observée (Corbel et al. 2003, 2013). Dans la Fig. 3.1, je montre le diagramme HID et la corrélation radio-X pour cette source et obtenue par Corbel et al. (2013).

Pour le premier test spectral du modèle JED-SAD, j'utilise les données X d'archive de RXTE/PCA (3-40 keV) de la décennie 2000-2010. Pour conserver une uniformité des données, je rejette les données RXTE/HEXTE (15-200 keV) qui n'existent pas pour l'éruption de 2010 (suite à l'arrêt de l'instrument). La réduction des données est présentée dans Clavel et al. (2016). Le satellite RXTE n'étant pas un imageur, il est difficile d'extraire la lumière d'arrière plan de la source. Je trouve que dans la majorité des cas, la luminosité d'arrière plan est équivalente à celle de la source au dessus de 25 keV. Je limite donc l'étude à la bande 3-25 keV de l'instrument PCA.

En Fig. 3.2, je trace la courbe de lumière de GX 339-4 dans les rayons X tel qu'observé par RXTE. La courbe violet montre le flux de la loi de puissance X dure et la courbe bleu, le flux du corps noir du disque (les flux ont été obtenus par Clavel et al. 2016). Lorsque la courbe violet domine, nous sommes dans un état dur, lorsque c'est la courbe bleu qui domine, nous sommes dans un état mou. Pour l'étude, je ne sélectionne que les données X dures (région grisée dans la Fig. 3.2) où le modèle JED-SAD est le plus pertinent. Je marque aussi en rouge les dates où des observations radio ont eu lieu. Le Tab. 3.1 montre les données sélectionnées et le nombre d'observations X et radio disponibles pour chaque éruption. au total, ce sont 452 spectres X que j'analyse ave le modèle JED-SAD. Seul l'éruption de 2010 présente une bonne couverture radio avec 24 observations radio pour 80 observations X. Je peux alors interpolé le flux radio pour chaque observation X comme présenté dans l'annexe A.

Avant d'analyser les données, je souhaite mentionner que ces données ont déjà été étudié par Gregoire Marcel (Marcel et al. 2019, 2020) avec le modèle JED-SAD. Cependant, la méthode employée n'est pas l'ajustement de données. Le travail de Grégoire repose sur la comparaison de paramètres spectraux tels que la luminosité, l'indice de la loi de puissance ou bien la coupure à haute énergie. Il a comparé les paramètres spectraux observés (obtenus par Clavel et al. 2016) avec les paramètres spectraux d'une grille de simulation JED-SAD. Il en a ensuite déduit les paramètres correspondant à chaque observation. Je prend maintenant le prochain pas, avec l'ajustement direct des données.

Ajustement et dynamique

Dans la Fig. 3.3, je présente l'ajustement de 5 observations répartis le long de la branche dure de l'éruption de 2010 de GX 339-4. Le panel en haut à gauche montre le HID pour

cette éruption et la position des 5 observations sélectionnées. Les autres panels montrent en haut, le spectre et les données, en bas, le rapport entre les données et le modèle. L'émission provenant du JED est montré en rouge, l'émission du SAD est en vert et la composante de réflection est en bleu. On peut noter qu'au cours de la montée de l'éruption, observation a) à c), le disque augmente en température et apparaît dans la figure. D'autre part, la forme de la raie du fer (autour de 6.4 keV) change et devient moins piqué. Cela s'explique parce que le disque sur lequel la réflection se fait s'approche du trou noir, augmentant les effets relativistes sur la raie du fer. On peut aussi noter la diminution de la coupure haute énergie dans la réflection bien que la coupure haute énergie n'est pas visible dans la composante du JED. Les paramètres de l'ajustement de chaque observation sont donnés dans le Tab. 3.2. Les autres paramètres du JED-SAD ont été fixés à: $m = 10, \mu = 0.5, r_{isco} = 2, \omega = 0.2, m_s = 1.5, b = 0.3, p = 0.01$ (Marcel et al. 2019). La valeur du χ^2/dof de l'ajustement montre que pour l'ensemble des observations, l'ajustement est bon.

Les Figs. 3.4 et 3.5 montrent respectivement l'évolution des paramètres $\dot{m}$ et r_J au cours de la phase dure de chaque éruption. La région marquée en vert correspond aux barres d'erreur obtenue par Marcel et al. (2019, 2020). Mes résultats d'ajustement sont en bleu avec des barres d'erreur en noir. On peut observer que mes résultats sont bien plus contraints comparé à ceux de Grégoire, surtout pour le rayon de transition r_J au cours de la montée de l'éruption. Lors de la descente de l'éruption, les résultats du rayon de transition ont de grandes barres d'erreur, cela est causé par une dégénérescence du modèle avec le paramètre à bas flux.

Maintenant que nous avons obtenu l'évolution des paramètres principaux r_J et $\dot{m}$ au cours de l'éruption, nous pouvons regarder comment ils évoluent l'un par rapport à l'autre. Pour cela, je représente en Fig. 3.13 l'évolution dans l'espace des paramètres $r_J - \dot{m}$ des observations de GX 339-4. Les points ne bleu, orange, vert et rose proviennent des résultats de Grégoire sur l'ensemble des éruptions et où on a sélectionné les résultats avec les meilleurs contraintes. Les résultats en violet avec barre d'erreur en noir proviennent de mes ajustements des données X dures de l'éruption de 2010. Je ne représente pas les autres éruptions par soucis de lisibilité. On voit bien que mes résultats sont globalement en accords avec ceux de Grégoire. Dans ce diagramme $r_J - \dot{m}$, on retrouve un comportement équivalent à celui observé dans le HID (voir Fig. 3.1). Cependant, nous pouvons maintenant voir que durant l'état dur, les paramètres r_J et $\dot{m}$ apparaissent corrélés entre eux. Ceci est un résultat de notre analyse des données et ne provient aucunement d'une hypothèse du modèle. Le modèle nous dit que pour reproduire les données, il faut une évolution des paramètres corrélés. Ceci est d'autant plus intéressant car nous pouvons maintenant étudier le comportement du champ magnétique au cours d'une éruption. En effet, on peut montrer que le flux magnétique dans le JED s'écrit comme Eq. 3.5. De ce fait, selon la loi $r_J(\dot{m}) \propto \dot{m}^{\delta}$ que l'on obtient, le flux magnétique dans le JED peut augmenter ($\delta > -2/3$), diminuer ($\delta < -2/3$) ou bien rester constant ($\delta = -2/3$). Dans le cas de GX 339-4, il semble que le flux magnétique dans le JED est quasi-constant ($\delta \sim -2/3$).

Émission radio et interprétation physique

*Seule l'éruption de 2010 possède suffisamment de point radio pour permettre l'interpolation du flux radio pour chaque observation X. C'est pourquoi je me concentre sur cette éruption pour tester les formules et méthodes dans ce paragraphe. Dans Marcel et al. (2019), une formule pour le flux radio dépendant des paramètres JED-SAD a été proposé (voir Eq. 3.3). Je commence par tester cette formule en assumant les valeurs des paramètres r_J et $\dot{m}$ tels que je les ai obtenus dans mes ajustements des données X. Je représente le rapport entre le flux radio observé et le flux radio déduit de l'Eq. 3.3 dans la Fig. **??** en fonction des paramètres $\dot{m}$ (gauche) et r_J (droite) pour la montée de l'éruption de 2010. On peut observer que dans*

les deux panels, une dépendance fonctionnelle manque dans la formule. Je repars donc de 0 en cherchant cette fois ci à contraindre les dépendances fonctionnelle phénoménologique du flux radio avec les paramètres r_J et $\dot{m}$. La nouvelle formule sera à l'Eq. 3.6 où $\tilde{f}^*$ sera une normalisation, α la dépendance fonctionnelle avec r_J et β celle avec $\dot{m}$. Ces trois paramètres doivent être commun à l'ensemble des observations de l'éruption.

Je commence par contraindre ces paramètres avec la montée de l'éruption de 2010, j'obtiens comme paramètre: $\tilde{f}^* = 7.1^{+15}_{-5} \times 10^{-8}$, $\alpha = -0.66 \pm 0.32$, and $\beta = 1.00^{+0.39}_{-0.38}$. Les contours des paramètres α et β sont tracés en bleu dans la Fig. 3.22. En Fig. 3.20, je montre de nouveau le rapport entre le flux radio observé et le flux radio déduit cette fois ci de ma nouvelle formule. Comme attendu, il ne reste quasiment aucune dépendance fonctionnelle et l'ensemble des points est reproduits à 15% près. J'utilise ensuite la solution obtenue pour la montée de l'éruption de 2010 pour les observations de la descente de l'éruption de 2010. Je constate dans la Fig. 3.21 que cette solution ne semble pas permettre de reproduire les données observées dans cette phase de l'éruption. en effet même avec une normalisation $\tilde{f}^*$ libre, les flux radio observés montrent des rapport proche de 2 avec les flux radio déduit de la formule. Cela signifie qu'il y a un changement de dépendance fonctionnelle entre la montée et la descente de l'éruption. Je contrains alors les paramètres pour la phase de descente de l'éruption: $\tilde{f}^* = 2.9^{+1.0}_{-0.9} \times 10^{-8}$, $\alpha = -0.13^{+0.15}_{-0.16}$, and $\beta = 1.02 \pm 0.23$. Les contours des paramètres α et β sont tracés en rouge dans la Fig. 3.22. Je reproduis la même étude pour chaque montée et descente des 4éruptions de GX 339-4. La Fig. 3.22 montre que les solutions des différentes montée sont en accord ensemble, et les solutions des différentes descentes sont en accord ensemble mais les solutions de montée et de descente des éruptions sont différentes. J'obtiens donc deux formules différentes pour la montée et la descente des éruptions. A l'aide de ces formules, je reproduit l'ensemble des observations radio de GX 339-4 à 15% près (voir Fig. 3.23).

Pour interpréter ces deux fonctions différentes, nous avons formuler un scénario compatible avec l'évolution attendue du champ magnétique dans le modèle JED-SAD. Ce scénario est représenté schématiquement dans la Fig. 3.28. Pour lancer des jets, il existe deux principaux modèles, le modèle Blandford-Znajek (BZ, Blandford & Znajek 1977) où la puissance alimentant les jets est extraite de la rotation du trou noir grâce au ligne de champ magnétique connecté au trou noir, et le modèle Blandford & Payne (BP, Blandford & Payne 1982) où le jet est alimenté en puissance par l'énergie d'accrétion disponible dans le disque. Le modèle JED-SAD suppose l'existance d'une composante BP mais la présence d'une colonne centrale BZ n'est pas impossible. Au cours d'une éruption, lors de la montée dans l'état dur, un large JED est présent et a accumulé du champ magnétique sur le trou noir depuis longtemps. De ce fait, de fort processus BZ et BP peuvent être présents. Dans l'état mou, le JED disparaît, le BP s'arrête et comme le confinement magnétique qui maintenait les forts champs magnétiques sur le trou noir est maintenant absent, le champ magnétique se diffuse dans le SAD et le BZ ne peut continuer. Au bout d'un certains temps, si le champ magnétique s'évacue plus lentement par diffusion que le taux d'accrétion ne diminue, une région de forte magnétisation, un JED, peut se former de nouveau des les régions internes. De retour dans les états durs, le JED grandit et recommence à advecter le champ magnétique sur le trou noir. Cependant le champ magnétique accumulé n'est pas encore suffisant pour créer un fort processus BZ et de ce fait, seul un jet BP existerait.

Ce scénario est intéressant ar il pourrait trouver écho dans les comportements observés des NAG. En effet, une manière de classifier les NAG est selon la morphologie du jet. On distingue alors les classifications Faranoff-Riley I (FR I) et Faranoff-Riley II (FR II). La première est caractérisé par la visibilité d'un jet astrophysique depuis le coeur alors que la seconde est caractérisé par la non détection de ces jets avant une zone de choc à grande distance. Les FR II pourraient être plus collimatés, possiblement en raison de la présence d'une colonne BZ, contrairement aux FR I. De même, il semble que les FR II soient observés

à tous niveau de rapport de luminosité Eddington, comme la phase de montée de l'éruption d'une binaire X. Alors que les FR I sont uniquement détecté à bas rapport de luminosité Eddington, et pourrait donc s'approcher de la phase de descente de l'éruption d'une binaire X.

3.1 Object and data selection

Thanks to the development of the Dyplodocus code, we are able to compute spectra of any given JED-SAD configuration. I build the first spectral tables of the JED-SAD model to directly fit observations in Xspec. This mark the start of the exploitation phase of the model.

3.1.1 Characteristics

To test our JED-SAD paradigm we chose to focus on observations of GX 339-4. The system is situated within our galaxy at a distance of 8 to 12 kpc (Zdziarski et al. 2004; Parker et al. 2016; Zdziarski et al. 2019). In binary systems, most of the time astronomers are not able to determine the exact mass of both components, especially when the secondary star is not very bright. However, they are able to produce a mass function, giving a relation between the mass of the primary, the mass of the secondary and the inclination of the system (e.g. Tauris & van den Heuvel 2006):

$$f_2(M_1) = \frac{M_1^3\, sin^3(i)}{(M_1 + M_2)^2} = \frac{P\,(v_2 sin(i))^3}{2\pi G} \tag{3.1}$$

Where M_1 and M_2 are the masses of the primary and secondary stars, i the inclination, P the periodicity of the orbit and v_1 and v_2 the orbital velocities. This results in some constrains and ranges for the mass. GX339-4 is a LMXrB composed of a donor star of mass between 0.5 and 1.4 $M_\odot$ and a black hole of mass between 4 and 11 $M_\odot$ (Parker et al. 2016; Zdziarski et al. 2019). The determination of the spin of a black hole is still highly debated as the results seems highly dependent on the method used.

GX339-4 is a well-known source as it presented multiple outbursts, making it one of the most active XrB, during the operational period of the Rossi X-Ray Timing Explorer (RXTE) satellite between December 1995 and January 2012. During this period, GX339-4 undergoes five complete outbursts, in 1999, 2002, 2004, 2007 and 2010, as well as a few hard-only or *failed* outbursts in 2006, 2008 and 2009 where the system did not show any sign of state transition. Except for the first outburst in 1999, the others were the subject of extensive multi-wavelength observation campaigns (see e.g. Corbel et al. 2003; Homan et al. 2005; Belloni et al. 2006; Cadolle Bel et al. 2011; Motta et al. 2011; Stiele et al. 2011; Corbel et al. 2013), allowing to catch the day to day evolution of both the accretion flow (RXTE) and the jets using the Australia Telescope Compact Array (ATCA). This allowed to study its multi-wavelength behavior and plot the first radio X-ray correlation extending on more than three order of magnitude (Corbel et al. 2003, 2013). In Fig. 3.1, I show the HID and radio–X-ray correlation of the multi-wavelength observations of GX339-4 obtained by Corbel et al. (2013).

3.1.2 Data selection

For the first spectral test of the JED-SAD model, I use X-ray spectra from the *RXTE/PCA* (3-40 keV) archive of GX339-4 during the 2000-2010 decade. In order to have a uniform data analysis, I reject the data from the *RXTE/HEXTE* (15-200 keV) instrument since they were not always usable (e.g., in the case of low flux observations or after March 2010 when the instrument definitely stopped observing). The data processing is detailed in Clavel et al. (2016). They also fitted the observations using phenomenological models (diskBB + power-law) to extract the main spectral parameters (disk

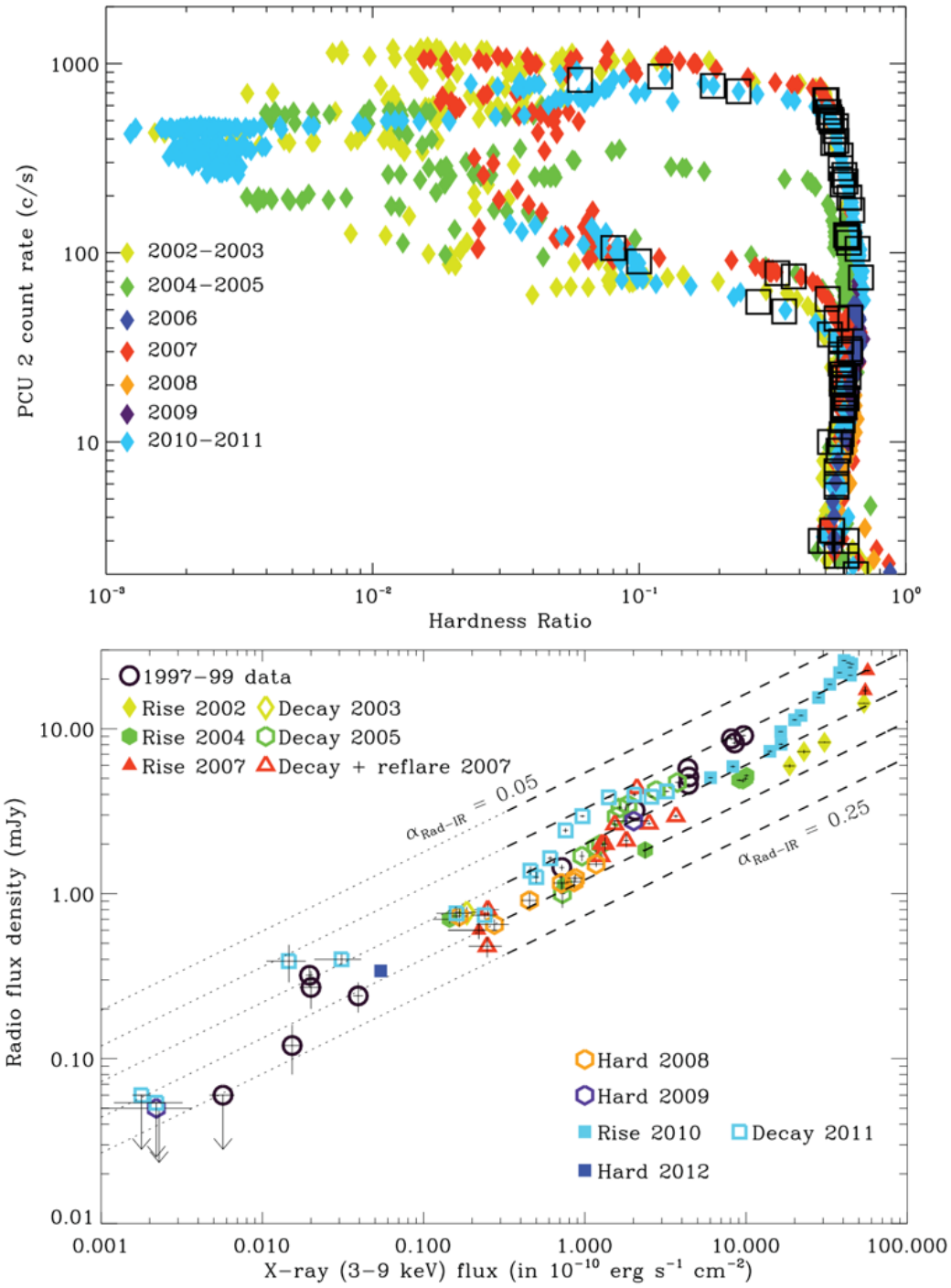

FIGURE 3.1: From Corbel et al. (2013). **Top**: HID of the multiple outbursts of GX339-4 as observed by RXTE during the 2000-2010 decade. The colors represent the different outbursts. The empty squares mark the position of the ATCA radio detection. The 2006, 2008 and 2009 outbursts are hard-only or *failed* outbursts where no state transition to the soft spectral states were observed. **Bottom**: Radio–X-ray correlation of GX339-4. The radio observation come from the 9GHz band of ATCA. Different markers are used for each outburst. The filled and empty markers represent respectively observations of the rising and decaying phase of the outburst. The dashed line represent predictions from the near-Infrared to X-ray correlation from Coriat et al. (2009), assuming different values of the radio to infrared spectral index α_{Rad-IR}.

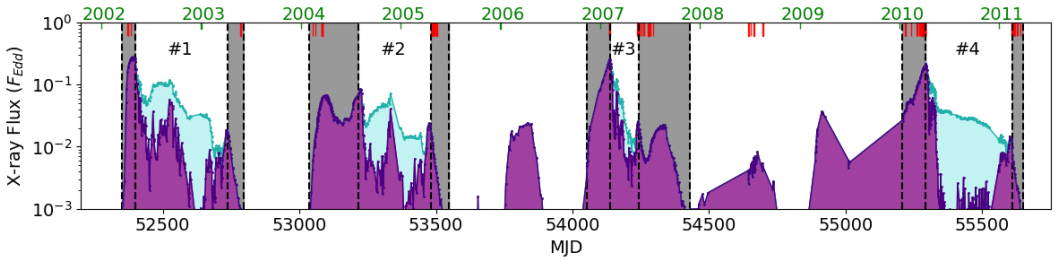

FIGURE 3.2: GX339-4 X-ray light curve in the 3-200 keV energy band of the 2000-2010 decade obtained with the Clavel et al. (2016) fits. The violet filled region shows the power law unabsorbed flux, while the cyan region represents the disk unabsorbed flux. The selected spectra for this study are highlighted in grey: the rising and decaying hard states of the four outbursts. At the top the red lines represent the observations when steady radio fluxes were observed at 9 GHz (from Corbel et al. 2013).

temperature, hard X-ray spectral index, etc...). RXTE is not an imager, as such it is difficult to separate the emission of the source from the background. I found that the instrumental background was generally of the order of, or larger than, the source emission above 25 keV. As such I limited the energy range of the spectral analysis to the 3-25 keV energy range of the PCA instrument.

I reject the failed outbursts as they are not yet fully understood. I only use "pure" hard states (i.e., those at the very right part of the HID), either in the rising or decaying phase, and do not include the transition phases of the outburst even when radio emission is detected (during the so-called Hard Intermediate state, HIS). The reasons for this choice are threefold. First, the radio flux is smoothly evolving during pure hard-states, a signature of stationary processes hopefully easier to catch. Furthermore, the flat radio spectra during the hard states are consistent with self-absorbed synchrotron emission from the optically thick region of a jet (Blandford & Königl 1979; Reynolds 1982). Conversely, an important radio variability is observed during the transition phases, especially during the hard-to-soft transition. At the same time, discrete radio-emitting ejecta can be followed (e.g. Carotenuto et al. 2021a). Second, the JED-SAD hybrid disk is the most relevant during the hard states where both a hot corona and the jet are observed. Third, during the transition states, the so-called hard-tail component progressively appears. As this component is not well understood and is not self-consistently included in the JED-SAD model, I do not select the transition states.

In Fig. 3.2, I plot the 2000-2010 PCA X-ray light curve of GX339-4 obtained by Clavel et al. (2016), I separate the flux coming from the disk blackbody component (cyan) and the hard X-ray power-law (violet). I also show the date of the radio observations from Corbel et al. (2013) using red marks at the top of the figure. I highlight in grey the selected hard states observations. I follow Clavel et al. (2016) for the definition of the hard state periods of each outburst. In Table 3.1 I report the corresponding starting and ending Modified Julian Dates (MJD) of the selected rising and decaying hard state phases.

In radio, I use the 9 GHz fluxes obtained with the Australia Telescope Compact Array (ATCA) and discussed in Corbel et al. (2013). Observations dating from before 2009 were made before the Compact Array Broadband Backend (CABB) upgrade of the instruments (resulting in significant improvement in sensitivity) and have a radio bandwidth of 128 MHz wide and are centered at 8.64 GHz. While observations from after the CABB update are 2 GHz wide and centered at 9 GHz. As such, small corrections to the older observations to correct for the different radio center band

TABLE 3.1: Hard state periods of the 4 outbursts and number of selected observations.

Outburst	Rise$^{(a)}$	Decay$^{(b)}$	X-ray$^{(c)}$	Radio$^{(d)}$
2002-2003	52345-52399	52739-52797	49	4 (3/1)
2004-2005	53036-53219	53482-53549	177	16 (7/9)
2007	54051-54137	54241-54429	146	13 (2/11)
2010-2011	55208-55293	55609-55640	80	24 (16/8)

Notes: $^{(a)}$ MJD of the rising phase of each outburst.
$^{(b)}$ MJD of the decaying phase of each outburst.
$^{(c)}$ Number of X-ray observations covering each outburst.
$^{(d)}$ Number of radio observations covering each outburst, I specify the number of rising phase observations or decaying phase observations using the notation: (rising / decaying).

was done assuming a flat radio spectra. Compared to the X-ray observations, the radio survey is quite sparse (see Fig. 3.2), as such I only selected the radio fluxes close to X-ray pointings by less than one day (which I will call in the following quasi-simultaneous radio–X-ray observations).

This selection corresponds to a total of 452 hard X-ray spectra and 57 radio fluxes distributed among the four outbursts. The 2010-2011 outburst has both the best X-ray and radio coverage, with about 80 X-ray spectra for 24 radio measurements well distributed along the outburst. Thanks to this dense radio-coverage I can linearly interpolate the radio light curve to estimate the radio fluxes for each of the 80 X-ray spectra of this outburst. This is supported by the smooth evolution of the radio light-curve during the pure hard states. The resulting interpolation is plotted in Fig. B.1 in appendix B. I add 10% systematic error to the interpolated radio pointings associated with each X-ray spectrum to take into account the non-simultaneity between the radio and X-ray observations. This is justified as the smooth radio light-curve show at maximum an evolution of around 3 mJy within three to four days for a total flux of around 20 mJy. Within the one day interval we allow in our definition of simultaneous radio–X-ray observation, the radio flux does not evolve more than the 10% systematic we add. Such an interpolation procedure for the radio emission was not possible for the other outbursts due to the too small number of radio pointings.

3.2 Greg's past results

Gregoire Marcel (Greg) already studied the same outbursts, not limited to the hard states, using a qualitative approach without fitting the data in Xspec (see Marcel et al. 2019, 2020). Instead he computed a grid of JED-SAD model and estimated their corresponding 3-200 keV luminosity (L_{3-200}), power law luminosity fraction ($PLF = L_{PL}/L_{3-200}$) and 2-10 keV spectral index Γ. Then he compared these parameters with the ones computed by Clavel et al. (2016) from their fit of the data with a diskBB + power-law model. Greg defined a function to minimize to identify the JED-SAD spectrum which best reproduced these spectral characteristics:

$$\xi_X = \frac{|\log[L_{3-200}/L^{obs}_{3-200}]|}{\alpha_{flux}} + \frac{|\log[PLF/PLF^{obs}]|}{\alpha_{PLF}} + \frac{|\Gamma/\Gamma^{obs}|}{\alpha_\Gamma} \tag{3.2}$$

The characteristic marked with ^{obs} are extracted from Clavel et al. (2016) and describe the observations. The coefficients α are arbitrary weights associated with each constrain. Greg used $\alpha_{flux} = \alpha_{PLF} = 1$ as both the total luminosity and power-law fraction are comparable. Since the hard tail in the *soft* spectral state is not taken into account in the JED-SAD model, Greg added Greg added "by hand" a power-law component whose flux corresponds to 10% of the 2-10 keV band as it is generally observed (Remillard & McClintock 2006) and used a weighted coefficient α_Γ which depends on the power-law fraction PLF.

Greg also introduced a function predicting the radio emission at a given frequency based on the JED-SAD parameters Marcel et al. (2018a, 2019) (following the work of Blandford & Königl 1979; Heinz & Sunyaev 2003):

$$\nu_R F_R = \tilde{f}_R \, \dot{m}^{17/12} \, r_{isco} (r_j - r_{isco})^{5/6} \, F_{Edd} \tag{3.3}$$

with ν_R the radio frequency, F_R the radio flux at the given radio frequency, $\dot{m}$ the JED-SAD mass accretion rate, r_J the transition radius between the JED and the SAD, r_{isco} the innermost stable circular orbit, F_{Edd} the Eddington flux of the source and $\tilde{f}_R$ a normalization factor that takes into account all unknown jet parameters. Eq. 3.3 allows to derive the radio spectrum emitted by the optically thick region of the jet assuming general assumptions (see Marcel et al. 2018a for its derivation). Using Eq. 3.3, Greg was able to qualitatively reproduce, simultaneously, the radio and X-ray observations of GX 339-4, fixing $\tilde{f}_R$ to be the same for all the radio pointings.

In this thesis, we take the next logical step and directly fit in Xspec the observations using tables of the JED-SAD model. I will be able to compare the results obtained from Greg's qualitative approach with my results. The fitting procedure put obviously much stronger constraints on the JED-SAD parameters compared to the approach of Greg. I have checked however (see Sec. 3.3.3) that both methods agree qualitatively quite well.

3.3 X-ray Fitting

3.3.1 Methodology

To fit the data, I use three different combinations of Xspec models and tables. I will name them model 1, 2 and 3. The First model is designed to fit the continuum of the spectrum. **Model 1: TBABS×(JED+SAD)**. It is composed of the Tuebingen-Boulder Inter-Stellar Medium (ISM) absorption model called TBABS in Xspec using the updated ISM abundances from Wilms et al. (2000). The two other components of Model 1 are the JED and SAD tables computed in Sect. 2.4.1. They represent the emission of the hot corona and disk blackbody respectively. In the second model I add the reflection table computed in Sect. 2.4.1, in order to fit the Iron Kα line as well as the Compton hump around $\sim 20keV$. **Model 2: TBABS×(JED+SAD+REFL)**. Finally, in the third model, I add relativistic blurring effects to the reflection table using the Xspec multiplicative model Kdblur, based on the computation from Laor (1991). **Model 3: TBABS×(JED+SAD+KDBLUR*REFL)**.

In each model, the JED-SAD parameters of the JED, SAD and reflection tables are linked together to ensure a consistent physical continuum. To compare my fitting results with Greg's qualitative approach, I choose to use the same general JED-SAD parameters ($m = 10, \mu = 0.5, r_{isco} = 2, \omega = 0.2, m_s = 1.5, b = 0.3, p = 0.01$, see Marcel et al. 2019) and only letting free the main JED-SAD parameters $\dot{m}$ and r_J. In each model, the hydrogen column density was frozen to $0.6 \times 10^{22}\,\mathrm{cm}^{-2}$ following

the published value (Zdziarski et al. 2004; Bel et al. 2011). Model 2 adds three free parameters to the fit, the ionisation parameter of the disk, the iron abundance and the reflection normalisation. In model 3, Kdblur introduces new parameters, I set the index of the disk emissivity to 3 (its default value), the outer disk radius to 400 R_G, and the inclination to 30°, consistent with the value expected for GX 339-4 (Parker et al. 2016). The last parameter of Kdblur is the inner radius of the reflecting region, which is linked to the value of r_J as the optically thick disk (the SAD) only start at r_J.

I devised an automatic fitting procedure fitting each observation using these three models in succession. After each fit using one of the model, I compute the errors on the main parameters $\dot{m}$ and r_J. When moving to the next model, I use the best-fit result of the precedent model as a starting point of the next fit. This procedure is designed to ensure that Xspec is fitting the continuum primarily using the JED and SAD tables, and not a highly ionised and relativistic reflection. The best fit of model 3 is then dominated by the JED and SAD table instead of the reflection table. Indeed, the normalisation of the reflection table being free results in the possibility of using a highly ionised ($log(\xi) \sim 4$[1]) reflection to fit the continuum and the iron line at the same time. The JED and SAD table sometimes being below the reflection by an order of magnitude. This solution requiring a very high reflection fraction and a highly anisotropic corona emission seems unrealistic and is then avoided using this 3-step procedure.

The addition of new components to the fitting model at each step always improves the fit. However this is not always by a significant statistical amount. Especially at low flux when the observation signal to noise ratio (SNR) is not the best. This is also the case of the observations where the reflection is produced at a large radius and thus the general relativistic effects of the Kdblur model are not so important. It should be noted that the difference in the JED-SAD main parameters between the different models are not very large (within a few R_G for r_J), and as such I choose to keep the best fit using model 3 for all observations, even if the addition of kdblur is not always statistically significant.

In the first series of fit, the iron abundance of the reflection table was mostly stagnant around a rather high value of 7 times the Solar iron abundance, in agreement with similar spectral analysis of GX 339-4 (e.g., García et al. 2015; Fürst et al. 2015; Parker et al. 2016; Wang-Ji et al. 2018), and I freeze it to this value in the following. Such a high iron abundance could be a consequence of the Xillver reflection model. Newer version of the model, using higher disk density, more consistent to what is expected in XrB, results in values closer to the solar abundance (e.g. Tomsick et al. 2018; Jiang et al. 2019).

3.3.2 Examples

As examples, I show in Fig. 3.3 a few of the best fits using model 3 for observations distributed along the hard X-ray states of the 2010-2011 outbursts. In the top left panel of this figure I represent the HID of the outburst and highlight the hard states as blue diamond and the five observations showcased in the other panels of the figure. The best fit parameters for these five observations are shown in Tab. 3.2

[1] At these values, the disk acts almost as a mirror, reflecting the power-law and presenting a very small and broadened iron line. Furthermore, the computation of the Xillver table at such high ionisation are not the most reliable (J. Garcia private communication).

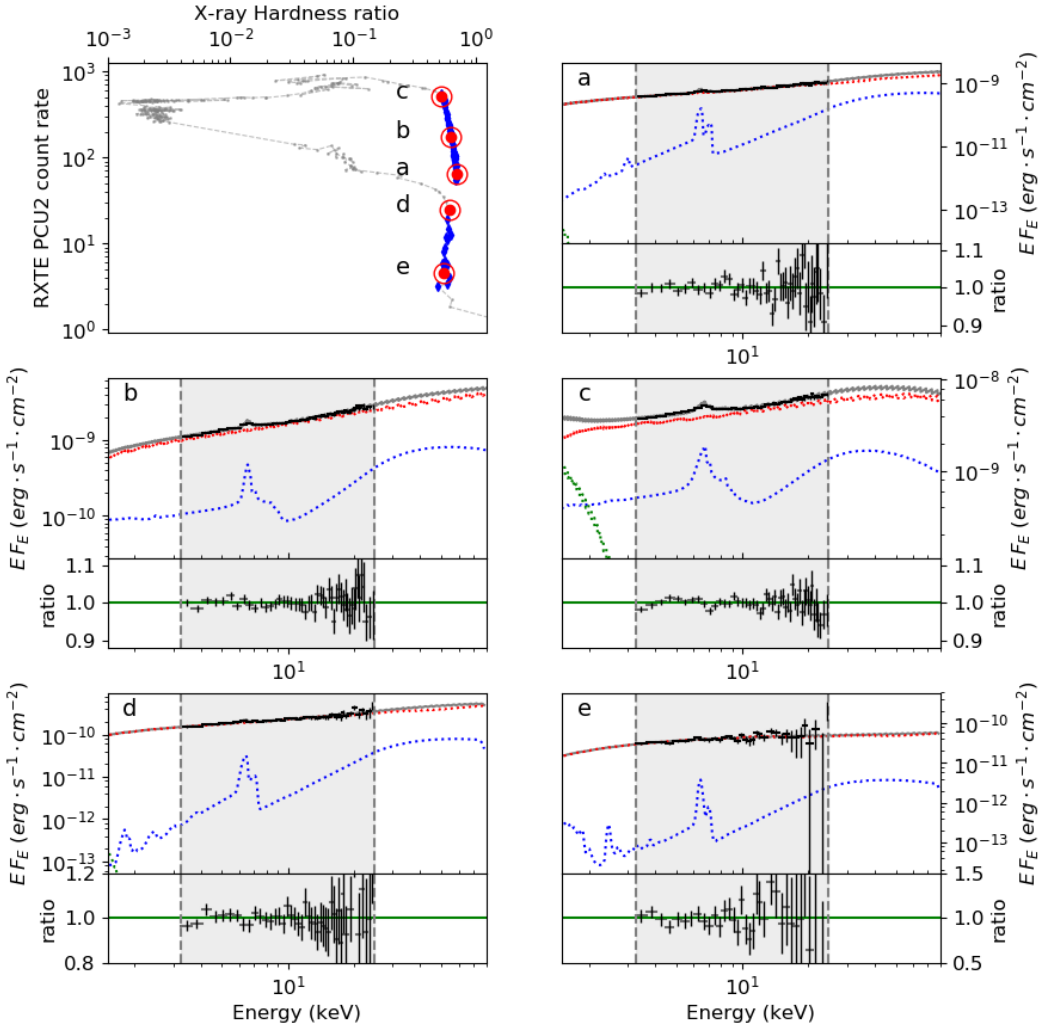

FIGURE 3.3: Best fits of some observations of outburst 4. **Top left**: Hardness intensity diagram of the 2010-2011 outburst. The blue diamond shows the hard state used for this outburst. The five red points are the five observations plotted in the different figures from a to e. **a-e):** Best fit spectra and the data/model ratio for the five observations indicated in red in the HID. The gray region shows the *RXTE*/PCA energy range used for the fit. The data are in black and the best fit model in gray; the JED spectrum is in red, the SAD spectrum in green, and the reflection component in blue. The best fit parameters for each observation are listed in Table 3.2.

During the rising phase (observations *a*, *b*, and *c*), the high-energy cutoff slowly decrease and appear in the figure with the rise in luminosity. Even though the high-energy cutoff is not visible in the fitted energy range (3-25 keV), the JED-SAD continuum predicts a decrease in the high-energy cutoff during the rising phase, similarly to what is observed (Motta et al. 2009; Droulans et al. 2010). At the same time, the iron line changes shape under the influence of both the evolution of the disk ionization parameter and the black hole gravity as the transition radius r_J decreases (general relativity effects). During the decaying phase (observations *d* and *e*), as the luminosity decreases, the standard accretion disk component disappears

TABLE 3.2: Fitting parameters of the five observations presented in Fig. 3.3.

Obs	MJD [a]	χ^2/DoF [b]	r_J [c]	$\dot{m}$ [d]	$\log(\xi)$ [e]	N [f]
a	55214	42/45	$44.0^{+2.5}_{-4.0}$	$0.87^{+0.01}_{-0.03}$	< 2.0	$9.9^{+0.2}_{-9.4} \times 10^{-4}$
b	55260	32/45	$35.7^{+2.8}_{-2.1}$	$1.25^{+0.03}_{-0.01}$	$3.08^{+0.03}_{-0.02}$	$1.3^{+0.1}_{-0.2} \times 10^{-6}$
c	55293	59/45	$14.3^{+0.6}_{-0.6}$	$2.31^{+0.02}_{-0.02}$	$3.22^{+0.10}_{-0.06}$	$1.5^{+0.2}_{-0.2} \times 10^{-6}$
d	55610	22/40	$27.2^{+5.8}_{-4.5}$	$0.37^{+0.04}_{-0.03}$	< 4.5	$< 2.0 \times 10^{-4}$
e	55634	23/31	> 57	$7.4^{+0.5}_{-1.0} \times 10^{-2}$	< 4.6	$< 2.8 \times 10^{-4}$

Notes: [a] MJD of the observations.
[b] χ^2 statistics of the fit and the number of degrees of freedom (DoF).
[c] Transition radius r_J in R_G.
[d] Mass accretion rate $\dot{m}$ in $\dot{M}_{Edd}$.
[e] Disk ionization ξ from the reflection model.
[f] Reflection normalization N, units of the XILLVER reflection model.

r_J increases, putting the optically thick disk further away from the black hole and reducing its maximum temperature.

3.3.3 Evolution of the parameters

Evolution of $\dot{m}$

In Fig. 3.4, I show in blue the light-curve of the mass accretion rate $\dot{m}$ resulting from the fits for the 4 outbursts. The green line and shaded region represent the qualitative results obtained by Marcel et al. (2019, 2020). My fitting results are in quite good agreement with the qualitative result obtained by Greg, they however are much more constrained, presenting very small error bars (see Tab. 3.2).

The overall evolution of the mass accretion rate is quite smooth and similar to what is expected. During the rising phase of the outburst, when the total luminosity of the source increases in the hard state, the mass accretion rate is also increasing. While in the decaying phase, when the luminosity decreases and the source returns to quiescence, the mass accretion rate decreases. Note that the 2007 outburst present a small re-flare during the decaying phase, explaining the bump observed in the mass accretion rate light-curve.

A few remarks can be pointed out. During the rising phase, even though the mass accretion rate reaches above 1, this does not mean that the source is accreting at a super-Eddington regime. Indeed, the definition of the mass accretion rate used in the JED-SAD model is based on the physical mass accretion rate feeding in the accretion flow ($\dot{m} = \dot{M}c^2/L_{Edd}$) and does not take into account any radiative efficiency[2]. Secondly, as observed in the HID, all GX 339-4 outbursts seem to transit from the Hard to Soft state and vice-versa around the same X-ray Eddington ratios[3]. In the JEDSAD framework this translates into transition at the same value of the mass accretion rate. Here, we obtain a transition from the Hard to Soft state at $\dot{m} \sim 3$ and a transition from the Soft to Hard state at $\dot{m} \sim 0.5$. It should however be noted that the 2004-2005 outburst present the particularity of a transition to the soft state at about half the usual mass accretion rate compared to the other outbursts.

[2] A rough estimate predicts: $1/(2r_{isco}) \sim 1/4$.
[3] Except for the 2004-2005 outburst, which transits from the Hard to the Soft states at around half the usual Eddington ratio. This puzzling change in behaviour has yet to be explained.

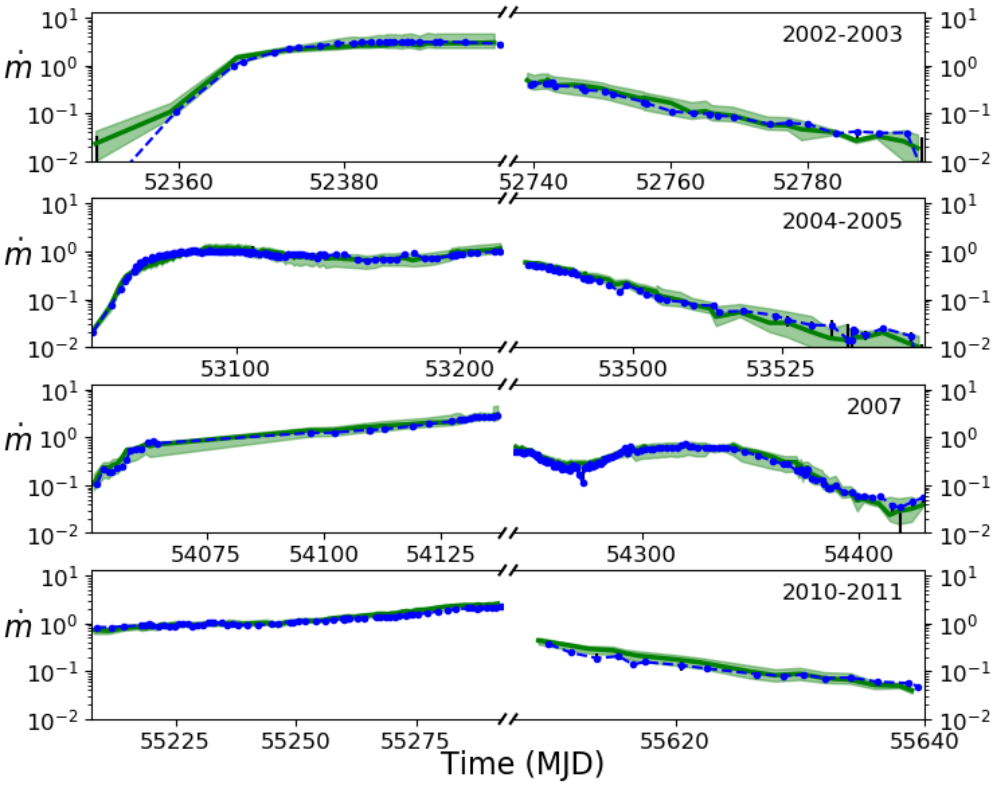

FIGURE 3.4: Evolution of the mass accretion rate $\dot{m}$ (in units of $\dot{M}_{Edd}$) obtained by fitting the hard X-ray spectra of the 4 outbursts of GX 339-4 observed by *RXTE*. The left panel shows the rising phase of the outbursts and the right panel the decaying phase of the outbursts. The green line and shaded region shows the qualitative estimate and its 90% confidence region obtained by Marcel et al. (2019) and Marcel et al. (2020). The blue points shows the result of the fitting procedure. The error bars are shown in black.

Evolution of r_J

In Fig. 3.5, I show in blue the light-curve of the transition radius r_J resulting from my fits for the 4 outbursts. The green line and shaded region represent the qualitative result obtained by Marcel et al. (2019, 2020). Greg's results for some observations show smaller error bars compared to others (reducing the errors from hundreds of R_G to a few tens of R_G). These results were obtained by adding the radio flux as a constraint in his procedure using Eq. 3.3.

Compared to Greg's results, my best fits are naturally much more constrained, especially in the rising phase (left panel) where the luminosity, mass accretion rate and observation statistics are the highest. During the decaying phase, the evolution of the transition radius is much more erratic. Sometimes jumping from a few tens of R_G to a few hundreds (see for instance the 2004-2005 or 2007 decaying phases). This is explained by multiple factors. First the lower signal to noise ratio as the source luminosity decreases. And second, because the spectral constrains on the transition radius r_J become less important at low mass accretion rate ($\dot{m} \leq 0.3$). This can be already seen in the lower panel of Fig. 6 of Marcel et al. (2018b). This figure shows that at low $\dot{m}$ (especially around 3×10^{-2}) the 3-9 keV luminosity can be reproduced

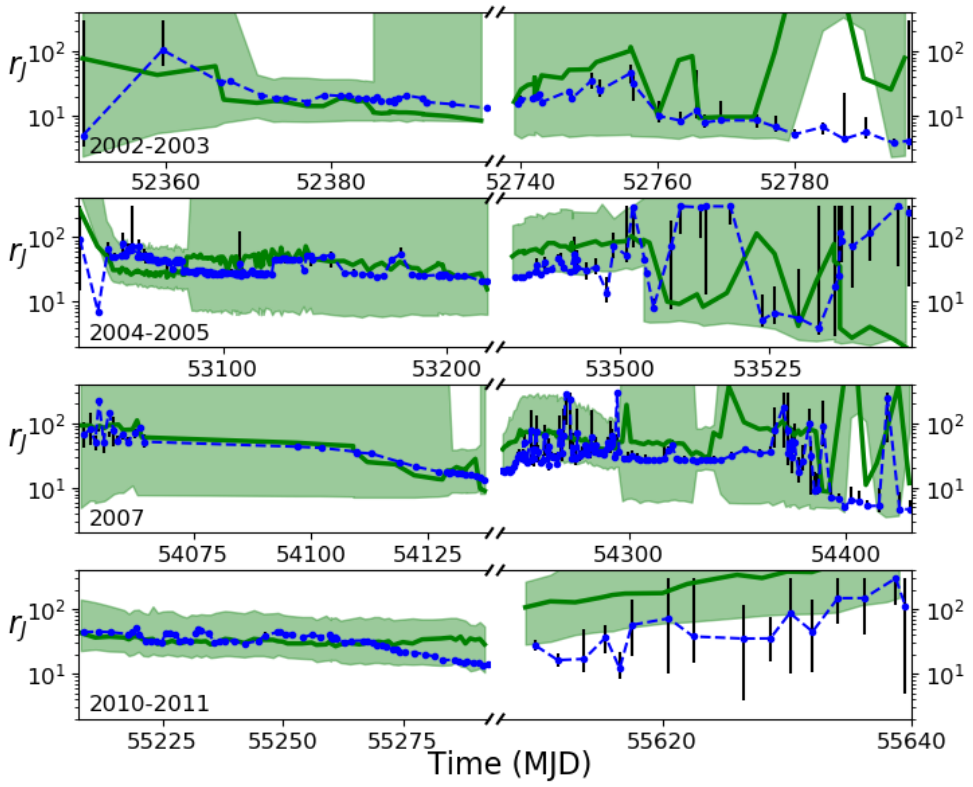

FIGURE 3.5: Evolution of the transition radius r_J (in units of R_G) obtained by fitting the hard X-ray spectra of the 4 outbursts of GX 339-4 observed by *RXTE*. The left panel shows the rising phase of the outbursts and the right panel the decaying phase of the outbursts. The green line and shaded region shows the qualitative estimate and its 90% confidence region obtained by Marcel et al. (2019) and Marcel et al. (2020). The blue points shows the result of my fitting procedure. The error bars are shown in black.

by any values of r_J. Another way to understand this loss of constraints on the transition radius is as follows: when the mass accretion rate decreases, the density and efficiency of the cooling processes decrease too. As such, the JED becomes hotter and the hard X-ray JED emission extends to higher energy. Furthermore, as seen in

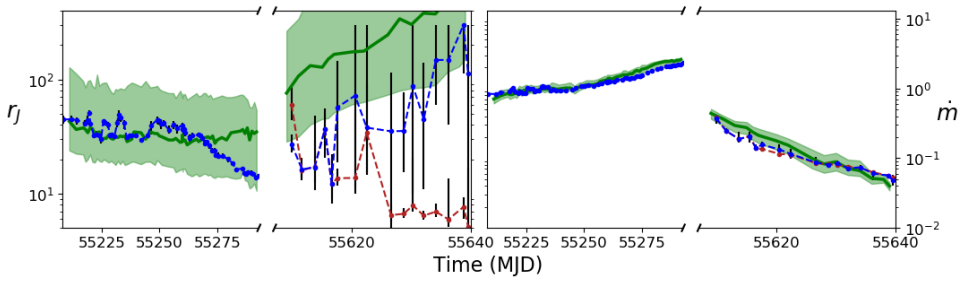

FIGURE 3.6: Light-curve of the main JED-SAD parameters r_J and $\dot{m}$ during the 2010-2011 outburst. The blue dashed line represents the final results presented in Fig. 3.5. The red dashed line represents the initial results obtained by the fitting procedure.

Fig. 2.2, an optically thin JED result mostly in all JED ring having a high temperature. In the 3-25 keV band fitted, the spectrum is mostly a power law, the standard disk being too cold to be observed, the only constrain remaining is the power-law index. Yet as all JED ring have almost the same temperature above a hundred keV, the Compton power-law index of all ring are quite similar and the range of the total power-law index Γ will be limited. As such, we do not have much constrain on the transition radius at low luminosity.

This lack of constraint on r_J at low flux was a bit problematic with my automatic procedure as explained now. Initially, the results from the automatic gave small value of r_J during the decaying phase and were in disagreement with the result from Greg's work and the general JED-SAD framework. These are the red points in Fig. 3.6 where I plot the evolutions of r_J and $\dot{m}$ during the 2010-2011 outburst. Using the Xspec command STEPPAR, the evolution of the χ^2 statistic with r_J is plotted in Fig. 3.7 for a few observations of the decaying phase of the 2010-2011 outburst. These observations show a non-trivial χ^2 space with multiple local minima. Most of them presented either a slightly better fit or a statistically equivalent solution at

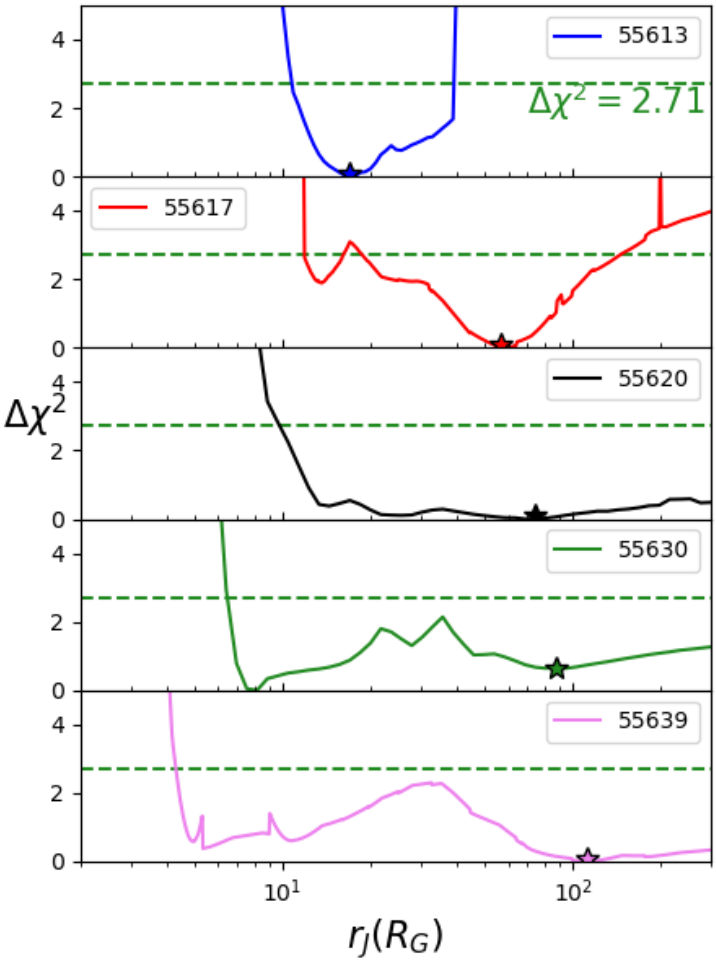

FIGURE 3.7: Evolution of the $\Delta\chi^2 = (\chi^2(r_J) - \chi^2_{min})$ with r_J for a few observations from the decaying phase of outburst 4. From top to bottom in chronological order: MJD 55613, 55617, 55620, 55630, 55639. The 90% confidence threshold $\Delta\chi^2 = 2.71$ is shown as a dashed green horizontal line. We indicate with a star the solutions with higher values of r_J.

higher r_J. For some reason, Xspec did not find these solutions even during the error calculations. I chose to always prefer the higher r_J solutions for all observations for multiple reasons. The χ^2 statistic along the parameter space almost generally shows a better fit for the higher r_J solution. Since we do not expect significant (by few hundreds of R_g) variation of r_J within a few days the slightly better fit obtained at smaller r_J were not realistic. Such large variation would be challenging to explain by any model. The choice of the higher r_J solution allows for a rather smooth increase of the transition radius during the decaying phase, consistent with what is expected in the JED-SAD paradigm.

I did another test in the case of MJD 55630 which shows apparently a better fit at low r_J (see Fig. 3.7). I performed a Markov Chain Monte Carlo (MCMC) with 5000 steps in the case of observation 55630, starting from both a solution with a small value of r_J and another from a high value of r_J. In both cases, the MCMC converged within a few steps (less than 10). In Fig. 3.8, I plot the results of the MCMC procedure as well as the histograms obtained for the first and last thousand steps. When starting with a high value of r_J, the MCMC explores the complete parameter space of r_J, with both low and high value of r_J in both the first and last thousand steps.

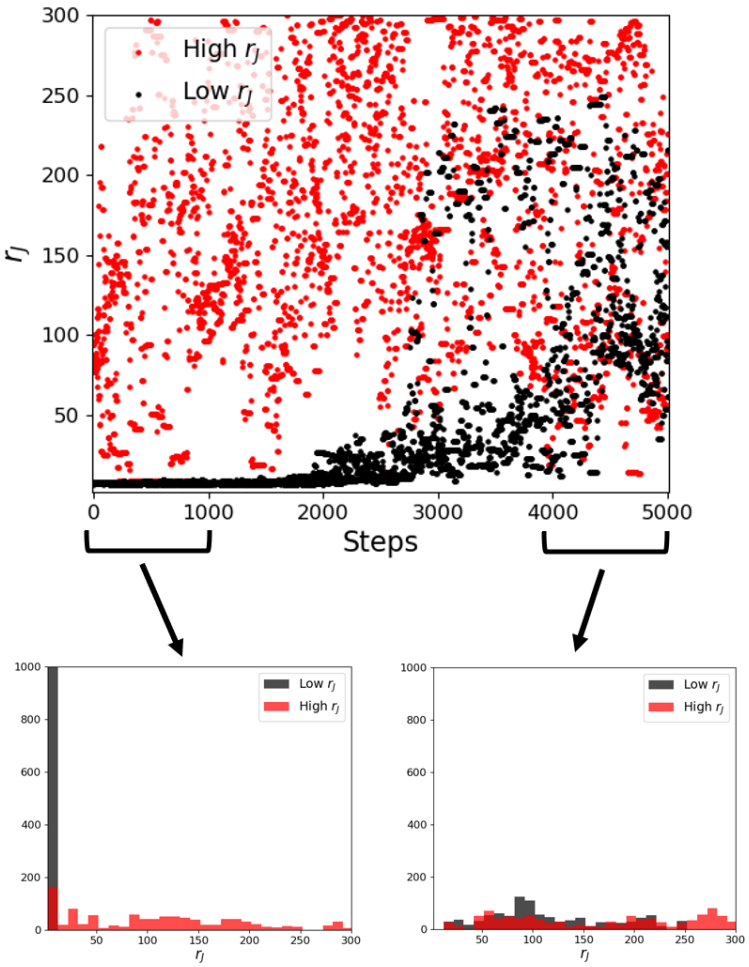

FIGURE 3.8: Results of the MCMC procedure for observation 55630 (see the χ^2 parameter space in Fig. 3.7 in green) starting from two different initial priors. In black starting with a lower r_J prior, in red starting with a higher r_J prior. **Bottom:** Histograms of r_J during the first 1000 steps (left) and the last 1000 steps (right). Both procedures explore only the higher r_J solution.

When starting from the low value of r_J, the procedure is stuck within the low solution. However in the last thousand steps, the MCMC explores both high and low values of r_J. This lead me to think that the results obtained by the automatic procedure was stuck in the low r_J solution and did not explore the possibility of the higher r_J solution, certainly due to the non trivial parameter space. The result of the MCMC shows that the error bars are much larger than what was initially obtained and that the higher r_J solution should be preferred. Notably the histogram of the last thousand steps starting from the low value of r_J show a maximum occurrence around the second minimum, at large r_J, in the χ^2 parameter space of Fig. 3.7 (observation 55630).

The same method was applied only to the the quasi-simultaneous radio and X-ray observations for the decaying phase of the three other outbursts for multiple reasons. First, this method is a rather time consuming approach and the decaying phase of the three other outbursts represent more than a hundred observations (to compare to the 16 decaying phase observations of the 2010-2011 outburst). Second, a clear picture of the transition radius is only required for those quasi-simultaneous observations as we will see in the radio emission study. The radio coverage of the three other outbursts being rather poor compared to the 2010-2011 outbursts, this represent only a hand-full of observations.

Evolution of log(ξ)

The ionisation parameter log(ξ) of the disk is not well constrained for low luminosity observations (see observations a, d and e in Tab. 3.2), mostly due to low signal to noise ratio and the fact that RXTE/*PCA* is not optimal to study spectral lines due to its poor energy resolution. However when the statistics becomes good enough, the ionisation parameter is constrained and show a weak increase during the rising phase (see Fig. 3.9).

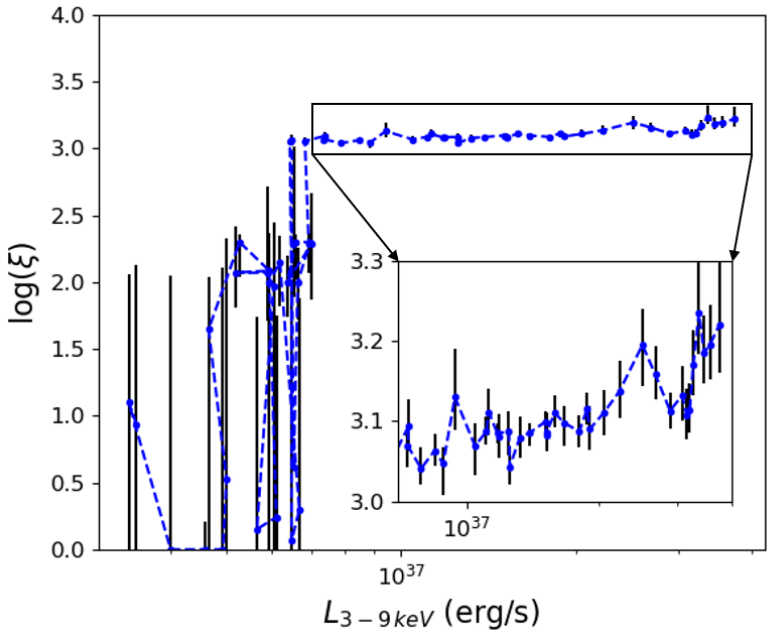

FIGURE 3.9: Light-curve of log(ξ) during the rising phase of the 2010-2011 outburst. The panel show a zoomed-in version of the constrained part of the evolution.

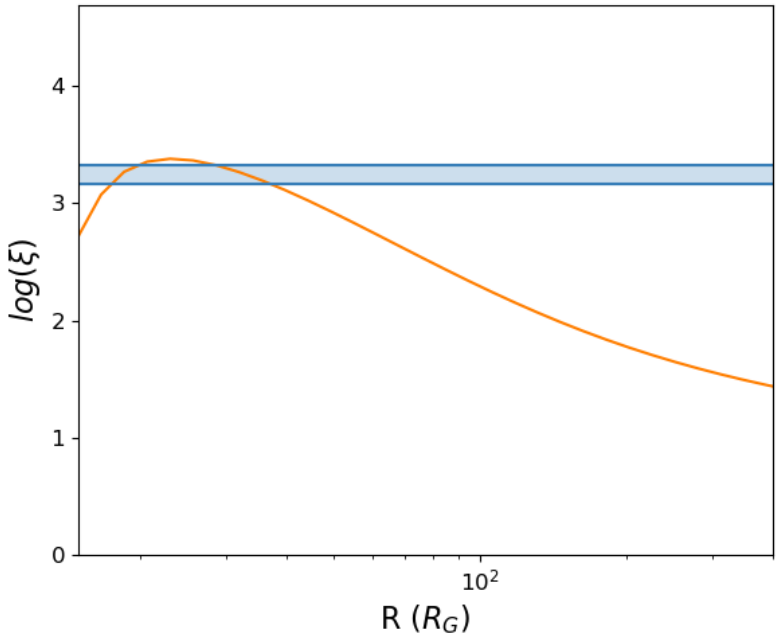

FIGURE 3.10: Radial profile of the disk ionisation parameter inside the standard disk assuming the JED-SAD solution found for observation 55293 (marked c in Tab. 3.2). The x-axis only represent $r \geqslant r_I$. The orange line shows the estimated ionisation at a given radius R and the blue shaded region represent the error region of the ionisation parameter obtained by the fit.

One can ask ourselves if the value of the ionisation parameter we measure is consistent with the physical solution obtained with the JED-SAD. The ionisation parameter is defined as $\xi = 4\pi F_X^{inc}(r)/n(r)$ with $F_X^{inc}(r)$ the X-ray incident flux illuminating the disk at a radius r and $n(r)$ the surface Hydrogen density at radius r. Using the best fit solution of observation 55293 (observation c in Tab. 3.2), one of the brightest hard states observed in GX 339-4, the JED-SAD model can provide the complete physical solution of the disk. I am thus able to estimate the ionisation parameter at the disk surface making a few simplifying assumption. First I assume a gaussian vertical stratification inside the standard disk (Eq. 2.4), the surface density is given by $n(r) = n_0(r) * exp(-1/2) \approx 0.6\, n_0(r)$. And second, I consider the JED emitting region to be a point source placed at the black hole position (r=0). In Fig. 3.10, I plot the resulting radial profile of the ionisation parameter at the standard disk surface. Even with this crude approximation, the estimation of the ionisation parameter in the inner region of the standard disk is found not too far from the value obtained from the fit.

The simplifying assumption should however be discussed, especially the assumption of a point source centered on the black hole, which is rather crude. It forgets that part of the emitting JED is hidden by the black hole, however such effect could be partly counter-balanced by the GR effects bending the photons from the hidden JED. Secondly, the JED is not emitting uniformly, some rings are more luminous than others. If one computes the weighted mean of the surface luminosities (total luminosity divided by the surface of the JED ring) emitted by each JED ring, one find a luminosity center around 3.19 R_G. Meaning that looking at the radial profile of the emission along one side of the disk, one could consider the JED emission to be a point source situated at 3.19 R_G. Combining this information with

the assumption that the light is received from both side of the black hole ($\theta = 0$ and $\theta = \pi$), one can compute the ratio between the fluxes received by each side at a given radius r inside the SAD: $\frac{(r-3.19)^2}{(r+3.19)^2}$. At the inner edge of the SAD $r = r_J$=14.3, this ratio is $\frac{(14.3-3.19)^2}{(14.3+3.19)^2} \approx 0.4$, meaning that the emission coming from the other side of the black hole is approximately half of the emission coming from the front side of the black hole. If one computes the luminosity center between these two diametrically opposed point sources as seen from $r = r_J$=14.3, this center is off-centered radially by $-1.05\ R_G$ from the black hole, toward the illuminated disk (the distance between the illuminated disk and the point source is r-1.05). One can do the same for all diametrically opposed points along the JED ring and find that the furthest luminosity center would be coming from the $\theta = \pm\pi/2$ point sources and is off-centered radially by $+0.35\ R_G$ from the black hole as seen from $r = r_J$=14.3. As such the assumption of a luminosity center for the total emission from the JED being centered on the black hole is not so far off. To get the real value of the ionisation would require the use of Monte Carlo simulation code taking into account GR effects.

Influence of other parameters

The result of the fitting procedure assumed fixed values for some of the other JED-SAD parameters. In this short paragraph, I wanted to present the influence that these other parameters could have on the evolution of the main JED-SAD parameters. I applied my automatic procedure to the 2010-2011 outburst assuming different values of the sonic mach number m_s and different values of the power going into

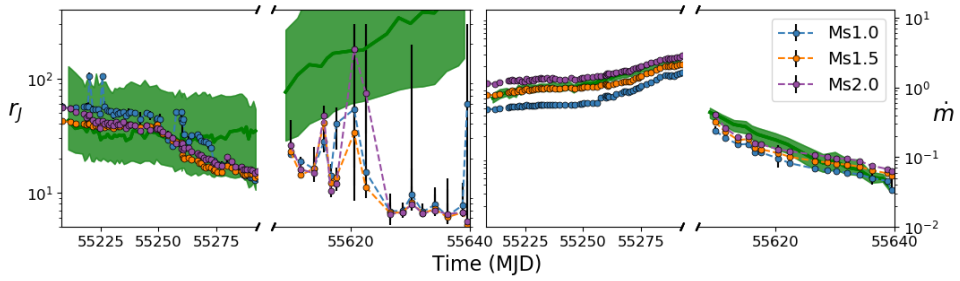

FIGURE 3.11: Influence of the sonic mach number m_s on the main JED-SAD parameters obtained from the automatic fitting procedure for the 2010-2011 outburst. Manual fits for the decaying phase were not performed (see discussion in Sec. 3.3.3 for r_J).

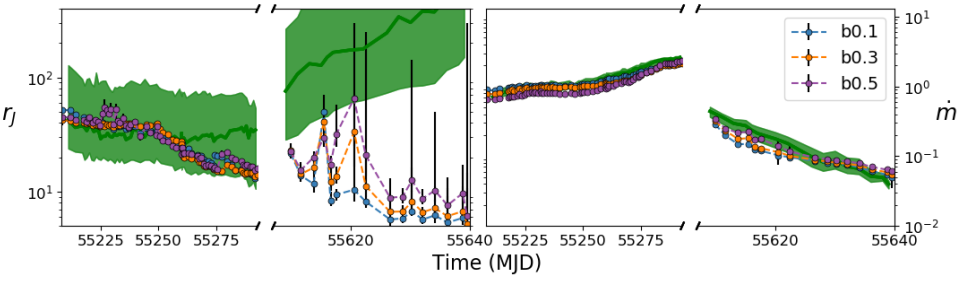

FIGURE 3.12: Influence of the power going in the jets b on the main JED-SAD parameters obtained from the automatic fitting procedure for the 2010-2011 outburst. Manual fits for the decaying phase were not performed (see discussion in Sec. 3.3.3 for r_J).

the jet b. The results are shown in Figs. 3.11 and 3.12. I did not perform manual fits for the decaying phase as discussed in Sec. 3.3.3 for r_J, and in consequence only the small values of r_J are shown. In both cases, the global evolution of r_J and $\dot{m}$ stays the same whatever the value of m_s or b. The main difference is observed in the range of value reached by $\dot{m}$ which depends in the value of the sonic mach number. From the model point of view, this is explained as the faster the accretion is in the JED, the lower the density, and thus the lower the luminosity is. To keep the same luminosity, for a higher sonic mach number, the mass accretion rate $\dot{m}$ must be higher.

3.4 Outbursts dynamic

One can plot the evolution of the JED-SAD parameters during an outburst in an visualisation analogous to the HID. In Fig. 3.13 I plot the evolution of the outburst in the r_J-$\dot{m}$ plane using both the values obtained by Marcel et al. (2020) and my fitting results. This plot shows the evolution of the transition radius as a function of the mass accretion rate and is of particular interest to discuss the general dynamic observed during an XrB outburst. For clarity, I limited the results of Greg to what he called the 'constrained' observations (defined in paper Marcel et al. (2022)) where the use of the radio flux allowed for smaller error bars for r_J. Similarly, I limited the results from my fits to the 2010-2011 outburst, which was the subject of an extensive manual procedure for the decaying phase (see Sec. 3.3.3. As I only fitted the hard states, I do not have any points for the transition and soft states. The results from Greg show that all outbursts seem to follow the same path in this figure, similarly to how they usually follow the same path in the HID. This figure also show the presence of an hysteresis cycle, similar to the HID (see the discussion in Marcel et al. 2020). To get an exact copy of the 'q' shape, one would have to plot $\dot{m}$ as a function of the decreasing r_J.

The result of the rising phase are consistent with the errors of Greg's qualitative approach. More interestingly, the results show the existence of a correlation between the transition radius r_J and the mass accretion rate $\dot{m}$ during the hard states, $r_J \propto \dot{m}^{\delta}$. However, if Greg's results show a power index close to $\delta \sim -2/3$, the results from my fitting procedure suggest two different correlations, one in the rising phase with an index close to $\delta \sim -1.1$ and another one during the decaying phase with an index closer to $\delta \sim -0.5$.

3.4.1 Magnetic flux evolution

The evolution of r_J as a function of $\dot{m}$ during an outburst can actually inform us on how the magnetic flux inside the JED evolves during the hard states. The vertical magnetic flux inside the JED is expressed as:

$$\begin{aligned}\Phi_{JED} &= \int_{r_{isco}}^{r_J} 2\pi\, r\, B_z(r)\, dr \\ &= 2\pi\, r_{isco}^2 \int_1^{r_J/r_{isco}} B_z(x)\, x\, dx\end{aligned}$$

From Eq. 2.30, the magnetic field $B_z(r)$ can be expressed as (with the approximation $p/2 = 10^{-2}/2 \ll 5/4$):

$$B_z(r) = B_z(r_{isco}) \left(\frac{r}{r_{isco}}\right)^{-5/4} \tag{3.4}$$

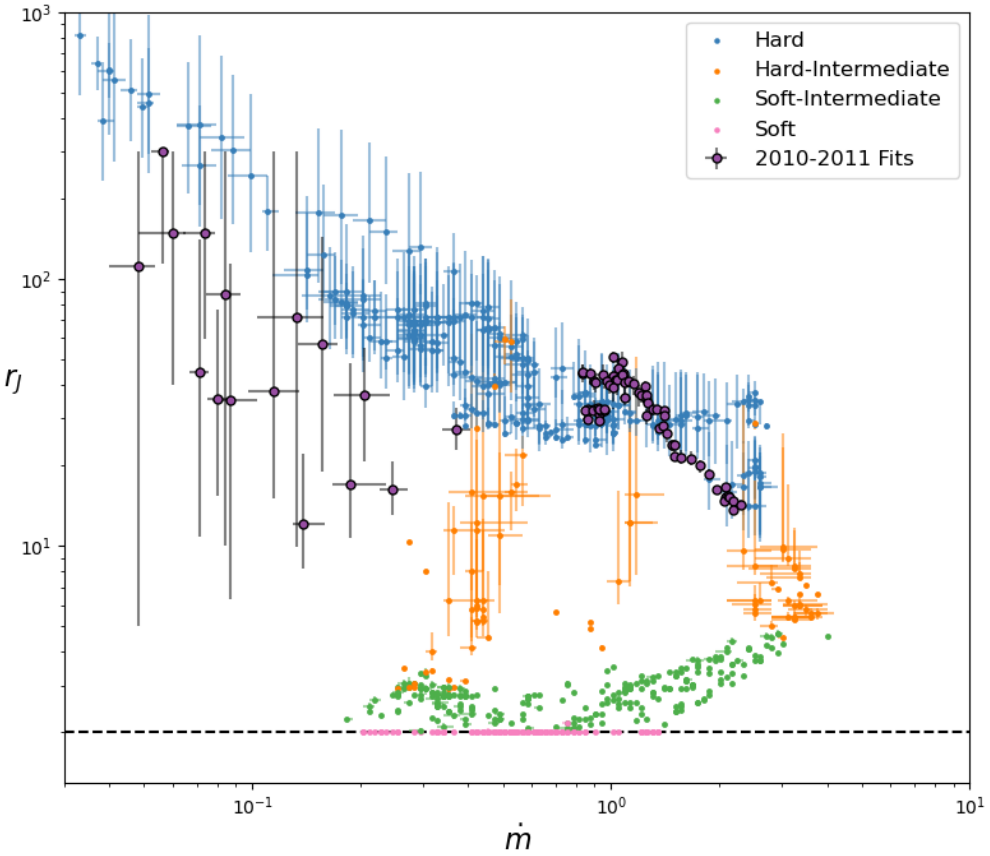

FIGURE 3.13: Evolution of the main JED-SAD parameters r_J and $\dot{m}$ during an outburst. This plot is analogous to the HID, presenting an hysteresis cycle. The blue, orange, green and pink points are the 'constrained' observations, respectively hard, hard intermediate, soft intermediate and soft states, defined in Marcel et al. (2022). The purple points with black errors bars are the results from my fitting procedure for the 2010-2011 outburst.

And thus:

$$\begin{aligned}\Phi_{JED} &= 2\pi\, r_{isco}^2\, B_z(r_{isco}) \int_1^{r_J/r_{isco}} x^{-1/4}\, dx \\ &= \frac{8\pi}{3}\, r_{isco}^2\, B_z(r_{isco}) \left[\left(\frac{r_J}{r_{isco}}\right)^{3/4} - 1\right]\end{aligned}$$

Where $B_z(r_{isco})$ is mainly depending on the mass accretion rate at the ISCO $\dot{m}$ to the power $1/2$ (see Eq. 2.30). As such, the magnetic flux inside JED follows:

$$\Phi_{JED} \propto r_J^{3/4}\, \dot{m}^{1/2} \tag{3.5}$$

Assuming a correlation between r_J and $\dot{m}$, written as $r_J \propto \dot{m}^{\delta}$, there are three possibilities:

- $\delta = -2/3 \Leftrightarrow \Phi_{JED}$ remains constant.
- $\delta < -2/3 \Leftrightarrow \Phi_{JED}$ decreases.
- $\delta > -2/3 \Leftrightarrow \Phi_{JED}$ increases.

The correlation obtained by Greg is consistent with a constant magnetic flux inside the JED during the hard states ($\delta \sim -2/3$). The result I obtained from the fits suggest however a decrease of magnetic flux inside the JED during the rising phase of the outburst ($\delta \sim -1.1 < -2/3$), possibly due to diffusion to the outer region; and an increase of magnetic flux during the decaying phase ($\delta \sim -0.5 > -2/3$), most likely due to the advection of the magnetic field lines as the JED grows. The interpretations of this point will be further discussed later.

3.4.2 Evolution of the JED regime

In the presentation of the model, I showed the existence of three different JED regime, the radiatively efficient and advection dominated (READ) JED, the radiatively efficient and radiatively dominated (RERD) JED and the slim JED. In Fig. 3.14, I plot the evolution of r_J and $\dot{m}$, obtained by Greg to get the full outburst cycle, over the colormap of the advection to radiative power ratio (see Sec. 2.2.2). My result being consistent with Greg's, the next discussion also applies to what I obtained.

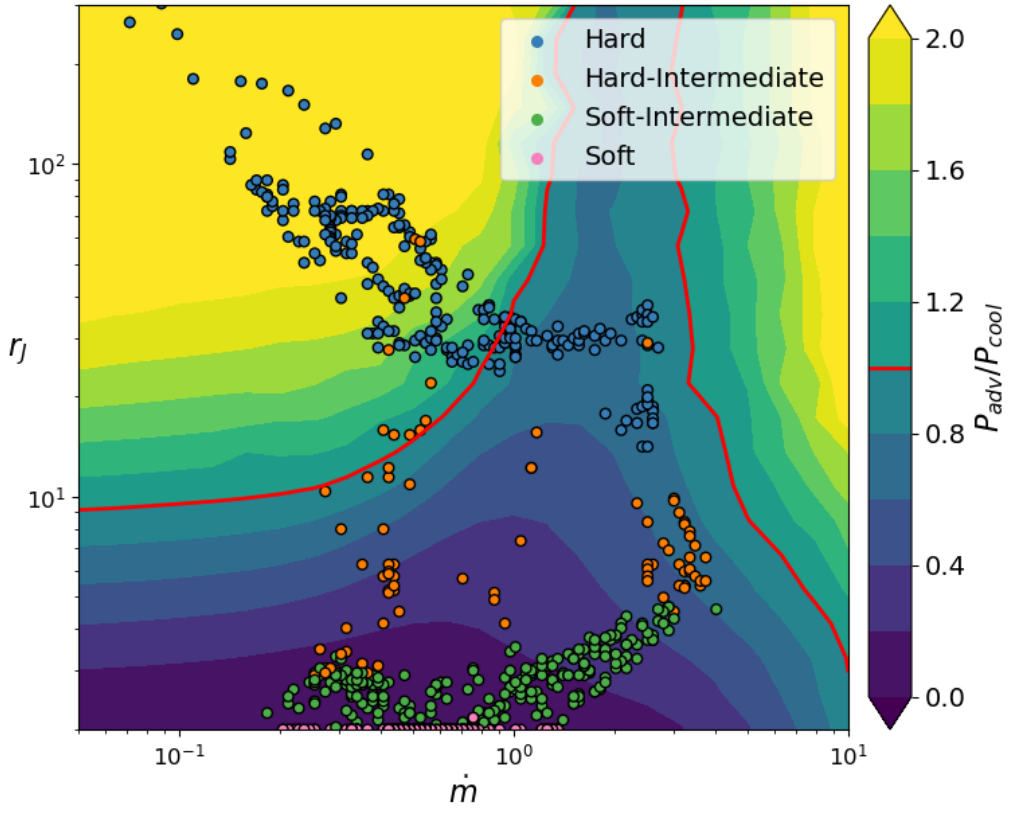

FIGURE 3.14: Evolution of the power budget during an outburst. The blue, orange, green and pink points are the 'constrained' observations, respectively hard, hard intermediate, soft intermediate and soft states, defined in Marcel et al. (2022). The colormap shows the ratio of the advection power and cooling power. The red line marks the equipartition $P_{adv} = P_{cool}$. The parameters used for the colormap are $m = 10$; $r_{isco} = 2$; $\omega = 0.2$; $m_s = 1.5$; $b = 0.3$; $p = 0.01$.

Fig. 3.14 shows the evolution of the power budget inside of the JED during an outburst. During the hard states, at low luminosity and thus low mass accretion rate, the JED is in the READ-JED regime but at higher luminosity, when the mass accretion rate reaches close to 0.5, the JED becomes more radiatively efficient and spend more energy in cooling, the RERD-JED. Interestingly, it is also around this transition from the READ-JED to the RERD-JED that the outbursts come back from the soft states to the hard spectral states. For more details and discussion, one can refer to Marcel et al. (2022).

3.4.3 Evolution of the temperature

Using the evolution of r_J and $\dot{m}$ as constrained by Greg allow to predict the evolution of spectral parameters along an entire outburst. Here I take a look at the prediction for the maximum disk temperature and the high energy cut-off of the hard power-law.

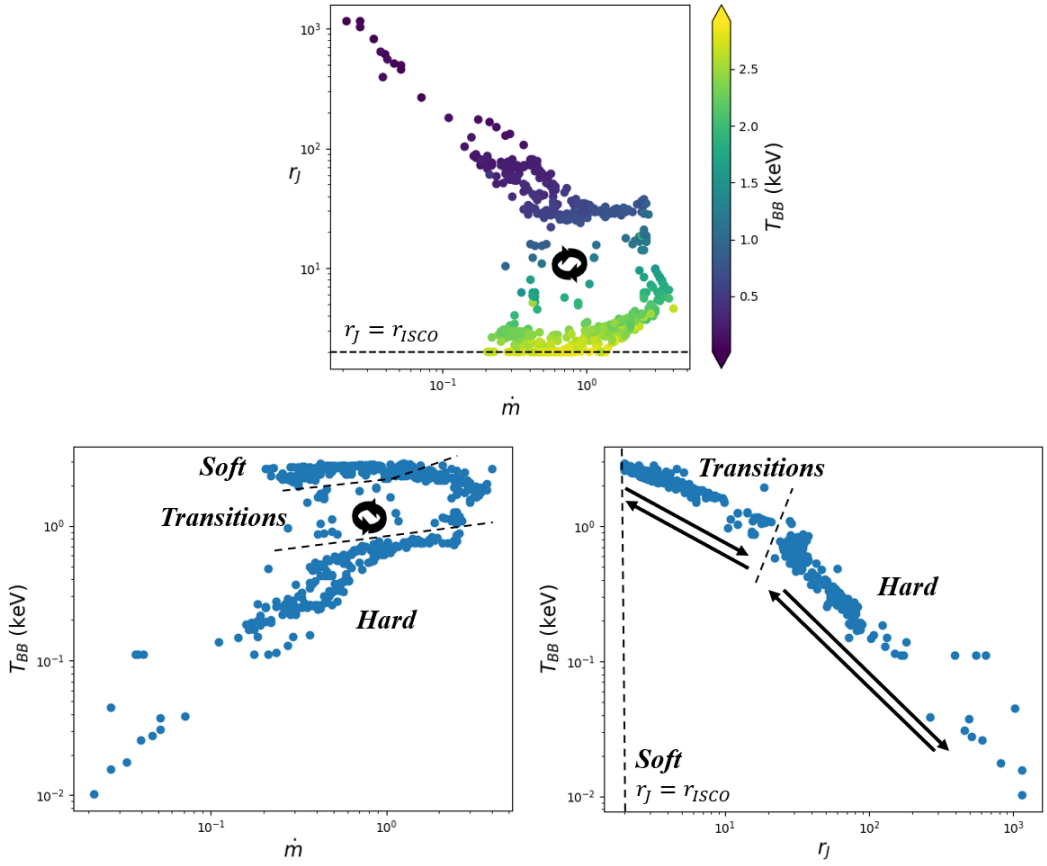

FIGURE 3.15: Evolution of the maximum temperature T_{BB} of the standard disk as predicted by the JED-SAD results from Marcel et al. (2018b, 2020). The top panel show the evolution of the temperature as color in the $(r_J;\dot{m})$ parameter space. The bottom left panel shows the evolution of T_{BB} as function of $\dot{m}$ and the right panel as function of r_J. The arrows show the rotation direction within the hysteresis.

Disk temperature

Observationally, the disk is not always detected during the hard state. Especially in *RXTE*/PCA spectra which start at 3 keV. Yet when fitting the continuum without a reflection component, a disk component is significantly detected around 1.5 keV (See Fig. 2 in Clavel et al. 2016 and also Dunn et al. 2008; Nandi et al. 2012). Even more unexpected is that this disk component show a decreasing temperature when transiting from the hard to the soft states. This was interpreted as a lack of a reflection component in the modelling which add emission at low energy (Clavel et al. 2016). The advantage of the JED-SAD model is that since both parameters r_J and $\dot{m}$ are in an interplay to produce the complete spectral shape (standard disk and hot corona), it can predict the evolution of the disk temperature. In Fig. 3.15, I plot the evolution of the disk temperature during the outburst and versus the evolution pf the main JED-SAD parameters r_J and $\dot{m}$. Here the global evolution of the disk temperature is consistent with the general picture. When the disk gets closer to the black hole (r_J decreasing) during the hard states, the temperature increases and is maximum when we reach the soft state.

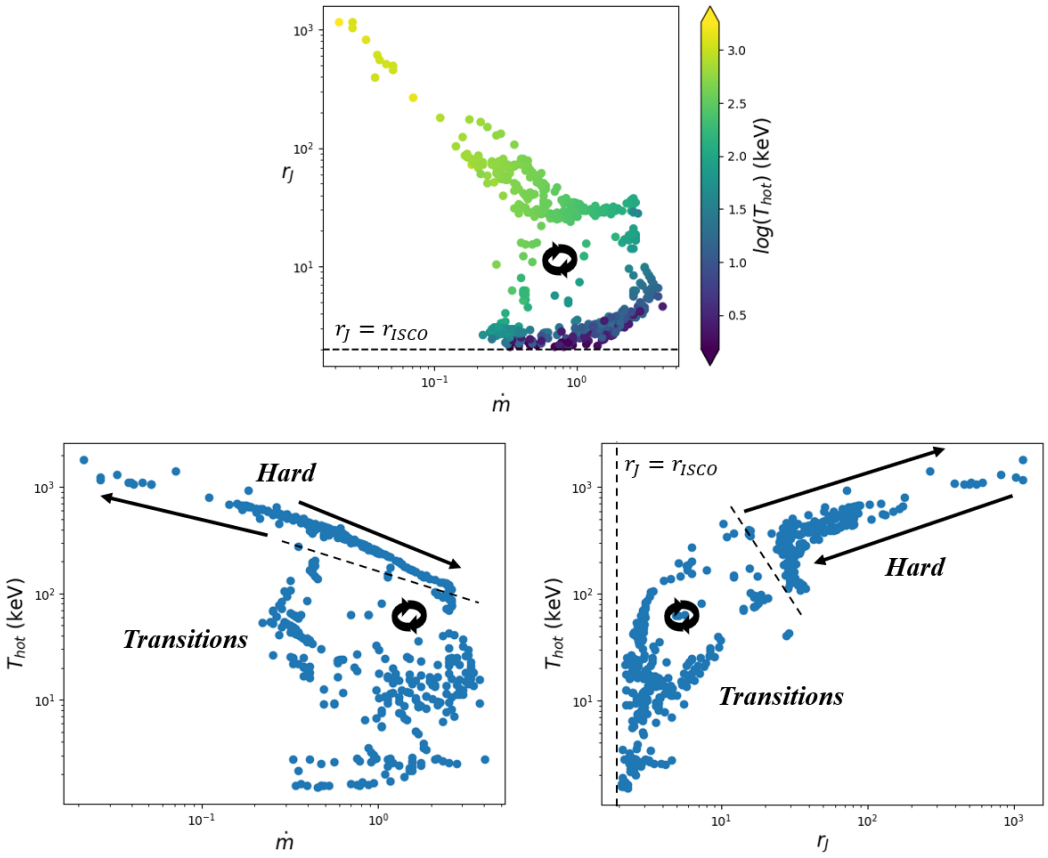

FIGURE 3.16: Evolution of the high energy cutoff T_{hot} of the hot corona as predicted by the JED-SAD results from Marcel et al. (2018b, 2020). The top panel show the evolution of the temperature as color in the (r_J;$\dot{m}$) parameter space. The bottom left panel shows the evolution of T_{hot} as function of $\dot{m}$ and the right panel as function of r_J. The arrows show the rotation direction within the hysteresis.

Corona temperature

Similarly, even though the energy range we look at is limited (3-25 keV) and we do not see the high energy cutoff, the constrains on the JED-SAD parameters allow to predict how the high energy cutoff (corona temperature) T_{hot} evolves along the outburst. In Fig. 3.16, I plot the evolution of this parameter as function of r_J and $\dot{m}$. During the hard state, the corona temperature decrease from 1000 keV for the lowest luminosity observation to about a 100 keV. Then during the transition states, the temperature keep decreasing until the JED emission fully disappear during the soft states. This evolution and the values of T_{hot} can be compared to the results obtained by Motta et al. (2009) (see their Fig. 6) which follows the 2007 outburst. The hot corona temperature decreases from around 130 keV to 60 keV during the hard states, which is generally a bit below what the JED-SAD predicts. Such temperature are only reached at the start of the transition in the JED-SAD simulations.

3.5 Radio emission

As mentioned in Sec. 3.1.2, only the 2010-2011 outburst has enough radio pointings to interpolate a radio flux for each hard X-ray observations (see the coverage in red Fig. 3.2 and the number of observations in Tab. 3.1). As such, the 2010-2011 outburst will operate as a test for the radio study before extending the study to the other outbursts.

3.5.1 Radio and X-ray emission

In this paragraph, I take a closer look at the evolution of the X-ray emission as well as the interpolated radio fluxes during the hard states of the 2010-2011 outbursts. In Fig. 3.17, I plot the radio and 3-9 keV X-ray luminosities as function of the mass accretion rate and transition radius. Interestingly, different correlations can be observed between the rising and decaying phase observations, respectively in blue and in red. In the following, the error I give on the power index are 1-σ errors.

The radio luminosity evolves as $\dot{m}^{1.85\pm0.04}$ during the rising phase and as $\dot{m}^{1.15\pm0.07}$ during the decaying phase. Whereas for r_J, the luminosity evolves as $r_J^{-1.43\pm0.06}$ during the rising phase and $r_J^{-0.47\pm0.11}$ during the decaying phase. Similarly multiple regimes are observed for the X-ray emission. During the rising phase, one can perceive two slopes: below $\dot{m} = 1.4$, the X-ray luminosity evolves as $\dot{m}^{2.48\pm0.15}$. Above $\dot{m} = 1.4$, the X-ray luminosity evolves as $\dot{m}^{1.76\pm0.04}$. During the decaying phase, however, the X-ray luminosity evolves as $\dot{m}^{1.08\pm0.05}$. Looking at r_J, the luminosity evolves as $r_J^{-1.57\pm0.06}$ in the rising phase and $r_J^{-0.5\pm0.12}$. For both the radio and X-ray luminosity, the decaying phase power index lies outside of the 1-σ errors of the rising phase power index.

The difference in the evolution of the X-ray luminosity between the rising phase and decaying phase observations can be explained as the rising phase observations of the 2010-2011 outbursts lie within the more radiatively efficient RERD-JED regime (see Figs. 3.13 and 3.14, see also discussion in Marcel et al. 2020), while the decaying phase observations lie within the READ-JED regime where the radiative cooling is less efficient. This change in radiative regime actually results in a faster increase of the X-ray luminosity with the mass accretion rate during the rising phase compared to the decaying phase. However, the origin of the difference of evolution of the radio luminosity between the rising and decaying phase remains unclear. This result suggest an evolution somewhere. Either in the emission regime inside of the ejection,

possibly related to the evolution of the accretion flow regime from the READ-JED to the RERD-JED. Or in the geometrical properties of the jet itself.

3.5.2 Generalization of Greg's radio function

In Marcel et al. (2018a, 2019), Greg introduced a function to predict the radio emission of the accretion-ejection system based on the JED-SAD parameters (Eq. 3.3). Greg used this function as an additional constrain to reduce the errors he obtained on the transition radius. In my case, the results from the X-ray fits show that r_J is rather well constrained in the hard states, and instead of using the radio emission as an additional constraint, I rather use the X-ray constraints on r_J and $\dot{m}$ to test Eq. 3.3. Using the results of the X-ray fits and assuming $\tilde{f} = 1.5 \times 10^{-10}$, the value used in Marcel et al. (2019), I compute the radio flux F_R using Eq. 3.3. In Fig. 3.18, I plot the ratio of the observed interpolated fluxes F_{Obs}^{interp} compared to the simulated radio fluxes F_R. A clear anticorrelation is observed with r_J, $F_{obs}/F_R \propto r_J^{\alpha}$ with $\alpha \sim -1.25$. Similarly, F_{obs}/F_R is correlated with $\dot{m}$, with a power $\beta \sim 1.56$. As such, the fitting procedure suggests that part of the a functional dependency of the radio emission on r_J and/or $\dot{m}$ is not taken into account correctly in Eq. 3.3.

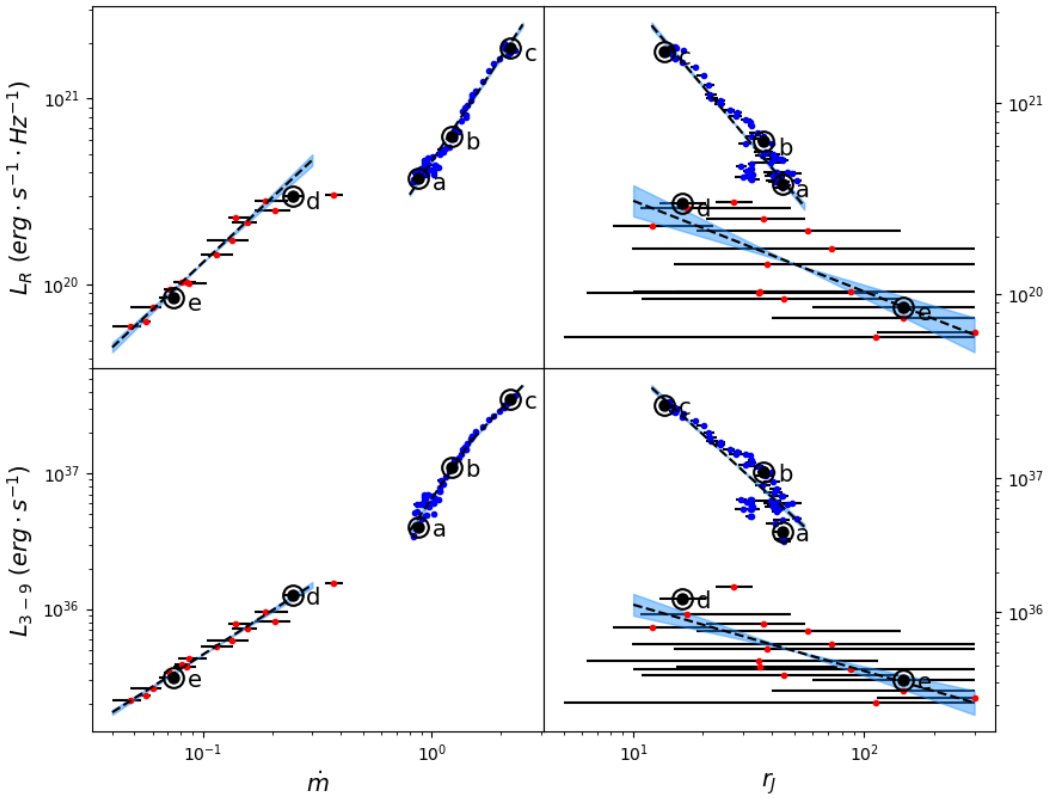

FIGURE 3.17: Evolution of the radio (top) and X-ray (bottom) luminosity as function of the mass accretion rate (left) and transition radius (right) during the 2010-2011 outburst. The blue points represent the rising phase observations and the red points represent the decaying phase observations. The black dashed line represent the fit with a power-law function and the blue shaded region the 1-σ error on the slope. The values of the power-law index are referenced in the text. To mark the chronological order of the outburst, the observations presented in Tab. 3.2 are highlighted.

3.5.3 New radio function

To separate the functional dependency of the radio emission with r_J and $\dot{m}$, I define a new empirical function written as:

$$F_R = \tilde{f}^* \, r_J^{\alpha} \, \dot{m}^{\beta} \left(1 - \frac{r_{isco}}{r_J}\right)^{5/6} \frac{F_{Edd}}{\nu_R} \tag{3.6}$$

where the dependency on the JED-SAD parameter is mainly controlled by the two power indexes α and β. $\tilde{f}^*$ is a free scaling factor. I now look for a unique triplet ($\tilde{f}^*$, α, β) that could reproduce the whole radio data set.

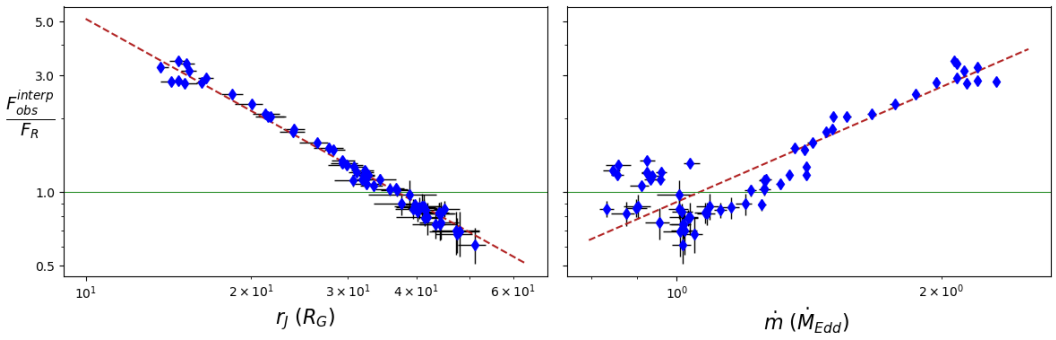

FIGURE 3.18: Ratio between the observed radio fluxes and the simulated radio fluxes obtained from Eq. 3.3 for the rising phase of the 2010-2011 outbursts. Left: as a function of the transition radius. Right: as a function o the mass accretion rate. All points in this figure use interpolated radio fluxes at the date of the X-ray observations. The dashed line shows the best fit power law: $\frac{F_{obs}}{F_R} \propto r_J^{-1.25}$ (left) and $\frac{F_{obs}}{F_R} \propto \dot{m}^{1.56}$ (right).

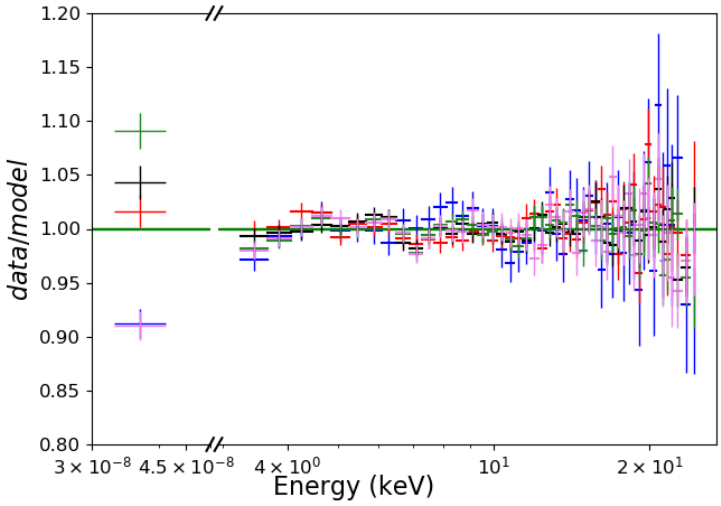

FIGURE 3.19: Ratio of the data to the model for the best fit of 5 of the 16 multiwavelength observations (radio–X-ray) of the rising phase of the 2010-2011 outburst (MJD 55217 in blue, 55259 in red, 55271 in black, 55288 in green, and 55292 in violet). Only five ratios are shown for purposes of visualization, but the best fit was obtained by using all the simultaneous or quasi-simultaneous radio–X-ray observations, while fixing the JED-SAD parameters to the best X-ray fitting values, and then fitting the radio points with Eq. 3.6.

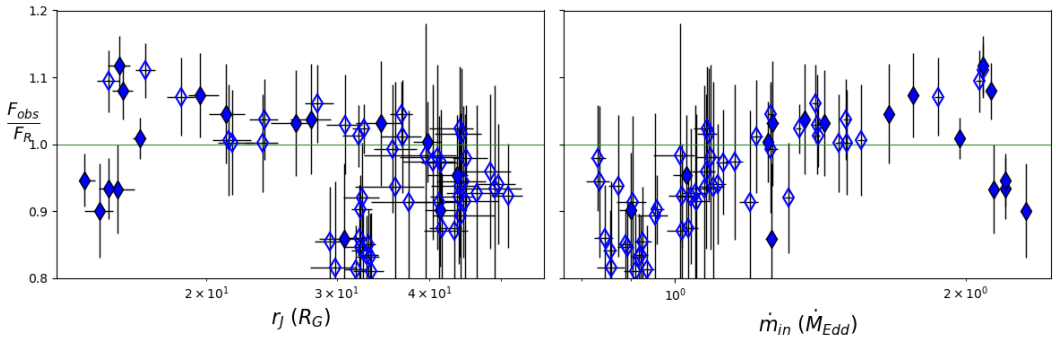

FIGURE 3.20: Ratio of the radio fluxes to the results of Eq. 3.6 for the rising phase of the 2010-2011 outburst, as function of r_J (left) and $\dot{m}$ (right). The filled blue points represent the 16 quasi-simultaneous radio–X-ray observations, while the empty points represent the interpolated radio fluxes. The radio observations are well reproduced using the values $\tilde{f}^* = 7.1 \times 10^{-8}$, $\alpha = -0.66$, and $\beta = 1.00$.

Rising phase of the 2010-2011 outburst

I first test Eq. 3.6 with the rising phase of the 2010-2011 outburst. I fit all 16 quasi-simultaneous radio–X-ray observations in XSPEC. I set the values of r_J and $\dot{m}$ of each observation to the best X-ray fit values (obtained in Sec. 3.3.3).[4] I implement in XSPEC a model to fit the radio emission following Eq. 3.6 and impose the same value of $\tilde{f}^*$, α, and β for all 16 rising phase observations.

The best fit gives $\tilde{f}^* = 7.1^{+15}_{-5} \times 10^{-8}$, $\alpha = -0.66 \pm 0.32$, and $\beta = 1.00^{+0.39}_{-0.38}$. I also report the contours α-β as thin blue solid lines in Fig. 3.22. The fit reproduces all the radio fluxes within an error lower than 10% (see examples of residuals in Fig. 3.19) suggesting that Eq. 3.6 works quite correctly. The positive value of β is consistent with the observed correlation between the radio emission and the luminosity of the binary system. The negative value of α agrees with a decrease in the inner radius of the SAD when the system reaches bright hard states with stronger radio emission as expected in our JED-SAD approach (and similarly to most of the truncated disk models like Esin et al. 1997; Zdziarski et al. 2021).

In a second step I compare the radio flux obtained with Eq. 3.6 to all the interpolated radio fluxes of the rising phase of the 2010-2011 outburst using the best fit values of $\tilde{f}^*$, α and β obtained precedently. I compute the expected radio flux F_R for all 64 X-ray observations of the rising phase. In Fig. 3.20, I plot the corresponding ratios F_{obs}/F_R. There is almost no remaining dependency on either r_J or $\dot{m}$. Compared to Fig. 3.18, this now shows a much more clustered distribution around 1, with a dispersion of about $\pm$15%.

Decaying phase of the 2010-2011 outburst

For the decaying phase of the 2010-2011 outburst I follow the same procedure applied to the rising phase. I use all eight quasi-simultaneous radio–X-ray observations. I set the values of r_J and $\dot{m}$ to the best X-ray fit, then fit the radio fluxes using Eq. 3.6.

[4] When simultaneously fitting X-ray and radio data, if the JED-SAD and reflections parameters are left free to vary simultaneously to $\tilde{f}^*$, α, and β, the X-ray fit is found to be significantly worse, especially around the iron line, for the benefit of a perfect match of the radio fluxes. By freezing the JED-SAD and reflections parameters to their best fit values obtained by fitting the X-rays, I instead choose to favor the X-ray fit for which I have a fully developed physically motivated spectral model.

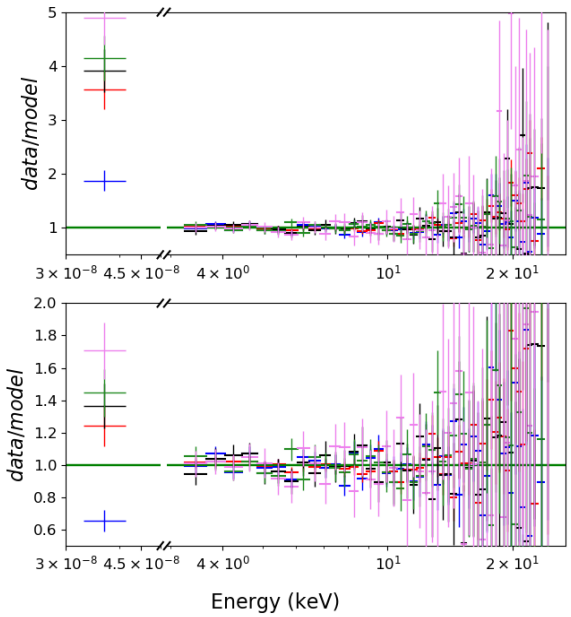

FIGURE 3.21: Ratio of the data to the model for the best fit of five of the eight multi-wavelength observations of the decaying phase of the 2010-2011 outburst (MJD 55613 in blue, 55617 in red, 55620 in black, 55630 in green, and 55639 in violet). **Top panel**: All fits were done simultaneously, fixing the parameters of Eq. 3.6 to those found in the rising phase: $\tilde{f}^* = 7.1 \times 10^{-8}$, $\alpha = -0.66$, and $\beta = 1.00$. **Bottom panel**: Fixing α and β to the values found for the rising phase, $\tilde{f}^*$ is free to vary and converges to the value 2.0×10^{-7}.

As a first test, I use the values of $\tilde{f}^*$, α, and β obtained for the rising phase. The corresponding data/model ratio is plotted in Fig. 3.21. The top panel shows that the disagreement between the observed and computed F_R reach up to a factor 5. The bottom panel shows that even if the scaling factor $\tilde{f}^*$ is free, converging to the value 2.0×10^{-7}, the radio flux is incorrect by a factor up to 1.8. Thus, the parameters $\tilde{f}^*$, α, and β cannot be the same as in the rising phase.

I now leave $\tilde{f}^*$, α, and β free to vary, but linked between all the observations of the decaying phase. The best fit values are $\tilde{f}^* = 2.9^{+1.0}_{-0.9} \times 10^{-8}$, $\alpha = -0.13^{+0.15}_{-0.16}$, and $\beta = 1.02 \pm 0.23$. The corresponding confidence contour α-β is plotted as red thin solid lines in Fig. 3.22. It is clearly inconsistent with the blue contour obtained in the rising phase.

Comparison with the other outbursts

The functional dependency of the radio emission for the other outbursts is constrained by repeating the same analysis. This however requires at least three observations taken in each rising and decaying phases to constrain the three free parameters α, β, and $\tilde{f}^*$. Only the 2004-2005 outburst and the decaying phase of the 2007 outburst have the sufficient number of quasi-simultaneous radio X-ray observations to apply this procedure. The number of radio fluxes used for each phase of the outbursts can be found in Tab. 3.1. The corresponding contour plots of α-β are plotted in Fig. 3.22 as dashed and dot-dashed lines, respectively. Two results are remarkable. First, and similarly to the 2010-2011 outburst, two different functional

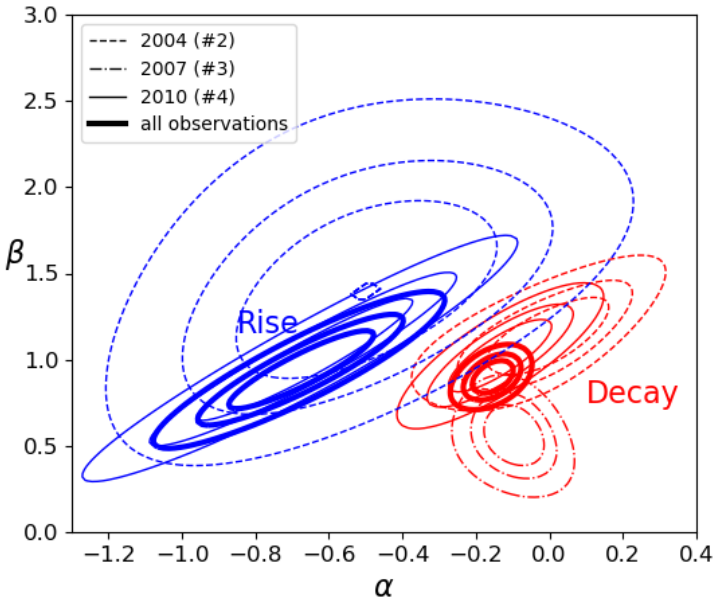

FIGURE 3.22: Contour plots α-β for the rising (blue) and decaying (red) phases of the of 2004-2005 outburst (dashed line), 2007 outburst (dot-dashed line), and 2010-2011 outburst (thin solid line). The contours in thick solid lines represent the dependency when fitting all rising (blue) or decaying (red) phase radio fluxes simultaneously. Confidence contour levels correspond to 68%, 90%, and 99% ($\Delta\chi^2$ of 2.3, 4.61, and 9.2, respectively). The contours are obtained when fitting only the quasi-simultaneous radio–X-ray observations (not the interpolated radio observations).

dependencies are required for the rising and decaying phase of the 2004-2005 outburst. Even more interestingly, the values obtained for α and β are in quite good agreement between the different outbursts and for the different phases (rise vs decay) of the outbursts, the contour of the decaying phase of all three outburst being quite similar. While this could be surprising given the simple expression used to model the radio emission, I believe that this result reveals intrinsic differences in the jet emission origin.

In the last step I use all the quasi-simultaneous radio observations, simultaneously fitting all the rising phase observations together with the same parameters α and β for all outbursts, but with different normalization $\tilde{f}^*$ for each outburst. I did the same for all the decaying phase observations. The resulting α-β contours are plotted in Fig. 3.22 as thick solid lines.

The process confirms the two different and mutually inconsistent functional dependencies of the radio emission with r_J and $\dot{m}$ between the rising and decaying phases. The radio flux observed in the rising phases is nicely reproduced (within about 15%) by the relation

$$F_R^{rise} \propto r_J^{-0.67^{+0.21}_{-0.22}} \dot{m}^{0.94^{+0.25}_{-0.24}} \tag{3.7}$$

While, in decaying phases the radio emission rather follows:

$$F_R^{decay} \propto r_J^{-0.15\pm0.06} \dot{m}^{0.9\pm0.1} \tag{3.8}$$

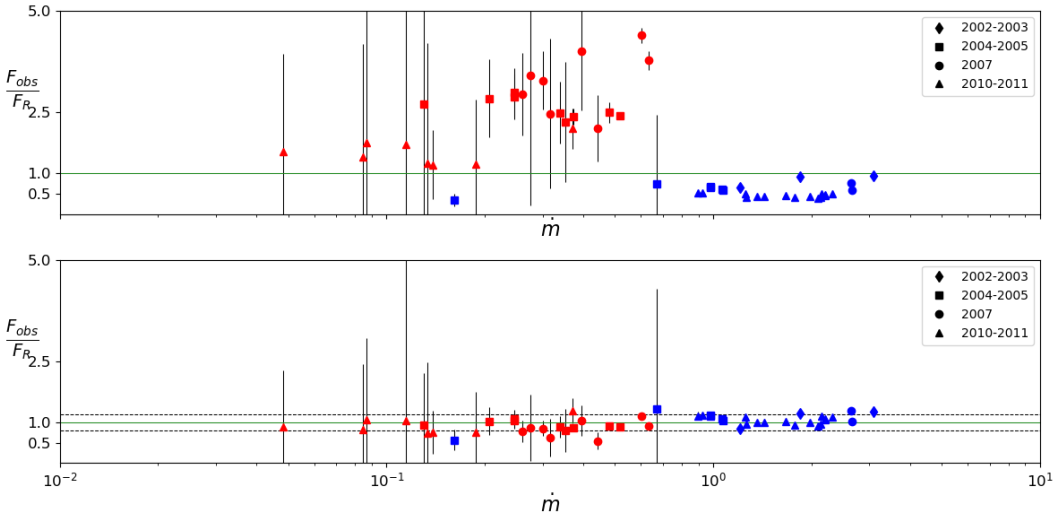

FIGURE 3.23: Ratios of the observed radio fluxes to the modeled radio fluxes for all the quasi-simultaneous radio–X-ray observations of the four outbursts. Each outburst is represented using a different symbol (see legend). In blue are shown the rising phases and in red the decaying phases. The modeled radio fluxes were obtained using Eq. 3.6. The parameters are ($\alpha = -0.67$, $\beta = 0.94$) for the rising phases and ($\alpha = -0.15$, $\beta = 0.9$) for the decaying phases. **Top panel**: $\tilde{f}^* = 4.1 \times 10^{-8}$ used for all outbursts. **Bottom panel**: Different $\tilde{f}^*$ used for each phase of the outbursts. All values of $\tilde{f}^*$ used are reported in Table 3.3. The horizontal dashed lines represent a 20% error margin.

with a weaker dependency on r_J.

Some variations of $\tilde{f}^*$ between the outbursts are however required to significantly improve the radio emission modeling. This can be seen in Fig. 3.23 where I plot the ratio F_{obs}/F_R using Eq. 3.7 to compute the radio flux if the observation is in the rising phase and Eq. 3.8 if in the decaying phase. In the top panel I use the same value $\tilde{f}^*$ for all outbursts. The ratios cluster around 1, although there is some scattering between the different phases of the different outbursts. I report in the bottom panel of Fig. 3.23 the same ratio but letting $\tilde{f}^*$ free to vary between outbursts and between the rising and decaying phases. The improvement is clear and almost all radio fluxes can be reproduced within a 20 % margin error. The different values of $\tilde{f}^*$ found are reported in Table 3.3. Variation up to a factor of three (e.g., between the rising phase of the 2002-2003 and 2010-2011 outbursts) are observed. This could be related to local changes in the radiative efficiency of the radio emission from outburst to outburst.

TABLE 3.3: Values of $\tilde{f}^*$ found for each phase of the outbursts. Obtained when fitting all the quasi-simultaneous observations simultaneously.

Outburst	Rise	Decay
2002-2003	$4.1^{+5.4}_{-2.3} \times 10^{-8}$	-
2004-2005	$5.5^{+6.6}_{-2.9} \times 10^{-8}$	$1.4^{+0.3}_{-0.3} \times 10^{-8}$
2007	$5.3^{+6.6}_{-2.9} \times 10^{-8}$	$1.0^{+0.3}_{-0.2} \times 10^{-8}$
2010-2011	$7.2^{+9.2}_{-3.7} \times 10^{-8}$	$2.3^{+0.7}_{-0.5} \times 10^{-8}$

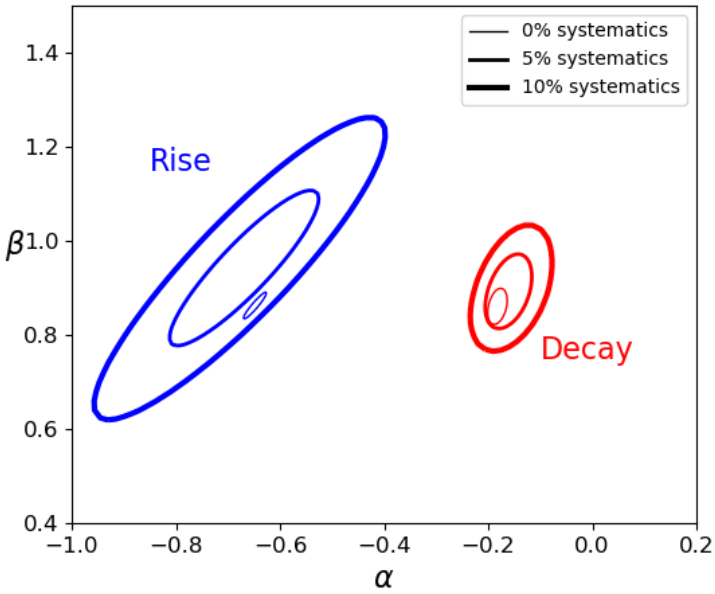

FIGURE 3.24: 90% Confidence contours α-β for different values of systematic error added to the radio fluxes (0%, 5%, and 10%). The thicker the line, the larger the systematic error added. Shown are the contours for all the rising phase observations (in blue) and the contours for all the decaying phase observations (in red).

Influence of the systematics

As mentioned in Sec. 3.1.2, I added 10% systematic errors to the radio fluxes, mainly to take into account the the non-exact simultaneity between the X-ray and radio observations.

However this has a major impact on the size of the confidence contour α-β. These contours depend directly on the χ^2 plane of the parameter space. In Fig. 3.24 I plot the confidence contour for a 90% confidence level ($\Delta\chi^2 = 4.61$) for all the rising phase observations (in blue) and for all the decaying phase observations (in red), and for different values of systematic errors added to the radio fluxes (0%, 5%, and 10% depending on the thickness of the line). As expected, the larger the systematic error added, the larger the contour plot, but even with a 10% systematic error the rising phase solution and decaying phase solution are inconsistent.

Influence of other parameters

As seen before, parameters like the sonic mach number m_s and the power going into the jets b, have a direct impact on the values of the main parameters r_J and $\dot{m}$ in the fitting procedure. This raises an important question: does the result I obtained for the radio persist when using other values of m_s and b ?

Figs. 3.11 and 3.12 show that the largest deviation of r_J and $\dot{m}$ are observed when using other values of m_s. I will thus focus on this parameter. I follow all the steps presented before for the 2010-2011 outburst, but this time assuming values of $m_s = 1$ and $m_s = 2$, and plot the corresponding contours α-β in Fig. 3.25. What is interesting is that for all values of m_s, the rising phase and decaying phase show different functional dependencies, confirming that the result remains robust even with different JED-SAD parameters.

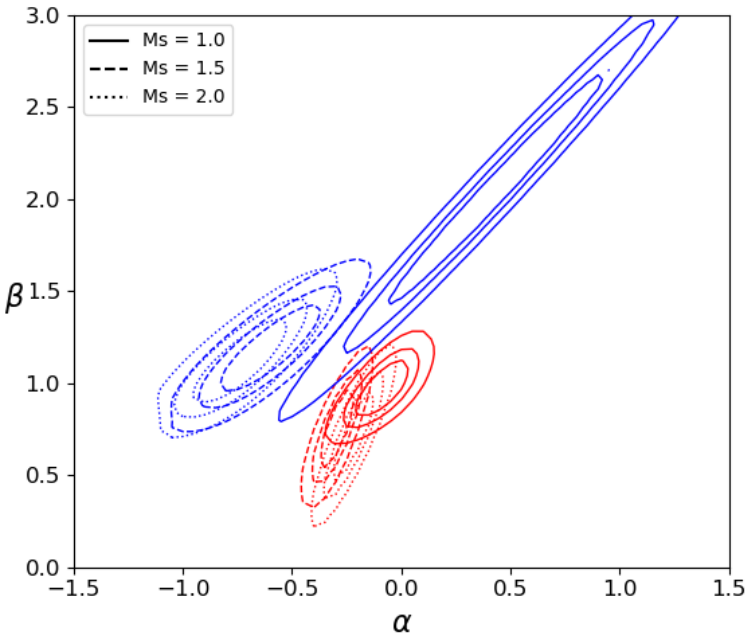

FIGURE 3.25: Confidence contours α-β for different values of m_s used in the fitting procedure of the 2010-2011 outburst: $m_s = 1.0$ (solid line), $m_s = 1.5$ (dashed line), and $m_s = 2.0$ (dotted line). In all cases the rising phase contour and decaying phase contour are inconsistent.

3.6 Discussion and interpretation

3.6.1 Indications of different radiative behaviors between the rising and decaying phases

Observational clues on the jet behavior can be derived from a set of different diagnostics: (i) the radio spectral index α_R, (ii) the measure of the spectral break frequency ν_{break}, (iii) timing properties, (iv) the correlation $L_R - L_X$, and (v) linking the radio luminosity L_R to disk properties $(\dot{m}, r_J)$. Items (i)-(iv) are discussed in this section, while item (v) is discussed in Sec.. 3.6.2.

The radio spectral index α_R can be analytically derived under the assumption of a self-absorbed synchrotron emission smoothly distributed along the jet. It depends on the particle distribution function, the jet geometry, and the way the dominant magnetic field varies with the distance (see Eq A.8 in the Appendix of Marcel et al. 2018b). There is no a priori reason to assume that these parameters should not vary with time. Observationally, however, there is no clear evidence of differences in the radio spectral index α_R between the rising and decaying phases of GX 339-4[5]. Although this is already an important piece of information, we note that these α_R are most of the time derived within a rather limited radio band and might therefore not be fully representative of the whole jet spectrum (see, e.g., Péault et al. 2019).

The evolution of the spectral break frequency, ν_{break}, marking the transition from self-absorbed to optically thin jet synchrotron radiation, could however be different in the two phases (rising and decaying). The radio spectral index being flat or

[5]private communication with Mathilde Espinasse; see also Espinasse & Fender (2018); Koljonen & Russell (2019) for more detailed discussion on this point and Tremou et al. (2020) for the quiescent state case where the radio spectrum is clearly inverted.

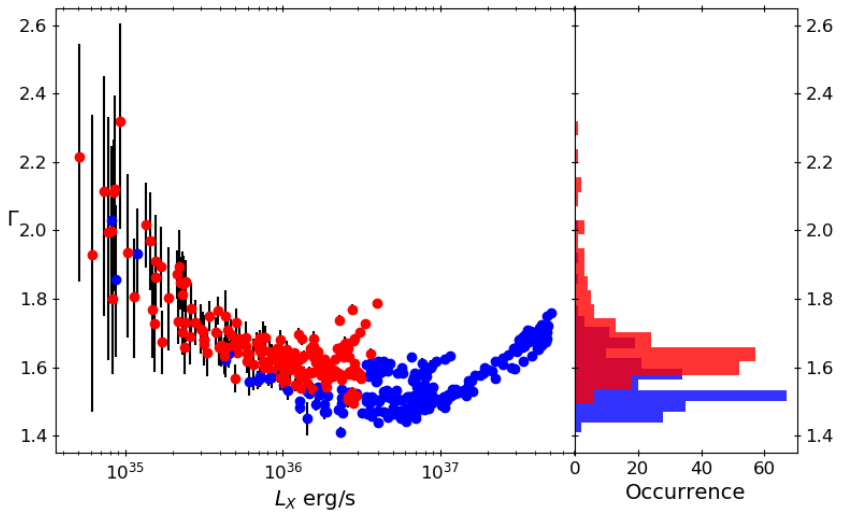

FIGURE 3.26: Evolution of the hard X-ray power law index Γ during the four outbursts of GX 339-4 (measured by Clavel et al. 2016). **Left:** Hard X-ray power law index Γ as a function of the 3-9 keV X-ray luminosity of the pure hard state observations during the four GX 339-4 outbursts (data from Clavel et al. 2016). In blue the rising phase and in red the decaying phase. **Right:** Histograms of Γ. These distributions are subject to a certain number of observational biases: inclusion of error bars and the number of observations per phase.

inverted in the hard state, the radiative power of the jets is mainly sensitive to the position of the spectral break. Gandhi et al. (2011) measured this break at $\sim 5 \times 10^{13}$ Hz in a bright hard state during the rise of the 2010-2011 outburst. By comparison, Corbel et al. (2013) constrain the break to be at lower frequency in the decaying phase, suggesting a less powerful jet in this phase. There is also a potential link between the X-ray hardness and the jet spectral break frequency, harder X-ray spectra having a higher ν_{break} (see Fig. 2 of Koljonen et al. 2015 as well as Russell et al. 2014). Interestingly, GX 339-4 shows on average a softer X-ray power law index in the decaying phase compared to the rising phase (see Fig. 3.26). Given the observed correlation between ν_{break} and the X-ray hardness, this also suggests a different behavior for ν_{break} (and consequently of the radiative jet power[6]) between the two phases.

There are other indications that the accretion (through X-ray emission) and ejection (through radio emission) processes could behave differently at the beginning and the end of the outburst. At first sight the radio–X-ray correlation followed by GX 339-4 agrees with a linear correlation of index ~ 0.7 in log-log space (e.g., Corbel et al. 2000, 2003, 2013) even down to very quiescent states (Tremou et al. 2020), but a more careful analysis shows the presence of wiggles along this linear correlation, especially between the high- and low-luminosity states (see Fig. 3.1 bottom panel from Corbel et al. 2013). When looking more precisely at the rising and decaying phase, two different correlations may even be observed (Islam & Zdziarski 2018).

[6]It should be noted that most of the jet power is not spend in radiation but in kinetic energy.

READ-JED vs RERD-JED

The difference between the rising and decaying phases may be linked to a change in the radiative efficiency of the X-ray corona with luminosity. The low X-ray luminosity states, below 2-20% of the Eddington luminosity, are less radiatively-efficient than the high X-ray luminosity states (see Fig. 3.14 as well as Koljonen & Russell 2019; Marcel et al. 2022). As noticed by Koljonen & Russell (2019), changes of the accretion flow properties could affect the jet launching, and therefore its radio emission properties.

In the JED-SAD model, the accretion power available in the accretion flow, $P_{acc} = \frac{GM\dot{M}}{2R_{isco}}\left[1-\left(\frac{r_{isco}}{r_J}\right)^{1-p}\right]$, is released in three different forms: advection, radiation, and ejection. The first two occur inside the JED, and their sum is defined as $P_{JED} = (1-b)\,P_{acc}$. The ejection power is released in the jets and is defined as $P_{jets} = b\,P_{acc}$. One can define the ratio $\eta_R = L_R/P_{jets}$ and the ratio $\eta_X = L_{3-9\,keV}/P_{JED}$ and interpret them respectively as the radiative efficiency in the radio and X-ray bands respectively. In Fig. 3.27 I plot the ratio η_R[7] as a function of the ratio η_X for the rising phase (blue points) and the decaying phase (red points) of the outbursts. I highlight in Fig. 3.27 the observations (labeled a to e) presented in Tab. 3.2 to mark the chronological evolution along an outburst. Figure 3.27 mostly depends on the well-constrained mass accretion rate obtained with our fits of each X-ray observations.

The blue points of the rising phases follow a similar trend for all the outbursts with an increase in the X-ray and radio radiative efficiency by a factor of $\sim$4 and $\sim$2, respectively. In the decaying phase, the radio radiative efficiency changes from outburst to outburst and does not seem to evolve much, while the X-ray radiative efficiency stays roughly constant at $\eta_X \sim 3-4\times10^{-2}$, the lowest values observed in the rising phase. These results suggest a change in the radiative properties of the accretion-ejection structure between the beginning and the end of the outburst (see also Marcel et al. 2022). These changes could be related to the transition from the RERD-JED regime observed during the high luminosity rising phases and the READ-JED regime observed during the low luminosity decaying phases (see Sec. 3.4). It is possible that it has some impact on the functional dependency of the radio emission highlighted in this paper.

However, contrary to the conclusion of Koljonen & Russell (2019), the accretion rate does not seem to be the only parameter that controls the evolution of η_R. Looking at the 2002-2003 and 2010-2011 outbursts separately, η_R stays roughly constant in the decaying phase of each outburst, whereas $\dot{m}$ varies by at least a factor of 10 (see Fig. 3.4). Furthermore, different radio efficiencies are observed between each outburst during the decaying phases even when they have similar values of $\dot{m}$. Something else seems to be at work.

3.6.2 Changes in the dynamical ejection properties

The existence of two functional dependencies $F_R(\dot{m}, r_J)$ for the rising and decaying phases of the outburst of GX 339-4 raises a profound question. Radiative processes in jets are local and should be independent of disk parameters such as $\dot{m}$ and r_J. However, the time evolution $F_R(t)$ can be quite accurately reproduced with a function of

[7] In the case of the 2010-2011 outburst, the full triangles are quasi-simultaneous radio X-ray observations, whereas the empty triangles use the interpolated radio luminosity L_R computed for all the X-ray observations.

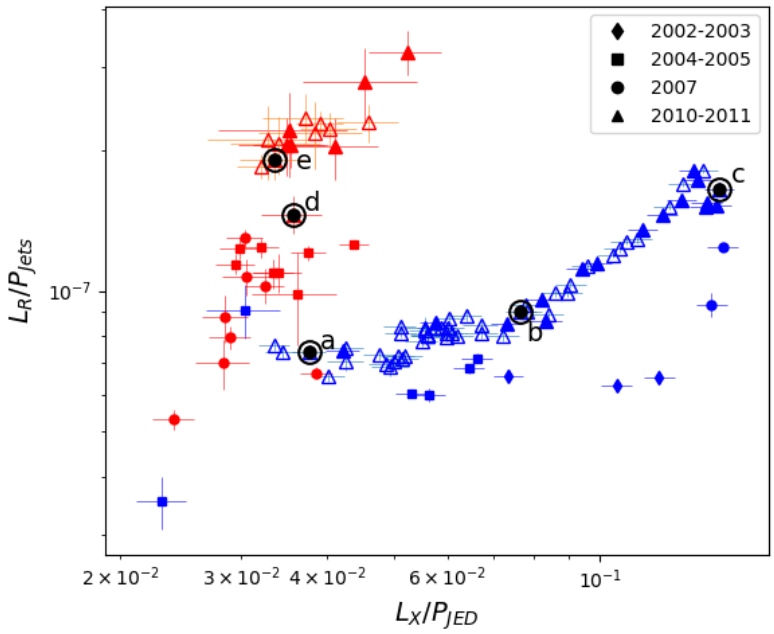

FIGURE 3.27: Radio emission efficiency ($\eta_R = L_{9GHz}/P_{Jets}$) vs. X-ray emission efficiency ($\eta_X = L_{3-9keV}/P_{JED}$) during the outbursts of GX 339-4. The blue points are the rising phases. The red points are the decaying phases. The symbols distinguish the different outbursts: diamonds for 2002-2003, squares for 2004-2005, dots for 2007, and triangles for 2010-2011 (filled for the quasi-simultaneous observations and empty for the interpolated radio fluxes). Five observations (labeled *a* to *e*) presented in Tab. 3.2 are highlighted to provide the chronological evolution along an outburst.

$(\dot{m}, r_J)$, which shows that global jet parameters do actually depend on them. These parameters, which constitute the jet dynamics, are for instance the magnetic field strength and geometry, the jet collimation degree, the existence of internal shocks or even jet instabilities. Our findings seem therefore to highlight two different jet dynamics.

A possible threshold in $\dot{m}$

The detected difference in the functional dependency of F_R could be due to some threshold in $\dot{m}$ that could, in turn, translate into some difference in the way the radio emission scales with the disk parameters. Above the threshold the radio emission would follow Eq. (3.7), and below the threshold Eq. (3.8). This threshold could be related to the transition from READ-JED at low luminosity to RERD-JED at higher luminosity. Indeed, the high luminosity RERD-JED is characterised by a slimmer accretion flow with an aspect ratio $\epsilon \sim 0.1$. Whereas the low luminosity READ-JED is characterised by a puffier flow with $\epsilon \sim 0.3$. This change in vertical height of the accretion flow could impact the way the jet is launched and change its global properties.

Unfortunately, the monitoring of the GX 339-4 outburst observed by *RXTE* (and of most XrB) start a bit too late to test this hypothesis. Most of the time, they are caught only after they rise to a few percent Eddington, when the transition from READ-JED toward the RERD-JED is already happening. The insufficient radio pointings (2 points out of 28) during the early start of the rising phase does not

allow to discriminate whether the different radio formula are related to the phase of the outburst (rising versus decaying phase) or to the JED power regime.

I, however, do not favor this interpretation. The main reason is that the rising and decaying hard states are temporally disconnected. The source stays in the soft state between these two hard-state phases for several months, and thus these two hard state phases do not have the same history. The hard states in the rising phase come from a quiescent, already radio emitting state, while the hard states in the decaying phase come from soft radio silent states. There is no apparent reasons the two jets would be identical. This supports a link with the global jet structure rather than a threshold in $\dot{m}$.

A change in the dominating ejection process

Since the commonly invoked radiative process is synchrotron, the first thing that comes to mind to explain this difference is the magnetic field strength. The only reasonable assumption to make is that this field is proportional to the field anchored in the JED, which writes (see Eqs. 2.29 and 2.30):

$$B_z(r) = (\mu\,\mu_0\,P_{tot})^{1/2} \simeq \left(\mu\,\mu_0\,P_*\frac{\dot{m}r^{-5/2}}{m_s}\right)^{1/2}, \tag{3.9}$$

Assuming constant JED parameters $\mu = 0.5$ and $m_s = 1.5$ used in our model, we evaluate the magnetic field strength measured in r_{isco} at around 10^9 G during the outbursts.

It should be noted that a JED exists within a small interval $[\mu_{min}, \mu_{max}]$ of disk magnetization μ, with $\mu_{min} \sim 0.1$ and $\mu_{max} \sim 0.8$ (Ferreira 1997). The existence of such an interval has led Petrucci et al. (2008) to propose that the hysteresis observed in XrB could be a consequence of a JED switch-off during the hard to soft transition related to the fact that the magnetization μ could reach the lower possible value μ_{min}. On the other hand the JED would switch on during the soft to hard transition when μ reaches μ_{max}. In the spectral analysis shown in the present paper, we suppose a constant μ since, as shown in Marcel et al. (2018b), the JED spectra are weakly affected by μ within the allowed parameter space. However, the possible difference in magnetization between the rising and decaying phase could anyway have a direct impact on the jet dynamical and radiative properties, explaining the change of the observed radio behavior. According to Eq. 2.29, a dichotomy of the magnetization μ at a given value of the mass accretion rate $\dot{m}$ entails a dichotomy in the magnetic field strength. Thus, the rising phase, switching-off with $\mu = \mu_{min}$, would present a weaker magnetic field strength compared to the decaying phase, switching-on with $\mu = \mu_{max}$. This difference in the magnetic field strength could play a role in the difference of functional dependency of the radio emission. This could also explain the higher radio efficiencies observed in Fig. 3.27 during the decaying phases (e.g., Casella & Pe'er 2009).

Another possibility could be suggested by the most recent numerical simulations showing that the vertical magnetic field is carried in and accumulates around the black hole (building up a magnetic flux Φ_{bh}) until the surrounding disk magnetization reaches a maximum value near unity (see, e.g., Tchekhovskoy et al. 2011; Liska et al. 2020). In our view, the inner disk regions are nothing else than a JED driving a Blandford & Payne (BP, Blandford & Payne 1982) jet, although a Blandford & Znajek

(BZ, Blandford & Znajek 1977) spine launched at its midst has attracted more attention in the literature[8]. Then another possible explanation for the existence of two functional dependencies for $F_R(\dot{m}, r_J)$ could be that jets are made of two-component MHD outflows: a BZ spine, tapping into the rotational energy of the black hole, surrounded by a BP jet, tapping into the accretion energy reservoir of the disk. The jet dynamics and subsequent radio emission then depend on the relative importance of these two flows, which can be roughly measured by the ratio of the magnetic flux associated with each component, namely Φ_{bh} for the spine and Φ_{JED} for the outer BP jet. By construction, Φ_{bh} builds upon Φ_{JED} and reaches large values, such as $\tilde{\Phi}_{bh} = \Phi_{bh}/(< \dot{M} > R_G^2 c)^{1/2} \sim 50$, only if a large magnetic flux is available initially in the disk (Tchekhovskoy et al. 2011; Liska et al. 2020). The functional dependency on r_J that we observe for the radio flux in our fits of the rising phase spectra could thus come from the dependency of $\tilde{\Phi}_{bh}$ on r_J.

A simple scenario can then be designed and is sketched in Fig. 3.28. During the rising hard-state phase, r_J is initially large and decreases in time (top right). The system comes from a quiescent state and the presence of a JED over a large radial extent allowed the disk to build up a maximum Φ_{bh}. The spine is very important and affects the overall jet dynamics, which translates into a radio flux described by Eq. 3.7. When the disk magnetization becomes too small, the JED transits to a SAD accretion mode (left, top and bottom). The magnetic field diffuses away, thereby decreasing Φ_{bh}, and no more jets are observed (neither BP nor BZ). As long as the system remains in the soft state, the field keeps on diffusing away until some equilibrium is eventually reached. At some point however the outburst declines, which translates into a decrease in mass accretion rate and the inner disk pressure, and thus an increase in the disk magnetization. In this decaying phase an inner JED build itself inside-out, with its bipolar BP jets, but with a limited magnetic flux available (bottom right). By construction, Φ_{bh} remains small and the BZ spine has a limited impact on the overall jet dynamics. This would translate into a radio flux described by Eq. 3.8 until the JED is rebuilt over a large enough radial extent.

There are many uncertainties in the different interpretations, since the JED-SAD modeling has its own simplifications. This last scenario is only an attempt to provide an explanation to the puzzling findings. Quite interestingly, it also provides a means of observationally testing it. It relies on the existence of a BZ spine in the case of GX 339-4, which is a black hole candidate. Around a neutron star the invoked scenario of magnetic flux accumulation into the central object clearly should not work. It would therefore be useful to investigate any changes in the radio properties during the rise and decay phases for neutron star binaries.

This scenario may look similar to the ones proposed by Begelman & Armitage (2014) or Kylafis & Belloni (2015) where the presence of a hot inner corona (an ADAF-like accretion flow in both cases) would help in accumulating or creating the required magnetic field that will eventually produce a jet. However, in these two approaches it is not clear why the process would differ between the rising and decaying phases, and how the functional dependency of the radio emission would depend on the ADAF properties.

[8]The inner disk regions are usually called magnetically arrested accretion disks (MADs) (Narayan et al. 2003; Tchekhovskoy et al. 2011); however, as accurately noted by McKinney et al. (2012), a thin or even slim disk is not arrested. The deviation from Keplerian rotation is only on the order of the disk thickness, and its structure resembles the JED, with a near-equipartition magnetic field.

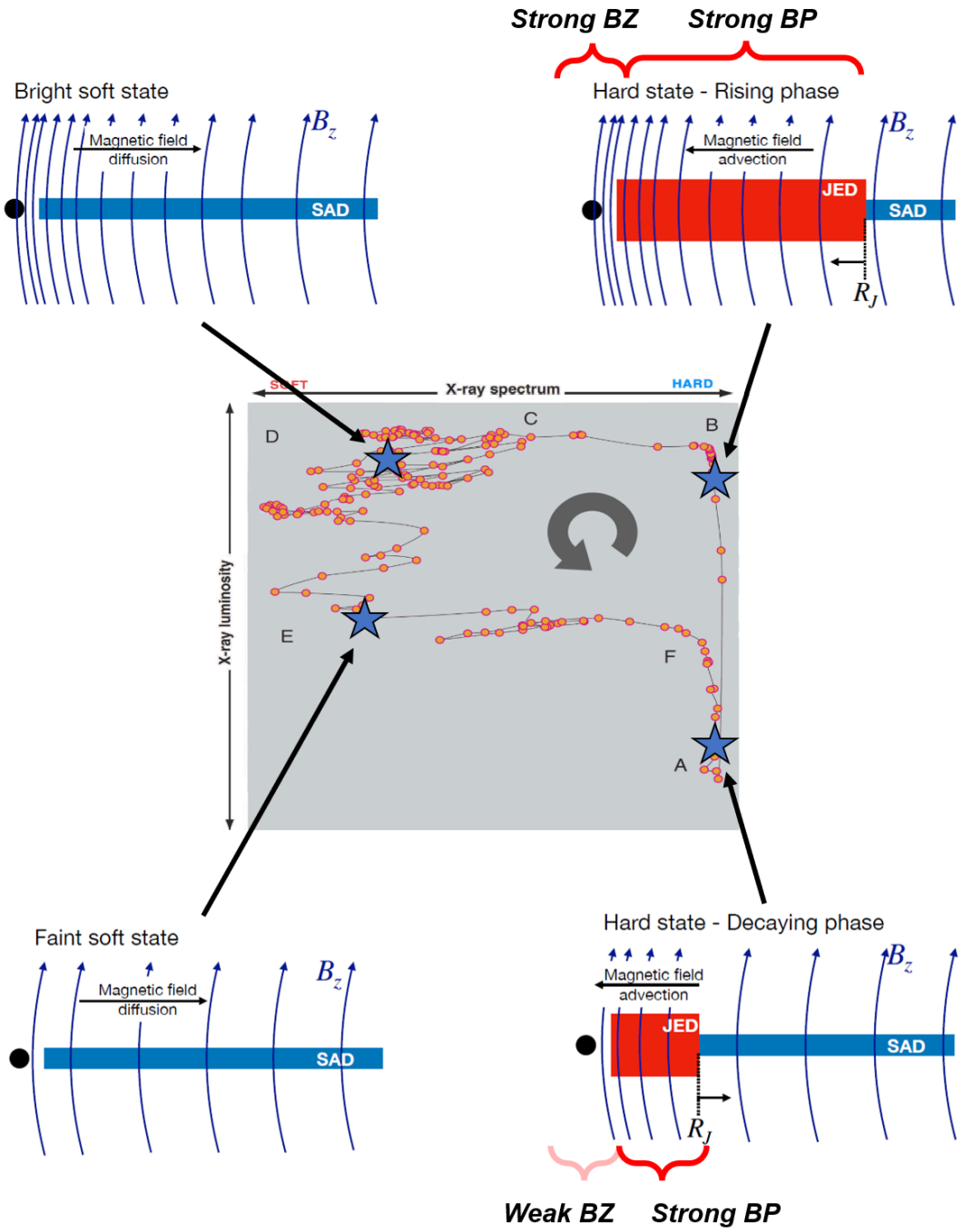

FIGURE 3.28: Sketches of the inner regions of an accretion flow around a black hole during the different phases of the outburst. **Top right:** In the rising hard phase the JED is settled over a large region (r_J is large), leading to efficient magnetic flux accumulation on the black hole. The radio emission arises from a two-component outflow, made of an important BZ spine surrounded by a BP jet. **Top left to bottom left:** During the soft state there is no more JED, the magnetic field diffuses away, and the BP and BZ jets both disappear. Weak or no radio emission is expected (jet-line). **Bottom right:** In the decaying phase a JED reappears in the innermost region, and the magnetic field advection becomes efficient again. The magnetic flux on the black hole is still weak, and the BZ spine has little or no impact on the jet dynamics and subsequent radio emission.

Clearly, more dedicated work should be done in this subject (see for instance Jannaud et al. 2022, in preparation, which mentions the influence of a jet spine with the outer BP jet).

Echoes in AGN

Interestingly, the differences in the radio properties observed in the rising and decaying phase of GX 339-4 could find some echoes in AGN. Radio loud AGN are generally sub-classified in two categories depending on the brightness shape of their radio images (Fanaroff & Riley 1974). Fanaroff & Riley type 1 AGN (FR I) are centre-brightened objects, the jet radiating on scales of a kpc close to the galaxy. Fanaroff & Riley type 2 AGN (FR II) are edge-brightened objects, their jets are weakly luminous on kilo to mega parsecs and terminate in regions of high-surface brightness called “hot spots".

At a given host galaxy optical magnitude, the division between FR I and FR II was generally associated with a separation in radio power, FR II being brighter than FR I (Owen & Ledlow 1994; Ledlow & Owen 1996). Given the link between the host galaxy optical magnitude and the central black hole mass (McLure & Dunlop 2001), Ghisellini & Celotti (2001) suggest that the FR I-FR II dichotomy could be controlled by the properties of the underlying accretion process and not (only) by a different environment. On the contrary Tchekhovskoy & Bromberg (2016) suggests, through 3D relativistic MHD simulations, that the ambient medium plays a crucial role in the jet morphology. The critical power for the jet to stably escape the galaxy core depends, in their simulations, on the galaxy optical luminosity in agreement with the above observations.

Very recent radio studies with better sensitivities show however that the division between FR I and FR II with respect to the radio luminosity is not at all so strict (e.g Mingo et al. 2019). While FR I have generally the weakest radio emission, there is a very large overlap in luminosity between the two morphologies.

Compared with the radio characteristics of XrB, Körding et al. (2006) proposed that FR I would populate the low luminosity hard states whereas FR II would populate the bright hard states. A possibility then arises, that FR I could correspond to the hard states of the decaying phase of the XrB outburst and FR II to the hard state of the rising phase. In this case, the interpretation discussed in Sec. 3.6.2, i.e. the dominance between BZ and BP processes, would also play a role in the difference between FR I and FR II. In the case of FR I, the BP process would dominate. A null asymptotic current is expected on the jet axis, and recollimation shocks may be naturally present. This would explain the poorly collimated FR I jets and their center-brightened aspect. On the other hand, if FR II correspond to hard state in the rising phase of the outburst, our interpretation suggest the presence of both BP and BZ processes. The presence of the BZ spine would maintain an electric current asymptotically different from zero. This would produce the necessary hoop stress to collimate the jet until large distances where the BZ spine encounter the intergalactic medium.

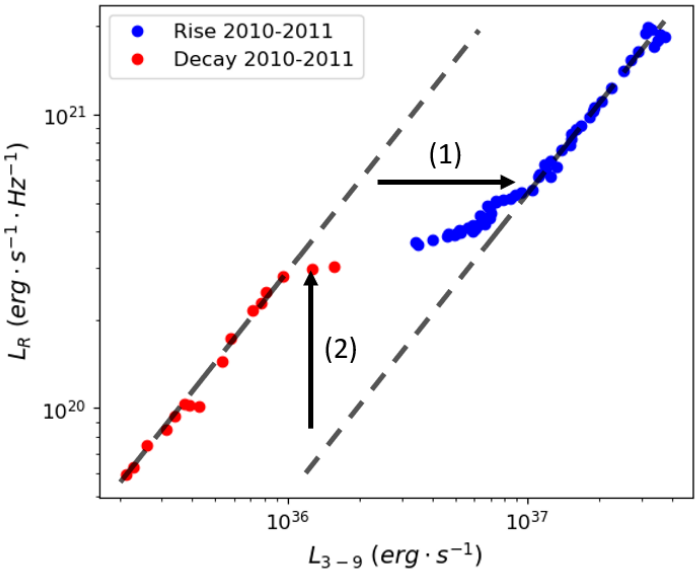

FIGURE 3.29: Radio–X-ray correlation of the 2010-2011 outburst from GX 339-4. The radio was interpolated at the date of each X-ray observation. The blue and red points represent respectively observations of the rising and decaying phase of the outburst.

3.6.3 The radio X-ray correlation

I mentioned before that the radio–X-ray correlation followed by GX 339-4 agrees with a linear correlation of index ∼0.7 in log-log space (e.g., Corbel et al. 2000, 2003, 2013) even down to very quiescent states (Tremou et al. 2020). Yet looking at each outbursts separately, this correlation shows the presence of wiggles along this linear correlation, especially between the high- (read rising) and low- (read decaying) luminosity states. This is especially visible in the bottom panel from Fig. 3.1 (adapted from Corbel et al. 2013) and in Fig. 3.29. In this second figure, I plot the radio X-ray correlation for the 2010-2011 outburst using the interpolated radio fluxes. Given the results obtained in this study and complemented by Marcel et al. (2022), there are two ways to interpret these wiggles.

1. An increase of the X-ray radiative efficiency. The transition from the READ-JED to the even more radiatively efficient RERD-JED around $\dot{m} \sim 0.5$ would increase the X-ray luminosity output and transit horizontally between the two branches plotted in Fig. 3.29.

2. An increase of the radio radiative efficiency. Motivated by the difference in the jet radiative efficiency between the rising and decaying phases observed in Fig. 3.27, changes in the global structure of the jet between the two phases could increase the radio output of the decaying phase and thus create a vertical transition between the two branches.

Most likely both of these explanations acts simultaneously. I take these two explanation as an important reminder that the evolution of an XrB is not contained uniquely in the accretion flow and visualised in the HID, nor can it be fully understood only with the radio-X-ray correlation. An outburst is a 3D problem, involving the radio luminosity, the X-ray luminosity and the spectrum hardness as output of three different way to spend the power: jets, radiation and advection (see Fig. 3.30).

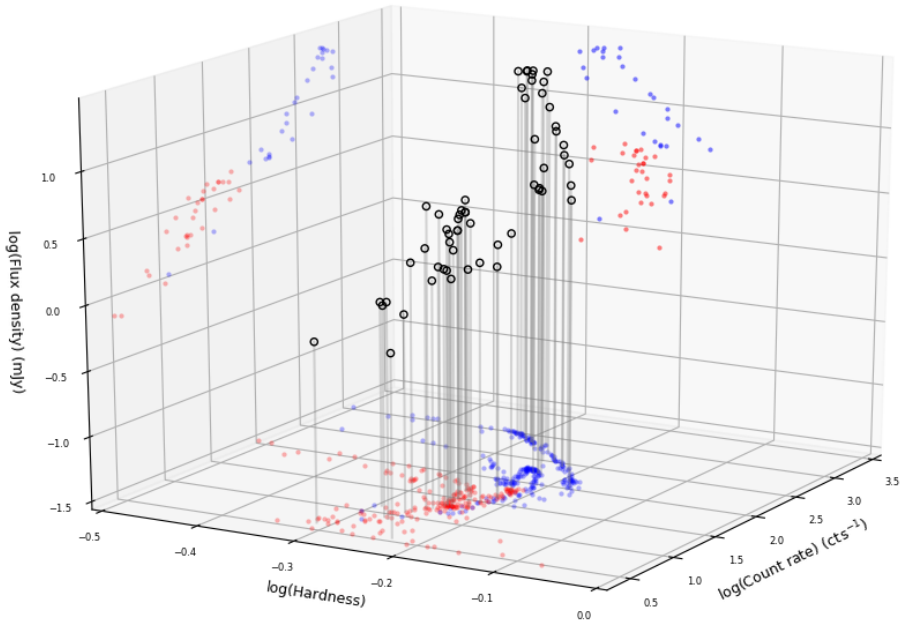

FIGURE 3.30: 3D visualisation of GX 339-4 outbursts with a focus on the hard states. The axes are: the X-ray hardness ratio, the X-ray RXTE/PCA count rate and the radio flux density. The blue and red points are respectively the rising and decaying phase observations. The radio coverage being generally scarce, only a few points are present in the projection involving the radio flux.

Chapter 4

Other XrB applications and prospects

Contents

4.1 MAXI J1820+070 113
4.1.1 Characteristics and bibliography 113
4.1.2 X-ray Fits 113
4.1.3 Interpretations 114
4.2 Outliers 117
4.2.1 Motivations 117
4.2.2 H 1743-322 117
4.2.3 MAXI J1348-630 119
4.3 Comparison to Monte Carlo simulation – The MONK code 121
4.3.1 Collaboration goal and methodology 121
4.3.2 Spectral components 122
4.3.3 Estimation of ω 123
4.3.4 Prospects – Cyg-X1 and polarisation 123

Dans ce chapitre, je présente deux autres applications du modèle JED-SAD aux binaires

X. *MAXI J1820+070*

En collaboration avec Alessio Marino, nous avons étudié la binaire X MAXI J1820+070 avec le modèle JED-SAD. Ce travail a été publié dans **?**. *Cette source a été le sujet d'un très grand nombre d'articles récents du fait de son éruption de 2018 extrêmement brillante (Kawamuro et al. 2018; Tucker et al. 2018). Il s'agit d'un système composé d'un trou noir d'environ* $8.5M_{\odot}$ *et d'un compagnon de* $0.4M_{\odot}$ *(Torres et al. 2019, 2020), à une distance de* 3.0 ± 0.3 *kpc et avec une inclinaison assez forte* $\sim 60-70^{\circ}$ *(Atri et al. 2020). Plusieurs modèles concurrents ont été appliqué avec succès à cette source (Kara et al. 2019; Buisson et al. 2019; Zdziarski et al. 2021; De Marco et al. 2021). Tous ont eu besoin d'une réflection avec deux composantes, une réflection élargies par des effets relativistes et une réflection avec une raie du fer plus fine.*

Nous avons réuni des données de 4 différents instruments X: Swift/XRT, Swft/BAT, NuSTAR and NICER, donnant une excellente visibilité sur la bande d'énergie 0.5 à 200 keV. Cela constitue un noveau test pour le modèle. Alessio, avec mon aide, a ajusté 8 observations de l'état dur avec les tables JED-SAD que j'ai créées. Avec cette plus large bande de données, nous avons rencontré des problèmes pour ajuster la coupure à haute énergie. Afin de l'ajuster correctement, nous avons étudié l'espace des paramètres et libéré la vitesse d'accrétion m_s. *Tout comme les autres articles sur cette sources, nous avons besoin de deux composantes de réflections. La première émise par l'interaction de l'émission de la couronne avec les régions internes du SAD subit de faible déformation en raison de la proximité avec le trou noir mais est surtout caractérisé par une forte ionisation. La seconde réflection est elle plus lointaine et subit aucun effet relativiste. Celle ci est quasiment neutre. L'interprétation que l'on propose est la présence d'une région caché que le JED n'illumine pas (voir Fig. 4.1).*

Comparison Monte Carlo

En collaboration avec Wenda Zhang, Giorgio Matt et mon directeur de thèse Pierre-Olivier Petrucci, nous avons comparé l'émission du modèle JED-SAD à au code de simulation Monte Carlo MONK. Ces simulations extrêmement coûteuse en temps de calcul sont bien plus précises que les approximations employés pour calculer l'émission du modèle JED-SAD et peuvent inclure les effets relativistes que nous ne prenons pas en compte. En Fig. 4.7, je présente deux cas de comparaison de l'émission du modèle JED-SAD telle que calculée par le code Dyplodocus (ligne pointillée) et le code MONK (histogramme continu). Dans le premier cas, les deux approches sont en bon accord, dans le second, le modèle JED-SAD sur-estime un peu l'émission. Cette comparaison nous permet aussi de mesurer la valeur exacte du paramètre de dilution ω *que nous supposons libre dans le code Dyplodocus. De manière générale, nous nous sommes rendu compte que les valeurs de* ω *doivent être environ 10 fois plus faibles que ce que bous obtenons pour ajuster les données. La mise ne oeuvre d'une correction en passant par le code MONK est en cours.*

Grâce au code MONK, nous sommes aussi capable de prédire la polarisation (angle et degré) de l'émission X. Cela est particulièrement intéressant du fait du lancement récent du satellite IXPE dédié à l'étude de la polarisation X. La dernière (seule) mesure (détection) de la polarisation des photons X date de près de 40 ans. J'ai ajusté les données de l'observation X simultanée à l'observation de IXPE de la source Cyg-X1 avec le modèle JED-SAD (voir Fig. 4.8). L'ajustement est bon et nous attendons maintenant les prédictions du modèle JED-SAD de la polarisation X afin de les comparer avec les résultats de IXPE.

4.1 MAXI J1820+070

In this section I discuss briefly the work produced in collaboration with Alessio Marino and published in Marino et al. (2021).

4.1.1 Characteristics and bibliography

MAXI J1820+070 is a recently discovered LMXrB. It was first observed in 2018 (Kawamuro et al. 2018; Tucker et al. 2018) when it entered into a year-long outburst which was the subject of an intensive multi-wavelength observing campaign. The system is composed of a black hole of $\sim 8.5 M_\odot$ and a secondary star of approximately 0.4 $M_\odot$ (Torres et al. 2019, 2020). The source is estimated at a distance of 3.0 ± 0.3 kpc (Atri et al. 2020) and its inclination around 60° and 80° (Kajava et al. 2019; Torres et al. 2019; Atri et al. 2020) from different methods (presence of X-ray dips, optical spectroscopy, jet axis). Many papers have studied these outbursts in X-rays. Controversies surround the very different results obtained using different models concerning the truncation radius. Study of the hard states observations using a contracting lamp-post corona model suggest that the standard disk reaches the ISCO (Kara et al. 2019; Buisson et al. 2019), whereas truncated disk models have also been successfully fitting the same data set (Zdziarski et al. 2021; De Marco et al. 2021).

Interestingly, the iron line profile observed in the NICER data suggest a complex reflection. Indeed, the line present a shrinking narrow core above a constant broad iron line (Kara et al. 2019; Buisson et al. 2019). They interpreted this result as a contacting lamp-post corona producing two reflection components. The top of the corona illuminates a distant region of the accretion disk, producing the narrow line component while the bottom part of the corona illuminates the inner part of the disk reaching the ISCO and thus producing a blurred iron line. During the hard states, as the corona shrinks (from the top), the narrow line component gradually disappear whereas the broad line component remains stable as the inner part of the accretion flow is always illuminated by the corona.

4.1.2 X-ray Fits

Alessio collected quasi-simultaneous observations from four different instruments: *Swift*/XRT, *Swft*/BAT, *NuSTAR* and *NICER*, producing an excellent view on a wide energy range (from 0.5 to 200 keV). He fitted the data of 8 observations in the bright hard states of the outburst using my JED-SAD and reflections tables (see in Marino et al. 2021, Figs. 4 and 5 for the residuals and Tab. 3 for the fitting parameters). Similarly to the results from Kara et al. (2019), a model using two different reflections component was necessary to fit the complex iron line profile. In the JED-SAD model, the reflection is usually produced on the SAD and we link the inner edge of the SAD (r_J) to blur the reflection using the kdblur model (see discussion in Sec. 2.4.2). Here, the relativistic reflection was linked to the inner edge of the SAD (r_J), its outer edge was fixed to the inner edge of the non-relativistic narrow reflection. The inner edge of the narrow reflection component was fixed to a distance $R = 300 R_G$[1]. The Iron abundance was fixed between the two reflections, however the ionisation parameter was free for both reflection components.

[1]The observations did not constrain the inner radius of the second reflection. Thus it was fixed to a value agreeing with all observations.

While fitting the observations, Alessio was confronted with a recurring problem. The first JED-SAD table I gave him had difficulties to reproduce the correct spectral shape while reaching the right level of luminosity. Instead the fit preferred to use a dominating highly ionized (log(ξ)>4) and blurred reflection to fit the continuum, while the JED-SAD emission was 10 times less luminous. To reach correct fits required the use of another JED-SAD parameter: the sonic mach number m_s. m_s controls the accretion speed within the JED. A smaller m_s means a denser, cooler and more X-ray luminous JED. I build the JED-SAD and corresponding reflection tables with m_s as a free parameter. This allowed to explore another region of the JED-SAD parameter space and fit the continuum with the JED-SAD table correctly.

The results showed that the observations could be classified into three different spectral states. The first observation showed a large truncation $r_J \sim 57$, with a small mass accretion rate $\dot{m} \sim 0.8$ and $m_s \sim 1.3$. It is the only observation that agrees with a single reflection component. The second series of observations (2 to 6) showed a similar spectral shape. The transition radius is constant $r_J \sim 40$, the mass accretion rate first increases to $\sim$ 2.3 (during obs 3) and than decreases gradually to $\sim$ 1.0 (reached at obs 7). All observations from 2 to 6 had a sonic mach number $m_s \sim 1.25$. The last two observations are characterised by a small re-hardening of the spectrum, with a small decrease in luminosity (see Fig. 2 in Marino et al. 2021). These two observations showed an increase of the sonic mach number m_s to 1.5 and a transition radius r_J of the order of 30. The evolution of the two reflection components shows an increase of the ionization parameter for both the inner, relativistically blurred, reflection (from $log(\xi) \sim 3.5 \rightarrow 3.7$) and the outer, narrow, reflection (from $log(\xi) \sim 2 \rightarrow 3$). Observations 7 and 8 can also agree with a one reflection component model. All 8 observations are characterized by a RERD-JED regime (see Sec. 2.2.2 for the definition).

4.1.3 Interpretations

JED-SAD geometry

Here I detail some of the interpretations to the presence of these two reflections component, involving the geometry. In Fig. 4.1, I show the schematic view proposed by Marino et al. (2021) to explain the different geometrical interpretations. In Marino et al. (2021), two main geometric interpretations are proposed. The first looks like the left panel of Fig. 4.1. The JED illuminates the entire SAD. Each ring of the SAD

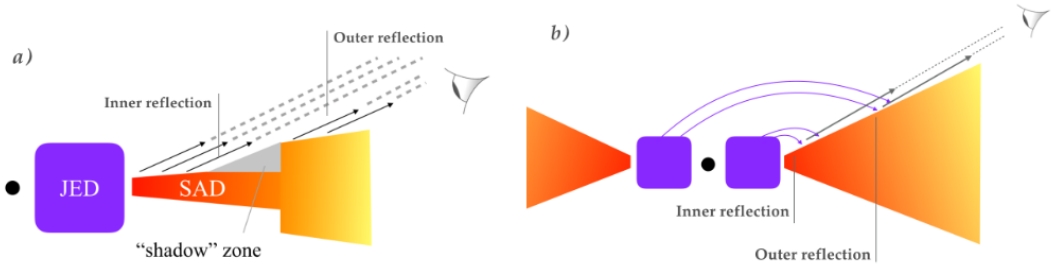

FIGURE 4.1: Fig. 10 from Marino et al. (2021). Schematic view of the geometry of the JED-SAD allowing to explain the different interpretations developed to explain the two reflection components. On the left, a region of the SAD emits a reflection component which is absorbed by a puffed-up region of the disk, creating a shadow region that is not observed. On the right: The JED emission from the other side of the black hole is bent due to GR effects and illuminates a region in the outer part of the disk.

is than emitting a reflection spectrum with different ionization parameter and relativistic blurring effects as both of these depends on the distance of the ring to the illumination source or to the black hole. A region of the disk is puffed-up, hiding part of the standard accretion disk and the reflection spectrum emitted by these hidden ring. These ring being in the middle, they would have been characterized by a mild ionization and relativistic blurring. Instead, we only see the broad iron line component coming from the inner region of the SAD, and the narrow iron line component emitted by the outer region of the SAD. The increase of the vertical height of the SAD can be explained by two different possibilities: if the outer region of the SAD has an important mass accretion rate, the corresponding SAD rings would be hotter and puffier. Another possibility stems from the transition from the Thomson opacity dominated region to the free-free opacity dominated region inside of the SAD. Such a transition is expected in a standard disk (Shakura & Sunyaev 1973). However estimates place this transition at more than 10^4 R_G and thus the puffed-up region would never be illuminated enough to produce such a strong narrow line component.

Another interpretation depending on a variation of the disk height with radius exists. This one was not presented within Marino et al. (2021). Instead of having the external disk flared-up height hide part of the disk from the observer, a region of the disk is in a depression (lower height) due to variation of the mass accretion rate. This depression region is not illuminated by the corona, as the inner region are hiding it, and does not produce any reflection component. This is motivated by the evolution of the mass accretion rate during this phase of the outburst (see the HID in Fig. 1 of Marino et al. (2021) or the evolution of $\dot{m}$ we obtained): Observations 3 to 7 are characterized by a mass accretion rate $\dot{m} \sim 2.3$ but then observation 7 and 8 show a decrease of luminosity, a small re-hardening of the spectrum and a lower mass accretion rate $\dot{m} \sim 1$. In the JED-SAD model, the mass accretion rate is measured at the ISCO and is supposed constant within the SAD $\dot{m}(r > r_J) = \dot{m}(r_J)$. However this is an approximation as the evolution of the mass accretion rate with time entails variations of the mass accretion rate in the radial profile of the SAD. Considering the variation of $\dot{m}$ between observation 2 and observation 8 ($\dot{m} = 2.3 \rightarrow 1$), the delay of 90 days between the two observations, and the accretion time scale within the SAD ($\alpha = 10^{-3}$): we estimated that, within a disk with $\dot{m} = 2.3$, placing a depression $\dot{m}(r) = 1$ at a distance $r = 1000\,R_G$ implies a shadow region of about 300 R_G. This region is not directly illuminated by the JED. This can be another explanation for the shadow region proposed in the left panel of Fig. 4.1. However, the values of $\alpha = 0.001$ in the disk is a bit smaller compared to the usual value used for a standard disk ($\alpha \sim 0.01$). Stronger values of α would place the depression further away from the black hole and the corona, decreasing the normalisation of the narrow reflection produced by the outer region.

The second sketch (right panel of Fig. 4.1) shows another possible geometry. The JED immediately adjacent to the SAD illuminates the inner region of the SAD, producing the inner, broad, reflection component. The JED region situated on the other side of the black hole would emits photons that are bent by the black hole and thus illuminates a distant region of the SAD, producing a distant, narrower reflection component.

Any of these scenario should be checked using a GR Monte Carlo code allowing to compute the reflection spectrum from any given part of the disk.

Optical winds

Another possible interpretation concerning the two reflection components can be attributed to the presence of winds. Indeed, P-Cygni profile are observed in the emission lines of HeI at 5876 and 6678 Å, as well as on the Hα line during the hard states (Muñoz-Darias et al. 2019). The corona emission could illuminate these winds emitted far from the central black hole, producing the outer, narrower, reflection component.

4.2 Outliers

In this section, I present a few results I obtained while trying to reproduce the method applied to GX 339-4 in Chapter 3 with a few XrB belonging to the outlier population.

4.2.1 Motivations

In Chapter 3, I studied the radio–X-ray behaviour of GX 339-4 which is known to follow the '*universal*' radio–X-ray correlation (e.g. Corbel et al. (2013)). However another population of XrB following a different radio–X-ray correlation exists. First discovered with H 1743-322 (Coriat et al. 2011), this population present breaks in the correlation (see Fig. 1.7 in the introduction). At low luminosity, this population seem to follow the '*universal*' track. But at intermediate luminosity, the radio seem to no longer evolve (or the X-ray suddenly increases by a large amount). And at higher luminosity, the correlation is harder ($L_R \propto L_X^{\sim 1.4}$) than the '*universal*' track ($L_R \propto L_X^{\sim 0.7}$). Are the accretion disk parameters different between the outlier and 'universal' XrB populations? Does the difference originate from the radio dependency on the disk parameters? Or are these two populations actually the same? After all similar wiggles around the radio–X-ray correlation, but on smaller luminosity scale, are observed in GX 339-4.

4.2.2 H 1743-322

Characteristics and data

H 1743-322 is composed of a $\sim 11\ M_\odot$ black hole (Molla et al. (2017)). The distance of the system is not well known, however the usual value seen in the literature is a distance of 8 kpc (Corbel et al. 2005; Steiner et al. 2012) It should be noted that, unlike GX 339-4, H 1743-322 is located near the Galactic bulge, meaning the X-ray spectrum will be polluted by the Galactic ridge emission. Extreme values of spin seem unlikely (Steiner et al. (2012)), making H 1743-322 the third reported XrB with jets and a moderate value of spin. The typical values of hydrogen column density N_H seen in the literature is $1.6 \rightarrow 2.4 \times 10^{22}\ cm^{-2}$ (McClintock et al. 2009; Prat et al. 2009; Capitanio et al. 2009). I use $N_H = 2.3 \times 10^{22}\ cm^{-2}$.

TABLE 4.1: Selected hard state observations of H 1743-322 outbursts and number of observations.

Outburst	Rise$^{(a)}$	Decay$^{(b)}$	X-ray$^{(c)}$	Radio$^{(d)}$
2003	52729-52752	52944-52952	19 (6/13)	5 (4/1)
2008a	–	54492-54512	11 (0/11)	5 (0/5)
2008b	54742-54752	54788-54789	9 (6/3)	3 (3/0)
2009	54980-54982	55019-55031	10 (4/6)	7 (2/5)

Notes: $^{(a)}$ MJD of the rising phase of each outburst.
$^{(b)}$ MJD of the decaying phase of each outburst.
$^{(c)}$ Number of X-ray observations covering each outburst.
$^{(d)}$ Number of radio observations covering each outburst.
I specify the number of rising phase observations or decaying phase observations using the notation: (rising / decaying).

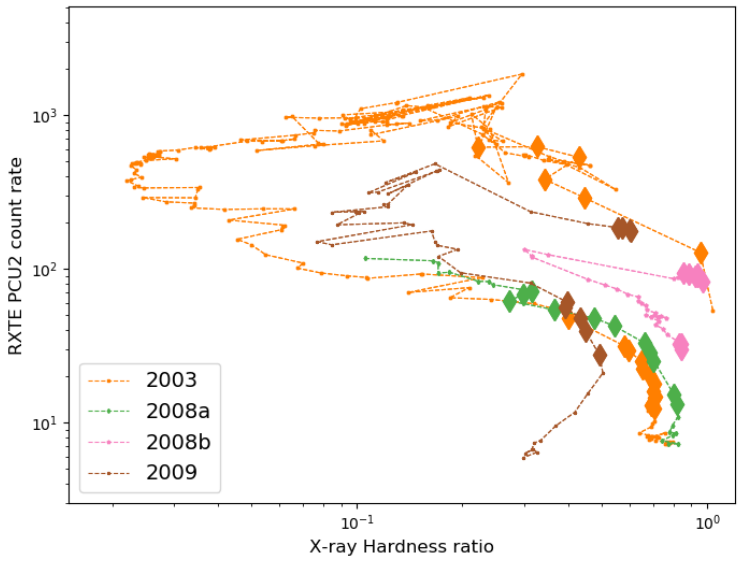

FIGURE 4.2: Hardness Intensity Diagram for the four H 1743-322 outbursts observed by *RXTE*. The dots represent X-ray observations. The diamonds show the selected hard X-ray spectra.

I had access to the X-ray spectra observed by *RXTE* and analysed in Coriat et al. (2011). In Fig. 4.2, I plot the HID of the multiple outbursts observed by *RXTE*. I selected the hard states of the 2003, 2008a, 2008b and 2009 outbursts for the analysis (plotted as diamonds). At the end of the outbursts, the observations seem to cluster around the same X-ray luminosity and hardness ratio. This is due to the presence of the galactic ridge which contaminates the *RXTE* spectra. Indeed, the instruments on board of *RXTE* are not imagers and can not effectively separate the source emission from the galactic bulge emission. I discard these spectra from the selection. As such I do not have access to the less luminous points present in the H 1743-322 radio–X-ray correlation presented in Fig. 1.7. The points below $L_{3-9\,keV} \sim 10^{35}\ erg \cdot s^{-1}$ were obtained using the Chandra observatory which can separate the source emission from the galactic ridge emission. In Tab. 4.1, I reference the MJD of the rising and decaying phase of each outburst as well as the number of X-ray and radio observations in each phase. This correspond to a total of 49 X-ray spectra and 20 radio fluxes. Unfortunately, the radio coverage of the outbursts was not sufficient to reproduce the study performed on GX 339-4.

I did however fit these spectra and present the results in Fig. 4.3, comparing them to what was obtained for GX 339-4. The decaying hard states obtained for H 1743-322 show a similar behaviour and the values of the parameters are comparable with the GX 339-4 outburst track. It is harder to conclude for the rising phase as the 2003 outburst is caught quite late in the rising phase and the outburst transits to the soft state early. The fitted observations might just be transition states. The other fitted rising phases (2008b and 2009) show different behaviours compared to the 2003 outbursts. And the 2008b outburst is a 'failed-outburst', never reaching the soft states.

It should be noted that all observations within the steep part of the radio–X-ray correlation at high luminosity were rising hard states, while all the points within the

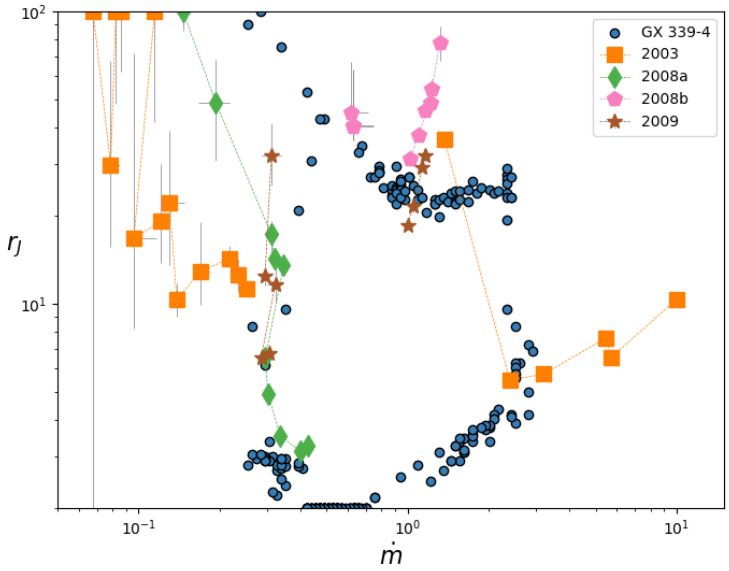

FIGURE 4.3: Results of the X-ray fits in the parameter space (r_J;$\dot{m}$) for the four outbursts of H 1743-322 fitted. I add the track followed by GX 339-4 for comparison (Constrained states obtained in Marcel et al. 2022).

flat and lower part of the correlation were decaying phase observations. This is similar to what was observed around the wiggles of GX 339-4 radio–X-ray correlation in Chapter 3. Once again low luminosity rising phase are not observed, and thus conclusions are hard to obtain.

4.2.3 MAXI J1348-630

MAXI J1348-630 is a XrB discovered in 2019 (Yatabe et al. 2019) when it displayed typical outburst followed by multiple re-flares. The mass and distance of the source were estimated at $\sim 7\ M_\odot$ (Tominaga et al. 2020) and $2.2^{+0.5}_{-0.6}$ kpc (Chauhan et al. 2021). MAXI J1348-630 was observed by multiple X-ray observatories: Chandra, NuSTAR, NICER, XMM, HXMT, Swift and Integral. In radio it was observed with both MeerKAT and ATCA (Carotenuto et al. 2021b). This source is also known to have produced ejecta during the transition states with the highest proper motion ever measured for an XrB (Carotenuto et al. 2021b). The radio–X-ray correlation follows the outlier track. However it does not seem to present a flat part similar to H 1743-322, instead the flat portion is characterized by a low power relation $L_R \propto L_x^{0.24\pm0.05}$ (see Fig. 1 in Carotenuto et al. 2021c).

My PhD advisor and myself supervised the master internship of Maïmouna Brigitte during which she analysed and fitted hard X-ray spectra with the JED-SAD model. In Fig. 4.4, I show a few examples of the residuals of the fits for the rising and decaying phase of the outburst. The parameters of these fits show during the rising phase values of r_J ranging from 28 to 21 with no particular evolution, and $\dot{m}$ from 1.2 to 6 with a steady evolution at the start of the transition. For the NICER observations of the decaying phase, r_J seems to gradually increase from 15 to 27, and $\dot{m}$ is constant around 0.7.

Maïmouna then reproduced the radio study I performed on GX 339-4 and obtained the contours presented in Fig. 4.5 (to be compared to Fig. 3.22 for GX 339-4).

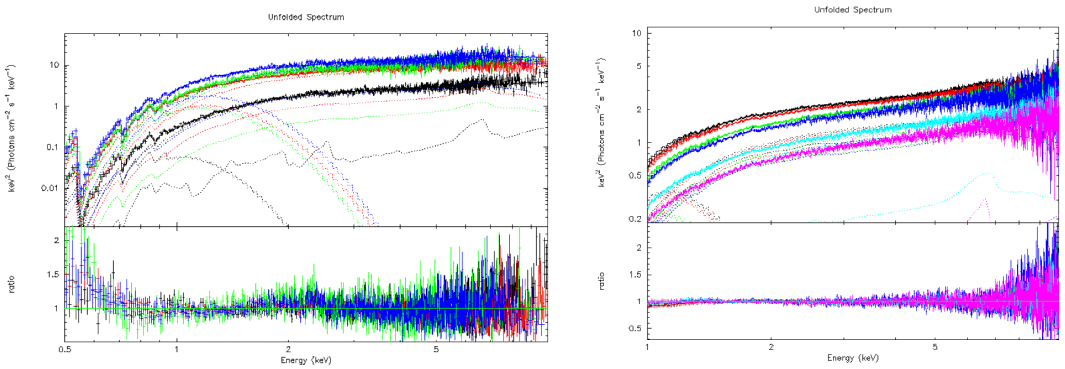

Multi-Swift
$\chi^2 = 4788.98$
dof=3387

Multi-Nicer
$\chi^2 = 8261.18$
dof=5369

FIGURE 4.4: Examples of X-ray fits with the JED-SAD performed by Maïmouna Brigitte during her internship. Left: Different Swift spectra during the rising phase of the outburst (MJD 58510, 58511, 58512, 58512, 58515). Right: Different Nicer spectra during the decaying phase after the first re-flare (MJD 58650, 58656, 58660, 58663, 58672, 58677).

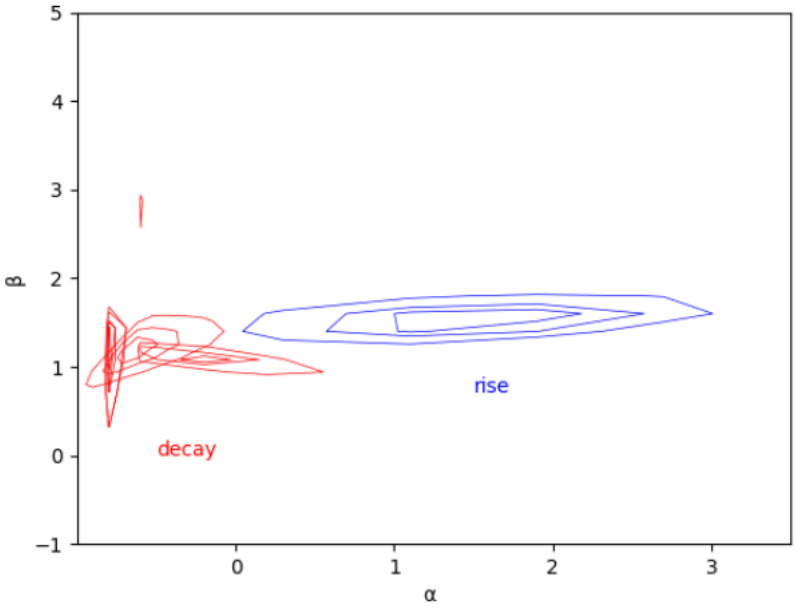

FIGURE 4.5: Contours of the parameters α and β obtained for MAXI J1348-630 by Maïmouna Brigitte during her internship. To be compared to Fig. 3.22 obtained for GX 339-4. The blue contours show the dependence of the radio emission with the JED-SAD parameters during the rising phase of the outburst. And the red contours show the dependence during the decaying phase after each re-flare.

Similarly to what I obtained for GX 339-4, the rising and decaying phase solution do not agree. Furthermore the $\alpha - \beta$ contours computed at different period during the decaying phase agree with each other. However the values of the parameters do not seem the same compared to GX 339-4. Clearly more works need to be done on this subject.

4.3 Comparison to Monte Carlo simulation – The MONK code

This section details a work in progress lead by my PhD advisor, Pierre-Olivier Petrucci and in collaboration with Wenda Zhang and Giorgio Matt. Here I report the latest results we obtained.

4.3.1 Collaboration goal and methodology

Initially, the collaboration had for objective to compute the expected polarisation of any JED-SAD configurations in preparation for the launch of the Imaging X-ray Polarimetry Explorer (IXPE). This requires the use of a Monte Carlo code like the MONK code provided by Wenda Zhang (Zhang et al. 2019). This was also the occasion to compare the spectral output from the JED-SAD model to the output from a Monte Carlo code. The other interest of MONK is that it can directly give an estimate of the dilution factor ω by following the travel of the SAD photons in the JED.

We selected 12 observations from the constrained results obtained by Marcel et al. (2019) of the 2010-2011 outburst of GX 339-4. They are distributed evenly along the outburst. In Fig. 4.6, I show the 12 selected observations within a Hardness Intensity Diagram as well as the JED-SAD parameters constrained for these 12 observations. The JED-SAD parameters for the 12 selected observations are referenced in Tab. 4.2. The other JED-SAD parameters are: $m = 5.8$, $r_{isco} = 2$, $\omega = 0.2$, $m_s = 1.5$ and $b = 0.3$. The 12 observations contains 5 rising phase hard state, 2 high-intermediate state, 1 soft, 1 low-intermediate and 3 decaying phase hard state spectra. For all

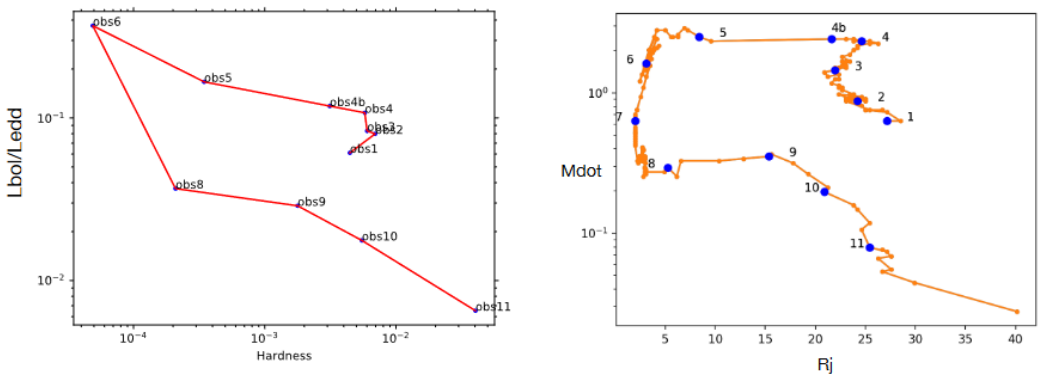

FIGURE 4.6: Observations selected among the contrained observations from the 2010-2011 GX 339-4 outburst (Marcel et al. 2019). Left: Hardness Intensity Diagram. Right: Observations in the $(r_J;\dot{m})$ plane. The orange dots connected by a line show the evolution of the parameters during the outbursts. The blue points represent the 12 selected observations.

TABLE 4.2: JED-SAD parameters of the 12 selected observations.

	1	2	3	4	4b	5	6	7	8	9	10	11
State	HH	HH	HH	HH	HH	HI	HI	S	LI	LH	LH	LH
r_J	27.1	24.2	22.0	24.6	21.6	8.39	3.11	2.0	5.23	15.3	20.9	25.4
$\dot{m}$	0.63	0.88	1.46	2.34	2.42	2.51	1.62	0.63	0.29	0.35	0.2	0.08

Notes: HH means High Hard state (rising phase hard states); HI means High-Intermediate state (hard to soft transition); S stands for Soft state; LI means Low-Intermediate state (soft to hard transition); and LH stands for Low Hard states (decaying hard states).

12 of these spectra, we computed the physical parameters everywhere within the accretion flow (density, scale height, optical depth, magnetic fields...). Wenda used these radial profiles as input of the MONK code to compute 1) the spectrum, 2) its composition and 3) the X-ray polarisation.

4.3.2 Spectral components

The first step was to compute the total spectrum and the different spectral components using both the Dyplo (computing the JED-SAD spectra) and the Monte Carlo code. In Fig. 4.7, I show as examples the spectral comparison between the two codes for two observations (2 and 4b). In all simulations the standard disk emission was in agreement at its maximum but was found larger at low energy in the MONK code compared to the JED-SAD spectra ($10^4 R_G$ in Dyplo, 10^5 in MONK). This is due to a difference in the outer disk radius used in both codes.

Synchrotron, Bremsstrahlung and their comptonization

Generally in all simulations, the synchrotron, bremsstrahlung and their comptonization components are comparable between the two codes. There are however a few difference for the bremsstrahlung and its comptonization at low energy: a bump is observed within the JED-SAD spectra around 0.1→1 keV, which is not observed within the MONK code. The MONK bremsstrahlung also seem to reach a higher energy compared to the JED-SAD code. This suggests that the comptonization of the bremsstrahlung component is stronger within the MONK code. To understand the reason, one must look at the way the two codes compute spectra. In the JED-SAD code, the spectra are computed outside-in (from large to lower radii) in a single iteration. Only the SAD photons (through the dilution factor ω) are cooling the JED rings, the photons emitted by the other JED rings are not used for comptonization to the other JED rings. As such the JED-SAD code only present local comptonization, within the same rings from which they are emitted, of the bremsstrahlung and

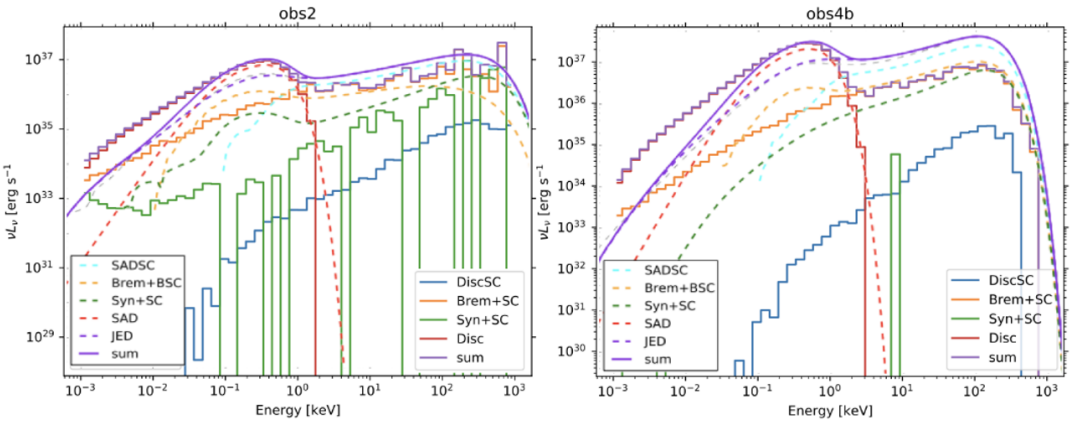

FIGURE 4.7: Examples of spectral comparison between the JED-SAD and MONK codes output for observations 2 (left) and 4b (right). The JED-SAD spectral components are plotted in dashed line. The full line show the MONK spectral components. The comptonization from seed photons from the disk is plotted in blue and noted SADSC or DiscSC. The bremsstrahlung component and its comptonization is plotted in orange and called Brem+SC. The synchrotron component ans its comptonization is plotted green and called Syn+SC. The disk component is plotted in red and the total spectrum in purple.

synchrotron components. These components are thus up-scattered up to the same electron temperature that emitted them. The MONK code propagates all the emitted photons in every JED rings and thus bremsstrahlung photons emitted from a colder, outer, JED ring can cool down the inner JED ring and be up-scattered to higher energy. Concerning the synchrotron emission: some spectra show an absence of synchrotron emission in the MONK code (see Obs 4b in Fig. 4.7 for example). This is due to the low number of photons followed in the MONK code to gain computation time.

External comptonization

In all simulations, the comptonization of seed photons coming from the SAD is significantly larger in the JED-SAD spectra compared to the MONK code. This show that the value of the dilution factor ω was overestimated in the JED-SAD code. Since the external comptonization dominates a few spectra, discrepancies were found in the total JED luminosity between both codes (see observation 4b in Fig. 4.7).

4.3.3 Estimation of ω

With MONK, we estimated the effective value of ω from the number of photons reaching each JED rings. The comparison shows that the value of ω can be overestimated by a factor of 10 within the JED. The outer JED regions, closer to the SAD, receive and are cooled down by more seed photons than the inner regions. On the other hand the inner JED regions receive less SAD photons since the radial optical depth in the JED diffuses most of them away. This suggest we need to use different a radial profile of ω in the JED.

the need of a large value $\omega \sim 0.2$ in the JED-SAD fit (see Chapter 3), compared to the effective one computed by MONK, questions the accuracy of the external comptonization in the JED-SAD model. Now, the large value of ω in the JED-SAD can also compensate approximations of the model like 1) the vertical stratification of the JED, which we assume uniform, 2) the absence of non-local photons coming from the other JED rings in the Compton process. However, concerning this last point, the temperatures of seed photons coming from the disk and of photons emitted by the other JED rings are different, possibly introducing errors within the cooling of the JED rings and the resulting comptonized components could be slightly wrong.

The idea is now to couple the Dyplo (JED-SAD) and MONK codes, preforming iterations. Dyplo computes the thermal equilibrium and geometry of the disk, than the MONK code computes the *true* value of ω. Then the JED-SAD code computes a new equilibrium and geometry with the value of ω obtained by MONK... Until the two codes converges and the *true* value of ω computed by MONK is consistent with the value used in the JED-SAD simulations. In this case, ω will no longer be a free parameter of the model. However such a procedure is time consuming as the MONK code requires a lot of photons to produce a single spectrum and an estimation of ω. This is a work in progress.

4.3.4 Prospects – Cyg-X1 and polarisation

The original goal of the Dyplo-MONK project was to compute the polarization of the JED-SAD model in preparation for the launch and first observations of the IXPE satellite. IXPE was launched on December 9th 2021 and observed the HMXrB Cyg X-1 on the 15th of May 2022. The polarization results have not yet been published.

Simultaneous observations with NuSTAR and NICER were conducted. I analyzed the spectra and fitted them with the JED-SAD model. We can then compute the physical parameters of the disk in order to compute with MONK the expected polarization of the JED-SAD model and compare to the results of IXPE.

The distance of the source has recently been re-estimated to $2.22^{+0.18}_{0.17}$ kpc (Miller-Jones et al. 2021). They also estimated the black hole mass to $21.2 \pm 2.2\ M_{\odot}$. The companion star is a blue super-giant and estimated to have a mass of 20 $M_{\odot}$ (Orosz et al. 2011). As such the system is a HMXrB and the Cyg X-1 is continuously fed through the companion star stellar winds rather than Roche lobe overflow. In the JED-SAD model, I assume a distance of 2.2 kpc and a black hole mass of 21 in agreement with Miller-Jones et al. (2021). I fix the ISCO to 2 in agreement with the extreme spin measurements generally obtained for this source (e.g. Zhao et al. 2021). I use $\omega = 0.1$, $m_s = 1.5$, $b = 0.3$ and $p = 0.01$. The total Xspec model uses two reflections components to fit the iron line (similarly to what was obtained in MAXI J1820+070, see Sec. 4.1). The relativistic reflection is connected to r_J, inner radius of the SAD; and the outer reflection is fixed at distance of 400 R_G. I use a moderate inclination of 30°. To correctly fit both the NuSTAR and NICER spectra, I had to introduce a correction to the spectral index between the two instruments.

In Fig. 4.8, I plot the results of the fit. The left panel shows the fit residuals and the right the absorbed model. The fit has a $\chi^2/dof = 1602/1313 = 1.22$. The broad and narrow iron line are a factor 10 below the JED-SAD continuum. In Tab. 4.3, I reference the best fit parameters. Similarly to MAXI J1820+070 (Sec. 4.1), the inner reflection is characterized by a strong ionization ($log(\xi) \sim 3.0$) and the outer reflection by a weak ionization ($log(\xi) \sim 0.7$). I computed the resulting JED-SAD geometry and the radial profiles of the physical parameters (density, optical depth, temperature...). The work to estimate the polarization using the MONK code is currently in progress.

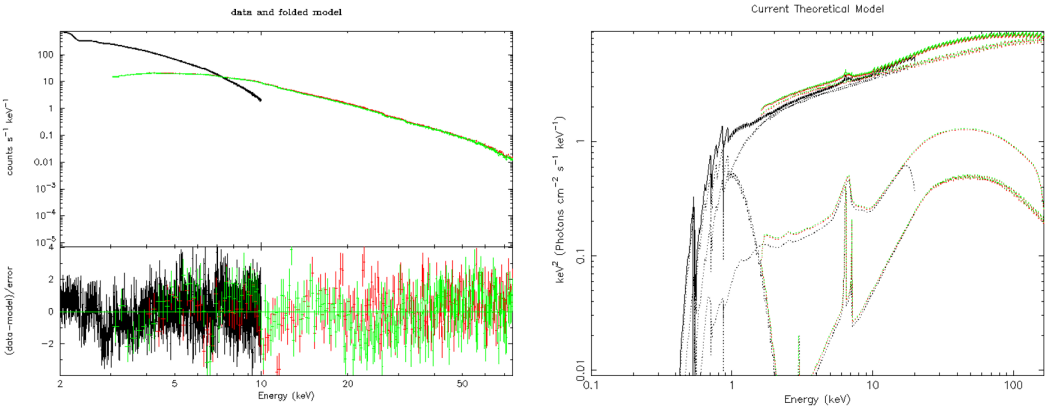

FIGURE 4.8: Fit of the NuSTAR and NICER spectra observed at the same date IXPE observed Cyg X-1. Left: residuals of the fits. Right: Total model. Similarly to MAXI J1820+070 (see Sec. 4.1), two reflections components were required to correctly fit the iron line: one broad and one narrow component.

TABLE 4.3: JED-SAD parameters of the best fit of Cyg X-1.

r_J	$\dot{m}$	$log(\xi)_1$	$R_{in,1}$	$log(\xi)_2$	$R_{in,2}$	$A(Fe)$	N_1	N_2	$\Delta(\Gamma)$
17.5	0.6	3.0	(=r_J)	0.7	(=400)	2.15	$7.0 \cdot 10^{-6}$	$5.5 \cdot 10^{-4}$	0.07

Part III

Active Galactic Nuclei

Chapter 5

The UV–X-ray correlation

Contents

5.1 Motivations and Bibliography . . . 131
5.1.1 Motivations and goals . . . 131
5.1.2 Existing models . . . 131
5.1.3 Strategy, tables and spectra . . . 133
5.2 Sample . . . 134
5.2.1 Description of the samples . . . 134
5.2.2 Black hole mass distribution . . . 135
5.2.3 X-ray spectral index Γ distribution . . . 138
5.3 Breaking down the UV–X-ray correlation . . . 139
5.3.1 The UV emission . . . 140
5.3.2 The X-ray emission . . . 142
5.4 JED-SAD UV–X-ray correlation coverage . . . 143
5.4.1 Grid r_J–$\dot{m}$ . . . 143
5.4.2 Relation r_J–$\dot{m}$ . . . 146
5.5 MC draw . . . 149
5.5.1 Drawing statistically equivalent sample . . . 150
5.5.2 Stratification . . . 153
5.5.3 Equivalent sample? . . . 155
5.5.4 Other samples . . . 158
5.6 AGN outbursts . . . 162
5.7 Discussion . . . 163
5.7.1 Radio-quiet AGN and JED-SAD . . . 163
5.7.2 Clues from spectral shape . . . 164
5.7.3 Inefficient or starved massive AGN? . . . 165
5.7.4 Toy model for an AGN outburst . . . 169
5.7.5 Conclusion and prospects . . . 169

Motivations et spectres JED-SAD

Comme présenté dans le chapitre 1, la corrélation UV-X est une corrélation non-linéaire qui relie l'émission monochromatique à 2500 Å (dans les UV) et à 2 keV (dans les X): $L_{2\,keV} \propto L_{2500\,\text{Å}}{}^{\gamma}$*, avec un indice* $\gamma = 0.586 \pm 0.061$ *(voir par exemple Lusso et al. 2020). Cette corrélation est donc intéressante car elle relie l'émission du disque standard avec l'émission de la couronne chaude. Elle permet donc de tracer comment évolue le flot d'accrétion dans les NAG. Par ailleurs elle peut constituée un excellent test pour tout modèle d'accrétion appliqué aux NAG. Mes objectifs sont ici:*

- *Tester le modèle JED-SAD et vor si nous sommes capables de reproduire la corrélation.*
- *Contraindre l'espace des paramètres qui reproduit au mieux la corrélation.*
- *Chercher à comprendre l'origine de la non-linéarité de la corrélation.*

D'autres études comme Kubota & Done (2018) et Arcodia et al. (2019) ont réalisé des études similaires avec leur modèles mais aucun n'a été capable de reproduire la corrélation dans son entièreté correctement. Quelque chose semble toujours nous échapper dans la compréhension de l'accrétion des trous noirs super-massifs.

Afin de reproduire cette corrélation, j'ai créé une table de spectres JED-SAD contenant 7 paramètres libres que je vais étudier et près de 600 000 spectres. Les détails de cette tables peuvent être vu en Tab. 5.1. On peut maintenant jeter un oeil aux spectres JED-SAD d'un NAG. Dans la Fig. 5.8, je montre 2 exemples pour 2 masses de trous noirs différentes (10^7 $M_\odot$ *en ligne continue et* 10^{10} $M_\odot$ *en pointillé). Tout les autres paramètres JED-SAD sont similaires dans cet exemple. Ici, il faut bien comprendre que chaque spectre JED-SAD va fournir un couple de valeurs (*$L_{2\,keV}$; $L_{2500\,\text{Å}}$*) qui représentera donc un point dans le plan UV-X de la Fig. 5.4. On peut voir que selon la masse du trou noir, la bosse du SAD visible à basse énergie ne piquera pas à la même énergie. Cela signifie que selon la masse, la luminosité UV ne sera pas mesuré à la même position dans la forme du spectre. Un disque chaud (faible masse m, haut taux d'accrétion* $\dot{m}$ *et faible rayon de transition* r_J*) sera mesuré dans la somme des fonctions Rayleigh-Jeans des corps noirs du disque. Un disque froid (forte masse m, bas taux d'accrétion* $\dot{m}$ *et grand rayon de transition* r_J*) sera mesuré dans la fonction de Wien du corps noir le plus chaud ou directement dans l'émission du JED. Un autre point à noter est que la forme spectrale de la couronne est identique dans les deux solutions. Cela signifie que pour expliquer une corrélation non linéaire et inférieur à 1, quelque chose doit être différent dans les paramètres du JED-SAD avec la masse.*

Echantillons

J'ai réuni 3 échantillons de NAG différents: l'échantillon historique de cette corrélation de Lusso & Risaliti (Lusso et al. 2010; Risaliti & Lusso 2015; Lusso & Risaliti 2016, 2017; Risaliti & Lusso 2019; Lusso et al. 2020). Il s'agit d'un échantillon de quasars lumineux et non-absorbés, comprenant un total de 2421 objets à faible émission radio. Quand bien même cet échantillon est caractérisé par une faible luminosité radio, je considère qu'il peut être intéressant pour le modèle JED-SAD car l'origine de l'émission radio même dans les sources à faible luminosité radio est toujours débattu. J'utilise cet échantillon comme test pour toutes mes méthodes dans ce chapitre. Le second échantillon provient de Zhu et al. (2020). Il s'agit de 729 objets à forte émission radio. Zhu et al. (2020) rapporte que cet échantillon possède possiblement un index de corrélation un peu plus élevé comparé à celui de l'échantillon de Lusso & Risaliti. Le dernier échantillon est celui de Liu et al. (2021) qui ne comprend que 47 NAG mais à plus basse luminosité. Ils présentent aussi 21 sources à luminosité supérieur à la limite d'Eddington. Liu et al. (2021) rapporte que quelle que soit le rapport d'Eddington

des sources, la corrélation semble rester la même. Dans la Fig. 5.4, je montre la dispersion des ces 3 échantillons dans le plan UV-X.

La première étape a été d'étudier ces échantillons et leurs caractéristiques. Pour cela j'ai commencé par chercher les masses de chaque trou noirs des échantillons en croisant les sources avec un échantillon de masse de NAG mesuré à partir de propriétés optiques (Shen et al. 2011). Dans la Fig. 5.5, je montre la répartition des masses de chaque échantillon ainsi que leur répartition dans le plan UV-X. On constate que les sources les plus lumineuses sont le sources les plus massives. On peut aussi regarder ces figures avec les rapport des luminosités UV et X à la luminosité d'Eddington des sources (voir Fig. 5.6). On constate cette fois ci que les sources les plus massives sont les sources présentant le plus faible rapport d'Eddington en UV et en X. Dans la Fig. 5.7, je trace la distribution de l'indice spectral dans les rayons X de l'échantillon de Lusso & Risaliti (seul échantillon pour lequel une telle étude était possible). On constate que plus la source se trouve dans la partie inférieur de la corrélation, plus son indice spectral est élevé.

Grilles de simulations JED-SAD

Dans la Fig. 5.11, je représente une grille de simulation JED-SAD dans le plan UV-X pour une valeur de masse m fixée à 10^9 $M_\odot$ et pour différentes valeurs de $\dot{m}$ et r_J. Je montre aussi comment ces paramètres évoluent à l'intérieur de cette grille. Déjà avec cette grille aec une masse unique de trou noir, on se rend compte que le modèle JED-SAD est capable de reproduire la quasi totalité des objets présents dans les échantillons réunis. Cela est montré plus clairement dans les 4 panels de la Fig. 5.12. J'ai ensuite étudié l'impact de chaque paramètre JED-SAD sur cette grille dans les Figs. C.1 (influence de l'ISCO), C.3 (influence du facteur de dilution ω), C.2 (influence de la vitesse d'accrétion m_s), C.4 (influence de la puissance dans les jets b). Nous avons donc ici la réponse à la première question que je m'étais posé: le modèle JED-SAD semble à priori capable de reproduire l'ensemble des couples UV-X observés dans la corrélation.

Méthode Monte Carlo

Afin de contraindre l'espace des paramètres capables de reproduire les échantillons, j'utilise une méthode de tirage aléatoire Monte Carlo. Je commence par tirer un très grands nombres de points (10 000) ayant comme seule condition de succès de se trouver à l'intérieur des échantillons. J'ai alors un échantillon simulé de 10 000 points couvrant la même région du plan UV-X que mon échantillon observé mais n'ayant pas la même distribution statistique dans le plan UV-X. J'attribue alors à chacun des 10 000 points une probabilités liés 1) au nombre de points de l'échantillon observés se trouvant dans le même bin de luminosité et 2) tenant compte du nombre total de point simulé se trouvant dans le même bin. Je fais alors un second tirage sans remise parmi ces 10 000 points afin d'aboutir à un échantillon simulé de 500 points présentant exactement la même distribution statistique que l'échantillon observé. Ce processus en 2 étapes est visible pour l'échantillon de Lusso & Risaliti dans les Figs. 5.17 et 5.18. Dans ces figures, je montre la distribution des spectres simulés dans l'espace des paramètres et dans le plan UV-X. Je réalise second tirage de multiple fois pour m'assurer que j'obtiens des résultats similaires.

On constate que la plupart des paramètres ne sont pas contraints (r_{isco}, ω, m_s et b). Seuls 3 paramètres semblent intéressants et contraints: la masse m, le taux d'accrétion $\dot{m}$ et le rayon de transition r_J. Pour reproduire l'échantillon de Lusso & Risaliti, les spectres JED-SAD doivent généralement avoir un rayon de transition faible entre 5 et 20. On constate aussi que plus la masse du trou noir est élevé, moins le taux d'accrétion l'est.

On peut maintenant se demander si d'autre observables sont cohérents entre l'échantillon observé de Lusso & Risaliti et mon échantillon simulé. Par exemple, la distribution des

masses dans le plan UV-X (voir Fig. 5.22. Ici, on voit que la distribution des masses dans mon échantillon simulé est un peu sur-estimé. Cette sur-estimation se fait par ailleurs principalement à basse luminosité dans le plan UV-X. Un autre observable que l'on peut regarder est l'indice spectral dans les X (voir Figs. 5.23 et 5.24). Ici on se rend compte que les indices spectraux dans mon échantillon sont globalement plus dur comparé aux données. Une possible explication à cette différence vient de la manière dont est défini l'indice spectral dans l'échantillon de Lusso & Risaliti. Celui ci dépend aussi du flux X dans la bande 0.5-2 keV. Or les NAG présentent une composante appelé l'excès X mou sous 2 keV. Cette composante n'a pas d'équivalent dans les binaires X et n'est pas présent dans le modèle JED-SAD. Ainsi les spectres JED-SAD que je simule n'ont pas cet excès X mou, qui aurait tendance à augmenter la valeur de l'indice spectral.

Avec cette méthode, j'ai identifié l'espace des paramètres capables de reproduire l'échantillon, mais cela ne signifie par pour autant qu'il s'agit du bon espace des paramètres. Pour aller plus loin, on peut essayer de faire des tirages Monte Carlo avec de plus fortes conditions d'acceptation (comme la masse ou l'indice spectral).

5.1 Motivations and Bibliography

5.1.1 Motivations and goals

As introduced in Chapter 1, the UV–X-ray non linear correlation is useful to track the evolution of the accretion flow. The work from Lusso and Risaliti and collaborators showed that this correlation remains similar ($L_{2\,keV} \propto L_{2500\,\mathring{A}}{}^{\gamma}$, index $\gamma = 0.586 \pm 0.061$, see e.g. Lusso et al. 2020) up to redshift of 4, suggesting that the accretion flow keeps similar properties over cosmic times and that the UV-X-ray SED of quasars can be used as standard candles. This correlation linking the UV emission coming from the cold disk and the X-ray emission from the hot corona of AGN is also useful to understand the process of accretion. It can serve as a powerful test for any given accretion flow model. The non-linearity shows that the more UV luminous an AGN is, the less X-ray bright it is. Does this mean that a larger power in the standard disk mean less power in the hot corona? In most models, one can identify three main characteristics that control the luminosity and power distribution of an accretion flow: the mass of the black hole, the mass accretion rate and the size of the hot X-ray corona. As such this correlation allows to extract information on the evolution of the hot corona and the "cold" accretion disk. Even though the Lusso & Risaliti sample is composed of radio-quiet AGN, I believe the JED-SAD model can still be relevant (see discussion in Sec. 5.7.1).

My goal is then to:

1. Test the JED-SAD model and see if it covers the complete UV–X-ray correlation.
2. Constrain the parameter space that best reproduces the correlation.
3. Understand the evolution of the accretion flow and the physical process explaining the non-linearity of this correlation.

5.1.2 Existing models

A few studies attempted to model the AGN accretion flow and searched for a theoretical explanation to the non linearity of the correlation. In this paragraph I will present the most recent studies i.e. Kubota & Done (2018) and Arcodia et al. (2019).

Kubota & Done (2018) developed a broadband spectral model for bright luminous quasars using three different regions, an outer cold disk, a warm comptonizing region, in the middle, producing the soft X-ray excess observed in most AGN, and a hot corona somewhere close to the black hole. The hot corona is fixed in the

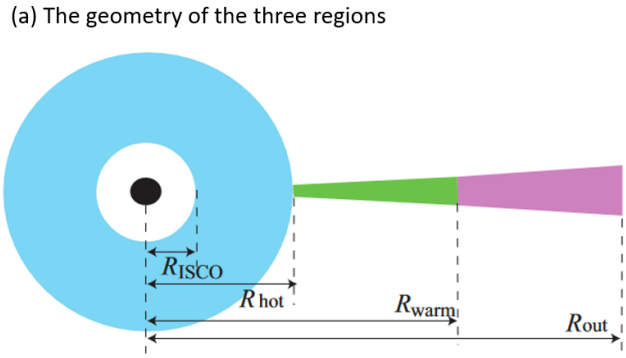

FIGURE 5.1: Adapted from Kubota & Done (2018). Geometry of the AGN-SED model from Kubota & Done (2018). The accretion flow is divided in three regions: the standard disk (pink), the warm corona (green) and the hot corona (blue). The exact geometry of the corona is not precised.

inner region of the accretion flow. They define thus four different radii, the ISCO, the outer radius of the hot corona and the outer radius of the warm corona, and the outer radius of the accretion flow (see Fig. 5.1). They tie the different regions energetically assuming a Novikov-Thorne emissivity. They fit the data from three AGN with different spectral shape akin to a hard, an intermediate and a close to soft XrB state. Even though these AGN had different mass accretion rate, the luminosity of the hot corona region is always close to 2% Eddington. By fixing the power in the corona to 2% Eddington, the geometry (the three radii) can then be recovered from the value of the mass accretion rate and black hole mass. Using this model, they partially cover the UV–X-ray correlation. They however had difficulties to reproduce large UV/X-ray ratios and the highest luminosity objects of the sample from Lusso & Risaliti (2017).

Arcodia et al. (2019) developed a disk model where the corona extends above the standard disk (see Fig. 5.2). The disk pressure can be locally dominated by the gas pressure or by the radiation pressure. Assuming a general formula: $P_{mag} \propto P_{gas}^{\mu} P_{tot}^{1-\mu}$ with the power-law index μ taking values between 0 and 1 depending on the alternative viscosity prescription, they can play with different disk-corona energetic couplings. In the more luminous inner regions, where the radiation pressure dominates, the alternative viscosity decreases the power in the corona and the X-ray output decreases. Varying the mass accretion rate increases the size of this radiation pressure dominated region, decreasing the spectral output of colder regions and thus decreasing the slope of the UV–X-ray correlation. They study the impact of the parameters μ on the slope in the UV–X-ray correlation when the mass accretion rate increase. They found that the slope of the UV–X-ray correlation is best reproduced with a viscosity prescription $\mu \sim 0.5$.

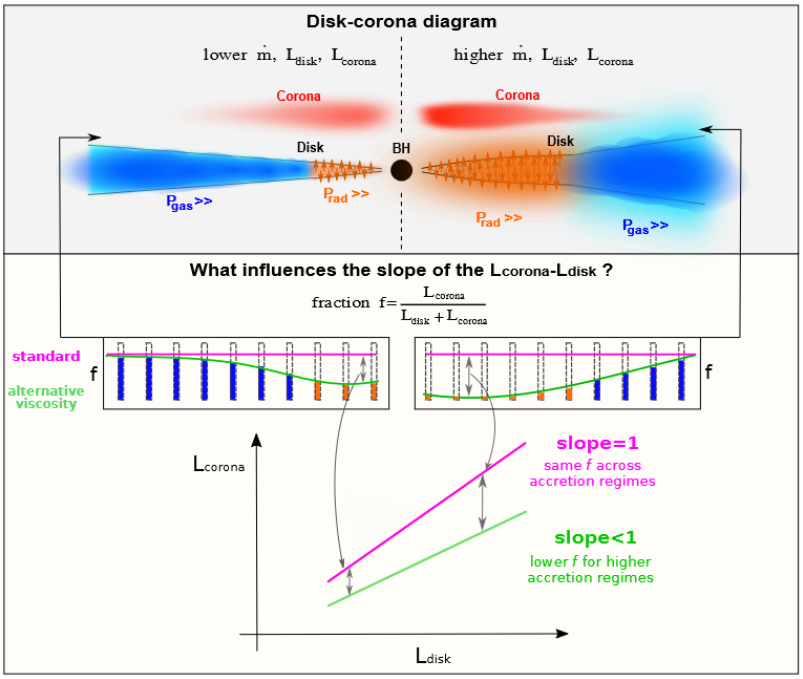

FIGURE 5.2: From Arcodia et al. (2019). General idea behind the disk-corona coupling model from Arcodia et al. (2019). Left: at low mass accretion rate, the radiative pressure dominated region is small and only the innermost region are affected by the alternative viscosity, decreasing the corona output. Right: at higher mass accretion rate, the radiative pressure dominated region is much larger and thus a larger region is affected by the alternative viscosity, decreasing the X-ray output of a larger region.

5.1.3 Strategy, tables and spectra

To study the correlation, I collected multiple samples (presented in Sec. 5.2) and confront them to the JED-SAD model. To compute the large number of spectra required for the different tests during this study, I computed a large JED-SAD table of AGN SED, containing more than 600k JED-SAD spectra. The parameters and their range of variations of this table are presented in Tab. 5.1. As we have explained in Chapter 2, the magnetization μ and the ejection index p have a negligible spectral impact (Marcel et al. 2018a) (see also Fig. 2.15). As such, they can not be constrained and I fix them to $\mu = 0.5$ and $p = 0.01$. To simulate spectra, I read the tables in Xspec with the following model SAD + JED. I then extract the values of the monochromatic luminosity at 2500 Å and at 2 keV for each simulated AGN SED. Thus each JED-SAD set of parameter produce a spectrum and a corresponding point in the UV–X-ray plane.

Weak effect of the soft excess

The JED-SAD model does not present any component to reproduce the presence of the soft X-ray excess. Instead, to take into account the effect of a warm corona comptonizing the cold disk photons, I use the Xspec model SIMPLCUT (e.g. Steiner et al. 2017). This multiplicative Xspec model comptonize the spectral component to which it is applied. In this case, it is applied to the standard accretion disk table: SIMPLCUT × SAD + JED. There are 4 parameters in SIMPLCUT: the power law index Γ of the comptonized emission, the electron temperature kT_e of the warm corona which entails a high energy cutoff for the comptonized emission, the reflection parameter that I set to 0, and the fraction of photons that will be scattered fsc. Typical values observed in AGN are: $\Gamma \sim 2.6$ and $kT_e \sim 0.1$–1keV. In Fig. 5.3, I plot two JED-SAD parameter sets for a black hole mass $m = 10^9$. The solid lines represent the JED-SAD model without comptonization effects and the dashed lines show the JED - comptonized SAD. Part of the photons emitted by the SAD are Compton up-scattered to higher energies, producing a power-law shape between the peak of the SAD and the cutoff of the warm corona. This can impact the monochromatic luminosity at 2500 Å as long as the standard accretion disk temperature is low ($kT_e^{disk} \leqslant 5$eV). The warm corona will also have a small impact on the 2 keV luminosity for low value of the power-lax index ($\Gamma \leqslant 2.4$) and high value of the electronic temperature ($kT_e \geqslant 1$), but these range of parameter is not usually observed.

TABLE 5.1: Parameters of the AGN JED-SAD table.

Parameters	Lower limit	Upper limit	Bins$^{(a)}$	Binning$^{(b)}$
$\mu^{(c)}$	0.5	0.5	1	
m	10^7	10^{10}	4	log
r_J	2	300	30	log
$\dot{m}$	10^{-2}	10	31	log
r_{ISCO}	2	6	3	lin
ω	0.01	0.2	3	log
m_s	0.5	3.0	6	lin
b	0.1	0.7	3	lin
p$^{(c)}$	0.01	0.01	1	

Notes: $^{(a)}$ Number of bins.
$^{(b)}$ Method of binning, *log*: logarithmic binning ; *lin*: linear binning.
$^{(c)}$ Both parameters are fixed for this study.

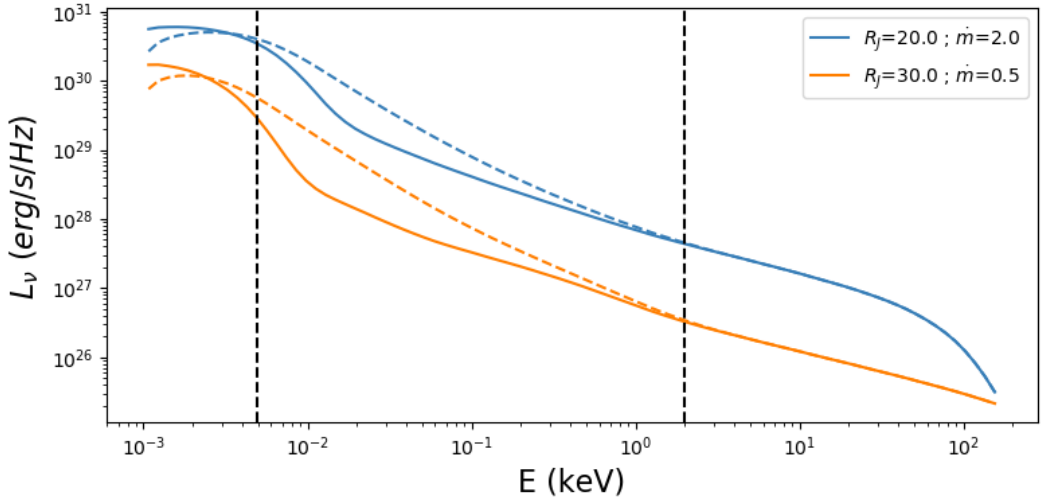

FIGURE 5.3: Example of AGN spectra from the JED-SAD tables (in L_ν). Both spectra assume a 10^9 solar mass black hole. In blue, r_J=20 and $\dot{m}$=2 and in orange, r_J=30 and $\dot{m}$=0.5. The other JED-SAD parameters are fixed: r_{isco}=2, ω=0.1, m_s=1.5, b=0.3. The solid line represent the JED-SAD model without warm comptonization. The dashed line represent the same model but with the warm comptonization model SIMPLCUT applied to the SAD emission. The warm corona parameters are fixed to $\Gamma = 2.6$, $kT_e = 0.5$ and $fsc = 0.75$. The dashed vertical line marks the two energies used for the UV–X-ray correlation (2500 Å in the UV and 2 keV in the X-ray).

From now on, unless said explicitly in the text, I do not use any warm comptonization component.

5.2 Sample

5.2.1 Description of the samples

Lusso & Risaliti

The Lusso & Risaliti sample is the result of an extensive effort to compile an as unbiased as possible AGN sample to study the UV–X-ray correlation with the redshift (e.g. Lusso et al. 2010; Risaliti & Lusso 2015; Lusso & Risaliti 2016, 2017; Risaliti & Lusso 2019; Lusso et al. 2020) and use this correlation to show that quasars can be used as standard candle for cosmology. I will focus on the latest sample (Lusso et al. 2020). The sample consists of 2421 radio-quiet, unabsorbed, bright quasars. They report a correlation with index $\gamma = 0.586 \pm 0.061$. I use this sample as a test run for all procedures of this study. In fig. 5.4, I plot the distribution of the sample in blue. For simplification, I will refer to this sample as the L&R sample from now on.

Zhu et al.

In Zhu et al. (2020), they collected 729 radio loud quasars in order to compare the disk-corona connection obtained for a radio loud population with the radio-quiet case observed in the L&R sample. In fig. 5.4, I plot the distribution of the sample in green. As reported in Zhu et al. (2020), the correlation for radio loud quasars is harder compared to the L&R sample ($\gamma = 0.69 \pm 0.03$). I will refer to this sample as the Zhu+ sample from now on.

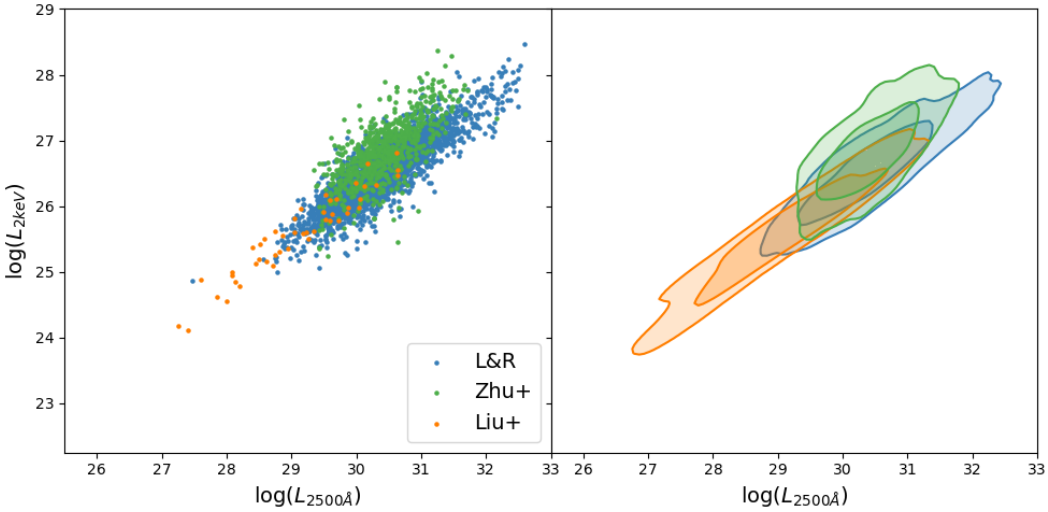

FIGURE 5.4: The three collected samples. **Left**: scatter plot of each sample in the UV–X-ray plane. **Right**: 95% and 68% percentile contour for each collected sample in the UV–X-ray plane. Data in blue comes from the work of L&R sample (Lusso et al. 2020), in green from the Zhu+ sample (Zhu et al. 2020) and in orange from the Liu+ sample (Liu et al. 2021).

Liu et al.

Liu et al. (2021) collected 47 AGN with different accretion properties. 21 of them present a super Eddington accretion regime. 26 of them present a sub Eddington regime. They report no difference between these two populations. In fig. 5.4, I plot the distribution of the sample in orange. This sample reaches 2 orders of magnitude lower compared to the L&R sample. I will refer to this sample as the Liu+ sample from now on.

5.2.2 Black hole mass distribution

Among the three samples, only the Liu+ sample contains information on the black hole mass, coming from reverberation mapping (Du & Wang 2019). To obtain the information on the black hole masses for the other samples, I cross-referenced the samples with the AGN catalogue from Shen et al. (2011) using the cross-match service provided by CDS, Strasbourg (Boch et al. 2012; Pineau et al. 2020). This catalogue contains spectral information including continuum and emission line measurements around the Hα, Hβ, Mg II, and C IV, for 105 783 quasars from the Sloan Digital Sky Survey Data Release 7 (SDSS-DR7, Schneider et al. 2010). They compute the black hole masses based on the line measurements using various calibrations (Vestergaard & Peterson 2006). I was able to recover the black hole masses for 1271 quasars of the L&R (1271/2421) and 420 for the Zhu+ sample (420/729).

In Fig. 5.5, I plot the distribution of the black hole masses for each samples. The L&R and Zhu+ samples present a similar black hole mass distribution, however the Liu+ sample contains less massive black hole in comparison. Furthermore, the distribution of the masses in the UV–X-ray plane show a stratification of the correlation with the mass: generally the more massive black holes are the more luminous ones. There are multiple interpretation to be extracted: 1) The black hole mass distribution

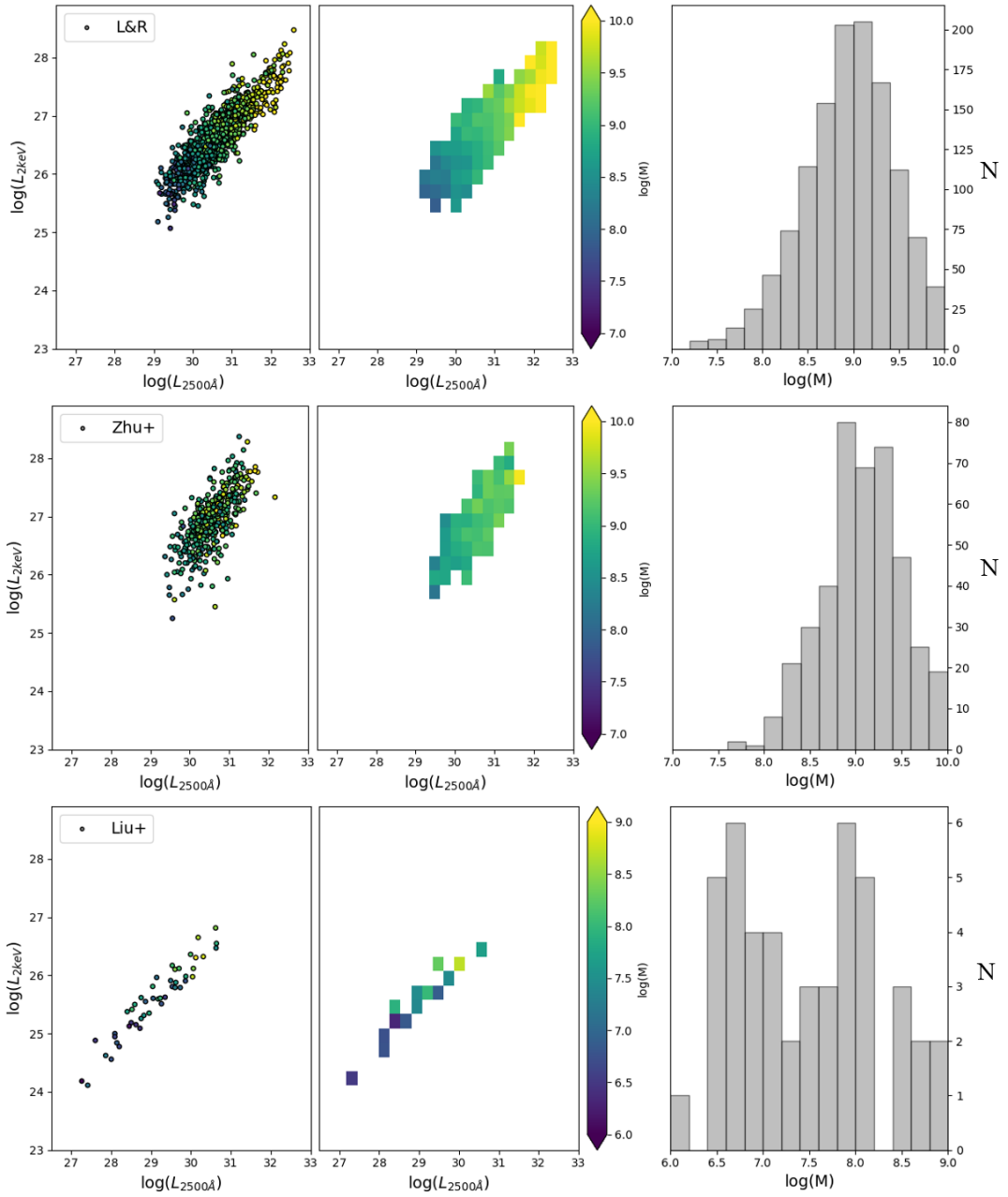

FIGURE 5.5: The black hole masses distribution within the UV-X-ray correlation for the three collected samples. **From top to bottom**: the L&R sample (Lusso et al. 2020), the Zhu+ sample (Zhu et al. 2020) and the Liu+ sample (Liu et al. 2021). **Left**: scatter plot of the black hole masses for each sample in the UV–X-ray plane. **Middle**: Averaged masses along the UV–X-ray correlation for each sample. Both of these panels use the same color scheme. **Right**: Histogram distribution of the black hole masses for each sample.

with redshift suggest that more massive black hole are distant sources and more distant black holes can only be observed if they are brighter. 2) The Eddington luminosity limit and thus the Eddington mass accretion rate grows with the black hole mass; as such, higher black hole masses can mean higher accretion rate (in physical units not necessarily in Eddington units), and thus the higher black hole masses can be more luminous compared to lower black hole masses.

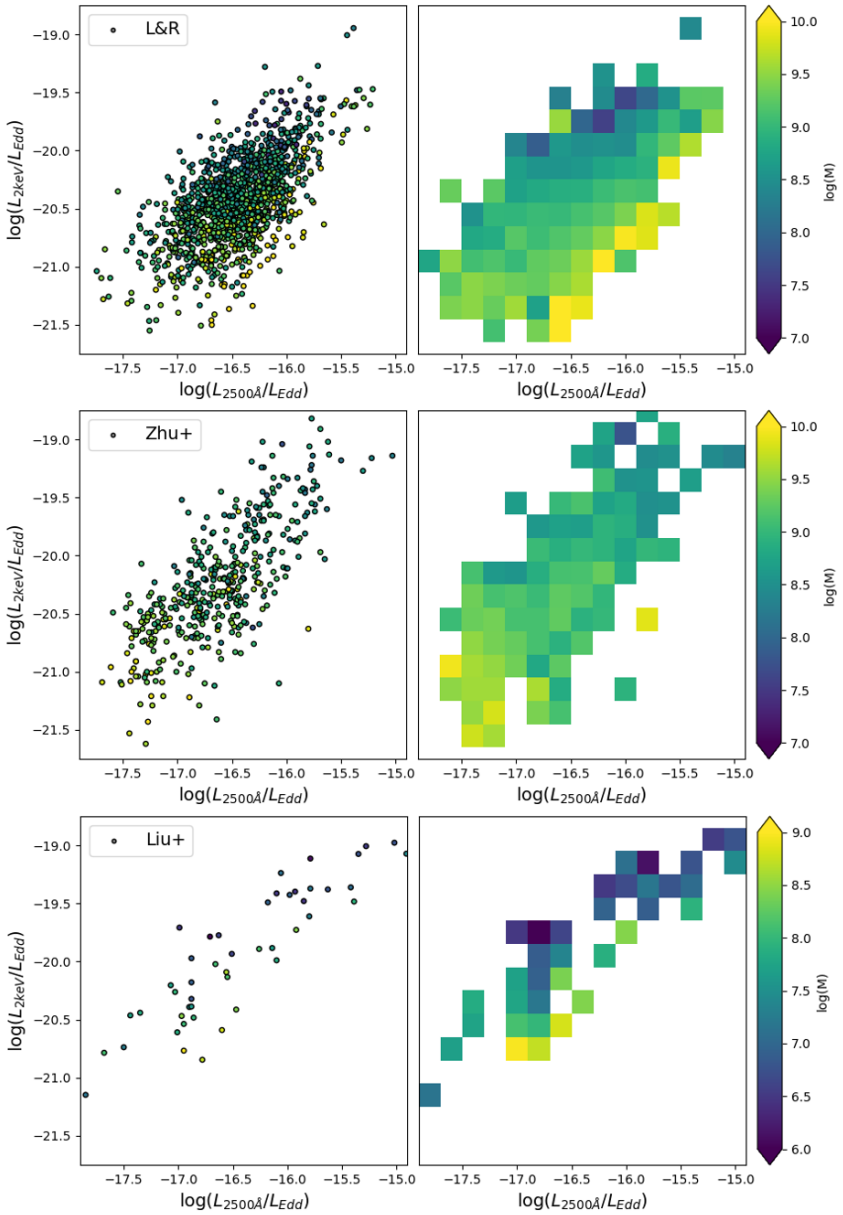

FIGURE 5.6: The Eddington ratio UV-X-ray correlation for the three collected samples. **From top to bottom**: the L&R sample (Lusso et al. 2020), the Zhu+ sample (Zhu et al. 2020) and the Liu+ sample (Liu et al. 2021). **Left**: scatter plot of the black hole masses for each sample in the UV–X-ray plane. **Right**: Locally averaged masses along the UV–X-ray correlation for each samples. Both of these panels use the same color scheme.

In Fig. 5.6, I plot the UV–X-ray correlation using the Eddington ratios instead of the luminosity ($L_{2500\text{Å}} \rightarrow \lambda_{Edd}(2500\text{Å}) = L_{2500\text{Å}}/L_{Edd}$ and $L_{2\,\text{keV}} \rightarrow \lambda_{Edd}(2\,\text{keV}) = L_{2\,\text{keV}}/L_{Edd}$) to get an idea of the accretion regime of each sample. Each points is colored using the black hole masses. Two information can be recovered from Fig. 5.6: 1) the index of the UV–X-ray correlation ($\gamma \sim 0.6$) predicts that more luminous and thus certainly more massive AGN are less X-ray bright compared to lower masses and thus will have a lower X-ray Eddington ratio $\lambda_{Edd}(2keV)$. This is indeed observed as higher black hole masses are mostly on the lower edge of the distribution, especially for the L&R and Liu+ samples. 2) Higher black hole masses appear also mostly present on the lower left part of the correlation, especially visible for the

Zhu+ and Liu+ samples, meaning that they would have both a lower UV and X-ray Eddington ratio. This suggest that higher black hole mass could generally have lower mass accretion rate (in Eddington units) in comparison to the lower black hole masses.

5.2.3 X-ray spectral index Γ distribution

In Risaliti & Lusso (2019), they present a method to estimate the X-ray spectral index for each AGN of their samples. Cross-referencing the observation they use in their sample with the 4XMM DR9 (Webb et al. 2020), they obtain the fluxes in various X-ray bands. They notably use the soft X-ray (0.5-2 keV) and hard (2-12 keV) X-ray bands. All band are corrected for the galactic absorption and highly absorbed sources have already been screened from the sample. They notice that when fitting a simulated spectrum composed of single power-law ($\Gamma = 1.42$, Lusso et al. 2020) within the soft X-ray band, with a power-law parameterized as $f(E) = f(E_0)(E/E_0)^{\Gamma}$ with a fixed value E_0, the error contours on the measured Γ and normalization $f(E_0)$ are generally elongated due to non-zero covariance between the two parameters. However, a pivot energy $E_0 = E_S$ exist, for which the error on the parameters are no longer elongated. This value divides the X-ray band in two regions of similar statistical weight (see their supplementary figure 10, Risaliti & Lusso 2019). This energy is interesting as it allows the measured monochromatic flux $f(E_S)$ to be independent of the spectral index used to compute the soft X-ray band flux (zero covariance) and minimizes the error on the monochromatic flux $f(E_S)$. The same procedure can be repeated for the hard X-ray band to measure a monochromatic flux $f(E_H)$. Thus they obtain two points along the X-ray spectrum: [$E_S = 1.$ keV ; $f(E_S)$] and [$E_H = 3.45$ keV ; $f(E_H)$] for each AGN of their sample Risaliti & Lusso (2019); Lusso et al. (2020). They then derive the 2 keV luminosity (in the rest frame) and an estimation of the X-ray spectral index.

It should be noted that the spectral index measured with this method depends on the soft X-ray band flux between (0.5-2 keV). This band is know to be impacted by the soft X-ray excess component. And thus the measured spectral index must

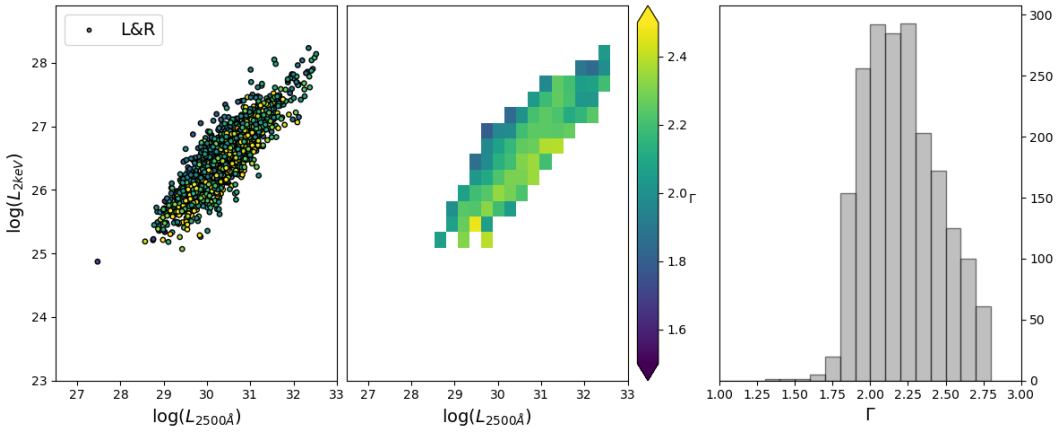

FIGURE 5.7: X-ray spectral index Γ distribution in the UV-X-ray correlation for the L&R sample (Lusso et al. 2020). **Left**: scatter plot of the X-ray spectral index Γ for the sample in the UV–X-ray plane. **Middle**: Averaged X-ray spectral index Γ along the UV–X-ray correlation for the sample. Both of these panels use the same color scheme. **Right**: Histogram distribution of the X-ray spectral index Γ for the sample.

not be interpreted as the hard X-ray power-law index usually presented in XrB spectra. In fact due to the soft X-ray excess, the measured X-ray index should be softer compared to the typical 2-10 keV hard X-ray power law.

In Fig. 5.7, I plot the distribution of the X-ray spectral index Γ for the L&R sample. I use the value reported within their catalogue. The X-ray spectral index ranges from ~ 1.8 to ~ 2.8. They show a stratification within the UV-X-ray correlation. The sources with a high UV/X-ray ratio (lower part of the dispersion) show in average softer X-ray spectra. I tried to replicate the same methodology for the other two samples. However, when cross-referencing the catalogues with the 4XMM-DR11 (Webb et al. 2022) with the CDS cross-match service, one should consider the same observation as the one used to extract the UV and X-ray luminosities. The X-ray photon index may differ from one observation to another due to possible X-ray variability. For XMM, unique observations in the 4XMM catalogue are flagged in the DETID column, so one should cross-match by using this number. Unfortunately the Zhu+ and Liu+ catalogues do not provide enough information to extract the exact observation and thus only averaged X-ray spectral index over multiple observations can be recovered.

5.3 Breaking down the UV–X-ray correlation

Before trying to reproduce the UV–X-ray correlation, I believe it is important to understand from where the UV and X-ray luminosities are extracted, and what will impact the values we will obtain in our simulated spectra.

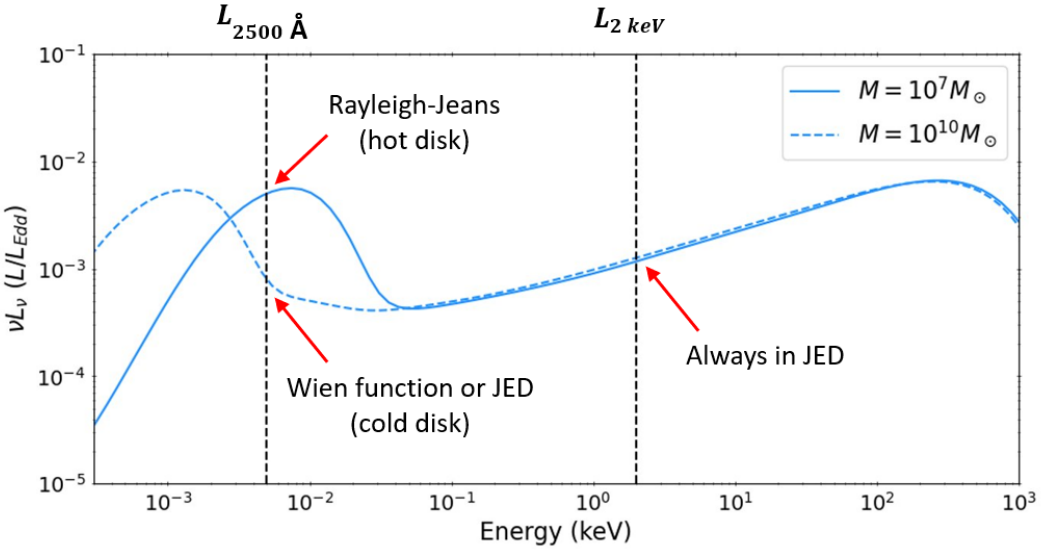

FIGURE 5.8: The UV and X-ray luminosities extracted from two different spectra. In solid line, a black hole mass $m = 10^7$ and in dashed line, a black hole mass $m = 10^{10}$. The other parameter are fixed to $r_J = 30$; $\dot{m} = 0.5$; $r_{isco} = 2$; $\omega = 0.1$; $m_s = 1.5$; $b = 0.3$; $p = 0.01$. The dashed vertical line marks the 2500 Å and 2 keV energy at which are extracted the UV and X-ray luminosity for the correlation.

5.3.1 The UV emission

Origin

In Fig. 5.8, I plot the simulated JED-SAD spectra for two different black hole masses $m = 10^7$ and $m = 10^{10}$ respectively in solid and dashed line. All other parameters are fixed to $r_J = 30$; $\dot{m} = 0.5$; $r_{isco} = 2$; $\omega = 0.1$; $m_s = 1.5$; $b = 0.3$; $p = 0.01$. Due to the different black hole mass, the standard disk temperature is different and the SAD spectrum peaks at a different energy. As such, the UV luminosity can be measured at different places within the spectra depending on the standard disk temperature:

- When the disk is hot enough ($T_{BB} \gtrsim 4.96$ eV, which is the equivalent energy to 2500 Å), the UV luminosity is measured within the sum of the Rayleigh-Jeans of the different black-body emitted by the standard disk (see the solid line in Fig. 5.8 for instance).
- When the disk is a little bit colder, the disk peaks at a lower energy and the UV luminosity will be measured within the high energy cutoff of the Wien function (see the dashed line in Fig. 5.8 for instance).
- Finally, if the standard disk is even colder, it is possible that the JED emission surpasses the SAD emission at 2500 Å.

When the UV luminosity is dominated by the optically thick emission of the standard disk, its value is analytical. However, when the UV luminosity is dominated by the optically thin JED emission, one need to solve the complete thermal equilibrium. One can approach the standard disk maximum temperature using the following reasoning: Assuming an optically thick radiation from the standard disk, the luminosity emitted by a ring $[R_{in}, R_{out}]$ of the SAD can be written as:

$$L = \sigma T^4 \, ds = \frac{1}{2} GM\dot{M} \left(\frac{1}{R_{in}} - \frac{1}{R_{out}} \right) \tag{5.1}$$

$$\sigma T^4 \, 4\pi RR \approx \frac{1}{2} GM\dot{M} \frac{\Delta R}{R^2} \tag{5.2}$$

$$\sigma T^4 \approx \frac{1}{8\pi} \frac{GM}{c^2} \frac{\dot{M}c^2}{R^3} \tag{5.3}$$

$$\sigma T^4 \approx \frac{1}{8\pi} \frac{\dot{M}c^2}{r^3 R_G^2} \tag{5.4}$$

$$\sigma T^4 \approx \frac{1}{8\pi} \frac{\dot{m}}{r^3} \frac{L_{Edd}}{R_G^2} \tag{5.5}$$

Where we used the definitions of $R_G = GM/c^2$, $r = R/R_G$ and $\dot{m} = \dot{M}/\dot{M}_{Edd} = \dot{M}/(L_{Edd}/c^2)$. We thus obtain:

$$T \approx \left(\frac{1}{8\pi\sigma} \frac{\dot{m}}{r^3} \frac{L_{Edd}}{R_G^2} \right)^{1/4} \tag{5.6}$$

The temperature of a ring is thus depending on three main parameters: the mass accretion rate, the radius of the ring and the black hole mass (through L_{Edd}/R_G^2). And in fact we have: $T \propto \dot{m}^{1/4} \, r^{-3/4} \, m^{-1/4}$. The maximum temperature T_{BB} of the SAD is reached near the inner region of the SAD, at $r \sim r_J$ (not exactly at r_J due to the no-torque condition). Thus the disk will be hotter for large value of the mass accretion rate and smaller value of the transition radius and black hole mass.

JED-SAD map

In Fig. 5.9, I plot the evolution of the UV luminosity measured at 2500 Å in the (r_J; $\dot{m}$) plane for different black hole masses. The arrows represent the local derivative of the UV luminosity, showing the UV luminosity undergoes the largest evolution. As the scale for the arrow is the same in each panels, we can compare them. The red solid line corresponds to the case when the disk maximum temperature corresponds to 2500 Å (4.96 eV). Three different regimes can be observed: 1) Below the red solid line, the arrows are quite small. The UV luminosity measured at 2500 Å can be impacted by two factors: the vertical translation due to the evolution of the total luminosity of the disk, and the horizontal translation of the spectrum due to the evolution of the disk maximum temperature. In this first region the disk is peaking at a higher energy than 2500 Å. This means the 2500 Å monochromatic luminosity is measured within the power-law resulting from the sum the Rayleigh-Jeans profile emitted. This power-law has a spectral index close to 1/3 ($L_\nu \propto \nu^{1/3}$, Shakura & Sunyaev 1973). As such, the evolution of the UV luminosity due to the horizontal translation can be written as $L_{2500\text{Å}} \propto (\dot{m}^{1/4}\, r_J^{-3/4}\, m^{-1/4})^{1/3}$, whereas the evolution of the UV luminosity due to the vertical translation can be seen as $L_{2500\text{Å}} \propto m\dot{m}/r_J$. And thus the total variation is written as $L_{2500\text{Å}} \propto \dot{m}^{1+1/12} r_J^{-1-1/4} m^{1-1/12}$. 2) Above the red solid line, there is a region where the length of the arrow increases and the variation with r_J is also important. This is explained as the 2500Å energy mark is

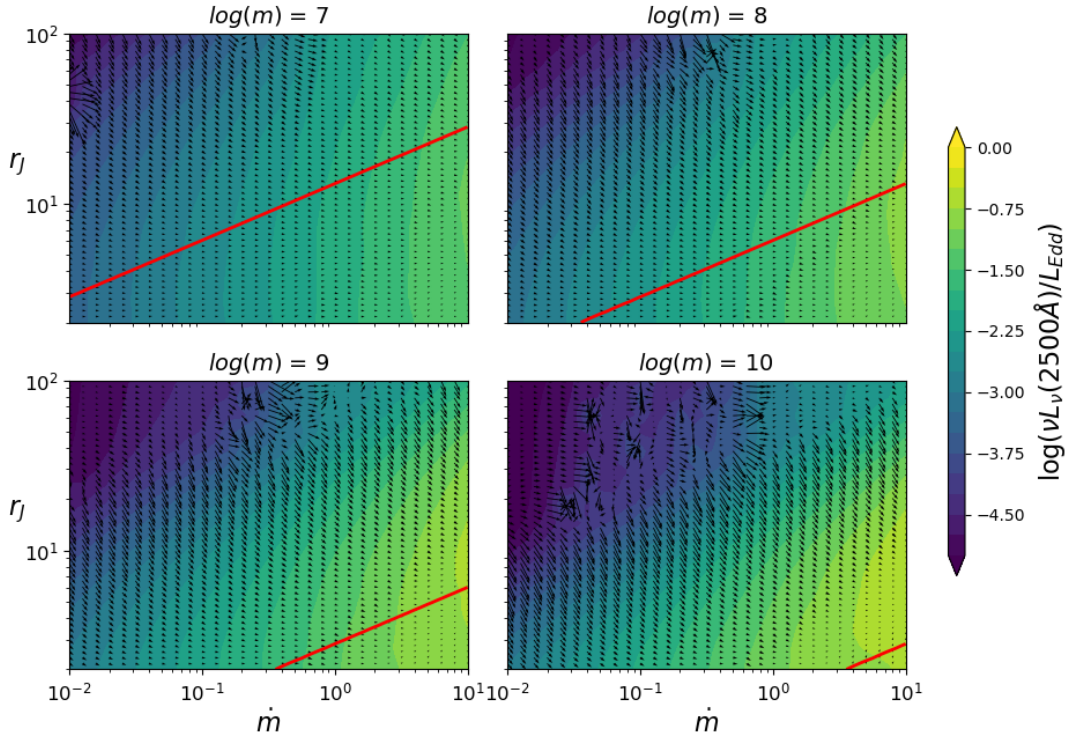

FIGURE 5.9: Map of the UV emission (in $\nu L\nu / L_{Edd}$) in the JED-SAD parameter space (r_J; $\dot{m}$) for four different values of the black hole mass. The other parameter are fixed to $r_{isco} = 2$; $\omega = 0.1$; $m_s = 1.5$; $b = 0.3$; $p = 0.01$. The arrow represent the local derivative of the UV luminosity and use the same scaling factor for comparison between the different plots. The red solid line shows the equality between the disk maximum temperature and the energy at which is measured the UV luminosity (2500 Å $\Leftrightarrow$ 4.96 eV).

now in the cut-off of the Wien law, resulting in an important dependency with the disk temperature and thus with its main dependency: r_J. 3) Finally there is a regime mostly visible in the upper left corner for high masses ($m = 10^9$ and $m = 10^{10}$). There, the mass accretion rate is low, the transition radius is large and the black hole mass large, thus the disk is quite cold. The UV luminosity is measured directly within the optically thin JED emission. Different Compton orders due to the low optical depth can create bump in the spectra, changing the arrows' direction locally.

Soft excess

As mentioned before, the JED-SAD model does not include any component reproducing the soft X-ray excess. Assuming a warm comptonization model, from the examples of Fig. 5.3, the addition of Simplcut to comptonize the SAD emission create a power-law linking the peak of the UV emission and the X-ray. Its addition will thus negate the existence of the two last regimes presented above. Instead, the UV emission will either be measured within the sum of the Rayleigh-Jeans profile when the disk is hot enough or within the warm comptonized power-law (index ~ 2.5). As such the UV luminosity will be increased for cold disk and its variation within the parameter space will become more steady.

5.3.2 The X-ray emission

Origin

The X-ray luminosity will always be measured within the JED emission (see Fig. 5.8), which can sometime be optically thin. As such its evolution with r_J and $\dot{m}$ is not trivial and hard to estimate analytically. We have to solve the complete radiative equilibrium to get it. This requires the use of the JED tables.

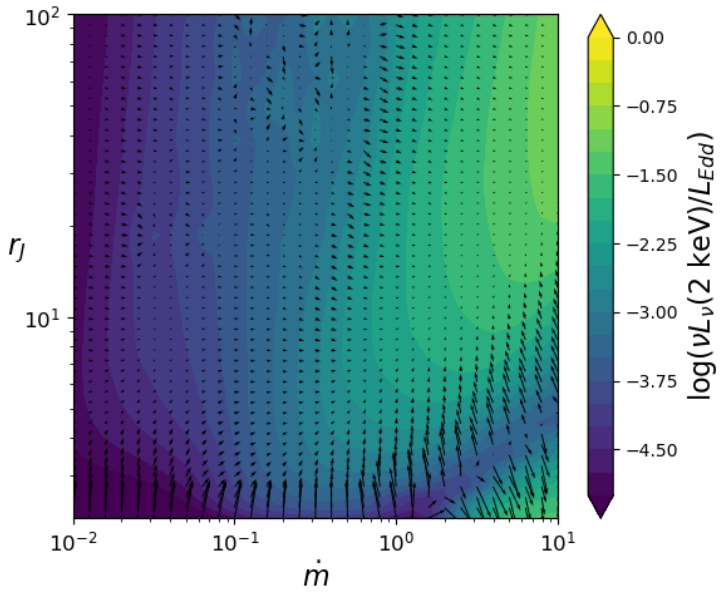

FIGURE 5.10: Map of the X-ray emission (in $\nu L\nu / L_{Edd}$) in the JED-SAD parameter space (r_J; $\dot{m}$). The other parameter are fixed to $r_{isco} = 2$; $\omega = 0.1$; $m_s = 1.5$; $b = 0.3$; $p = 0.01$. The arrow represent the local derivative of the UV luminosity and use the same scaling factor for comparison between the different plots.

Furthermore, contrarily to the SAD, the JED emission is not impacted by only three parameters, instead we have to look at all the JED-SAD parameters (r_J; $\dot{m}$; r_{isco}; ω; m_s and b). I excluded the mass from the list of parameters as we have seen that the JED emission is almost the same for all black hole masses (see Fig. 2.7).

JED-SAD map

In Fig. 5.10, I plot the evolution of the monochromatic X-ray luminosity at 2 keV. Once again the arrow represent the local derivative of L_X with the parameters. What can be noted is the large arrows visible at $r_J \gtrsim r_{isco}$. There the JED radial extension is very small and small variation of r_J increases the the X-ray luminosity by a large margin by a large amount as the 2 keV energy is in the high energy cutoff of the JED emission. Another region near $\dot{m} \sim 0.5 \rightarrow 1$ present strong variations of the X-ray luminosity. It can be related to the increase of the JED radiative properties as it transits from the READ to the RERD regime (see discussion in Sec. 2.2.2). Interestingly, the transition radius does not seem to have much impact on the monochromatic flux at 2 keV anywhere else in the parameter space.

5.4 JED-SAD UV–X-ray correlation coverage

In this paragraph, I produce the first test to see what portion of the UV–X-ray plane the JED-SAD model is able to cover.

5.4.1 Grid r_J–$\dot{m}$

As a first step, I produce spectra along a grid of the two main parameters r_J and $\dot{m}$ for different values of the black hole mass. This grid is build using a logarithmic

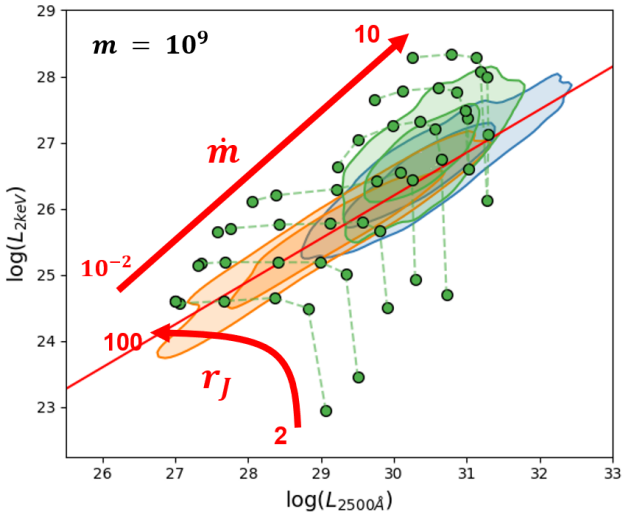

FIGURE 5.11: Grid of JED-SAD spectra in the UV–X-ray plane. Values of r_J go from $2 \rightarrow 100$ (2.1, 4, 8, 15, 27, 52, 100) and of $\dot{m}$ from $10^{-2} \rightarrow 10$ (0.02, 0.08, 0.2, 0.8, 2, 8). All other parameters are fixed to: $m = 10^9$; $r_{isco} = 2$; $\omega = 0.1$; $m_s = 1.5$; $b = 0.3$; $p = 0.01$. The points connected with a dashed line have the same mass accretion rate. In the background: 95% and 68% percentile contour for each sample. In blue from the L&R sample (Lusso et al. 2020), in green from the Zhu+ sample (Zhu et al. 2020) and in orange from the Liu+ sample (Liu et al. 2021).

scale with r_J varying from the value of the ISCO to 100 and of $\dot{m}$ from 10^{-2} to 10. Let us start with one example using the JED-SAD parameters: $m = 10^9$; $r_{isco} = 2$; $\omega = 0.1$; $m_s = 1.5$; $b = 0.3$; $p = 0.01$. In Fig. 5.11, I plot the grid of $L_{2500} - -L_X$ from the simulated AGN JED-SAD spectra over the 95 and 68 percentiles contours of the different sample discussed in Sec. 5.2. The points connected by a dashed line use the same value of the mass accretion rate (equi-$\dot{m}$ track). I mark the general evolution with r_J and $\dot{m}$ using red arrows. From the bottom left to the top right, the mass accretion increases, increasing both the UV and X-ray luminosities. From the bottom right to the left of each equi-$\dot{m}$ track, the transition radius increases from the ISCO (2 here) to 100. Indeed, the smaller the transition radius is and the larger the energy released in the standard disk becomes, increasing the UV luminosity.

There are multiple point of interest that appear in most of these plot. I comment and connect them to different theoretical aspects already presented below:

- Left part of the equi-$\dot{m}$ track with low mass accretion rate. In this region, multiple JED-SAD simulations are almost overlapping even though the transition radius evolves from 30 to 100. There is almost no variation of both the UV and X-ray luminosities with r_J. For the UV, the disk is quite cold with these parameters and the UV emission is directly measured in the JED region (see Fig. 5.9). For the X-ray, except for a few regions of the parameter space, r_J does not impact the monochromatic flux at 2 keV by a large margin (see Fig. 5.10).

- Bottom right part of each equi-$\dot{m}$ track. In these region, small variation of the transition radius (2.1 to 4 between the two rightmost points) result in a large increase of the X-ray luminosity. This is explained by the fact that the JED emission vary very significantly around 2 keV between this two values due to the high energy cut-off crossing the 2 keV energy.

- In between these two regions, the UV luminosity increases steadily with a decreasing r_J as the high energy cutoff of the Wien function increases and go through the 2500 Å wavelength until it reaches the Rayleigh-Jeans part of the spectrum. There the UV luminosity does not increase much anymore. This is visible in the top right of the figure: for small r_J and for the highest $\dot{m}$ equi-$\dot{m}$ tracks.

- Around $\dot{m} \sim 0.5 - 1$ the JED transits from the READ to RERD regime (see Sec. 2.2.2), increasing the spectral output of the JED region. This is visible between the 4th and 5th equi-$\dot{m}$ tracks starting from the bottom.

- The 6th and 7th equi-$\dot{m}$ tracks have already reached the slim regime. At such high mass accretion rate, the density and optical depth of the JED are high and thus the JED is colder and softer. In fact the high energy cutoff reaches the 2 keV mark for larger values of r_J compared to low mass accretion rate simulations.

With this unique grid using a single value of the black hole mass, we see that the JED-SAD simulations are already able to cover almost all of the UV–X-ray samples. Furthermore, by plotting the straight line of the correlation, one can imagine extracting a relation between r_J and $\dot{m}$ that would reproduce the non linearity of the correlation.

In Fig. 5.12, I plot the same grid (r_J;$\dot{m}$) but for all the black hole masses. Assuming different black hole masses will allow to cover all three samples. We can however notice a trend between the different masses. For higher mass the grid shifts slightly

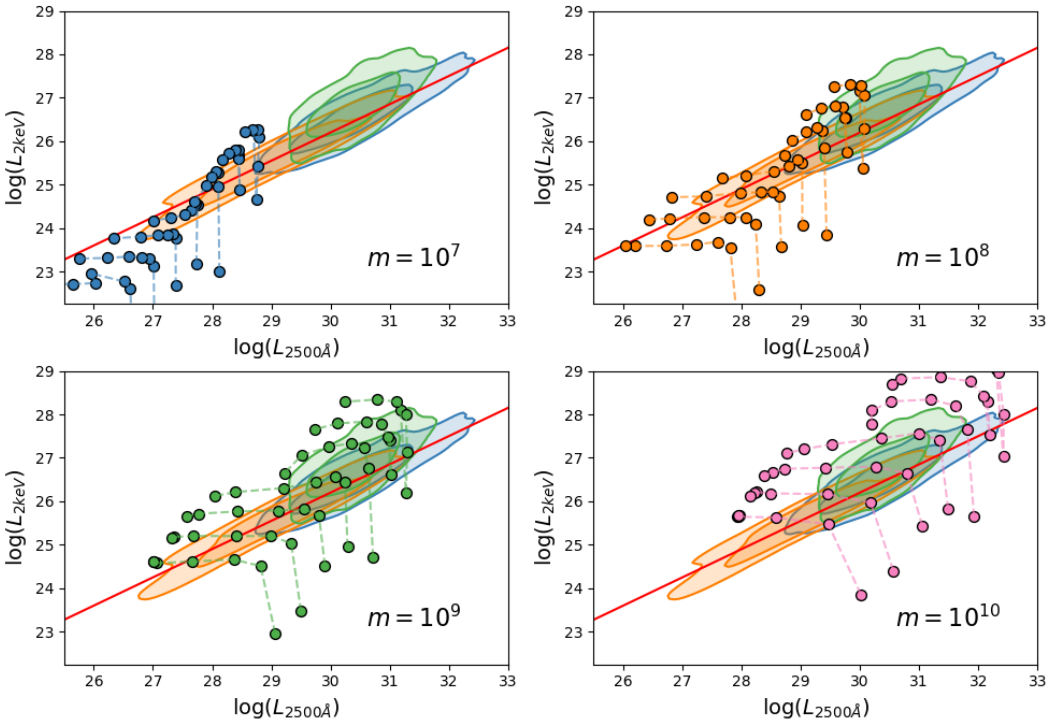

FIGURE 5.12: Grid of JED-SAD spectra in the UV–X-ray plane. Values of r_J go from $2 \rightarrow 100$ and of $\dot{m}$ from $10^{-2} \rightarrow 10$. Each panel assume a different black hole mass indicated on the plot. All other parameters are fixed to: $r_{isco} = 2$; $\omega = 0.1$; $m_s = 1.5$; $b = 0.3$; $p = 0.01$. The points connected with a dashed line have the same mass accretion rate. In the background: 95% and 68% percentile contour for each sample. In blue from the L&R sample (Lusso et al. 2020), in green from the Zhu+ sample (Zhu et al. 2020) and in orange from the Liu+ sample (Liu et al. 2021).

towards higher $L_{2\,keV}$. As such it seems that higher masses will require smaller value of r_J to reproduce the same position in the sample.

I produce a study of the evolution of this grid when changing the other JED-SAD parameters. As mentioned before, the other parameters (r_{isco}; ω; m_s and b) will only impact the JED emission and thus mostly change the X-ray luminosity. The corresponding figures (Figs. C.1, C.2, C.3 and C.4 respectively) are plotted in Appendix. C. The conclusion are similar to what was obtained in Chapter 2. Higher r_{isco}, m_s and b will allow to reach lower X-ray luminosities and thus change the relevant parameter space for r_J and $\dot{m}$. The impact of ω is negligible.

Effect of the soft excess

The last paragraph assumed no soft X-ray excess, yet from the example of Fig. 5.3, the addition of the warm comptonizing component can increase the UV luminosity and thus translates points horizontally along the UV–X-ray plane. However, this is only possible when the disk is cold enough so that the peak of the standard disk emission is below 5 eV (energy corresponding to the 2500 Å mark). In Fig. 5.13, I plot the same grid (r_J;$\dot{m}$) while applying the warm comptonization model to the SAD emission. I test for different values of the scattering fraction: $fsc = 0$ (no comptonization); $fsc = 0.5$ and $fsc = 1$. The other warm comptonizing parameters are fixed to: $\Gamma = 2.6$ and $kT_e = 0.5$. As expected the main effect is seen for high masses, high transition radius and low mass accretion rate, when the disk is the colder. There the points are translated horizontally by half a dex at maximum. The other main difference is observed for $r_J \sim r_{isco}$ (rightmost point of each equi-$\dot{m}$ track) where the

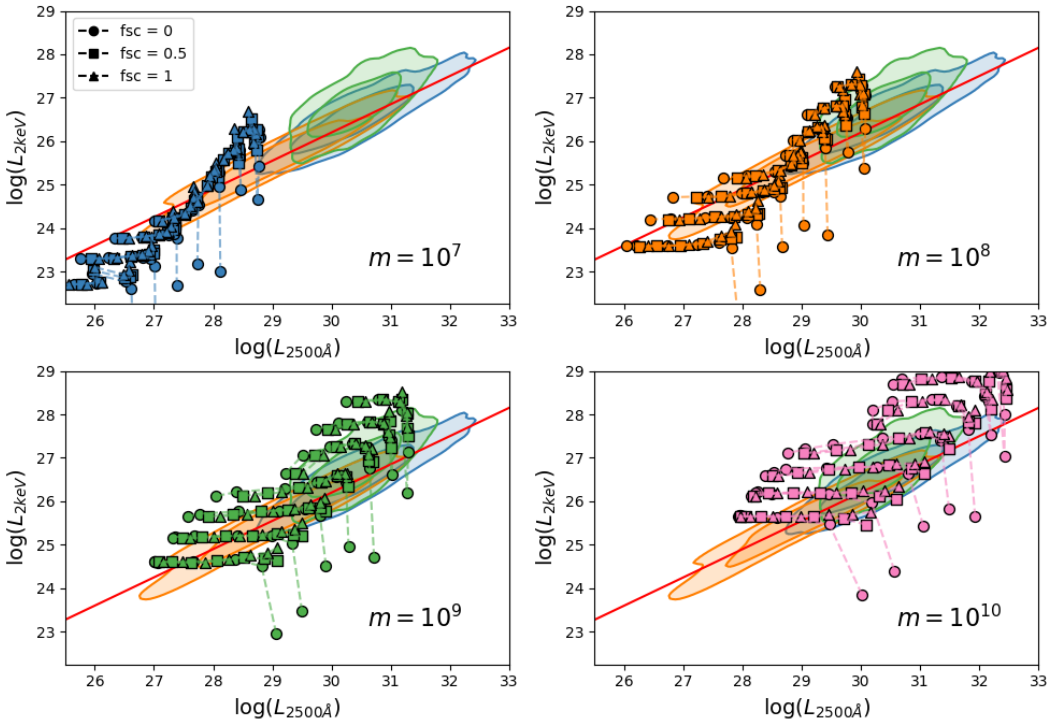

FIGURE 5.13: Grid of JED-SAD spectra in the UV–X-ray plane for different scattering fraction in the warm comptonization model applied to the standard disk. Values of r_J go from 2 $\rightarrow$ 100 and of $\dot{m}$ from 10^{-2} $\rightarrow$ 10. Each panel assume a different black hole mass indicated on the plot. All other parameters are fixed to: $r_{isco} = 2$; $\omega = 0.1$; $m_s = 1.5$; $b = 0.3$; $p = 0.01$. The warm comptonization parameters are fixed to: $\Gamma = 2.6$; $kT_e = 0.5$ keV. The points connected with a dashed line have the same mass accretion rate. In the background: 95% and 68% percentile contour for each sample. In blue from the L&R sample (Lusso et al. 2020), in green from the Zhu+ sample (Zhu et al. 2020) and in orange from the Liu+ sample (Liu et al. 2021).

warm comptonized power-law cuts off around 0.5 keV and thus dominates the X-ray luminosity at 2 keV when the JED emission is no more dominant. I produced the same study with varying value of the warm comptonization power-law index Γ (between 2.4 and 3.0) and varying value of the warm corona temperature kT_e (between 0.1 and 1). However no variation are observable on the figures, meaning that these parameters have almost no impact on the correlation. Thus the presence of a warm comptonization only has qualitative effects on the relevant parameter space (r_J;$\dot{m}$).

5.4.2 Relation r_J–$\dot{m}$

From the grid of spectra produced in the precedent paragraph, one can imagine a relation $r_J(\dot{m})$ following a straight line inside of the grid to reproduce the observed UV–X-ray correlation. This type of correlation between the transition radius and the mass accretion rate have been observed during the XrB hard states (see discussion in Sec. 3.4 and Marcel et al. 2022). So let us assume a relation $r_J(\dot{m})$ of the form $r_J = \kappa \cdot \dot{m}^\delta$, depending on two parameters, a normalization κ and a power index δ. We have seen that this relation is especially interesting for the JED-SAD model as it allows to understand how the magnetic flux within the JED evolve through time (see discussion in Sec. 3.4.1). If $\delta = -2/3$ than the JED magnetic flux is constant, if $\delta \gtrsim -2/3$, than it increases and if finally if $\delta \lesssim -2/3$, it decreases.

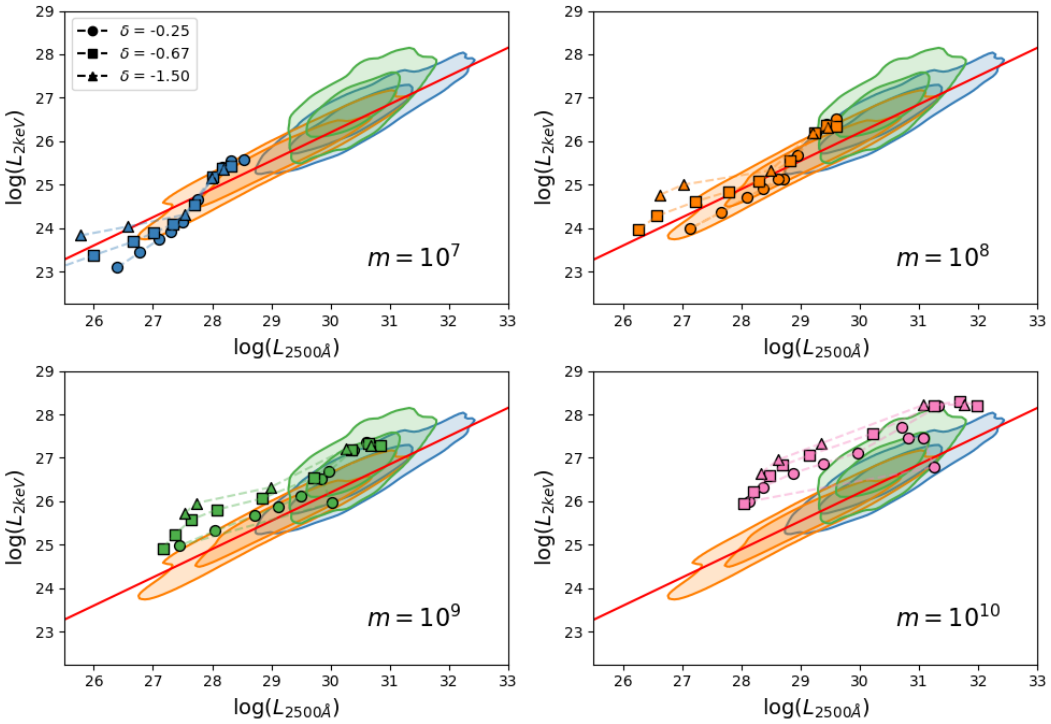

FIGURE 5.14: JED-SAD spectra simulated using the relation $r_J = \kappa \cdot \dot{m}^{\delta}$ for different values of the power index δ and assuming $\kappa = 10$ in the UV–X-ray plane. Each panel assume a different black hole mass indicated on the plot. All other parameters are fixed to: $r_{isco} = 2$; $\omega = 0.1$; $m_s = 1.5$; $b = 0.3$; $p = 0.01$. The points connected with a dashed line use the same power index δ. In the background: 95% and 68% percentile contour for each sample. In blue from the L&R sample (Lusso et al. 2020), in green from the Zhu+ sample (Zhu et al. 2020) and in orange from the Liu+ sample (Liu et al. 2021).

In Fig. 5.14, I plot the corresponding spectra for different values of the power index δ assuming a normalization $\kappa = 10$. I use 11 fixed values of $\dot{m}$ from 10^{-2} to 10 and compute the corresponding values of r_J. Some may exceed the table upper limit $r_J^{max} = 300$, as such some track contains less than 11 points as I had to cut the spectra with $r_J > 300$. Similarly, the function can produce values of r_J close to the ISCO, which are not observed during the hard XrB states. As such I apply a lower cut at the value $r_J = 10$. The other JED-SAD parameters were fixed to $r_{isco} = 2$; $\omega = 0.1$; $m_s = 1.5$; $b = 0.3$; $p = 0.01$. The three power index δ that are shown are quite different: -0.25 ; -2/3 ; -1.5. Yet all three seem to cover more or less part of the correlation at least up to a mass $m = 10^9$. Even though the correlation obtained for these relation $r_J(\dot{m})$ is more or less parallel to the observed UV–X-ray correlation, they appear above the correlation. This is especially the case for a black hole mass $m = 10^{10}$. The wiggles observed around the middle of each track is due to the transition from the READ to RERD JED regime, during which the X-ray output increases. For small black hole masses ($m = 10^7$ and $m = 10^8$), this transition coincides with the transition from the Wien function to the sum of Rayleigh-Jeans of the UV energy mark. As such the UV luminosity is no longer increasing by a large margin and the sudden increase of the X-ray luminosity result in sharp vertical track around $\dot{m} \sim 0.5$. Such sharp vertical turn is not observed for larger masses as they can only reach a high enough temperature for very large mass accretion rate of very small transition radius ($\dot{m} > 10$, $r_J < 6$, see Fig. 5.9). Instead the UV luminosity is always measured within the Wien function and thus always increase along the JED-SAD parameter space.

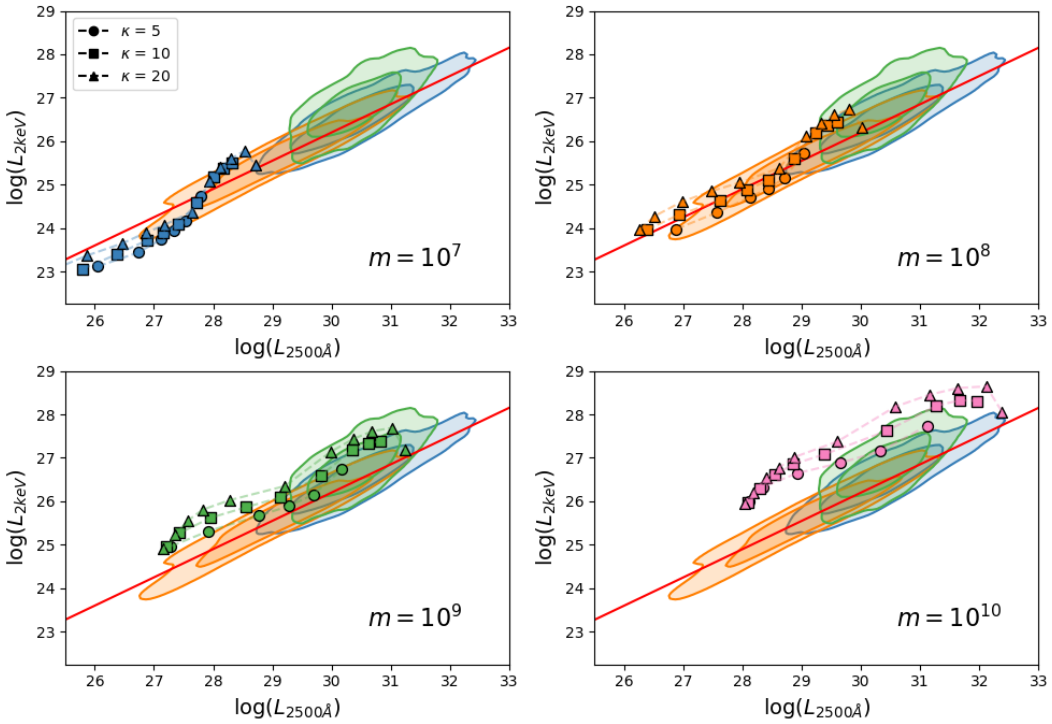

FIGURE 5.15: JED-SAD spectra simulated using the relation $r_J = \kappa \cdot \dot{m}^{\delta}$ for different values of the power index κ and assuming $\delta = -0.5$ in the UV–X-ray plane. Each panel assume a different black hole mass indicated on the plot. All other parameters are fixed to: $r_{isco} = 2$; $\omega = 0.1$; $m_s = 1.5$; $b = 0.3$; $p = 0.01$. The points connected with a dashed line have the same normalization κ. In the background: 95% and 68% percentile contour for each sample. In blue from the L&R sample (Lusso et al. 2020), in green from the Zhu+ sample (Zhu et al. 2020) and in orange from the Liu+ sample (Liu et al. 2021).

Similarly, in Fig. 5.15, I plot the corresponding spectra for different values of the normalization κ assuming a power index $\delta = -0.5$. For all three values of κ, the tracks are once again almost parallel to the correlation. However for large masses ($m = 10^9$ and $m = 10^{10}$) the track is above the correlation by at least a dex. There is still something missing to explain the UV/X-ray ratios that are observed for the more luminous sources of the L&R sample. One possibility is a variation of the other JED-SAD parameters. We know that r_{isco}, m_s, and b can to some extent decrease the X-ray luminosity. However loosing a dex in X-ray luminosity is quite a stretch using these three parameters (see Figs. C.1, C.2 and C.4). We will see that in Sec. 5.5.

Effects of the soft excess

The effects of the warm comptonization have already been discussed in Sec. 5.4.1. The main impact is an increase of the UV luminosity, translating the JED-SAD simulations horizontally, when the SAD is cold enough, meaning the effects are larger for large black hole masses. And as we have just seen, it is precisely for the larger black hole masses that the $r_J(\dot{m})$ tracks end up above the correlation. Can the addition of a warm comptonization translate horizontally the tracks to cover the samples?

In Fig. 5.16, I plot the tracks obtained for different values of the normalization κ with a power index $\delta = -0.25$, and assuming a warm comptonization of the SAD emission with parameters: $fsc = 0.75$, $\Gamma = 2.6$; $kT_e = 0.5$ keV. The tracks at low black hole masses are now a steeper compared to the UV-X-ray correlation as the coldest disk simulation (low $\dot{m}$, high r_J, in the bottom left) have been translated horizontally.

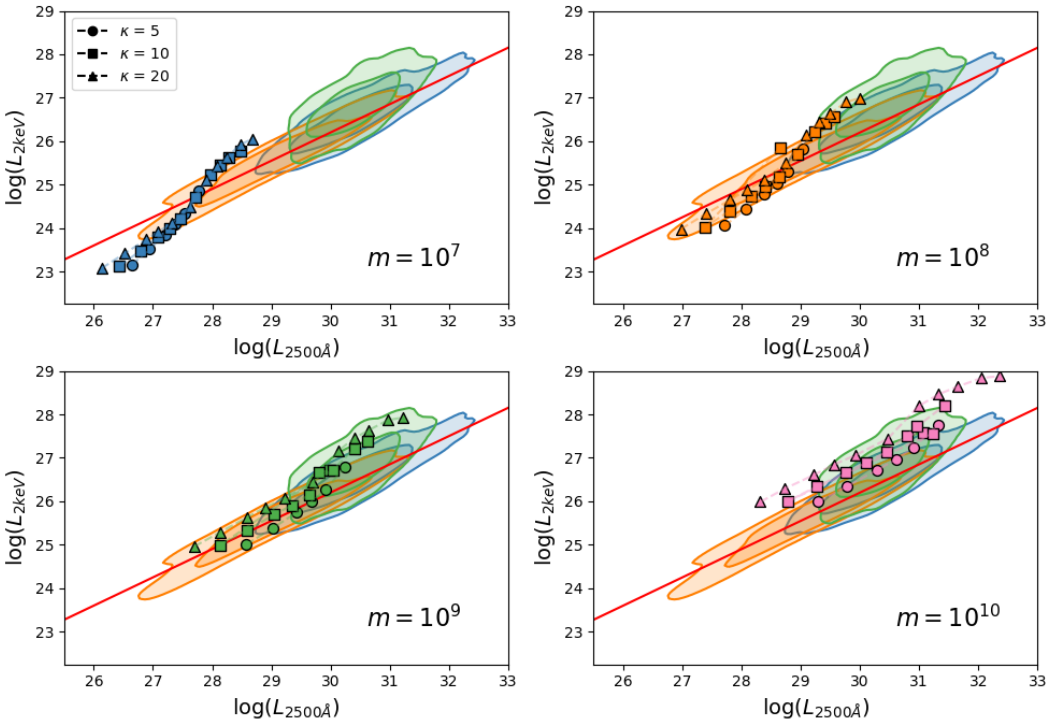

FIGURE 5.16: JED-SAD spectra simulated with a warm comptonization and using the relation $r_J = \kappa \cdot \dot{m}^{\delta}$ for different values of the power index κ and assuming $\delta = -0.25$ in the UV–X-ray plane. Each panel assume a different black hole mass indicated on the plot. All other parameters are fixed to: $r_{isco} = 2$; $\omega = 0.1$; $m_s = 1.5$; $b = 0.3$; $p = 0.01$. The warm comptonization parameters are fixed to: $fsc = 0.75$, $\Gamma = 2.6$; $kT_e = 0.5$ keV. The points connected with a dashed line have the same normalization κ. In the background: 95% and 68% percentile contour for each sample. In blue from the L&R sample (Lusso et al. 2020), in green from the Zhu+ sample (Zhu et al. 2020) and in orange from the Liu+ sample (Liu et al. 2021).

However the track observed for high black hole masses are now covering part of the sample. Yet, both the most luminous sources of the L&R sample and the sources presenting the lowest X-ray luminosities are still not covered by the tracks.

This study shows that even though a correlation between r_J and $\dot{m}$, as observed during XrB hard states, can produce tracks parallel to the correlation, part of the samples can not be reproduced with $r_J > 10$. Does this suggest that they might not be *hard states*? This will be further explored and discussed in the Sec. 5.5.

5.5 MC draw

In Sec. 5.4.1, we have seen how the JED-SAD parameter space is able to cover all of the samples. Using a Monte Carlo (MC) approach I now try to identify the relevant parameter space for each sample. This will lead to the production of simulated samples with similar density distribution within the UV–X-ray plane as the observed samples. I will then compare the black hole mass and X-ray spectral index distribution to the observed samples. In this section, I use the L&R sample to present the methodology and then apply the same method to the other samples. In Appendix D, I present the recently developed *Nested Sampling* method and apply it to the L&R sample. Unfortunately, the results do not achieve the goal established for this section.

5.5.1 Drawing statistically equivalent sample

Methodology

To draw a statistically equivalent sample, I will use a two step approach. First, I draw a large number of points (N=10 000) with the condition that their corresponding position in the UV–X-ray plane is within the sample of interest. Once again, each point means a set of the seven JED-SAD parameters (m, r_J, $\dot{m}$, r_{isco}, ω, m_s and b), its associated spectrum and the UV and X-ray luminosity I extract from the spectra. I draw the JED-SAD parameters assuming the following priors: for r_{isco}, ω, m_s and b, I use a uniform distribution. For m, r_J, $\dot{m}$, I assume a uniform distribution within a log-space so that I draw as many points in each decade range.

The second step consists in assigning a probability to each of the 10 thousands spectra. This probability depends on 1) the observed sample density at a given position in the UV-X-ray plane and 2) the number of simulated spectra in its vicinity. I then draw without replacement 500 spectra among the 10 thousands. I check that the number of simulated spectra I draw in each square $(dL_{UV}; dL_X)$ of the UV–Xray plane is inferior to the total number of simulated spectra available (from the 10 thousands spectra) in this region. This way I am able to recover a simulated sample with the same statistical distribution as the observed sample. To ensure that I have no selection biases, I repeat this procedure five times. The results were always similar.

Parameter space – L&R sample

In Fig. 5.17, I plot the corner plot obtained after the first step. The resulting simulated sample of 10 thousands spectra is not uniformly distributed inside of the L&R sample, nor does it respect the density distribution of the L&R sample within the UV–X-ray plane. Indeed, there are more points at low luminosity compared to the high luminosity region of the sample. This can be understood as the region of the parameter space producing high luminosity spectra is smaller compared to the parameter space producing low luminosity spectra: Only high black hole mass can reach a high luminosity while both high and low black hole mass can produce low luminosity spectra assuming different mass accretion rate. The resulting distribution of the points in the JED-SAD parameter space is then not relevant to reproduce a statistically equivalent sample. However it allows to identify all the parameters producing a point inside of the observed sample. It also allows to grasp the possible degeneracies of the model. For instance a weak correlation seem to be present between the mass accretion rate $\dot{m}$ and the sonic mach number m_s. This degeneracy has already been mentioned in Chapter 2 and in Sec. 3.3.3. Similarly to the result of the nested sample method, correlations between m and $\dot{m}$ or between r_J and r_{isco} are also visible.

In Fig. 5.18, I plot the results after the second step. The sample is then reduced to 500 spectra and its distribution in the UV–X-ray plane is consistent (same density distribution) with the statistical distribution of the L&R sample. As such, there is no need to assume any weight in the corner plot. Contrarily to the results of the nested sample approach (Fig. D.3), the sample is covering both the high and low luminosity part of the L&R sample consistently with the data distribution, including spectra in the high luminosity region of the observed sample. The JED-SAD parameters are however distributed quite similarly in the parameter space. Once again, r_{isco}, ω, m_s and b are not constrained as evidently shown by their flat histogram.

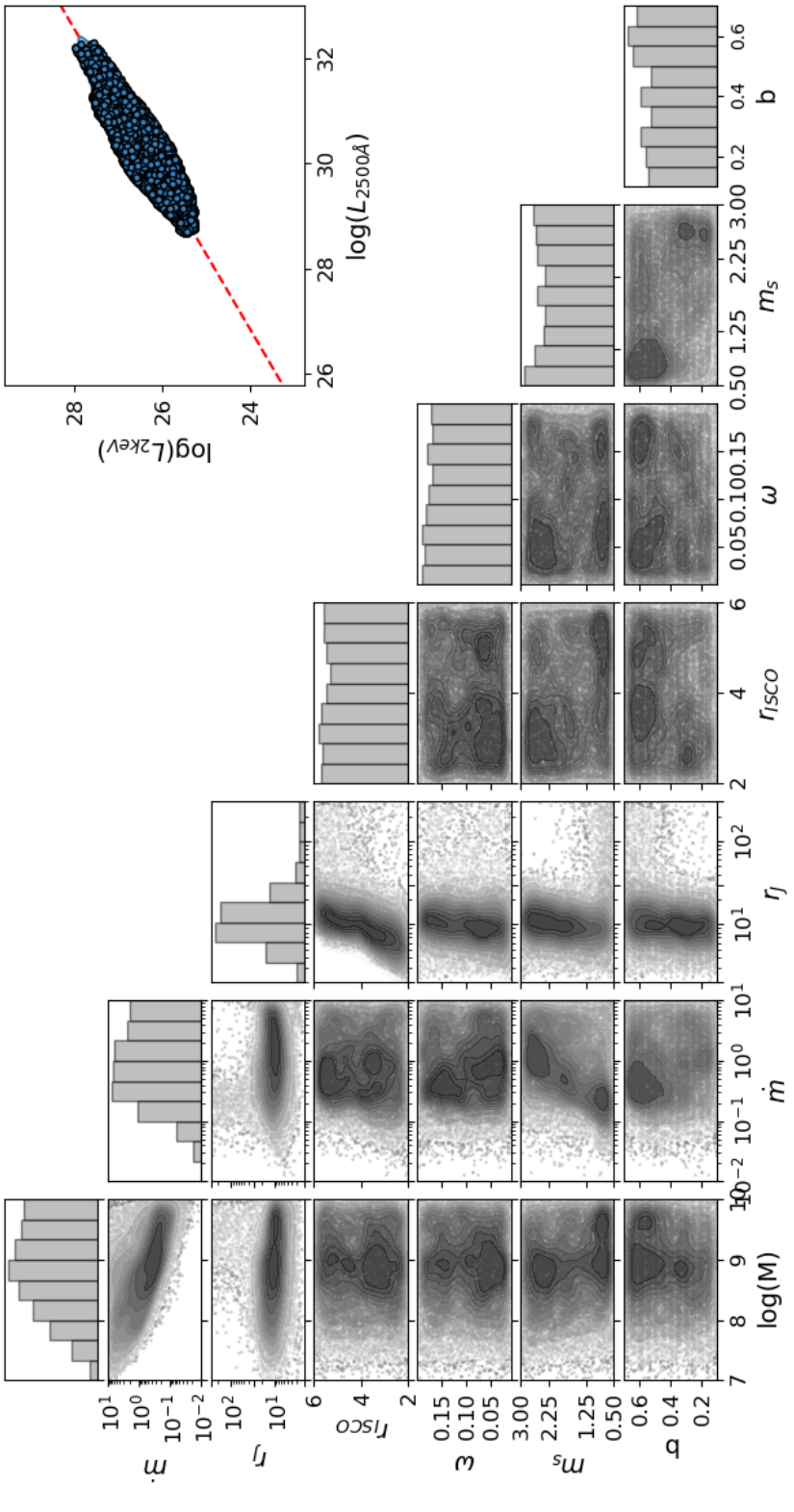

FIGURE 5.17: Corner plot of the 10 thousands simulated spectra in the JED-SAD parameter space. Each panel present the position of the 10 thousands spectra in projections of the parameter space on 2D planes. The grey contour plot beneath show the kernel distribution in the 2D planes. The upper panel of each column show the 1D distribution of the parameters. The top right panel present the position of the points in the UV–X-ray plane.

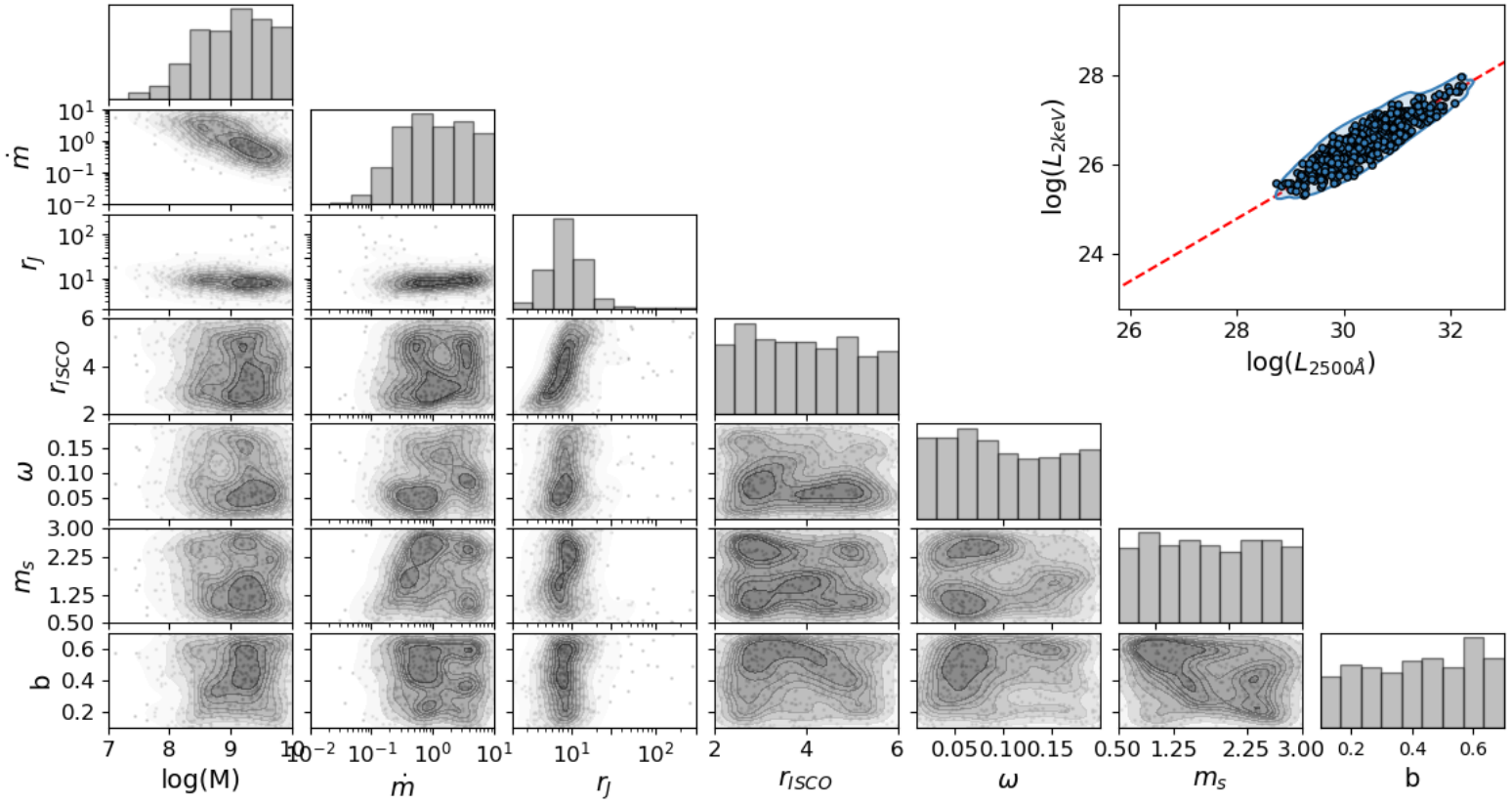

FIGURE 5.18: Corner plot of the 10 thousands simulated spectra in the JED-SAD parameter space. Each panel present the position of the 10 thousands spectra in projections of the parameter space on 2D planes. The grey contour plot beneath show the kernel distribution in the 2D planes. The upper panel of each column show the 1D distribution of the parameters. The top right panel present the position of the points in the UV–X-ray plane.

5.5.2 Stratification

In the last paragraph, I mention that r_{isco}, ω, m_s and b are not constrained. Yet a correlation between r_{isco} and r_J suggest that these parameters could still be important to understand the sample. In this paragraph, I take a look at the distribution of the JED-SAD parameters along the UV–X-ray correlation.

m, r_J and $\dot{m}$

In the upper panels of Fig. 5.19, I plot the simulated sample where the points are colored depending on the black hole mass (left), the transition radius (middle) and the mass accretion rate (right). The bottom panels show the same distribution but averaged. The three parameters show an evolution in the UV–Xray plane. There are on average larger black hole masses at higher luminosity. This is not so different than what is observed in the L&R sample (see Fig. 5.5). The transition radius show a side-way (bottom right to upper left) evolution with high values ($r_J \sim 15 \rightarrow 30$) on the upper left-most region of the correlation and smaller values ($r_J \sim 4 \rightarrow 10$) in the bottom right-most part of the correlation where the ratio between the UV and X-ray emission is the stronger. The mass accretion rate show generally stronger values at high luminosity. However, we also see points with high mass accretion rate at lower luminosity. They correspond to JED-SAD cases with low black hole masses and high mass accretion rate.

r_{isco}, ω, m_s and b

In Fig. 5.20, I plot the simulated sample while coloring the points according to the values of the JED-SAD parameters r_{isco} (upper left), ω (upper right), m_s (bottom

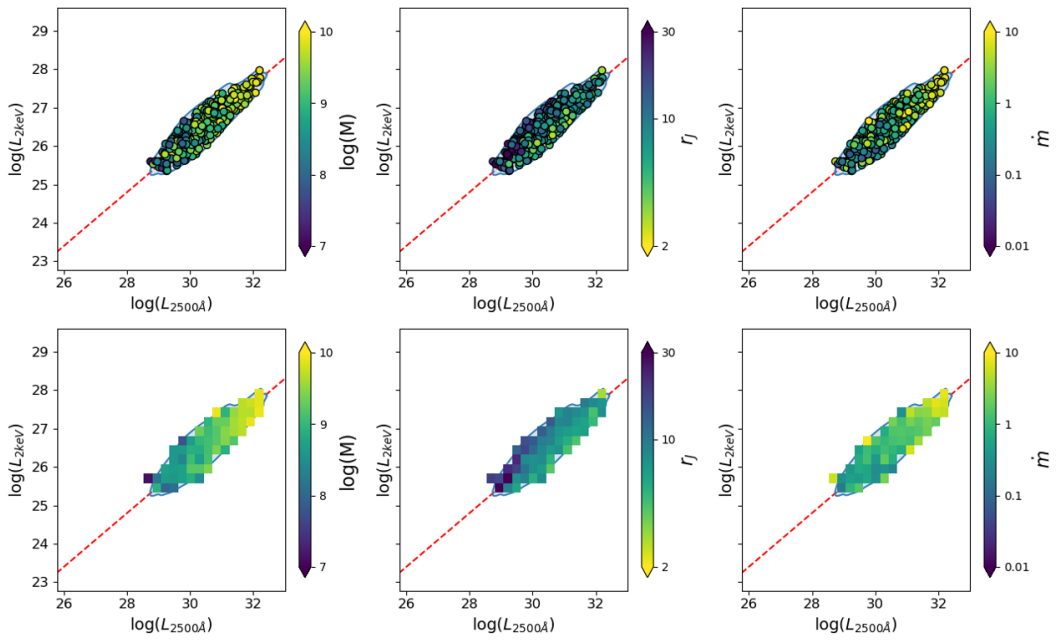

FIGURE 5.19: The simulated sample in the UV–X-ray plane. In the background the L&R sample is plotted in blue. **Top**: The simulated spectra are colored depending on the value of their JED-SAD parameters: black hole mass m (left), transition radius r_J (middle) and mass accretion rate $\dot{m}$ (right). **Bottom**: Evolution of the mean local value of the JED-SAD parameters along the correlation.

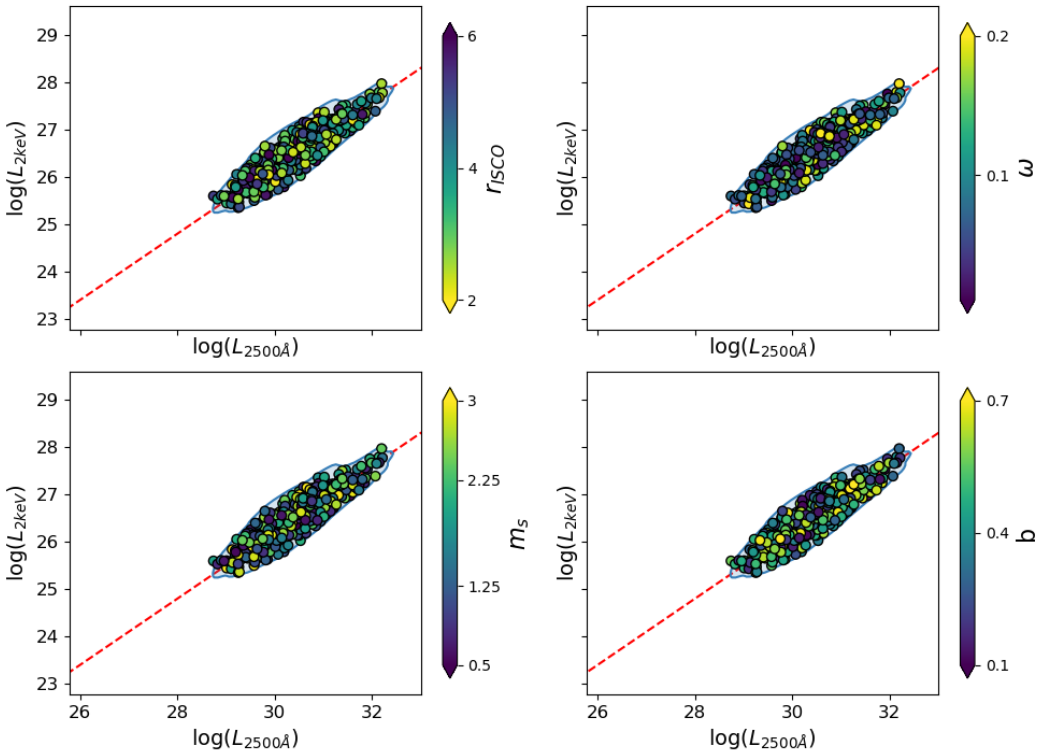

FIGURE 5.20: The simulated sample in the UV–X-ray plane. In the background the L&R sample is plotted in blue. The simulated spectra are colored depending on the value of their JED-SAD parameters: ISCO r_{isco} (upper left), dilution factor ω (upper right), sonic mach number m_s (bottom left) and power in the jets b (bottom right)

left) and b (bottom right). No clear stratification of any of these parameters can be observed. As such these parameters are not only unconstrained but their exact values do not seem to impact the position of the spectra within the sample.

Yet a correlation was observed in the different corner plots that I produced between the transition radius and the value of the ISCO. In Fig. 5.21 I plot the simulated sample coloring the points this time depending on the ratio r_J/r_{isco}. This ratio is relevant as it represent the size of the hard X-ray corona and thus is directly related

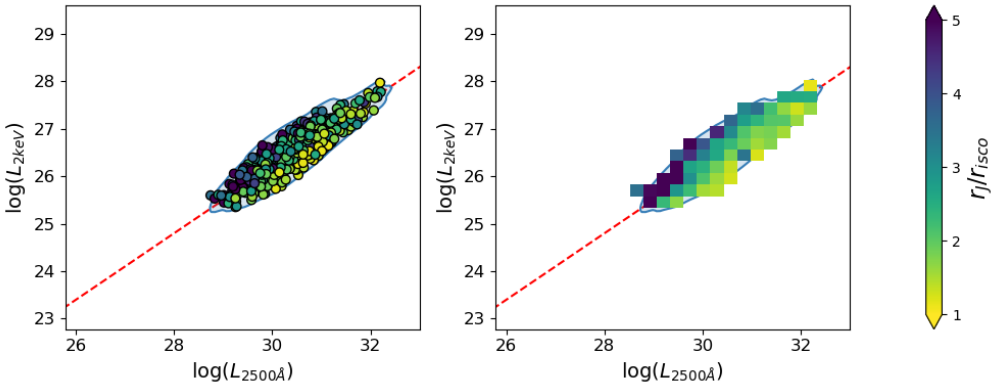

FIGURE 5.21: The simulated sample in the UV–X-ray plane. In the background the L&R sample is plotted in blue. The simulated spectra are colored depending on the ratio r_J/r_{isco} (left) or on the mean local value of the same ratio along the correlation (right).

to the accretion power available in the JED:

$$P_{JED} = (1-b)\,P_{acc} = (1-b)\frac{GM\dot{M}}{2R_{isco}}\left[1-\left(\frac{r_{isco}}{r_J}\right)^{1-p}\right] \tag{5.7}$$

Small ratios r_J/r_{isco} means less power within the JED. Fig. 5.21 shows the same bottom right to upper left distribution as the transition radius r_J. However now, it is clear that the spectra at the bottom right of the correlation not only have a small transition radius ($r_J < 10$) but also have a rather small corona with $r_J/r_{isco} \sim 1 \rightarrow 2$. As such even though the ISCO does not seem to be stratified along the correlation, it still remain a relevant parameter for the correlation, changing the minimum possible value of r_J.

5.5.3 Equivalent sample?

I produced a simulated sample whose density distribution within the UV–X-ray correlation is equivalent to the L&R sample. Yet does this simulated sample actually reproduce other observable properties? In this paragraph, I compare the distributions of the black hole masses and the of the X-ray spectral indexes between the simulated and observed samples.

Black hole mass

In Fig. 5.22, I plot the comparison of the black hole mass distributions between the simulated and observed sample. The normalized histogram (left) shows that the simulated sample tends to have higher black hole masses ($log(m) > 9.4$) compared to the L&R sample which peaks around ($log(m) \sim 9$). Yet the proportion of small black hole masses ($log(m) < 8.5$) is consistent between the simulated and observed samples. This is quite encouraging. The difference $\Delta(log(m)) = log(m_{sim}) - log(m_{data})$ along the UV–X-ray correlation, which I plot in the right panel, shows values ranging from -0.33 to 0.68. This difference is also showing a trend along the UV–X-ray correlation. The simulated sample seem to underestimate the black hole masses at higher luminosities ($\Delta(log(m)) < 0$) and overestimate the black hole masses at lower luminosities ($\Delta(log(m)) > 0$). This can infer a bias in the evaluation

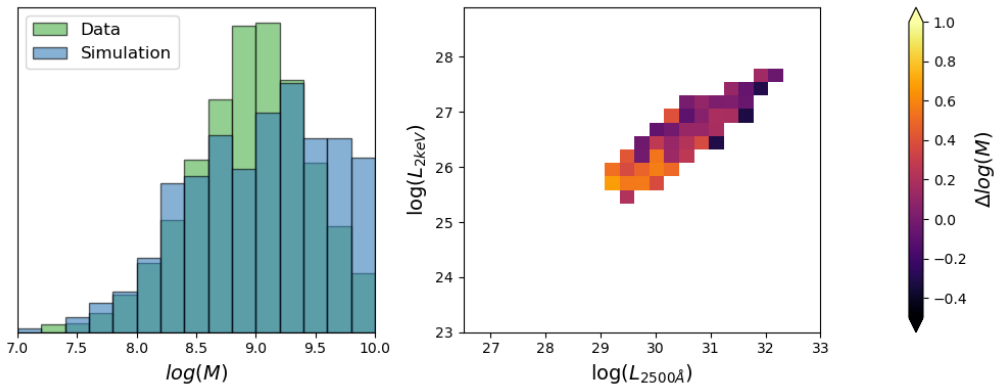

FIGURE 5.22: Comparison between the simulated and observed black hole mass distributions of the L&R sample. **Left**: Normalized histogram of the black hole masses. In green the observed sample and in blue the simulated sample. **Right**: Evolution of the mean difference $\Delta(log(m)) = log(m_{sim}) - log(m_{data})$ along the UV–X-ray correlation.

of the mass accretion rate along the sample. Lower luminosities AGN would have a larger mass accretion rate compared to what the simulated sample predicts and the higher luminosities AGN would rather have smaller mass accretion rates. Looking back to Fig. 5.19 and the stratification of the mass accretion rate, this would tend to harmonize the mass accretion rate along the correlation.

X-ray spectral index

To be able to compare the X-ray spectral index between the simulated and observed samples, I must use the same method of measurement. As such I follow the steps described in Sec. 5.2.3 (Risaliti & Lusso 2019) and using the same energies ($E_S = 1$ keV and $E_H = 3.45$ keV).

In Fig. 5.23, I plot the locally averaged X-ray spectral index in the UV–X-ray plane for the simulated sample (left) and the observed L&R sample. Both show a similar evolution of the averaged X-ray spectral index. The upper left edge of both samples show rather harder spectra compared to the bottom right edge of the samples.

In Fig. 5.24, I plot the comparison of the X-ray spectral index Γ between the simulated and observed sample. The normalized histogram, plotted in the left panel, show a difference of 0.2 to 0.3 between the mean spectral indexes. The L&R sample appearing generally softer and peaking around 2.2 and the simulated sample around 1.9. The values of the simulated sample spectral index range mostly from 1.6 to 2.3 which are partially consistent with the typical values observed in XrB high luminosity hard states and during the spectral state transition ($soft \Leftrightarrow hard$). The difference $\Delta(\Gamma) = \Gamma_{sim} - \Gamma_{data}$ along the UV–X-ray correlation, plotted in the right panel, shows values ranging from -0.54 to 0.87. Interestingly, even though the histogram distribution clearly show that the X-ray spectral index is generally underestimated by the simulated sample, it appears locally overestimated ($\Delta(\Gamma) > 0$) at very high luminosity where the mass accretion rate is the highest and the size of the corona the smallest (see Figs. 5.19 and 5.21) in the simulated sample. At very high mass accretion rate, the JED transits to a slim regime (similar to Abramowicz et al. 1980, 1988). Combined with the small JED ($r_J \gtrsim r_{isco}$), this result in very soft spectra ($\Gamma \sim 2.5 \rightarrow 3$) Otherwise, the spectral index is generally underestimated ($\Delta(\Gamma) < 0$) everywhere else along the correlation.

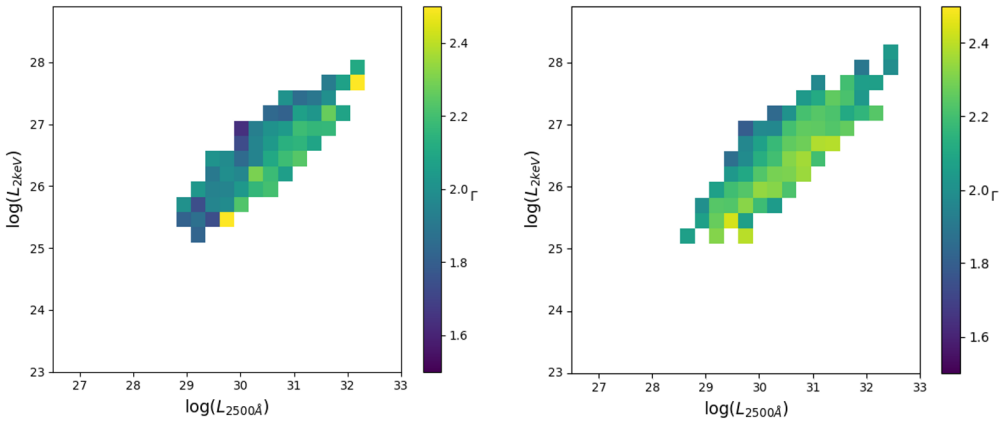

FIGURE 5.23: Comparison between the simulated and observed X-ray spectral index Γ of the L&R sample. **Left**: Evolution of the averaged X-ray spectral index within the UV–X-ray plane of the simulated sample. **Right**: Evolution of the averaged X-ray spectral index within the UV–X-ray plane of the observed L&R sample.

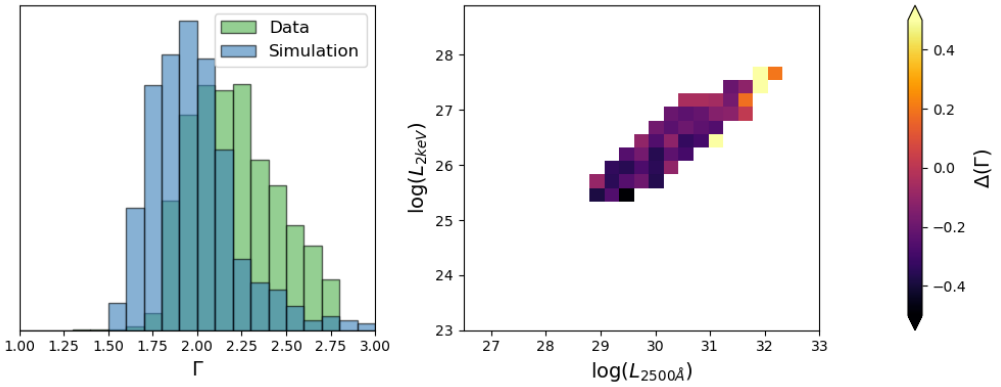

FIGURE 5.24: Comparison between the simulated and observed X-ray spectral index Γ of the L&R sample. **Left**: Normalized histogram of the spectral index Γ. In green the observed sample and in blue the simulated sample. **Right**: Evolution of the mean difference $\Delta(\Gamma) = \Gamma_{sim} - \Gamma_{data}$ along the UV–X-ray correlation.

I already mentioned that the methodology employed to measure the X-ray spectral index depends on the soft X-ray flux in the energy band [0.5 - 2 keV] which is known to be highly impacted by the presence of the soft X-ray excess. As such this method will naturally result in softer X-ray spectra compared to the usual hard X-ray spectral index presented in XrB. The simulated sample presented here do not use the warm comptonization component and thus do not present a soft X-ray excess. The spectral index measured for the simulated sample is thus similar to what would be measured in the hard energy band and thus similar to what can be observed in XrB. It is then natural that the data sample appear softer compared to the simulated sample.

Adding a warm comptonization model to the model however does not seem to resolve the problem. In fact the resulting simulated sample show too soft spectra with values mostly ranging between 2 and 3. One possibility to explain the discrepancy with the observed sample would be the absence of any Hydrogen absorption component in the model used to simulate the AGN spectra. Even though the L&R sample is mostly characterised by weakly absorbed quasars (due to a selection), small absorption due to the galactic Hydrogen column seem unavoidable and would reduce the flux in the soft X-ray band [0.5 - 2 keV] used to compute the X-ray spectral index, and could increase the measured hardness of the observed sample.

5.5.4 Other samples

Now that I produced a statistically equivalent sample to the L&R sample, let me take a look at the results I obtain for the Zhu+ and Liu+ samples using the same methodology.

Zhu et al. 2020

In Fig. 5.25, I plot the corner plot corresponding to the simulated sample of the Zhu+ sample. Conclusions are similar to what was observed with the L&R sample. r_{isco}, ω, m_s and b are not constrained. Similar correlations can be observed between r_J and r_{isco}, or between the black hole mass and the mass accretion rate. The only difference is that the Zhu+ sample has larger values of r_J. Here r_J is mostly constrained within the range [6;20]. Moreover, it seems the sample prefer even higher mass accretion rate compared to the L&R sample, with a distribution peaking around $m \sim \dot{6} \rightarrow 10$.

The distribution of the JED-SAD parameters along the UV–X-ray correlation are quite similar to what was obtained for the L&R sample: visible stratification with higher masses and mass accretion rate at higher luminosities and smaller r_J toward the bottom right part of the sample. No stratification are observed for the other parameters.

In Fig. 5.26, I plot the mass comparison between the simulated and Zhu+ sample. The normalized histogram (left) shows a quite similar distribution at the exception that the simulated sample is less peaked and a bit more flat between log(m)=8.5 and log(m)=10. Looking at the evolution of the difference between simulated and data set (right) shows that along the correlation the mass distribution is quite correct. Only at the high and low luminosity extremities of the sample do we see a difference.

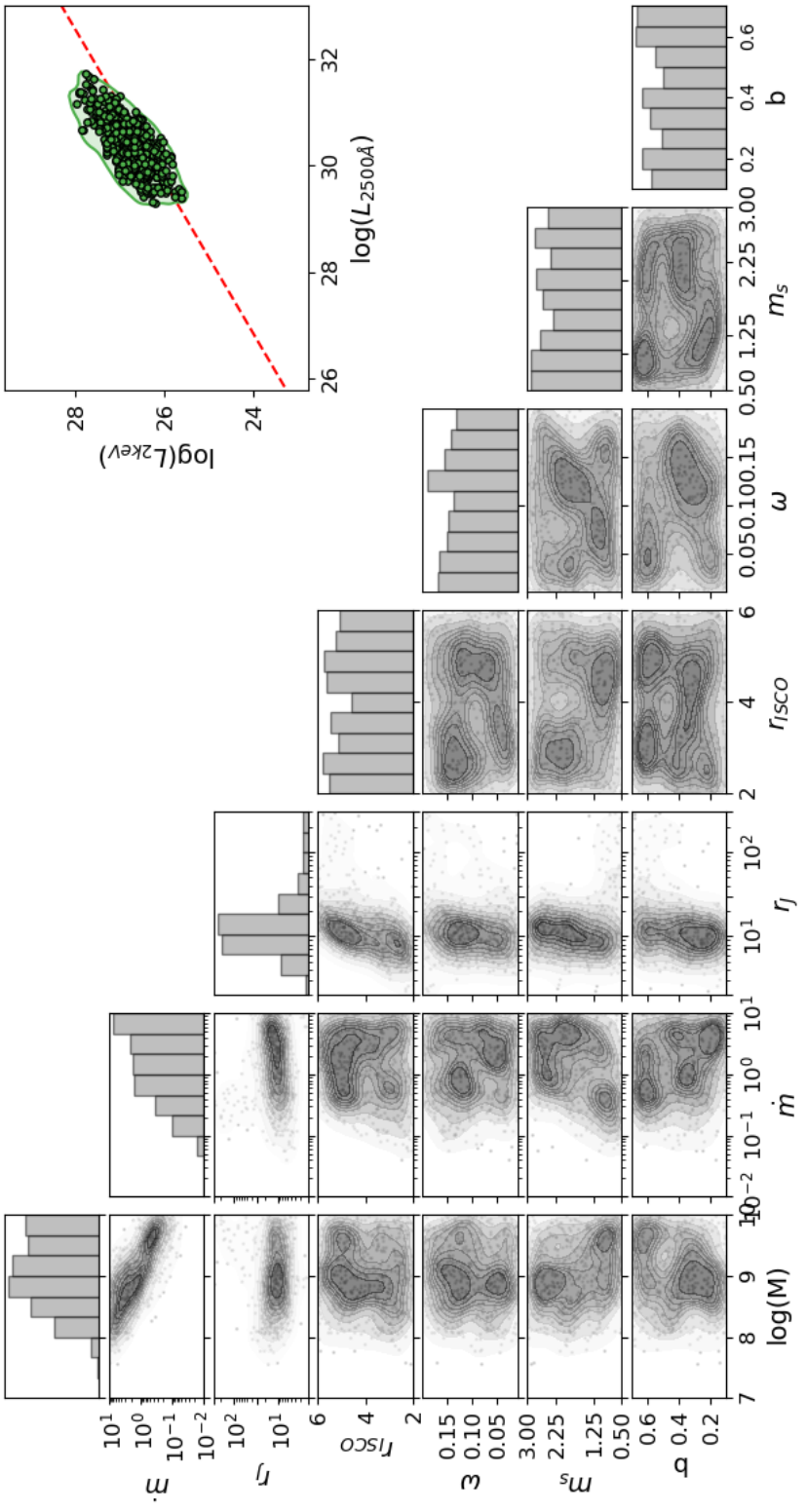

FIGURE 5.25: Corner plot of the 500 simulated spectra in the JED-SAD parameter space for the Zhu+ sample. Each panel present the position of the 500 spectra in projections of the parameter space on 2D planes. The grey contour plot beneath show the kernel distribution in the 2D planes. The upper panel of each column show the 1D distribution of the parameters. The top right panel present the position of the points in the UV–X-ray plane.

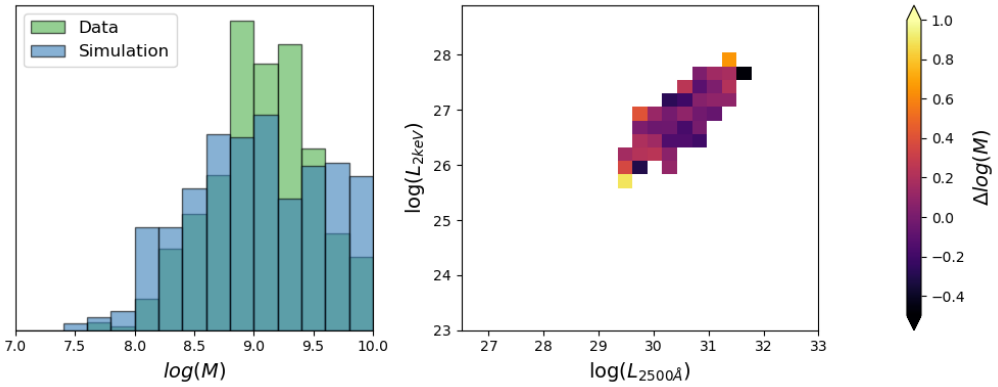

FIGURE 5.26: Comparison between the simulated and observed black hole mass distributions of the Zhu+ sample. **Left**: Normalized histogram of the black hole masses. In green the observed sample and in blue the simulated sample. **Right**: Evolution of the mean difference $\Delta(log(m)) = log(m_{sim}) - log(m_{data})$ along the UV–X-ray correlation.

As the sample did not reference which X-ray observations were used to compute the UV and X-ray luminosities, I was not able to extract a spectral index using the method of Risaliti & Lusso (2019). The determination of the X-ray spectral index and the production of a sample using these supplementary constrains is part of a work in progress.

Liu et al. 2021

In Fig. 5.27, I plot the corner plot corresponding to the simulated sample associated with the Liu+ sample. As the Liu+ sample is characterized by smaller black hole masses and lower luminosities, the relevant parameter space is quite different compared to what was obtained for both the L&R and Liu+ samples. First, once again r_{isco}, ω, m_s and b are not constrained. Second, r_J now reaches values up to 300 even though the majority of the spectra lies around $r_J = 6 \rightarrow 30$. The mass accretion rate is also smaller with the majority of the spectra within the range $\dot{m} \in [0.1; 1]$. Finally, the black hole mass is not well constrained with values ranging from log(m)=7 to log(m)=10. A word of caution should be raised. The Liu+ sample is characterized by black hole masses between log(m)=6 and log(m)=9, with the majority lying between log(m)=6.5 and log(m)=8. As such the simulation with large black hole masses should be replaced by smaller black hole masses with higher mass accretion rate. Concerning the stratification of the JED-SAD parameters along the correlation, no difference are observed compared to the two other sample.

Similarly to the Zhu+ sample, the estimation of the X-ray spectral index has not yet been realized and as such no comparison can be done. This is left for future work along with the computation of a better simulated sample using the same mass and spectral index distribution along the correlation.

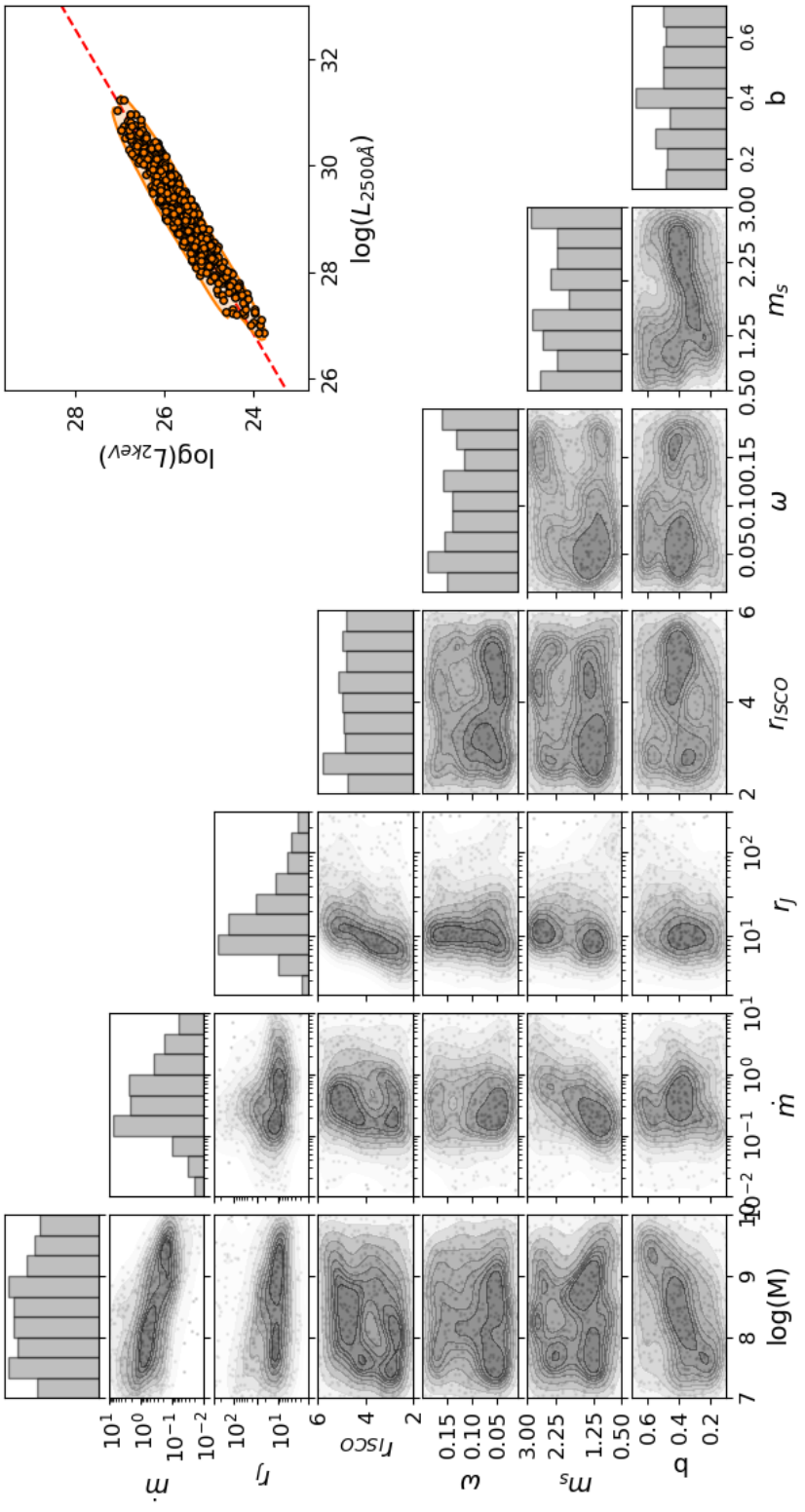

FIGURE 5.27: Corner plot of the 500 simulated spectra in the JED-SAD parameter space for the Liu+ sample. Each panel present the position of the 500 spectra in projections of the parameter space on 2D planes. The grey contour plot beneath show the kernel distribution in the 2D planes. The upper panel of each column show the 1D distribution of the parameters. The top right panel present the position of the points in the UV–X-ray plane.

5.6 AGN outbursts

Before starting the discussion on the interpretation of my results concerning the UV–X-ray correlation, I wanted to see what would an XrB outburst (fitted with the JED-SAD) look like, when re-scaled to AGN black hole mass, within the UV–X-ray plane.

Methodology

In Marcel et al. (2019, 2020, 2022), Greg was able to qualitatively follow the evolution of the main JED-SAD parameters along 4 outbursts of GX 339-4. Using these values of r_J and $\dot{m}$, and assuming AGN black hole masses, I can transpose the XrB outburst to an AGN outburst and see what path within the UV–X-ray plane is expected. For this I use what is called the constrained observations in Marcel et al. (2022), which are observations with small errors on the transition radius r_J. The evolution of these parameters can be seen in Fig. 3.13. There is however one question arising. How to handle the soft spectral state where no JED is present?

In XrB, the spectral soft state is characterized by the presence of a hard energy tail reaching up to the γ-rays. The origin of this steep and faint non-thermal power-law is not yet understood. Its spectral index is generally poorly constrained with values between 2 and 3. To add this component to the spectrum, I use a power-law. For all observations with $r_J < 10$, I assume a constant hard tail spectral index of 2.5 and a normalisation level of 10% of the peak SAD luminosity. To limit the impact

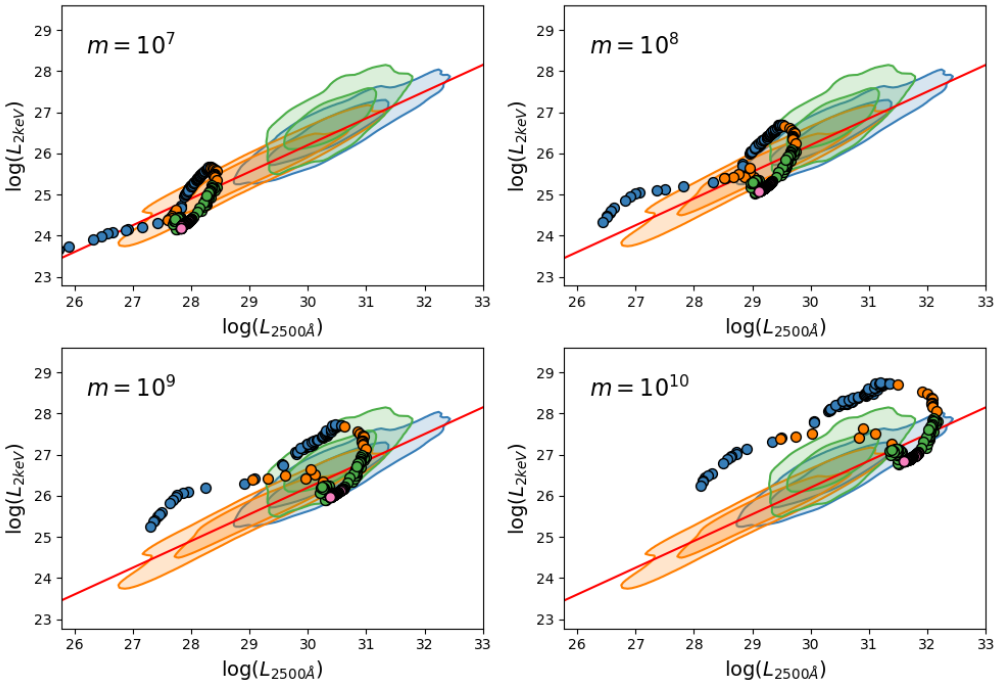

FIGURE 5.28: Simulation of an AGN outburst using the parameters extracted from four outbursts of GX 339-4 (Marcel et al. 2019, 2020, 2022) assuming 4 different black hole masses. The other JED-SAD parameters are fixed to: $r_{isco} = 2$, $\omega = 0.1$, $m_s = 1.5$ and $b = 0.3$. The color of the points represent the spectral state: hard states in blue, hard-intermediate in orange, soft-intermediate in green and soft states in pink. In the background: 95% and 68% percentile contour for each sample. In blue from the L&R sample (Lusso et al. 2020), in green from the Zhu+ sample (Zhu et al. 2020) and in orange from the Liu+ sample (Liu et al. 2021).

of the power law at low energy I add a low energy cut-off defined at the maximum temperature of the SAD. The addition of a warm comptonization to the SAD does not change the conclusions of this paragraph.

Outbursts simulation

The following JED-SAD parameters are fixed to: $r_{isco} = 2$, $\omega = 0.1$, $m_s = 1.5$ and $b = 0.3$. In Fig. 5.28, I plot for different black hole masses the tracks of the expected outburst in the UV–X-ray plane. If for small black hole masses ($m = 10^7$ and $m = 10^8$) the tracks are in agreement with the correlation it is not the case for larger black hole masses where the hard states (in blue) move above the correlation. All spectral state could result in points along the correlation. There is no reason why such AGN would not be observed if they exist. As such, and in accord with the results obtained in both Sec. 5.4 and Sec. 5.5, the values of r_J must be smaller in the hard states for large black hole mass.

5.7 Discussion

5.7.1 Radio-quiet AGN and JED-SAD

In this study I mainly focused on the L&R sample, composed of radio-quiet AGN. They are typically a few order of magnitude less radio bright compared to the radio loud population, and their radio to X-ray emission ratio thus much smaller. This characteristic raises questions concerning the relevance of the JED-SAD model, which implicates the presence of jets, for this particular sample. But what is the origin of the radio emission in radio-quiet AGN ?

Jets

Usually, the radio emission from radio loud AGN is attributed to relativistic jets, ranging from parsec to mega-parsec scale and emitting radio photons through synchrotron emission. The core emission is expected to present a flat or slightly inverted radio spectrum coming self absorbed synchrotron from the optically thick inner region of the jet (Blandford & Königl 1979; Reynolds 1982). Radio survey of optically selected local low luminosity AGN have shown that Seyfert galaxies sometime present compact nuclear radio emission, occasionally with a jetted structure on parsec scale (Roy et al. 2000; Middelberg et al. 2004; Panessa et al. 2019). Some bright radio-quiet AGN present similar but generally larger radio morphologies than Seyfert galaxies (Leipski et al. 2006). The emission of radio-quiet AGN is then sometime associated to scaled-down version of powerful-jets, possibly due to a difference in the electron acceleration and flow collimation (Falcke & Biermann 1995).

Winds

Another type of outflow could be responsible for the radio emission in radio-quiet AGN. Winds are usually detected thanks to the presence of line features in optical and UV for the slower winds launched on parsec to kilo-parsec scale, and X-rays for the higher velocity and ultrafast outflows launched from the inner most region (gravitational radius scale). The presence of broad high velocity components, usually observed in the [OIII] emission line profile, is sometime associated with diffuse

radio emission (Mullaney et al. 2013; Zakamska & Greene 2014; Panessa et al. 2019). A correlation between the [OIII] emission line and the radio emission of radio quiet AGN is even observed (Hwang et al. 2018). It has been proposed that the presence of winds could play a role in the distribution of the [OIII] emitting gas (Mullaney et al. 2013). Winds shocks could be responsible for the acceleration of electrons producing synchrotron emission with power similar to the one observed in radio-quiet AGN (Nims et al. 2015).

Hot corona

The presence of hot plasma close to the black hole has been evoked as the possible origin of the weak radio emission. Hot coronae are expected to be magnetized and produce non-thermal emission which could be observed in the radio band. The size R_{cm} of the self-absorbed synchrotron source can be estimated from its emission (Laor & Behar 2008):

$$R_{cm} \simeq 4 \times 10^{17} \left(\frac{F_\nu}{\mu\, Jy} \right)^{1/2} \nu_{GHz}^{-5/4} B_G^{1/4} z \tag{5.8}$$

Where the frequency ν_{GHz} is in GHz, B_G the magnetic field strength in Gauss and z the redshift. Observing the radio corona on its gravitational radius scale requires observations in the mm-band (100-300 GHz). Recently, excess emission in the mm-band has been detected in two nearby Seyfert galaxies IC 4329A and NGC 985 using ALMA. This excess-emission was attributed to radio emission from the hot corona (Inoue & Doi 2018; Inoue et al. 2021) super-imposed on the steep power-law of more extended radio structures.

Star formation

Star formation within the host galaxy results from dense region of molecular clouds collapsing. They produce both thermal and non-thermal radio emission. Radio emission from star formation region is generally diffuse, clumpy and low surface brightness (Olsson et al. 2010; Orienti et al. 2015; Panessa et al. 2019). The radio emission is characterized by a steep GHz spectrum and a flat free-free component above 30 GHz (Condon 1992). Far infrared emission can be used as a probe for dust and cold gas where star formation generally occurs. A correlation between the far infrared and radio emission has been found in both Seyfert galaxies and low redshift radio-quiet AGN, which is believed to be driven by the star formation (Sargent et al. 2010).

The origin of the radio emission in radio-quiet AGN is thus still highly debated and the possibility of small scale jets or wind-like outflows still possible. Furthermore, the addition to the study of the Zhu+ radio loud sample which partly overlap the L&R sample, suggests that the JED-SAD model is still relevant.

5.7.2 Clues from spectral shape

Already in Chapter 2, some clues could be extracted from the spectral shape observed for different black hole masses. In Fig. 2.7, I plotted the JED-SAD spectrum obtained for three different black hole masses. Even with the nine order of magnitude of difference between the XrB and AGN black hole mass, similar spectral shape can be observed when all the JED-SAD parameters are the same. In Sec. 2.3.2, I

showed that this can be explained as a solution $(\epsilon;\tau)$ is solution of the energy equation for any given black hole mass. However, as seen in Fig. 2.8, this does not mean that the spectral composition is similar.

The absence of difference in the X-ray spectral shape with the mass implies that something must be different in the JED-SAD parameters between the low and high black hole mass AGN. Indeed, the correlation between the UV and X-ray emission is not linear. The disk luminosity can be approximated by $L_{SAD} \sim \frac{GM\dot{M}}{2R_J}$ and the JED luminosity by $L_{JED} \sim \eta_X \frac{GM\dot{M}}{2R_{isco}} \left[1 - \left(\frac{r_{isco}}{r_J}\right)^{1-p}\right] \sim \eta_X L_{SAD} \left[\left(\frac{r_J}{r_{isco}}\right) - 1\right]$ (with the assumption $p = 0.01 \ll 1$), where η_X is the radiative efficiency in the X-ray. This is of course an over-simplification that forgets the evolution of the disk temperature with the parameters. As such, assuming the same JED-SAD parameters for all black hole mass, one would expect a linear correlation between the UV and X-ray monochromatic luminosities. Similar conclusions were pointed out of the JED-SAD simulations using different relations $r_J(\dot{m})$ in Sec. 5.4.1 (see Fig. 5.15 for instance) and from the relevant parameter space obtained from the MC draw in Sec. 5.5 (see Fig. 5.18). Something must evolve with the black hole mass.

5.7.3 Inefficient or starved massive AGN?

One possibility would rely on the variation of the X-ray emission efficiency η_X with the black hole mass. If the radiative efficiency is a function of the mass accretion rate $\eta_X(\dot{m})$, it could imply a non-linearity in the UV–X-ray correlation.

Power in the corona

One can compute the available power within the JED region from Eq. 5.7. This power is affected both by the mass accretion rate $\dot{m}$ and the ratio between the transition radius r_J and the ICSO r_{isco} and can be written as

$$P_{JED} = L_{Edd}\,\dot{m}\frac{(1-b)}{2r_{isco}}\left[1 - \left(\frac{r_{isco}}{r_J}\right)^{1-p}\right] \tag{5.9}$$

In Fig. 5.29, I plot in the top panel the Eddington ratio of the power available in the JED in the simulated L&R sample. I separate the functional dependency in two panels: $\dot{m}$ in the middle panel and $\frac{(1-b)}{2r_{isco}}\left[1 - \left(\frac{r_{isco}}{r_J}\right)^{1-p}\right]$ in the bottom panel. Multiple points can be raised: 1) the power available inside of the corona decreases with the black hole mass, and 2) this evolution is mostly driven by the variation of the mass accretion rate and not the size of the corona (r_{isco}/r_J).

One can go further, and compute the Eddington ratio of the cooling power: $P_{cool}/L_{Edd} = L_{JED}/L_{Edd} = \eta_X P_{JED}/L_{Edd}$. Since the main functional dependency of P_{JED} is in $\dot{m}$, P_{cool} is directly related to the product $\eta_X\dot{m}$. In Fig. 5.30, I plot the Eddington ratio of the cooling power as function of the black hole mass and mass accretion rate for the simulated L&R sample (with same density distribution in the UV–X-ray plane). The Eddington ratio of the cooling power seems to decrease with both the mass accretion rate and the black hole mass. This is confirmed within the 10 thousands spectra pool from which the simulated sample is drawn. One can estimate the X-ray radiative efficiency by computing $\eta_X \approx P_{cool}/(\dot{m}\,L_{Edd})$. Fitting the evolution $\eta_X(\dot{m})$ and $\eta_X(m)$ reveals correlation with a weak index: $\eta_X(\dot{m}) \propto \dot{m}^{-0.06}$ and $\eta_X(m) \propto m^{-0.02}$. Thus suggesting that the UV–X-ray correlation is rather driven

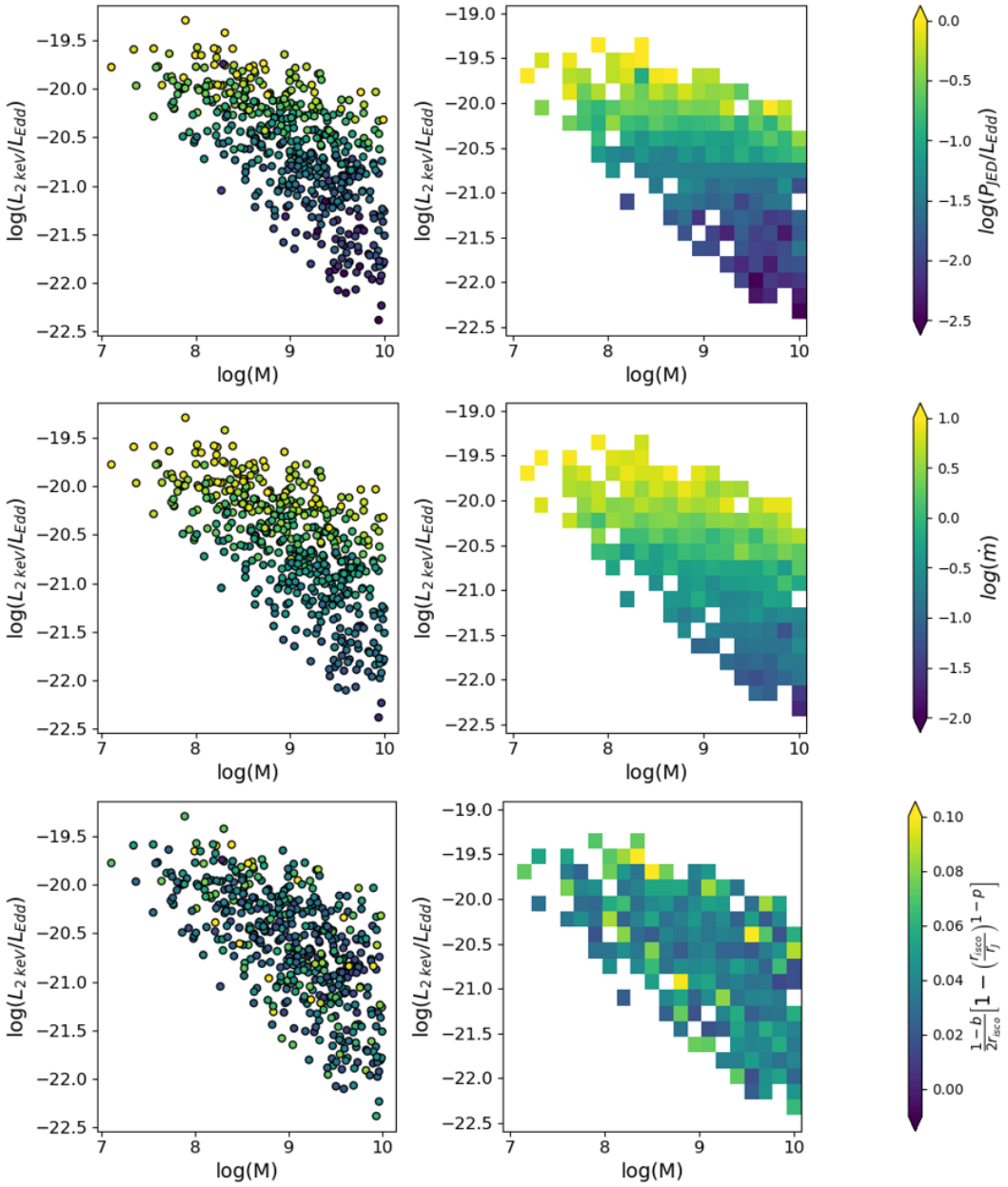

FIGURE 5.29: Distribution of the X-ray Eddington ratio $L_{2\,keV}/L_{Edd}$ with the black hole mass for the simulated L&R sample. Left: scatter plot, right: mean local value. The color shows the logarithm of the Eddington ratio of the power present in the JED $log(P_{JED}/L_{Edd})$ (top), the mass accretion rate $\dot{m}$ (middle) and the other functional dependency on the JED-SAD parameters $\frac{(1-b)}{2r_{isco}}\left[1-\left(\frac{r_{isco}}{r_J}\right)^{1-p}\right]$ (bottom).

by the evolution of the mass accretion rate with the black hole mass rather than from an evolution of the X-ray radiative efficiency.

Starved AGN

We observe a correlation between the black hole mass and the mass accretion rate in all three simulated samples. Its main implication is that one can reproduce a given luminosity by playing with either the black hole mass or the mass accretion rate.

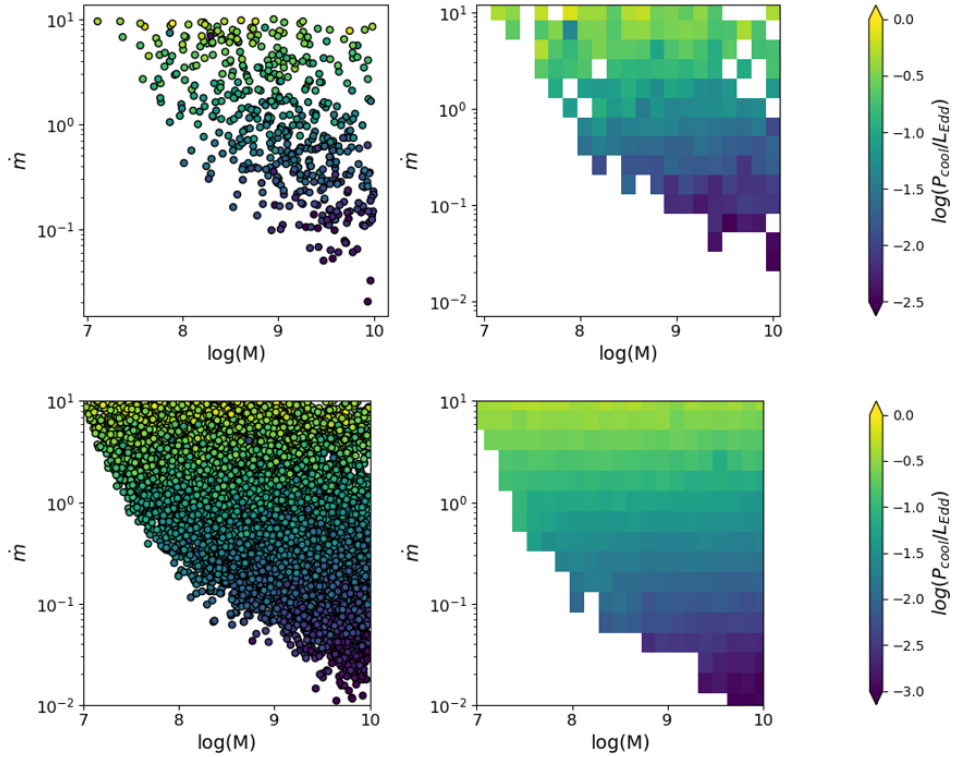

FIGURE 5.30: Distribution of the Eddington ratio of the cooling power P_{cool}/L_{Edd} within the plane $(m;\dot{m})$ for the simulated L&R sample. Left: scatter plot, right: mean local value. The color shows the logarithm of the Eddington ratio of the cooling power P_{cool}/L_{Edd} for the simulated sample with the same distribution within the UV–X-ray plane (top) and for the 10 thousands spectra pool from which it is drawn.

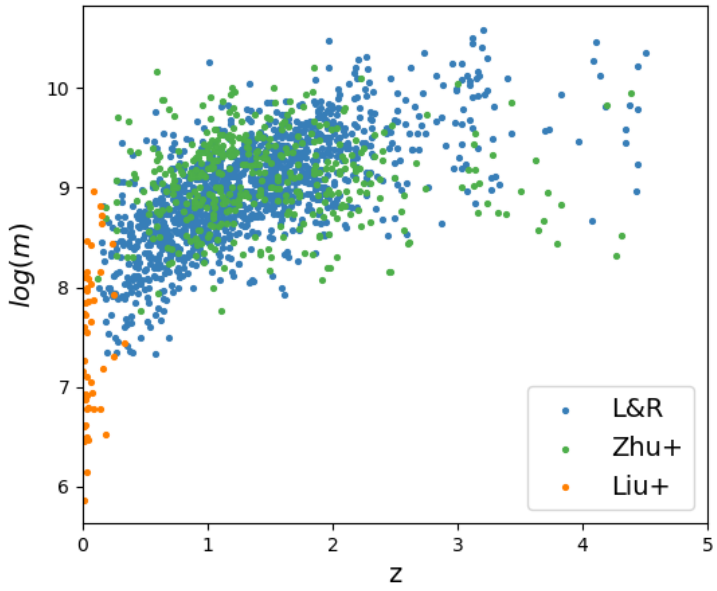

FIGURE 5.31: Distribution of the black hole mass with the redshift for all three samples. In blue the L&R sample (Lusso et al. 2020), in green the Zhu+ sample (Zhu et al. 2020), and in orange the Liu+ sample (Liu et al. 2021).

We can, however, understand the lack of AGN below the correlation since they may be to faint to be detected. This can imply a selection bias due to 1) the interplay between the mass accretion rate and black hole masses and 2) the distribution of black hole masses with redshift. Indeed large AGN are rare in the local universe and one must look at higher redshift to find them. There, low mass AGN are less likely to be observed as they would require a vary large mass accretion rate to be detected (the flux evolves as D^{-2}). In Fig. 5.31, I plot the distribution of black hole masses with the redshift z for all three observed samples. This effect is indeed visible in the samples. Low mass AGN ($log(m) \leq 8$) are not observed at high redshift ($z \geq 1$)).

The absence of points above the correlation at high black hole masses is also interesting. Indeed, large black hole mass AGN with high mass accretion rate should be even more luminous, and thus easier to detect. So why are they not observed in the samples? Their absence suggests that high black hole masses can not accrete at large Eddington rates. Massive AGN would then form a population of *starved* AGN for which the surrounding material is not sufficient to feed the black hole at large Eddington rate ($\dot{m} < 1$). Observationally, Aird et al. (2018) shows that the probability distribution of specific black hole accretion rates evolves with both redshift and black hole mass. In fact, at a given redshift, the peak of the distribution shifts toward lower accretion rates the larger the mass is (see their Figure 3 and 4), supporting the result obtained here. In Fig. 5.32, I present a sketch explaining how the correlation between the mass accretion rate and the black hole mass can result in the

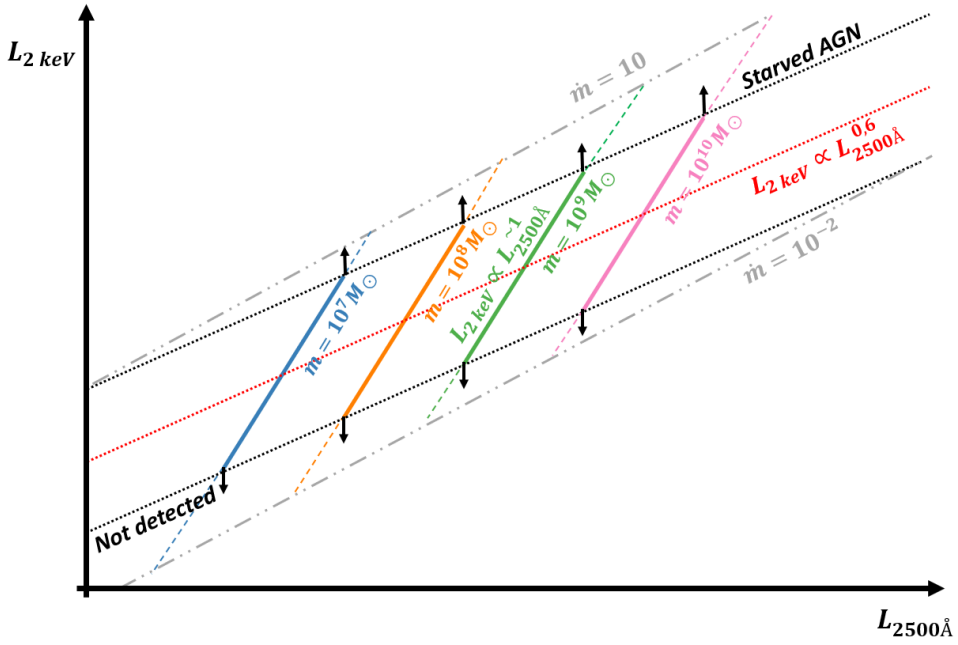

FIGURE 5.32: Interpretation of the non-linear UV–X-ray correlation based on the starved massive AGN idea. The red dotted line shows the observed UV–X-ray correlation, the black dotted line present the upper and lower limit of the observed AGN: Below the lower limit, AGN are not luminous enough in X-ray to be detected. Above the upper limit, the more massive AGN can not reach high mass accretion rate as there is not enough material to feed them and thus no AGN exist in this region. The grey dashed-dotted line show the equi-$\dot{m}$ lines. The solid line show the observed AGN at a given black hole mass (10^7 in blue, 10^8 in orange, 10^9 in green, 10^{10} in pink). These tracks follow a linear correlation (see discussion in Sec. 5.7.2. The colored dashed line show the continuity of the solid line at a given black hole mass in the regions where no AGN are observed.

non linear UV–X-ray correlation. The lower black hole masses can only be detected if they accrete at a high enough mass accretion rate, introducing a bias towards the higher $\dot{m}$ at low black hole mass. The higher black hole masses can not be fed up to high Eddington rate, introducing a bias towards the lower $\dot{m}$ at high black hole mass.

This interpretation is different to the one obtained by Kubota & Done (2018). They concluded that higher black hole masses required higher mass accretion rate to be on the correlation. They however used a constant power level within the hot corona (2% Eddington). In consequence, the size r_{hot} of their corona evolved with the mass accretion rate.

It should however be noted that the results obtained from my analysis are based on the luminosity and does not take into account any distance. Yet partially explaining the non linearity of the correlation using observational bias from detection limits arguments should involve the X-ray flux and not the X-ray luminosity. Further thought should be spend on this.

5.7.4 Toy model for an AGN outburst

When one does the simple exercise of plotting the values $(r_J; \dot{m})$ obtained from the XrB GX 339-4 outbursts (Marcel et al. 2022), re-scaled to AGN black hole masses, in the UV–X-ray plane, multiple interpretations and points can be discusses.

Trying to explain the UV–X-ray correlation from the accretion flow evolution observed during an XrB outburst shows that the samples can mostly be interpreted as transition states (between the hard and soft states). This is seen both in Fig. 5.28 and from the results of the MC draw where a constant value of $r_J \in [5, 20]$ was recovered to explain the L&R and Zhu+ samples, a range of values consistent with what is observed during the XrB transition states.

However, more intriguing is the absence of the detection of the equivalent hard branch re-scaled to high mass accretion rate ($m \geq 10^9 M_\odot$). Indeed, in Fig. 5.28, the equivalent hard branch appear above the samples at high black hole masses. Similarly, when testing relations between r_J and $\dot{m}$ akin to the one observed during XrB hard states, the tracks appear parallel but above the samples for the high black hole masses. So where is the AGN equivalent hard branch? As it should be more X-ray luminous than the observed samples, these objects should be easier to detect. Yet they are completely absent from the L&R sample and more generally from the UV–X-ray correlation. A possible explanation is that they are present within the sample and have much smaller transition radius r_J compared to an XrB outburst.

Re-scaling an XrB outburst up to supermassive black holes is however not a clear-cut process and one should be careful with its interpretation. The accretion within supermassive black hole is not fed from a companion star but from a large gas torus present in the center of the galaxy. The nature of the accretion flow is not necessarily the same, the disk density and temperature being much smaller in AGN compared to XrB. And what about the magnetic fields? In the JED-SAD paradigm, the accretion flow acts as a reservoir of magnetic fields that is being moved during an outburst.

5.7.5 Conclusion and prospects

I have shown that the JED-SAD model is able to reproduce all points along the UV–X-ray correlation. I have constrained the relevant parameter space for the L&R

(Lusso et al. 2020), Zhu+ (Zhu et al. 2020) and Liu+ (Liu et al. 2021) samples by drawing simulated samples with similar density distribution within the UV–X-ray plane. I argue that the accretion-ejection parameters within AGN must evolve with the black hole mass to explain the observed UV–X-ray correlation. The constrained parameter space for each sample is slightly different but could still generally be interpreted as equivalent to the transition states observed in XrB outbursts. Trying to explain the correlation as a sample of AGN at different stages of their outburst requires changes in the relation $r_J(\dot{m})$ with the black hole mass during the hard states. The absence of high Eddington rate massive black hole from our simulated sample finds echoes within the observational literature. My result suggests that this decrease of the mass accretion rate drives a lower coronal power within high mass black hole.

The physical explanation behind this evolution with the mass is however still unclear. Similarly, the natural dispersion of the correlation (± 1 dex) does not allow to constrain the possible power relation between r_J and $\dot{m}$ expected in the XrB hard states.

When I try to produce a sample with equivalent density distribution in the UV-X-ray plane I do not perfectly reproduce the black hole mass and X-ray spectral index distributions within the UV–X-ray plane. The next step would be to add these two new constrains in the drawing procedure so that I check the three conditions: 1) an equivalent density distribution of points in the UV–X-ray plane; 2) a mass distribution respecting the evolution observed along the UV–X-ray plane; and 3) a spectral index Γ distribution respecting the evolution observed along the UV–X-ray plane. Two of these conditions can be forced before computing any spectra: I can select a number of points to draw within each square $(dL_{UV};dL_X)_i$ based on the sample's kernel in the UV–X-ray plane. Simultaneously, I can assign a black hole mass to each of these points based on the local mass distribution within the square $(dL_{UV};dL_X)_i$. Similarly I can assign an X-ray spectral index Γ_i to each point. I will then have to find a set of JED-SAD parameters (r_J;$\dot{m}$;r_{isco};ω;m_s;b) which, combined with the preselected black hole mass, produces a spectrum verifying: $(L_{UV};L_X) \in (dL_{UV};dL_X)_i$ and $\Gamma \in \Gamma_i \pm \delta\Gamma$, where L_{UV}, L_X and Γ are the monochromatic UV and X-ray luminosity and the X-ray spectral index that I extract from the spectrum, and $\delta\Gamma$ is the error that I accept on the measurement of Γ. This is part of a work in progress.

Another direction for future works involves the presence of a Wind Emitting Disk (WED) instead of a JED. The WED is a solution of the MHD equations characterized by a low magnetization $\mu \sim 0.005 \rightarrow 0.1]$ and high a ejection index p $p \sim 0.1 \rightarrow 3$ (Jacquemin-Ide et al. 2019). The WED launches massive wind-like outflows instead of collimated jets. The main problem with the existence of a WED instead of a JED is that a WED is characterized by sub-sonic accretion speed and thus quite cold. A WED can not play the role of the hot corona. Another possibility would be the hot JED solutions (Casse & Ferreira 2000) where coronal heating is present. In this case, strong ejection index up to 0.5 were observed.

In this thesis, the ejection parameter p was frozen to 0.01 as within the range of existence of a JED ($p \ll 0.1$), the spectral variation is not very large. The mass accretion rate at the transition radius and within the SAD can be much more important than the mass accretion rate at the ISCO given strong ejection index: $\dot{m}(r_{SAD}) = \dot{m}(r_J) = \dot{m}\,(r_J/r_{isco})^p$. This can lead to a stronger UV emission while keeping the same global X-ray emission. However, assuming $r_J = 30$ and $r_{isco} = 2$, the variation of mass accretion rate within the SAD between a JED (p=0.01) and a hot JED (p=0.5) is only a factor 3.8 which does not seem enough to explain the dex missing in the UV

emission at high black hole mass to translate the XrB hard branch on the correlation track. Stronger ejection index would be required. This remains an interesting lead that should be further developed.

Chapter 6

Other AGN applications and Prospects

Contents

6.1 Soft X-ray excess 175
6.1.1 Context 175
6.1.2 TITAN-NOAR tables 176
6.1.3 XMM–HST survey of RX J1355+5612 177
6.2 Linking AGN population to outburst accretion states 179
6.2.1 Context and sample 179
6.2.2 Collaboration plan 179
6.2.3 First results 179
6.3 Other prospects 182
6.3.1 Other AGN correlation 182
6.3.2 Origin of the radio emission in radio-quiet AGN 182

Dans ce chapitre, je présente d'autres applications sur les NAG sur lesquelles j'ai travaillées au cours de ma thèse.

Excès X mou

J'ai déjà introduit l'excès X mou au cours du chapitre 5. Il existe plusieurs modèles concurrents pour expliquer cet excès sous 2 keV. Un de ces modèles est le modèle de couronne tiède. C'est avec ce modèle que j'ai travaillé dans une collaboration internationale financée par l'ISSI et dirigée par mon directeur de thèse Pierre-Olivier Petrucci et Giorgio Matt (voir le site web https://sites.google.com/view/issi-warmcorona/home?authuser=0). Dans le modèle de disque tiède, on trouve une couronne tiède au dessus du disque externe froid (voir schéma en Fig. 6.1). Cette couronne d'épaisseur optique moyenne ($\tau \sim 20$) et faible température ($kt_e \sim 1$ keV) va comptoniser les photons émis par le disque froid et produire une émission sous forme de power-law à fort indice spectral ($\Gamma \sim 2.5$). En utilisant le code TITAN-NOAR, Dominik Gronkiewicz a créé des tables de spectres de ce modèle. J'ai ensuite appliqué ces tables à 99 observations d'un échantillon de 22 NAG utilisé dans l'article Petrucci et al. (2018). Certains exemples de ces ajustements peuvent être vu en Fig. 6.2 et dans la Tab. 6.1. Un article est en préparation.

Dans le cadre de cette collaboration, j'ai aussi obtenu du temps d'observations avec les satellites XMM et Hubble Space Telescope pour observer un NAG particulier et étudier l'origine de son émission X mou à partir d'ajustements spectraux et d'arguments de variabilités. Les observations sont planifiées pour le mois de Novembre 2022.

Relier les populations de NAG aux états des binaires X

Au cours de ma thèse, j'ai eu l'occasion de commencer un projet de recherche en collaboration avec Jiri Svoboda et son équipe (Prague, Rep. Tchèque). L'objectif de ce projet est d'appliquer le modèle JED-SAD à un large échantillon de NAG, de contraindre leurs paramètres et ensuite de comparer aux résultats obtenus pour les éruptions de binaires X afin de créer des liens entre les différentes population de NAG et les différents états d'accrétion-éjection des binaires X.

Cette collaboration a commencé au mois d'avril 2022 lorsque j'ai rendu visite à leur institut. En Fig. 6.5, on peut voir les premiers résultats provenant de l'interpolation de l'échantillon de Jiri Svoboda dans une grille du modèle JED-SAD.

6.1 Soft X-ray excess

This section introduces the work I realized inside of an international collaboration with the ISSI group 'Warm coronae in AGN' (see Website: https://sites.google.com/view/issi-warmcorona/home?authuser=0).

6.1.1 Context

Most unabsorbed AGN show an excess of emission under 2 keV when extrapolating the hard X-ray power-law measured in the 2-10 keV energy range. This excess emission is known as the Soft X-ray excess (Walter & Fink 1993; Gierliński & Done 2004; Bianchi et al. 2009). Multiple model have been proposed to explain the origin of this excess emission. The blurred ionized reflection (Crummy et al. 2006; Walton et al. 2013; Jiang et al. 2020) interpretation generally requires a extreme value for the spin, disk ionization and high density within the disk. The warm corona model (Ballantyne 2020) would at the observed temperature of $1keV$ be dominated by atomic opacities and the spectrum would not be dominated by comptonization. At the same time, absorption and emission lines should be expected but they are not observed (see also García et al. 2019 for a discussion on the two models). The model of a warm comptonization atmosphere above the disk has been tested in the 'two-coronae' scenario (see sketch in Fig. 6.1). In this scenario, the inner region of the accretion flow is an optically thin ($\tau \sim 20$) and warm ($kt_e \sim 1$ keV) corona producing the usually observed hard X-ray emission, the outer region is vertically stratified with an optically thick ($\tau \sim 20$) and warm ($kt_e \sim 1$ keV) layer (the warm corona) above the standard

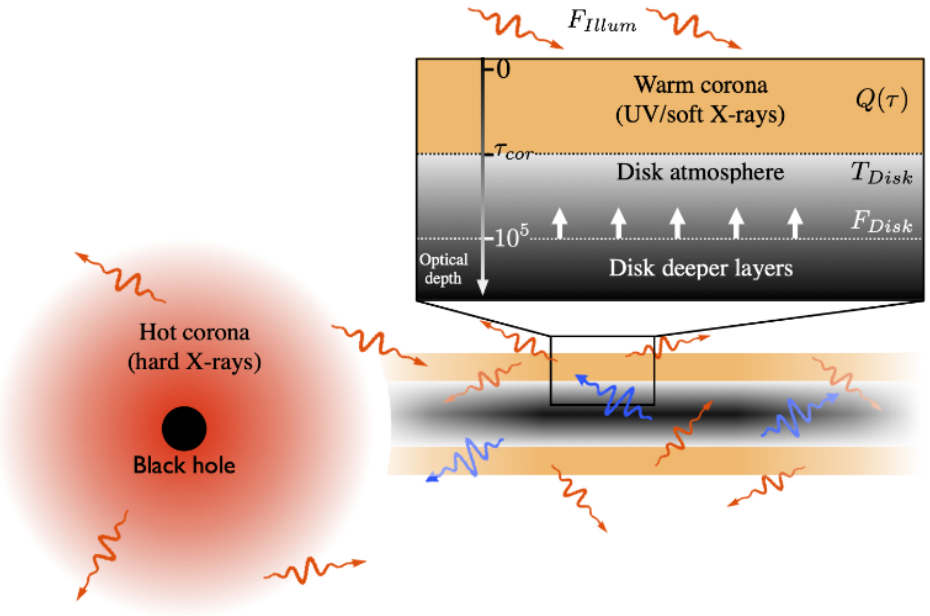

FIGURE 6.1: Fig. 1 from Petrucci et al. (2020). Sketch of the two coronae scenario. The optically thin ($\tau \sim 20$) and warm ($kt_e \sim 1$ keV) corona in the inner regions of the accretion flow produces the observed comptonized hard X-ray emission. Above the standard disk, an optically thick ($\tau \sim 20$) and warm ($kt_e \sim 1$ keV) atmosphere, possessing a source of internal heating q_h, is illuminated from above by the hot corona and produce the emission from the UV to the X-rays. See also Fig. 1 in Różańska et al. (2015).

cold accretion disk (Magdziarz et al. 1998; Jin et al. 2012; Petrucci et al. 2013, 2018). The warm corona reprocesses and transmits the photons coming from below and is also illuminated by the hot corona from above, producing emission from the UV to the soft X-ray. This warm corona must also be heated internally (Różańska et al. 2015; Petrucci et al. 2020). This internal heating is also supported by recent MHD simulations where a weakly magnetized standard disk appear vertically structured with an accreting layer on the surface (see for instance Figs. 3 and 4 in Jacquemin-Ide et al. 2021), possibly allowing most of the accretion power to be deposited at the disk surface. The two coronae scenario has been successfully applied to multiple AGN (Magdziarz et al. 1998; Jin et al. 2012; Matt et al. 2014; Ursini et al. 2016, 2018; Kubota & Done 2018; Middei et al. 2018, 2019, 2020). The goal of the ISSI collaboration 'Warm coronae in AGN' is to shed light on the origin of the soft X-ray excess observed in AGN by fitting observations using two different codes computing the effect of a warm corona above the disk. The REXCOR model (Xiang et al. 2022) and the TITAN-NOAR code.

6.1.2 TITAN-NOAR tables

One of the two codes used in this collaboration is the TITAN-NOAR code (used in Petrucci et al. 2020. TITAN is radiative transfer code (Dumont et al. 2000, 2003) able to compute, within a 1D box the structure and angle-dependent emergent spectra of hot photo-ionized gas by solving the radiative transfer simultaneously with ionization and thermal equilibrium. NOAR (Dumont et al. 2000; Abrassart & Dumont 2001) is a Monte Carlo code computing 1) the compton heating/cooling rate, 2) the reflection given an illuminating spectrum, and 3) fluorescent lines, given ionization levels, which can be Compton-broadened. The main parameters of the TITAN-NOAR model are the optical depth of the corona, the internal heating of the corona, the density of the corona, the temperature of the black-body emission radiating from below and the parameters of the illumination. Dominik Gronkiewicz produced tables of the TITAN-NOAR code with two parameters: optical depth τ and corona heating q_h. Following the results of Petrucci et al. (2020), the relevant parameters were estimated between: $\tau = 5 \rightarrow 30$ for the optical depth; and $q_h = 10^{-23} \rightarrow 3 \cdot 10^{-22}\, erg\ cm^3\ s^{-1}$. This first version of the table assume a single temperature underneath the corona and only present the warm corona transmission (no reflection spectrum). The development of a table adapted to accretion disks is a work in progress.

Fits

The sample we use is the PICS sample used in Petrucci et al. (2018), it is composed of radio-quiet, unobscured AGN ($N_H < 2 \times 10^{22} cm^2$). There are 100 *XMM* observations (PN+OM) for 22 different AGN. The combination of the X-ray spectrum from *XMM*/PN and optical fluxes from *XMM*/OM allows to get a good overview of the spectral shape stretching from the standard accretion disk to the soft X and hard X-rays. The current TITAN-NOAR table is only using a single balckbody of fixed temperature (instead of a disk blackbody) to illuminate the corona from below. In consequence, the table is missing the sum of the Rayleigh-Jeans function observed at low energy. As such I only fit the X-ray spectrum for the moment.

I fitted spectra from 8 different sources (the details of which are reported on the collaboration Website). I will not enter into the details of the fitting procedure. The model used is PHABS * (CST * TITAN-NOAR + NTHCOMP + XILLVER_CP). The

constant Cst is used to take into account the distance of the source. Some spectra presented absorption lines that required the introduction of Gaussian absorption lines. In Fig. 6.2, I show two examples of fits and residuals using the TITAN-NOAR tables for LBQS 1228+1116 (left, obsID: 0306630201) and Mrk 509 (right, obsID: 0130720101).

Optical depth τ and heating q_h

The next step will be the production of a TITAN-NOAR illuminated from below by a disk blackbody (instead of a single temperature blackbody), the addition of UV fluxes to the fit and fitting the complete PICS sample using the new TITAN-NOAR table. This will allow us to compare the warm corona parameters over a large sample and check whether indeed the parameters are always in the same region of the parameter space.

6.1.3 XMM–HST survey of RX J1355+5612

During my PhD, I had the opportunity to apply for observing time at the XMM AO21. The goal of the proposal is to observe an ultra-soft narrow line Seyfert 1 (US-NLS1) source named RX J1355.2+5612. Ultra Soft Narrow Line Seyfert 1 (US-NLS1) have very peculiar optical and X-ray spectral properties. Like standard NLS1 galaxies, they potentially host a black hole accreting around or above the Eddington limit. They are also characterised by strong [Fe II] emission, weak [O III] emission, and a

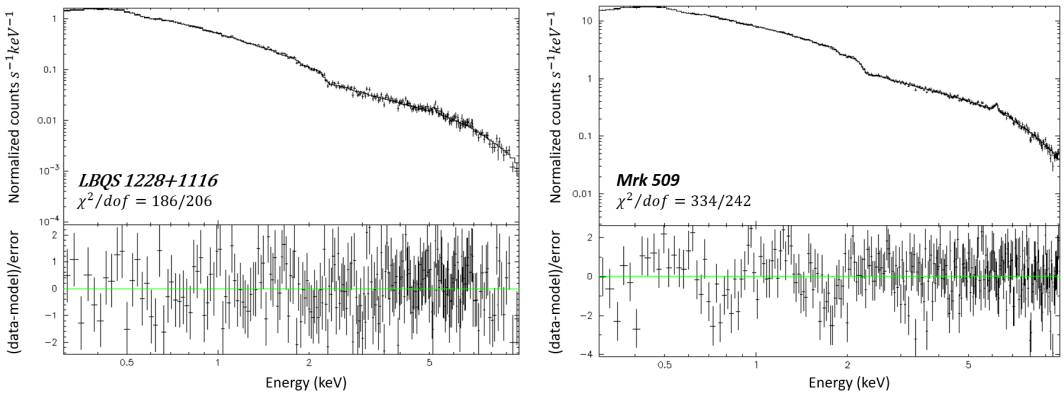

FIGURE 6.2: Examples of residuals while fitting some objects of the PICS sample using the TITAN-NOAR tables. Left: LBQS 1228+1116; Right: Mrk 509.

TABLE 6.1: JED-SAD parameters of the best fit of Cyg X-1.

Object	Observation ID	χ^2/dof	τ	$log(q_h)^a$
NGC 7469	0112170101	268/238	20.4	-22.59
	0112170301	265/240	20.4	-22.63
Mrk 509	0130720101	334/242	22.3	-22.48
1H0419-577	0112600401	169/203	10.4	-22.17
ESO198-G24	0067190101	313/240	18.2	-22.23
PKS 0405-123	0202210301	204/225	12.1	-21.91
HE1029-1401	0203770101	300/241	27.8	-22.46
LBQS1228+1116	0306630201	186/206	15.6	-22.32

Notes: $^{(a)}$: units are in $erg\ cm^3\ s^{-1}$.

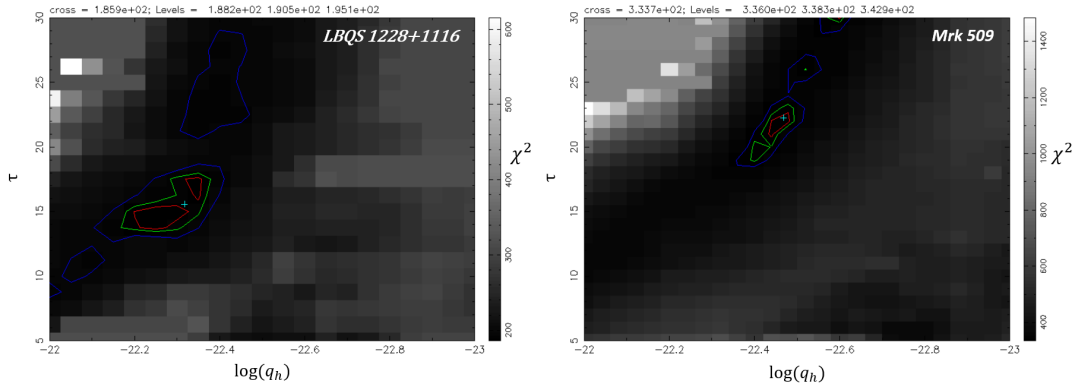

FIGURE 6.3: Contours between the two parameters of the TITAN-NOAR table: the optical depth τ and corona heating $log(q_h)$. Left: LBQS 1228+1116; Right: Mrk 509. The blue, green and red contours marks respectively confidence contour levels at 68%, 90%, and 99% ($\Delta\chi^2$ of 2.3, 4.61, and 9.2).

narrow Hβ line Osterbrock & Phillips (1977); Goodrich (1989). In the X-rays, they exhibit a much steeper continuum in comparison with average Seyferts (i.e. photon indices Γ of 2.0-2.5 instead of 1.5-2), and a strong, highly variable soft excess Gallo (2018). However, the origin of the broad-band continuum is still debated. A recent study has shown that the *XMM/OM+pn* data of five US-NLS1 are consistent with a relativistic blurred reflection model Jiang et al. (2020). Nevertheless, for at least one of these objects (RX J0439.6-5311), the two-corona model provides also a nice fit Jin et al. (2017a,b). These results show that, with the present data, it is not possible to conclude on the nature of the broad-band continuum in this peculiar class of objects. We thus proposed a multi-wavelength monitoring campaign to disentangle the different spectral components present in these sources and improve our understanding of this very atypical type of AGN. Considering the high temperature of the US-NLS1 disk, we asked for an coordinated *XMM/HST* monitoring to constrain the disc flux and shape up to the FUV. The monitoring campaign strategy is to observe the source 5 short times separated by a 3-4 days. This will allow to put strong constrain on the disk flux and shape, allowing 1) to test and discriminate between a warm comptonization model and a blurred reflection model; and 2) use correlated variability arguments between the UV and X-ray on both short (lite travel time) and long timescale to identify which model reproduces the observations. We were granted 140 ks of XMM observations and 5 *HST* orbits divided in 5$\times$(27 ks *XMM* + 1 orbit *HST*). The observation is scheduled for November 2022 (XMM program 09033701; HST GO program 16896). The full proposal is attached at the end of this thesis.

6.2 Linking AGN population to outburst accretion states

This section presents the work started recently in collaboration with the group of Jiri Svoboda in Prague. The goal of the project is to fit their AGN sample using the JED-SAD model and link back to the different accretion states observed during an XrB outburst.

6.2.1 Context and sample

As the black hole mass are millions of times larger in AGN compared to XrB, the expected timescale of an AGN outburst would be millions of times larger, meaning millions to billions of years long. We can instead use the Ergodic theorem to associate the time dependent sequence of accretion-ejection seen in a single XrB to the stationary snapshots seen in multiple different AGN. This means that each AGN would represent a single accretion state, and looking at all AGN simultaneously would reveal an AGN outburst. Following this idea, multiple studies have tried to connect AGN population to XrB accretion states (Kording et al. 2006; Svoboda et al. 2017; Fernández-Ontiveros & Muñoz-Darias 2021; Moravec et al. 2022), some of which have already been discussed in Sec. 1.3.2. Of course this idea is far from trivial and the different local parameters of each AGN (black hole mass, spin, disk inclination, obscuration...) might introduce dispersion and blur the AGN outburst track.

The sample collected by Jiri's team contains spectral information on the UV and X-ray spectral shape, the radio flux as well as the black hole mass and redshift, for 2127 objects. In Fig. 6.4, I show the complete sample in a plot analogous to the HID. The sample shows both hard and soft sources over almost 3 order of magnitude of Eddington ratio.

6.2.2 Collaboration plan

The idea of this collaboration are:

1. Fit objects with the best X-ray signal to noise ratio from different region of the HID. This will put strong constraints on the JED-SAD accretion flow parameters.

2. From an interpolation over the HID (and possibly more constraints like the X-ray spectral index, disk temperature etc..), we will extract the main JED-SAD parameters for the complete sample.

3. Comparison between results of the interpolation and a proper fit with the JED-SAD will estimate the errors we make on the JED-SAD parameters for the complete sample.

4. We will use an independent study to identify the different AGN population within the sample.

5. We will compare the JED-SAD parameters obtained for each sample and see A) if the different populations are separated within the JED-SAD parameter space and B) how each population can be connected to XrB accretion states.

6.2.3 First results

This collaboration was officially started when I visited Jiri's team in Prague in April 2022. The following show preliminary results that we were able to obtain.

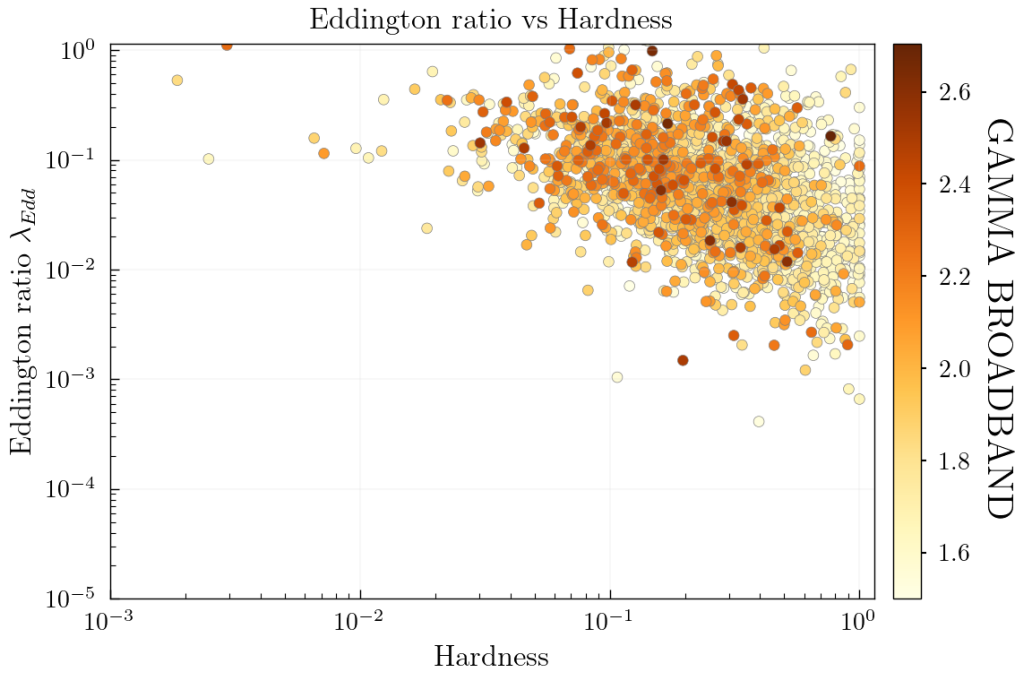

FIGURE 6.4: Sample collected by Jiri Soboda's team in an equivalent plot as the Hardness Intensity Diagram: Eddington ratio as a function of the power-law luminosity fraction. The Hardness here is defined as the ratio of the X-ray power-law luminosity over the total luminosity ($H = L_{pl}/L_{Tot} = L_{pl}/(L_{pl} + L_{disk})$). The points are coloured depending on the X-ray broad-band spectral index based on the comparison between the soft X-ray (0.5-2 keV) band and the hard X-ray (2-12 keV) band.

First fits

A selection of 30 observations over the complete HID with the best signal to noise ratio has been made. I fitted all 30 objects with the JED-SAD. However, if some spectra are easy to fit, others show very strong UV emission that the JED-SAD has difficulties to reproduce using the tabulated value of the black hole mass. I am currently computing a larger table that should alleviate this problem. The solution might actually lie with the presence of a hot JED solution (Casse & Ferreira 2000), with similar arguments as the one proposed in Sec. 5.7. This would involve the presence of massive winds that should allow to increase the mass accretion rate within the SAD and thus increase its emission.

To finish on a good note: the constrained JED-SAD parameters seem to show different values between the softest and hardest spectra, suggesting that we should be able to identify trend within the AGN population comparable to the one observed within XrB accretion states.

Interpolating the complete sample

I already extracted preliminary values of the JED-SAD parameters (r_J and $\dot{m}$) for the complete sample assuming constant values for the other parameters. This is obviously a caveat of this method as there is no reason for all of these objects to have e.g. the same ISCO (i.e. the same BH spin). In Fig. 6.5, I plot the coverage of the AGN HID with the JED-SAD simulations (left) and the resulting interpolated JED-SAD parameters (right) for the complete sample of Jiri. The dotted line at the

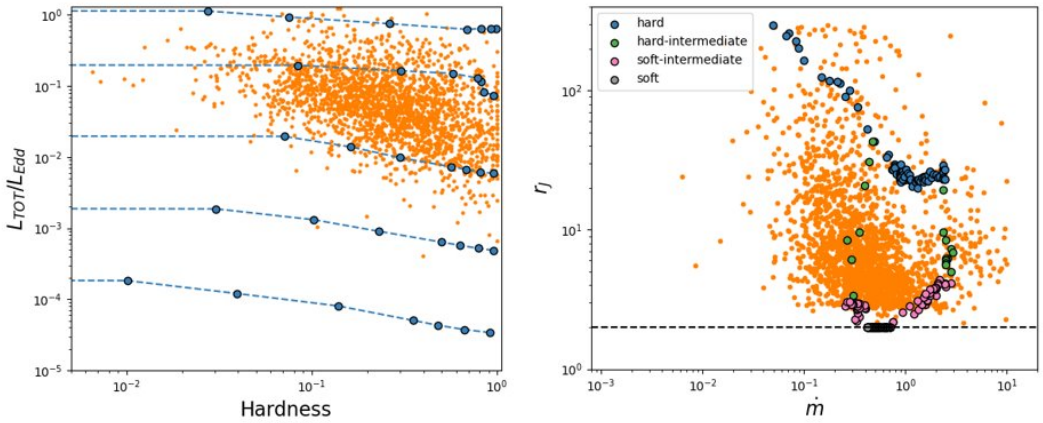

FIGURE 6.5: Interpolation of the main JED-SAD parameters (r_J and $\dot{m}$) over the complete sample. Left: HID, the orange points show the objects of Jiri's sample. The blue points show a grid of simulated JED-SAD spectra for different values of the the mass accretion rate $\dot{m}$ and the transition radius r_J. Right: Jiri's sample in the (r_J;$\dot{m}$) plane. The orange points are the objects of Jiri's sample. The blue, green, pink and grey points show the different spectral states observed during GX 339-4 outbursts (respectively hard, hard-intermediate, soft-intermediate and soft states, see Marcel et al. 2022).

bottom of the right panel show the ISCO. The fact that some AGN seem to be limited to $r_J = 3$ is an artifact of the preliminary method used: As simulated spectra with $r_J \sim r_{isco} = 2$ have almost no X-ray emission, the measured hardness is very small ($H \lll 10^{-3}$) and as such the interpolation stay close to the second lowest value in the grid: $r_J = 3$. Similarly to the results I obtained in the study of the UV–X-ray correlation, the sample seem mostly composed of transition state AGN.

6.3 Other prospects

6.3.1 Other AGN correlation

The work started by reproducing and drawing simulated sample consistent with the observed sample is only the beginning as many more spectral constrains can be added. In Jin et al. (2012), they studied a multitude of spectral shape parameters and the correlations they could find within their samples. These correlations can bring more constraints on the spectral shape of my simulated AGN sample.

Once a proper jet model related to the JED-SAD accretion flow parameters is added, one of the most interesting correlation to look at will be the fundamental plane of black hole activity (Merloni et al. 2003). This correlation linking the black hole mass with the hard X-ray and the radio emission, stretches from the XrB to the AGN and suggest strong similarities in the accretion-ejection processes of black hole at all mass scale. As such it is an interesting correlation to reproduce with the JED-SAD.

6.3.2 Origin of the radio emission in radio-quiet AGN

As discussed in Sec. 5.7.1, the nature of the radio emission in radio-quiet AGN is still highly debated. In Inoue & Doi (2018), they observed for the first time an excess of emission within the radio mm band above a flat radio continuum, attributed to the jet emission. This excess was interpreted as the emission from synchrotron emission from non-thermal particle present within the magnetized hot corona. They were able to put constraints on the size of the corona, its magnetic fields and the non-thermal population parameters. However some degeneracies still exist (Inoue et al. 2021). The addition of the JED-SAD constrains on the size and magnetic fields strength of the corona from the fit of the UV and X-ray thermal emission might be able to lift this degeneracy and put strong constrain on the non-thermal population. I am interested in adding a non-thermal electron population within the JED-SAD (from which they are currently absent).

Furthermore, in 2020 the IceCube collaboration reported the detection of a neutrino emission from NGC 1068, one of the nearest Seyfert galaxy. Inoue et al. (2021) proposed that this neutrino emission arises from Hadronic interactions (pp) or photomeson ($p\gamma$) of high energy particles inside the hot coronae of supermassive black holes. The physical process responsible for the acceleration of protons within the relatively small JED region $r_J \sim 20$ is however not clear. As such an hybrid thermal-non-thermal version of the JED-SAD should be able, for the first time with a single physical model, to fit: 1) the radio excess observed in the mm band, 2) the thermal emission in the UV and X-rays, 3) the -ray and possibly neutrino spectra coming from non-thermal emission inside of the corona, bringing unprecedented constrains on the non-thermal population and the accretion-ejection process in general. If a radio jet model linked with the JED-SAD model is added, one might also be able to add stronger constrains on the jet from fitting the flat radio jet spectrum.

Confrontation with XrB transitions states are also possible, as a hard non-thermal tail appear during these states. However the persistence of this hard tail during the soft states is hard to explain using the hybrid thermal-non-thermal JED-SAD paradigm.

Chapter 7

Conclusion

Contents

7.1 Summary of the work 184
7.2 Testing the JED-SAD model 185
7.2.1 Spectral energy distribution 185
7.2.2 Power density spectra, QPOs and timing 185
7.2.3 X-ray polarization 187
7.3 Future development and applications 187

7.1 Summary of the work

During my Ph.D. I had the opportunity to work on the accretion-ejection processes around black holes. The team I was part of is developing a model of accretion-ejection, the Jet Emitting Disk - Standard Accretion Disk (JED-SAD) model. In the JED-SAD model, the accretion flow is supposed threaded by a large-scale magnetic field. A radial startification of the magnetization is assumed with a highly magnetized inner region, allowing for the launch of the observed jets. Stemming from the self-similar solutions from (Ferreira 1997), this region is named the Jet Emitting Disk (JED). The outer region is lowly magnetized, resulting in a standard α-disc (Shakura & Sunyaev 1973), this region is named the Standard Accretion Disk (SAD). This radial stratification has been observed in multiple recent magneto-hydrodynamic simulations (Liska et al. 2020; Scepi et al. 2020; Jacquemin-Ide et al. 2021), validating our approach. Launching an outflow results in a magnetic torque exerted on the disk (Blandford & Payne 1982), transporting angular momentum vertically away and resulting in supersonic accretion speed inside the JED. This entails lower densities and optical depth, weaker cooling processes and thus a hotter (Electron temperature $kT_e \sim 100$ keV) and puffier disk (Height scale $H/R \sim 0.2$) compared to the SAD. It is thanks to this supersonic accretion speed that the JED can play the role of the hot corona and produce hard X-ray photons. One of the main asset of The JED-SAD model is that it is constrained to solutions that are physically viable. The model also presents a radial distribution of temperature and density which are not present in most model used in the community. Thanks to the work of Gregoire Marcel during his Ph.D. (Marcel 2018), a code producing the spectral output as well as the distribution of all physical parameters within the accretion flow exists. This code includes emission from bremsstrahlung, synchrotron and their comptonization, takes into account for cold seed photons produced by the SAD and comptonized within the JED as well as photons lost due to pair creation. This framework simultaneously explains both the spectral and jet dynamical evolution observed during XrB outbursts and has since been successfully applied to multiple X-ray binaries outbursts (Petrucci et al. 2010; Marcel et al. 2019, 2020; Barnier et al. 2022; Marino et al. 2021) as well as on a few AGN observations (Ursini et al. 2020). My PhD allowed me to get both an observational and theoretical expertise with the cutting-edge JED-SAD model as I applied the model on both XrB and AGN observations resulting in multiple publications (Barnier et al. 2022; Marino et al. 2021; Marcel et al. 2022, and Barnier et al. in prep.).

In Barnier et al. (2022), I produced the first spectral emission table of the JED-SAD model, allowing to directly fit observations of XrB. I fitted for the first time with the JED-SAD model 456 hard X-ray spectra of the XrB GX 339-4, allowing to constrain the physical configuration of the accretion flow and getting better constraints compared to the previous method used in Marcel et al. (2019). From this fits, we obtained a good picture of the evolution of the accretion flow during the hard states of GX 339-4 and allowing to understand the behaviour of the magnetic field during an XrB outbursts. I then studied the functional dependency of the radio flux coming from the jets with the accretion flow parameters. I discovered two mutually excluding solutions suggesting a possible change of the jet emitting processes and/or emission properties during the outburst. In Marino et al. (2021), I helped Alessio Marino to use the JED-SAD model and we successfully fitted observations of the XrB MAXI J1820 with data coming from 4 instruments (XRT, Nustar, BAT, Nicer), producing an exceptional spectral coverage between 0.8 and 190 keV.

In a second part of my Ph.D., I scaled the model up to the supermassive black hole and constrained the parameter space of the JED-SAD model able to reproduce the UV–X-ray correlation observed in the latest samples of AGN (Lusso et al. 2020). A paper is in preparation. Even though the conclusions of this work are not exactly clear yet, I showed that the model can be applied to AGN observations. As part of the 'Warm coronae in AGN' group of the International Space Science Institute in Bern (PI: Pierre-Olivier Petrucci and Giorgio Matt), I worked on the origin of the soft X-ray excess emission observed in most Active Galactic Nuclei. This soft X-ray excess (compared to the hard X-ray power law extrapolation at lower energy) has no clear counterpart in XrB. In this context I applied a newly developed model of warm atmosphere (optical depth $\tau \sim 10 \rightarrow 30$ and temperature $kT_e \sim 0.1$ keV, see Petrucci et al. 2020) standing above the accretion disk and comptonizing its emission. I applied the spectral model developed using the TITAN-NOAR code (Gronkiewicz & Różańska 2020) to a sample of AGN observations. Concurrently, I am also PI of a recently conducted XMM-HST simultaneous monitoring of a Narrow Line Seyfert 1 AGN (130 ks XMM program 090337 and 5 orbits HST GO program 16896 spred over 5 observations separated by 2-3 days each). The goal is to identify the origin of the soft X-ray emission in this source using both a spectral fitting approach and a variability argument.

7.2 Testing the JED-SAD model

7.2.1 Spectral energy distribution

The JED-SAD model is still in development and need to be tested against every physical quantities observable. In this thesis, the model was tested against the fundamental, elemental observable of astronomy: the spectral light emitted by the sources. I have thoroughly tested the model against X-ray spectra of XrB, I also applied the model to the broadband spectral correlation observed in AGN. This tests showed that the JED-SAD model could reproduce spectral energy distribution observed in the hard states of XrB outbursts. However, spectra are only a small fraction of the information astronomers are able to extract from a source, and the model needs to be confronted to many more observational aspects of the accretion-ejection process around black holes.

7.2.2 Power density spectra, QPOs and timing

As I have completely ignored these notions in my thesis, I feel it necessary to introduce them now. When an X-ray telescope observes a sources, it registers the number of photons impacting the detector at different energies and as a function of time. The averaging of these impacts during the complete observation produces the spectral energy distribution thoroughly discussed in this thesis. However, one can also extract the light curve (meaning the flux as a function of time) during the observation, or even further, the light curve within a given energy range.

The power density spectrum results from the Fourier transform from the X-ray light curve and thus show how the power is distributed as a function of the frequency of the light curve fluctuations. These fluctuations are believed to be created by perturbations within the accretion flow and characterised by a frequency equivalent to their accretion time scale which depends on the radius (see for instance Kawamura et al. 2022). This allows to map the regions of the accretion flow where perturbations exist. For instance, we know that the standard accretion disk observed

in the soft states of XrB present almost no fluctuations, whereas the region emitting the hard X-ray spectrum during the hard states is highly perturbed. Kawamura et al. (2022) showed that the inner region of the accretion flow need to present supersonic accretion to be able to explain the observed power density spectra, which is in accordance with the JED-SAD model.

Within the power density spectra close to the state transitions of XrB outbursts, one can observe 'peaks'. This means that at a given frequency a phenomenon is producing a lot of flux variations. These frequencies are called quasi-periodic oscillations (QPOs). Different types of QPOs have been identified and named A, B and C (see definition in Marcel et al. 2020 for instance). In Marcel et al. (2020), Gregoire Marcel identified a correlation between the frequency of the QPOs observed in the 4 outbursts of GX 339-4 discussed in this Ph.D. with the Keplerian frequency at the transition radius r_J deduced from the spectral analysis. This is encouraging, as the value of r_J are not deduced from the QPOs at all, only from the spectral energy distribution study. There is, a priori, no reason for us to obtain such a correlation between these two independent measurements. But the transition radius between the calm, lowly magnetized SAD and the perturbed, highly magnetized JED appears as a strong suspect for the production of the QPOs' perturbations. However a factor 100 remains unexplained. Usually, QPOs are explained using the Lense-Thirring precession (Lense & Thirring 1918), where the inner accretion flow is tilted and oscillating with respect of the outer accretion flow. The QPOs would then result from the perturbations at the interaction of the external accretion flow and the inner tilted accretion flow and from the propagation of sound waves within the inner accretion flow. However a recent (Marcel & Neilsen 2021) suggests that the condition for the Lense-Thirring effect as it is currently described in accretion flows can not be reached in the high luminous hard states of XrB outbursts where type C QPOs are observed. A new proposition from Ferreira et al. (2022) suggests that the perturbation could originate somewhere along the jets, possibly due to recollimation shocks, and get back down to the accretion flow along the outer edge of the jet, reaching the accretion flow at the transition radius of the JED and SAD. This is also investigated with the Ph.D. thesis of Thomas Jannaud in the same team, who is producing numerical simulation of MHD jets launched from a JED (expected to defend in 2023, see for instance Jannaud et al. 2022).

Finally, the light curves taken at different energy range can be used to study the timing and lags aspects. Indeed the light emitted at a given energy range can arrive 'later' compared to other energy range. For instance a perturbation produced at a given radius will then be propagated toward the black hole due to accretion. Yet the closer to the black hole one consider, the hotter the accretion flow will become. Thus the light fluctuation associated to this propagation will also change from one energy range to another as the perturbation approach the black hole. As such, there will be a delay of the harder energy range compared to the soft energy range due to the propagation of the fluctuations. However, at high frequencies, the inverse seems to be observed: the soft energy range will lags behind the hard X-ray energy range. This is explained as the soft band high frequencies oscillations mostly originate from the fluctuations in the reprocessed hard X-ray luminosity illuminating the flow. As such, the delay is now created by the light travel time between the different radii in the disc.

Julien Malzac (IRAP, Toulouse, France) and Gregoire Marcel are currently developing these aspects of the JED-SAD model, with a goal to one day fit simultaneously the spectral energy distribution, the power density spectrum and the lags of XrB observations. This is work in progress and a first paper is in preparation.

7.2.3 X-ray polarization

With the recent launch of the Imaging X-ray Polarimetry Explorer (IXPE) satellite, a window that was closed for 40 years was once again opened and we finally have measurements of the polarization of the X-ray photons coming from XrB. This point has already been briefly discussed in Chapter 4. What is interesting is that the recently measured polarisation angle observe din Cyg X-1 suggests that the region responsible for the hard X-ray emission is somewhere within the accretion flow rather than along the jets (Krawczynski et al. 2022). the results are strongly in favour of a geometry similar to the JED-SAD compared to the lamp-post geometry. To confront the JED-SAD model to this measurement, I have fitted the X-ray spectrum of Cyg X-1 and provided Wenda Zhang with the radial distribution of the physical quantities inside the accretion flow. With this, he is able to compute the expected polarization degree and angle for this JED-SAD configuration, that we will then be able to compare to the IXPE observation. This is part of a work in progress.

7.3 Future development and applications

Among the other development the team wants to pursue in the next few years, I can cite the development of a spectral jet radio model linked to the accretion flow. This is a difficult subject as there are many unknowns and uncertainties surrounding the jets. This project could be lead by Julien Malzac who has experience in developing spectral jet models (see the ISHEM model for instance Marino et al. 2020). Another possible development, is the introduction of the non thermal population within the JED-SAD model. This might change the thermal solutions used in this thesis. Both of these projects taken together could elevate the JED-SAD model to a broad-band spectral model whereas we are currently limited to the thermal emission in the UV and X-ray ranges. I am interested in both these projects and might be able to work on them during my first post-doctoral researcher position at the National Astronomical Observatory of Japan at Osaka university, Japan, with Yoshiyuki Inoue who is an expert in the modelisation of the non-thermal population emission.

One can also question the presence of slow but more massive winds emitted from either a Wind Emitting Disk (another region of the magnetization - ejection parameter space than the JED) or from the SAD itself. This work is lead by Maxime Parra, new Ph.D student of my supervisor Pierre-Olivier Petrucci.

Another interesting projects that I want to co-lead with my predecessor Gregoire Marcel is the continuation of the study of the radio X-ray correlation that I started with GX 339-4 and see what the JED-SAD model proposes for both the track of the outlier population and the track of the 'universal' correlation.

Finally, I wish to pursue the application of the JED-SAD model to AGN with the idea to try to connect the different population observe din AGN samples with different accretion states observed in the X-ray binaries' outbursts.

We are slowly but surely developing the model, confronting it to more and more observable quantities in both XrB and AGN. In some aspects, the model already performs quite well, in other, the model may require some modifications or adjustments to explain what is observed. But with each new problem we encounter, our understanding of how the model can work is progressing. The successful tests done until now offers a positive and encouraging work perspective for the future.

Appendix A

Opacity in the JED-SAD model

In this Appendix, I study the source of opacity within the JED-SAD. There are different processes that produces opacity (see Frank et al. 2002):

- Thomson scattering due to the elastic scattering of photons by an electron and producing the Thomson opacity κ_T. This opacity source generally dominates above 10^7 K. The Thomson opacity can be approximated by $\kappa_T \approx \sigma_T/m_p \approx 0.4\, cm^2 g^{-1}$.
- Free-Free absorption associated to the bremsstrahlung mechanism and is mostly important within highly ionized gas.
- Bound-Free absorption where a bound electron into a free state by a photon with sufficient energy, it is sometime called ionizing absorption and is responsible for the presence of edges within the spectrum.
- Bound-Bound absorption where a line photon is absorbed causing an electron to make an upward transition from a lower energy state to a higher energy state. It thus involves photons within a narrow energy range around given lines.

The Free-Free and Bound-Free absorption can be approximated through the Rosseland mean Kramer opacity law (Frank et al. 2002):

$$\kappa_K = 5 \cdot 10^{24}\, \rho T_c^{-7/2}\ cm^2 g^{-1} \tag{A.1}$$

Below 10^4 K, Hydrogen recombines and the Kramer opacity low is no longer valid. This might happen at the outer edges of the accretion disk.

One can show that within a standard disk (Shakura & Sunyaev 1973) Kramer's opacity dominates over the Thomson scattering above a radius R:

$$R \gtrsim 2.5 \cdot 10^7 \left(\frac{\dot{M}}{10^{16}\ g \cdot s^{-1}}\right)^{2/3} \left(\frac{M}{M_\odot}\right)^{1/3} f^{8/3}\ \ cm \tag{A.2}$$

with:

$$f = \left[1 - \left(\frac{R_{ISCO}}{R}\right)^{1/2}\right]^{1/4} \tag{A.3}$$

With $\dot{M}$ the mass accretion rate, M the black hole mass and R_{ISCO} is the radius of the ISCO.

Equivalently, we can show that Kramer's opacity dominates regions where:

$$\dot{M} = 3.3 \cdot 10^{-5} \left(\frac{R}{R_G} \right)^{3/2} f^{-4} \ \dot{M}_{Edd} \tag{A.4}$$

The JED-SAD model only takes into account the Thomson opacity and the Kramer opacity. Thus some region of the parameter space might not take into account the opacity correctly.

A.1 Kramer opacity

In Fig. A.1, I plot the value of the Kramer opacity (following Eq. A.1) as function of the radius for different values of the mass accretion rate and transition radius. This equation being independent of the black hole mass, I set the black hole mass to $5M_\odot$. The red line shows the equality between the Thomson opacity and Kramer opacity and is mostly consistent with Eq. A.4 inside of the SAD. Small deviations appear close to the transition radius due to the no-torque condition introduced there. For values of the transition radius generally encountered ($r_J < 100$), the Thomson opacity always dominates the JED region.

A.2 Other sources of opacity

In Fig. A.2, I plot the value of the electron temperature T_e as function of the radius for different values of the mass accretion rate and transition radius. I use a black hole mass of $10^8 M_\odot$ for an AGN. The red line shows the equi-temperature $T_e = 10^4$K below which hydrogen recombines and the Kramer opacity law is no longer valid. At high transition radius $r_J \gtrsim 100$, some ring of the JED are cold ($T_e \sim 10^5$K). For values of the transition radius generally encountered ($r_J < 100$), distant SAD rings ($r > 10^3 R_G$) can be cold enough to invalidate Kramer opacity law. It should be noted that higher black hole mass disk will be even colder and a smaller region of the disk will correctly take into account Kramer's opacity. At very high transition radius $r_J = 1000$ (a value not encountered for AGN within this thesis), even some rings of the JED can be cold enough to invalidate Kramer opacity law. However, the rings where the opacity is not well taken into account are not the most luminous rings of the JED or the SAD and shouldn't dominate the spectrum. Beside, this region of the parameter space is not encountered within this thesis.

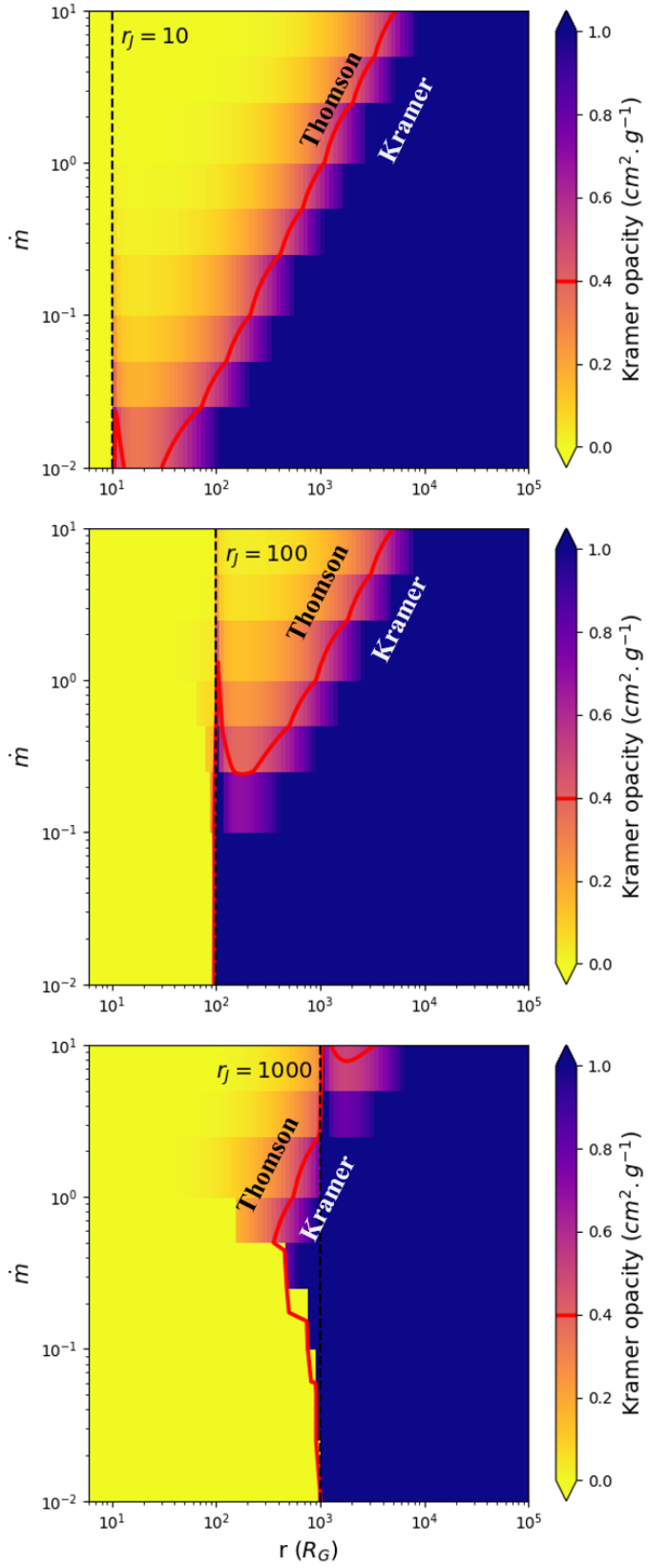

FIGURE A.1: Kramer opacity as function of the radius inside the JED-SAD for different values of the mass accretion rate and the transition radius r_J. Top: $r_J = 10$. Middle: $r_J = 100$. Bottom: $r_J = 1000$. The other JED-SAD parameters are fixed to: $m = 5$, $r_{isco} = 2$, $\omega = 0.1$, $m_s = 1.5$ and $b = 0.3$. The red line shows the equality between the Thomson opacity and Kramer opacity.

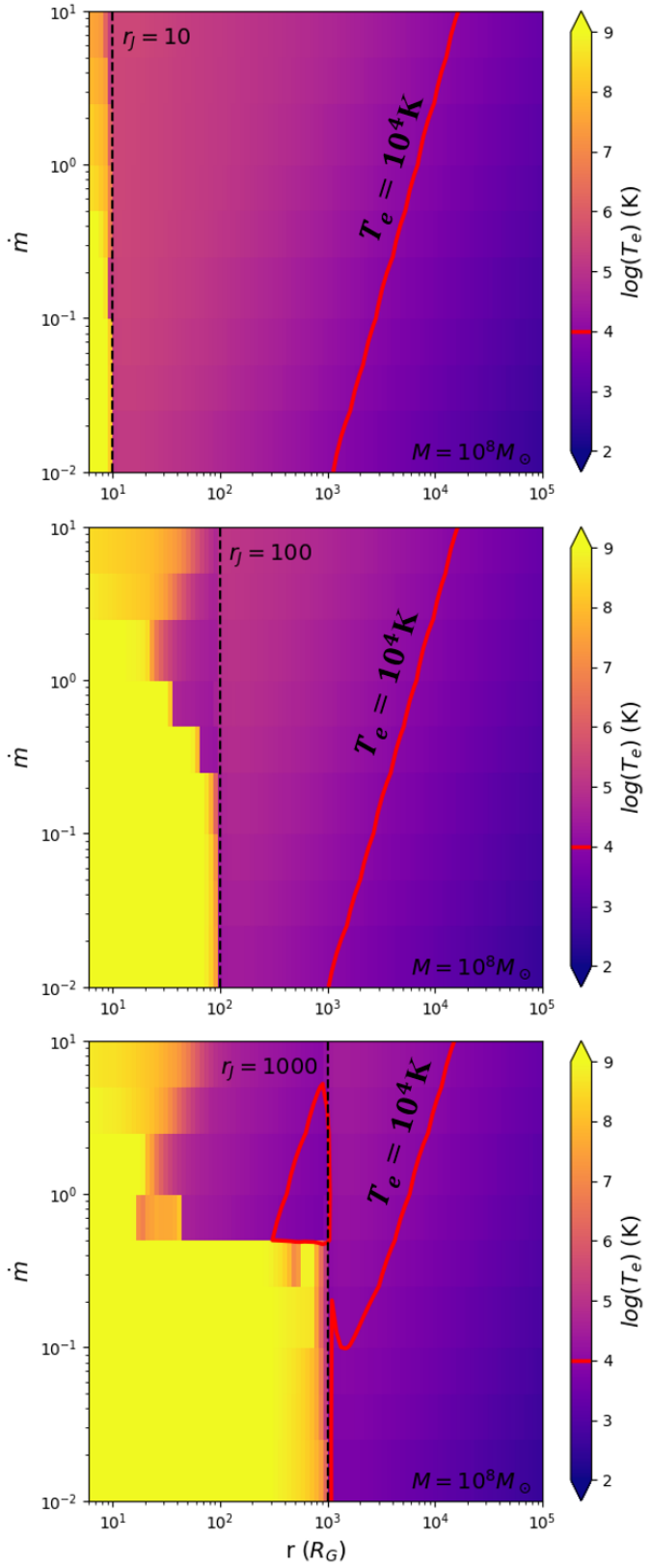

FIGURE A.2: Electron temperature as function of the radius inside the JED-SAD for different values of the mass accretion rate and the transition radius r_J. Top: $r_J = 10$. Middle: $r_J = 100$. Bottom: $r_J = 1000$. The other JED-SAD parameters are fixed to: $m = 10^8$, $r_{isco} = 2$, $\omega = 0.1$, $m_s = 1.5$ and $b = 0.3$. The red line shows the equi-temperature $T_e = 10^4$K below which the Kramer opacity law is no longer valid and the JED-SAD does not take into account opacity correctly.

Appendix B

GX 339-4 – Interpolation of the radio flux

With 80 almost daily X-ray observations and 24 radio flux measurements, the radio–X-ray survey of the hard states of the 2010-2011 outburst of GX 339-4 is the best in the available archive of *RXTE*. Considering the steady jet expected during the hard states of an outburst and the evenly spread radio survey, I opted to linearly interpolate the radio light curve to obtain a radio flux (at 9 GHz) for each X-ray observation. In Fig. B.1 I plot the radio light curve and the interpolated flux at the X-ray observation date.

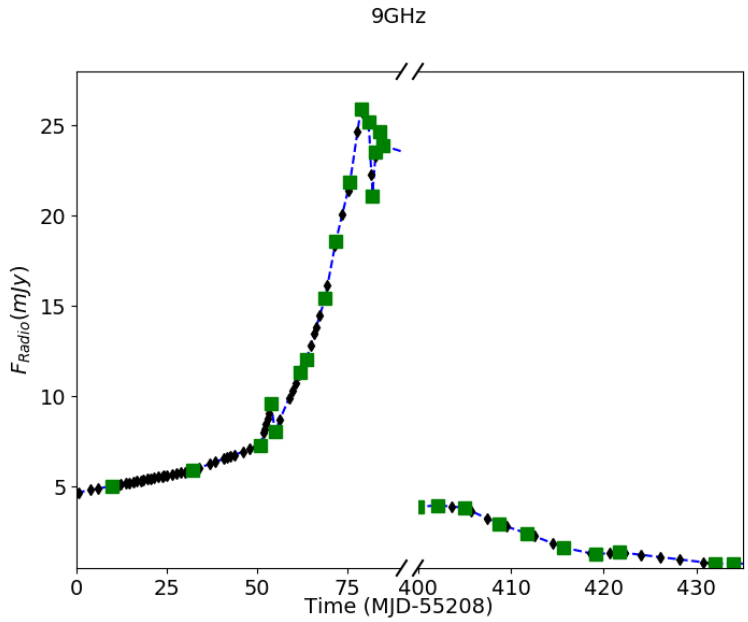

FIGURE B.1: Radio light curve of the 2010-2011 outburst during its hard states: between MJD 55208 and 55293, and between MJD 55608 and 55646. The green squares are the observed radio fluxes. The blue dashed line is the linearly interpolated/extrapolated function. The black diamonds are the interpolated radio fluxes at the date of the X-ray observations.

Appendix C

Grid (r_J;$\dot{m}$)

In this appendix, I show the figure presenting the influence of the JED-SAD parameters r_{isco}; ω; m_s and b on the JED-SAD coverage of the UV–X-ray plane. The corresponding figures are Figs. C.1, C.2, C.3 and C.4 respectively. At the exception of r_{ISCO}, these parameters only impact the JED thermal equilibrium and thus mostly impact the measured 2 keV luminosity. The ISCO can limit the lower range of r_J possible and thus limit the maximum temperature of the SAD. Thus it can in extreme cases have a small impact on the 2500Å luminosity just by limiting the possible range of values of r_J. These plots are discussed in Sec. 5.4.1.

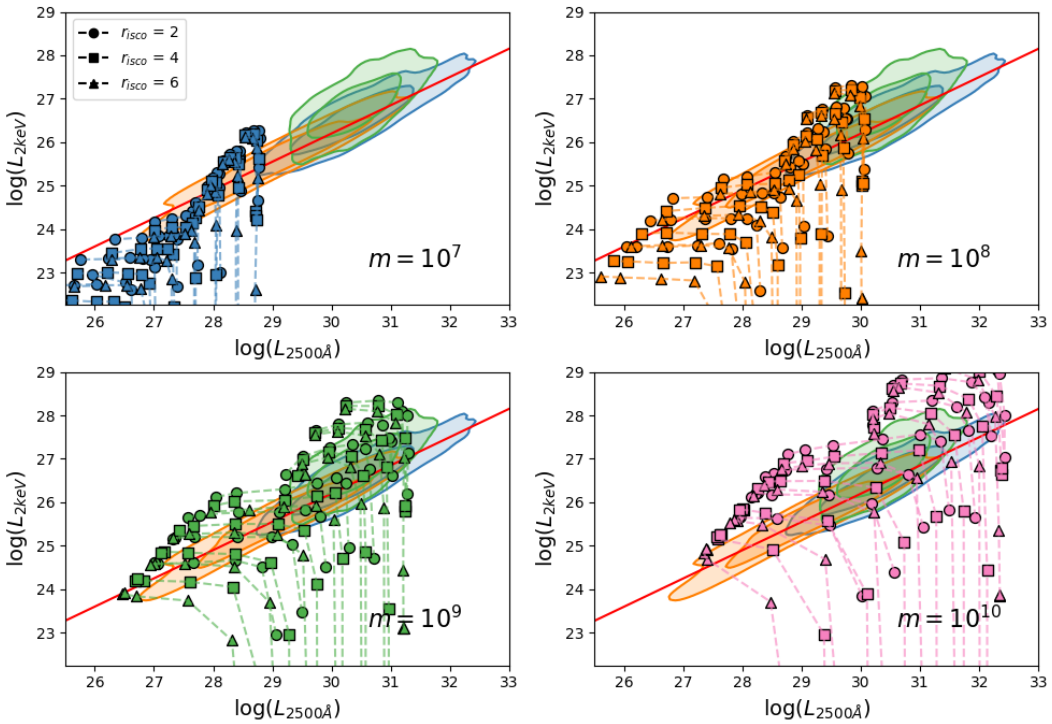

FIGURE C.1: Grid of JED-SAD spectra for different values of the ISCO in the UV–X-ray plane. Values of r_J go from 2 $\rightarrow$ 100 and of $\dot{m}$ from 10^{-2} $\rightarrow$ 10. Each Each panel assume a different black hole mass indicated on the plot. All other parameters are fixed to: $\omega = 0.1$; $m_s = 1.5$; $b = 0.3$; $p = 0.01$. The points connected with a dashed line have the same mass accretion rate. In the background: 95% and 68% percentile contour for each sample. In blue from the L&R sample (Lusso et al. 2020), in green from the Zhu+ sample (Zhu et al. 2020) and in orange from the Liu+ sample (Liu et al. 2021).

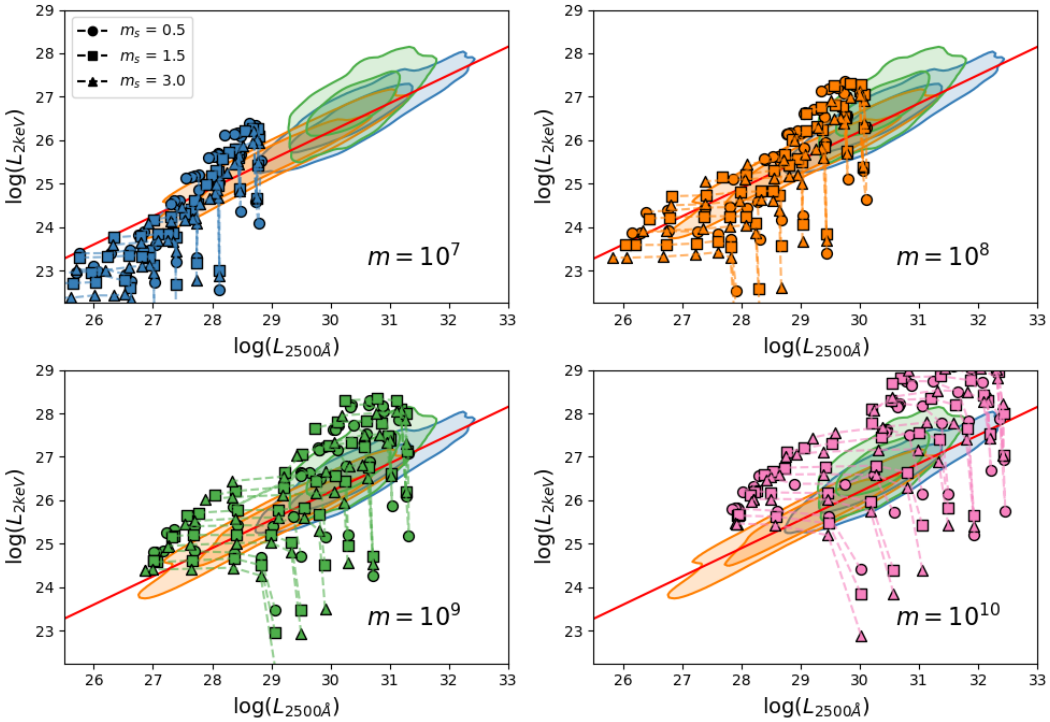

FIGURE C.2: Grid of JED-SAD spectra for different values of the sonic mach number m_s in the UV–X-ray plane. Values of r_J go from $2 \rightarrow 100$ and of $\dot{m}$ from $10^{-2} \rightarrow 10$. Each panel assume a different black hole mass indicated on the plot. All other parameters are fixed to: $r_{isco} = 2$; $\omega = 0.1$; $b = 0.3$; $p = 0.01$. The points connected with a dashed line have the same mass accretion rate. In the background: 95% and 68% percentile contour for each sample. In blue from the L&R sample (Lusso et al. 2020), in green from the Zhu+ sample (Zhu et al. 2020) and in orange from the Liu+ sample (Liu et al. 2021).

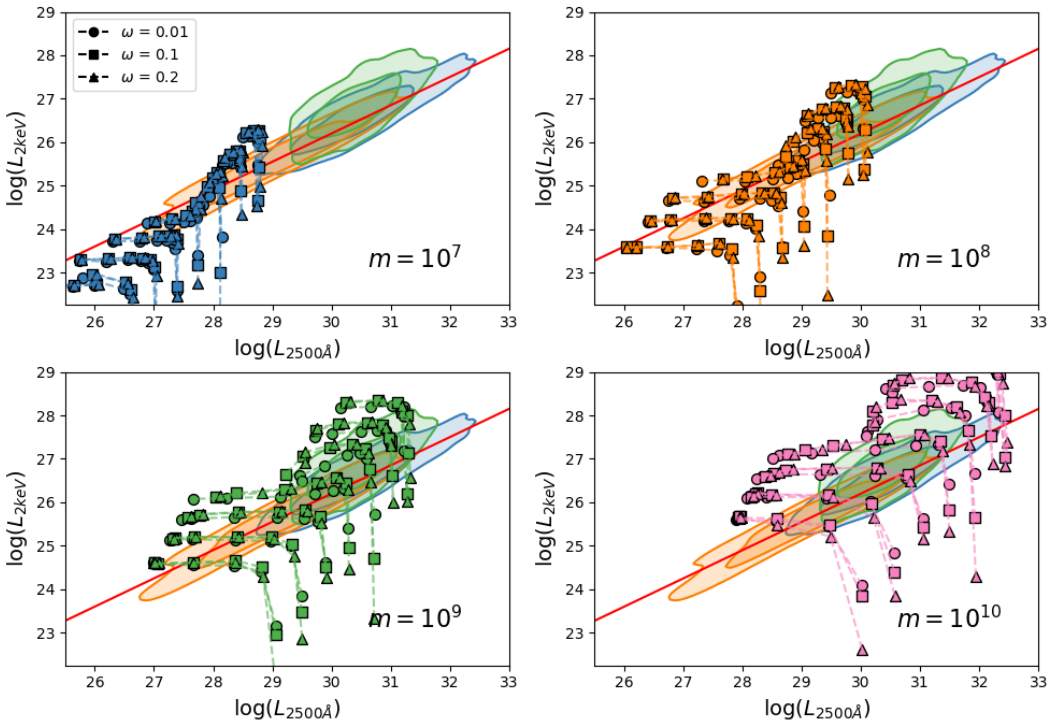

FIGURE C.3: Grid of JED-SAD spectra for different values of the dilution factor ω in the UV–X-ray plane. Values of r_J go from 2 $\rightarrow$ 100 and of $\dot{m}$ from 10^{-2} $\rightarrow$ 10. Each panel assume a different black hole mass indicated on the plot. All other parameters are fixed to: $r_{isco} = 2$; $m_s = 1.5$; $b = 0.3$; $p = 0.01$. The points connected with a dashed line have the same mass accretion rate. In the background: 95% and 68% percentile contour for each sample. In blue from the L&R sample (Lusso et al. 2020), in green from the Zhu+ sample (Zhu et al. 2020) and in orange from the Liu+ sample (Liu et al. 2021).

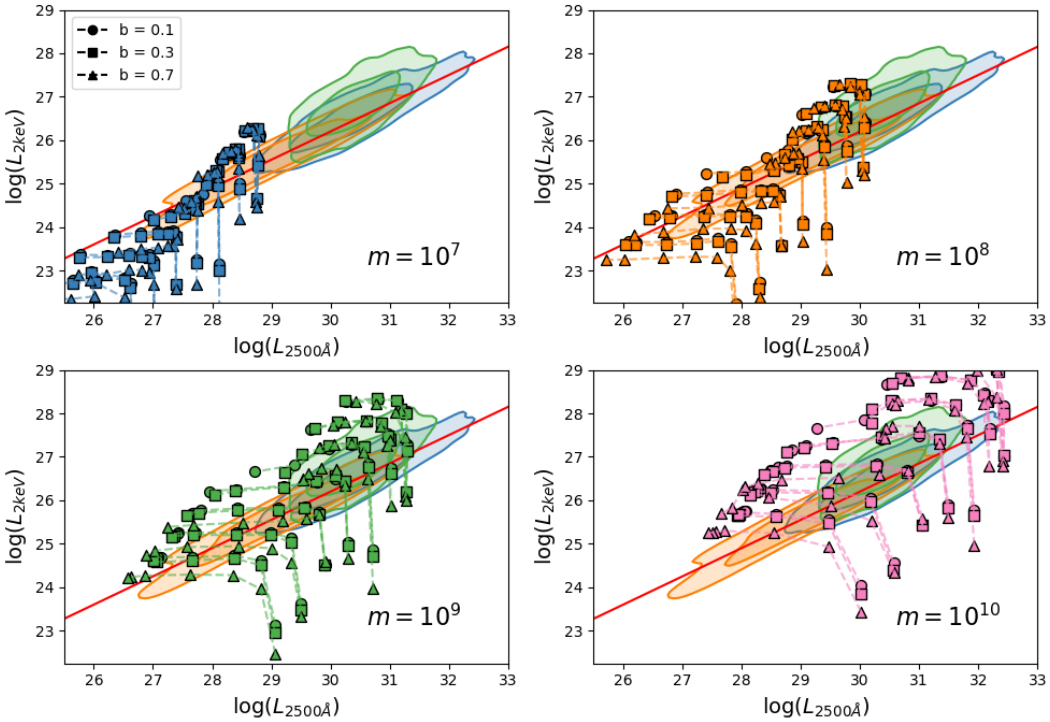

FIGURE C.4: Grid of JED-SAD spectra for different values of the power spend in the jets b in the UV–X-ray plane. Values of r_J go from $2 \rightarrow 100$ and of $\dot{m}$ from $10^{-2} \rightarrow 10$. Each panel assume a different black hole mass indicated on the plot. All other parameters are fixed to: $r_{isco} = 2$; $\omega = 0.1$; $m_s = 1.5$; $p = 0.01$. The points connected with a dashed line have the same mass accretion rate. In the background: 95% and 68% percentile contour for each sample. In blue from the L&R sample (Lusso et al. 2020), in green from the Zhu+ sample (Zhu et al. 2020) and in orange from the Liu+ sample (Liu et al. 2021).

Appendix D

Nested Sampling

D.1 Bibliography and methodology

The first method I will use is called NESTED SAMPLING (Skilling 2004, see also review in Buchner 2021). It is a recent MC algorithm which present multiple advantage. Let me introduce this method by first writing the Bayesian theorem:

$$P(M|D) = \frac{P(D|M)\ P(M)}{P(D)} \tag{D.1}$$

Where M and D represent respectively a model and a data set. $P(M|D)$ is called the posterior probability. P(M) is the prior, P(D) the evidence and $P(D|M)$ is the likelihood. Generally, the model depends on a number of parameters that I will group under the term θ and the likelihood can than be expressed as the following integration:

$$P(D|M) = \int d\theta\ P(D|\theta, M)\ P(\theta|M) \tag{D.2}$$

The nested sampling algorithm is useful to compute an estimation of this integral, also called the marginal probability density Z. Furthermore, this method generates a sample of the posterior distribution $P(\theta|D, M)$. This means that we can identify the relevant parameter space θ using this method. Below I present an abbreviated version of the algorithm:

Algorithm 1 Nested Sample algorithm.

Draw N *live* points [α_1, ..., α_N] sampled from priors
for i=1 to j **do** ▷ j requires guesswork
  L_i=min($\mathcal{L}(\alpha_1)$, ..., $\mathcal{L}(\alpha_N)$) ▷ Minimum likelihood of *live* points
  $X_i = (1 - 1/N)^i$ ▷ Volume of prior mass
  ▷ Multiple expressions possible, see text
  $W_i = X_{i-1} - X_i$
  $Z = Z + L_i \cdot W_i$ ▷ Integration of likelihood function
  Save the *live* point with least likelihood (L_i) as a sample point with weight W_i.
  Draw a new point according to priors, accepting only a likelihood superior to the least likelihood of the live points L_i: $\mathcal{L}$(new)> L_i.
  Update in the *live* points list the point with least likelihood (L_i) with the new point.
end for

Initially, we draw a list of N *live* points. During the algorithm, these live points will be replaced by new points with better likelihood. Whenever a point is replaced within the *live* points list, it is moved to another list which will contain the total simulated sample. We define L_i as the minimum likelihood of the *live* points at step i. Let us call the corresponding live point θ_i. X_i is an estimate of the volume of the prior mass covered by the hyper-volume in the parameter space of all points with a likelihood $\mathcal{L}(\theta)$ greater than $L_i = \mathcal{L}(\theta_i)$. W_i is an estimate of the prior mass laying between the two hyper-surface $\{\theta|P(D|\theta, M) = P(D|\theta_i - 1, M)\}$ and $\{\theta|P(D|\theta, M) = P(D|\theta_i, M)\}$. In other words $W_i = X_{i-1} - X_i$. The value of j might require some guesswork. Alternatively, one can stop the algorithm once the evolution of the likelihood $\mathcal{L}(\theta)$ becomes flat near the peak of the likelihood function. Further contribution $L_i \cdot W_i$ to the marginal probability density Z becomes negligible.

Multiple estimate of the prior mass $X(\theta)$ exist. Considering the initial N live points drawn, one can consider that each point represent a proportion 1/N of the total volume. When, for the first time, one replaces the live points with least likelihood with a point with higher likelihood, the explored volume has shrunk by $\delta V = 1/N$. At step i, the remaining volume of prior mass is then written as $X_i = (1 - 1/N)^i$. Other usual estimates used are $\delta V = 1 - exp(-1/N)$ and $\delta V = 1/(N + 1)$.

In Fig. D.1, I show an example obtained from a nested sample algorithm (from Buchner 2021). The three panel at the top show the likelihood function, the total sample and the live points at different step of the algorithm. On the left, we see the

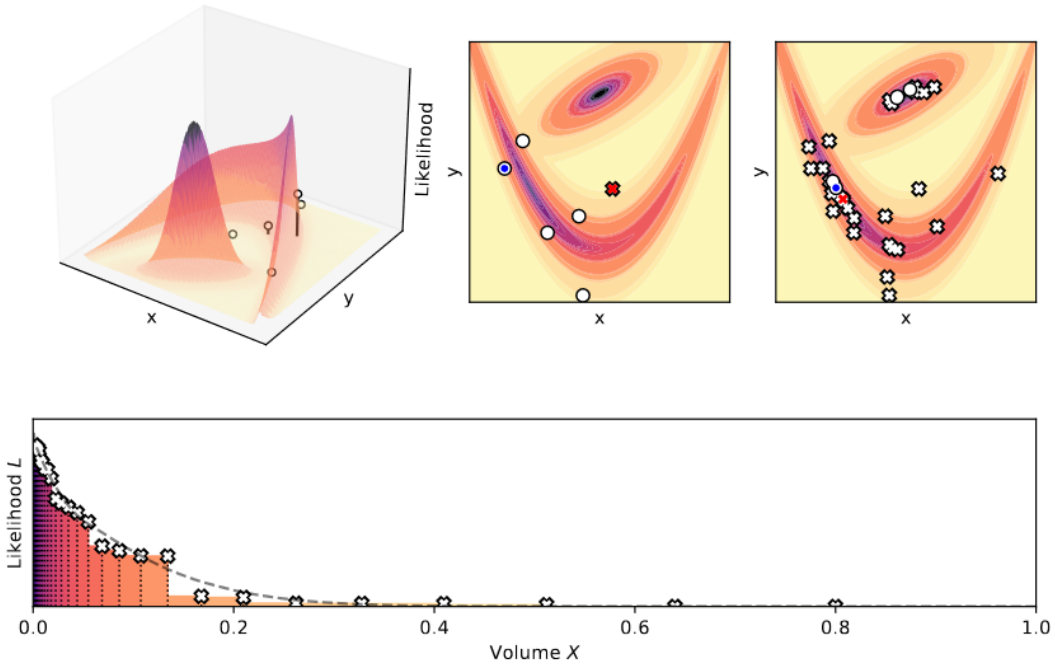

FIGURE D.1: Presentation of the nested sampling method (from Buchner 2021). **Top left**: Likelihood function in a 2D parameter space (x, y). Five initial *live* points are drawn. **Top Middle**: First step of the algorithm. The red cross has the least likelihood among the initial five live points. A new point in blue is drawn with a better likelihood and replace the red cross in the live points. **Top Right**: Total sample after N steps. The current live points are plotted as dots. The crosses are points drawn in precedent steps. **Bottom**: Likelihood of the points as function of the volume of prior mass for each step. At each step, the volume of prior mass is shrunk by a factor 1/N.

five initial live points drawn. In the middle, we see the first step, where the least likelihood point is saved to the total sample (red cross) and replaced by a new point (blue circle) with better likelihood. On the right, we see the total sample after a large number of steps. The white cross show the total sample drawn. The bottom panel shows how the likelihood is improved and the volume of prior mass is shrinking at each step.

D.2 Application to the L&R sample

I write a nested sample algorithm using N=25 initial live points. Each point represent a JED-SAD set of parameters and its corresponding spectra from which I extract the UV and X-ray luminosity. I assume a uniform prior for r_{isco}, b, m_s and ω; and a uniform prior in log-space for the black hole mass m, the transition radius r_J and the mass accretion rate $\dot{m}$. I use the kernel distribution of the data sample to compute the likelihood of a point. As such, a point outside of the sample will have a very small likelihood and a point at the center of the sample will have a strong likelihood, close to the maximum. I use j=500 maximum points however this is never reached as I break the algorithm once the contribution $L_i \cdot W_i$ is negligible before Z ($Z > 10^{-4} \times L_i \cdot W_i$). I then add all of the live points to the final drawn sample. For the L&R sample, this is reached at a total of 207 spectra.

In Fig. D.2, I plot the convergence of the nested sampling method applied to the L&R sample. Many points are not relevant with a very small likelihood and standing outside of the L&R sample. Furthermore, the higher luminosity region of the L&R sample are poorly explored. As such the total simulated sample can hardly represent the observed sample in its entirety. Since the nested sampling algorithm recovers the posterior distribution $P(\theta|D, M)$, let us take a look at the distribution of the simulated sample in a corner sample of the parameter space. In Fig. D.3, I plot the distribution of the simulated sample in the JED-SAD parameter space. Three parameters are constrained: the black hole mass mainly between 10^8 and 10^{10}. The mass accretion rate between 0.5 and 10. And the transition radius mostly below 10. Two correlations seem to appear, 1) between the mass accretion rate and black hole mass and 2) between the transition radius and the value of the ISCO. Both will be discussed later. The other parameters do not seem particularly constrained.

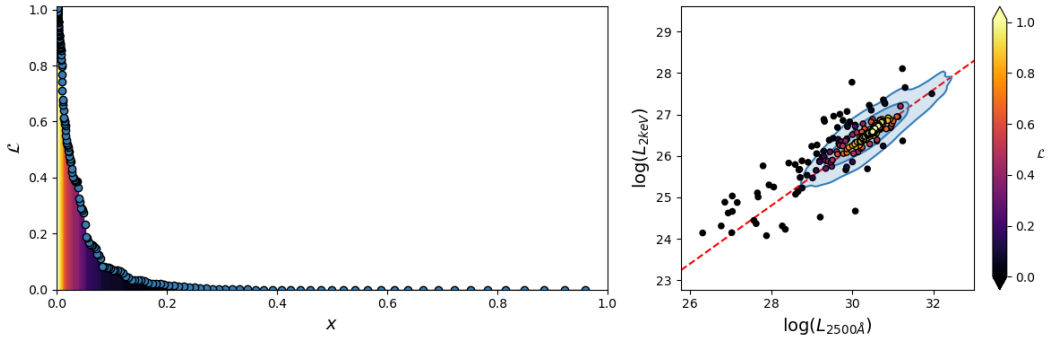

FIGURE D.2: Convergence of the nested sampling algorithm applied to the L&R sample. **Left**: Likelihood of the points as function of the volume of prior mass for each step. At each step, the volume of prior mass is shrunk by a factor 1/N. The color beneath the points represent the integration of the likelihood function and depends on the points' likelihood. **Right**: Total sample obtained with the nested sampling method. The points are colored by their likelihood.

However the total simulated sample are not representative of the observed sample as very few points were drawn in the high luminosity region of the sample, I will thus use another method to identify the complete relevant parameter space of the sample.

D.3 Effects of the soft excess

Once again, we can take a look at the impact of a warm comptonization on the results of the nested sample method. It converged in 180 spectra. In Fig. D.4, I plot the corresponding corner plot. The conclusion are quite similar. The relevant parameter space only change by a small margin. The mass accretion rate seems to be reduced a little and peaking around $\dot{m} \sim 1 - 2$. The transition radius present about a fourth of its points around 10-15.

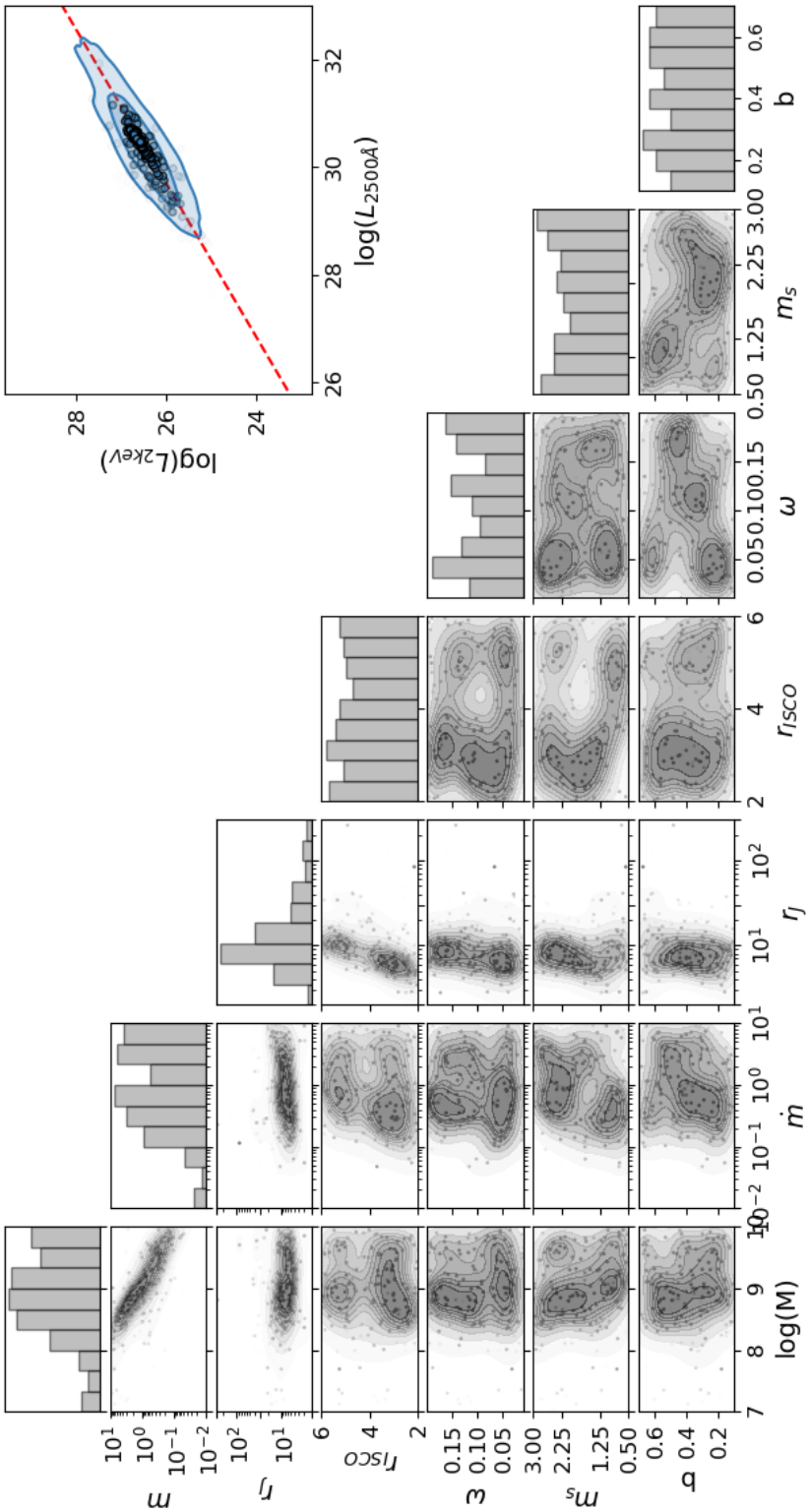

FIGURE D.3: Corner plot of the simulated sample resulting from the nested sample method in the JED-SAD parameter space. Each panel present the position of the 207 spectra in projections of the parameter space on 2D planes. The points are more visible the higher their likelihood is. The grey contour plot beneath show the kernel distribution in the 2D planes. Each point is weighted by its likelihood when computing the kernel. The upper panel of each column show the 1D distribution of the parameters, not weighted by the likelihood. The top right panel present the position of the points in the UV–X-ray plane.

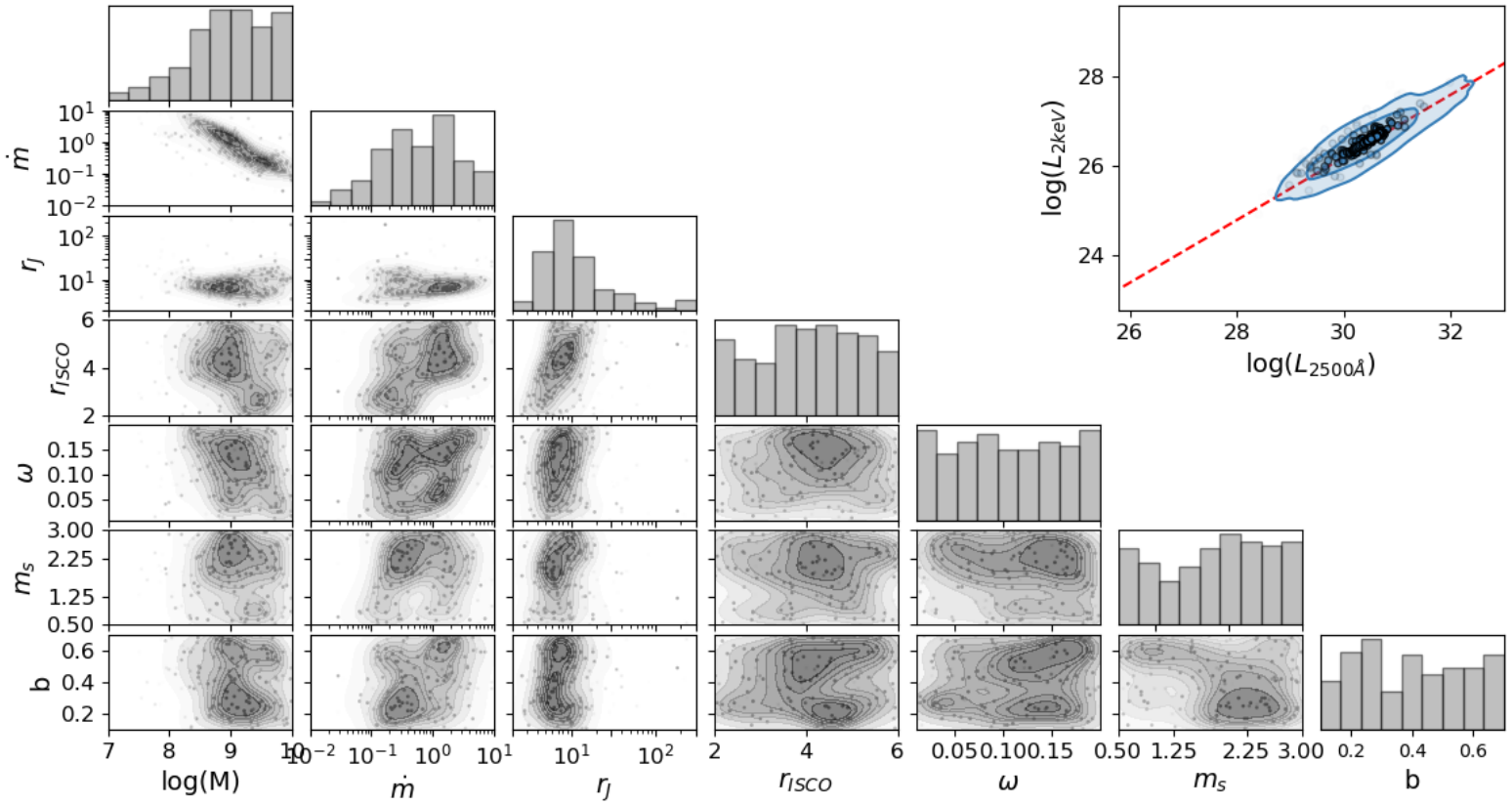

FIGURE D.4: Corner plot of the simulated sample resulting from the nested sample method in the JED-SAD parameter space. Warm comptonization model added to the model. Its parameters are fixed to $fsc = 0.75$, $\Gamma = 2.6$; $kT_e = 0.5$ keV. Each panel present the position of the 180 spectra in projections of the parameter space on 2D planes. The points are more visible the higher their likelihood is. The grey contour plot beneath show the kernel distribution in the 2D planes. Each point is weighted by its likelihood when computing the kernel. The upper panel of each column show the 1D distribution of the parameters, not weighted by the likelihood. The top right panel present the position of the points in the UV–X-ray plane.

References

Abbott, B. P., Abbott, R., Abbott, T. D., et al. 2016, Physical Review Letters, 116, 061102

Abramowicz, M. A., Calvani, M., & Nobili, L. 1980, The Astrophysical Journal, 242, 772

Abramowicz, M. A., Czerny, B., Lasota, J. P., & Szuszkiewicz, E. 1988, The Astrophysical Journal, 332, 646

Abrassart, A. & Dumont, A. M. 2001, in American Institute of Physics Conference Series, Vol. 599, X-ray Astronomy: Stellar Endpoints, AGN, and the Diffuse X-ray Background, ed. N. E. White, G. Malaguti, & G. G. C. Palumbo, 489–492

Aird, J., Coil, A. L., & Georgakakis, A. 2018, Monthly Notices of the Royal Astronomical Society, 474, 1225

Arcodia, R., Merloni, A., Nandra, K., & Ponti, G. 2019, Astronomy and Astrophysics, 628, A135

Arcodia, R., Ponti, G., Merloni, A., & Nandra, K. 2020, Astronomy and Astrophysics, 638, A100

Artemova, I. V., Bisnovatyi-Kogan, G. S., Bjoernsson, G., & Novikov, I. D. 1996, The Astrophysical Journal, 456, 119

Atri, P., Miller-Jones, J. C. A., Bahramian, A., et al. 2020, Monthly Notices of the Royal Astronomical Society, 493, L81

Bahramian, A., Miller-Jones, J., Strader, J., et al. 2018, Zenodo

Balbus, S. A. & Hawley, J. F. 1991, The Astrophysical Journal, 376, 214

Balbus, S. A. & Hawley, J. F. 1998, Reviews of Modern Physics, 70, 1

Ballantyne, D. R. 2020, Monthly Notices of the Royal Astronomical Society, 491, 3553

Barnier, S., Petrucci, P. O., Ferreira, J., et al. 2022, Astronomy and Astrophysics, 657, A11

Begelman, M. C. & Armitage, P. J. 2014, The Astrophysical Journal Letters, 782, L18

Bel, M. C., Rodriguez, J., D'Avanzo, P., et al. 2011, Astronomy and Astrophysics, 534, A119

Belloni, T., Parolin, I., Del Santo, M., et al. 2006, Monthly Notices of the Royal Astronomical Society, 367, 1113

Belmont, R. 2009, Astronomy and Astrophysics, 506, 589

Belmont, R., Malzac, J., & Marcowith, A. 2008, Astronomy and Astrophysics, 491, 617

Bianchi, S., Guainazzi, M., Matt, G., Fonseca Bonilla, N., & Ponti, G. 2009, Astronomy and Astrophysics, 495, 421

Biteau, J. 2013, Ph.D. Thesis

Blandford, R. & Payne, D. 1982, Monthly Notices of the Royal Astronomical Society, 199, 883

Blandford, R. D. & Königl, A. 1979, The Astrophysical Journal, 232, 34

Blandford, R. D. & Znajek, R. L. 1977, Monthly Notices of the Royal Astronomical Society, 179, 433

Boch, T., Pineau, F., & Derriere, S. 2012, in Astronomical Society of the Pacific Conference Series, Vol. 461, Astronomical Data Analysis Software and Systems XXI, ed. P. Ballester, D. Egret, & N. P. F. Lorente, 291

Buchner, J. 2021, arXiv e-prints, arXiv:2101.09675

Buisson, D. J. K., Fabian, A. C., Barret, D., et al. 2019, Monthly Notices of the Royal Astronomical Society, 490, 1350

Cadolle Bel, M., Rodriguez, J., D'Avanzo, P., et al. 2011, Astronomy and Astrophysics, 534, A119

Capitanio, F., Belloni, T., Del Santo, M., & Ubertini, P. 2009, Monthly Notices of the Royal Astronomical Society, 398, 1194

Carotenuto, F., Corbel, S., Tremou, E., et al. 2021a, Monthly Notices of the Royal Astronomical Society, 504, 444

Carotenuto, F., Corbel, S., Tremou, E., et al. 2021b, Monthly Notices of the Royal Astronomical Society, 504, 444

Carotenuto, F., Corbel, S., Tremou, E., et al. 2021c, Monthly Notices of the Royal Astronomical Society, 505, L58

Casella, P. & Pe'er, A. 2009, The Astrophysical Journal Letters, 703, L63

Casse, F. & Ferreira, J. 2000, Astronomy and Astrophysics, 361, 1178

Chauhan, J., Miller-Jones, J. C. A., Raja, W., et al. 2021, Monthly Notices of the Royal Astronomical Society, 501, L60

Clavel, M., Rodriguez, J., Corbel, S., & Coriat, M. 2016, Astronomische Nachrichten, 337, 435

Condon, J. J. 1992, Annual Rev. Astron. Astrophys., 30, 575

Contopoulos, I. & Kazanas, D. 1998, The Astrophysical Journal, 508, 859

Corbel, S., Coriat, M., Brocksopp, C., et al. 2013, Monthly Notices of the Royal Astronomical Society, 428, 2500

Corbel, S., Fender, R. P., Tzioumis, A. K., et al. 2000, Astronomy and Astrophysics, 359, 251

Corbel, S., Kaaret, P., Fender, R. P., et al. 2005, The Astrophysical Journal, 632, 504

Corbel, S., Nowak, M. A., Fender, R. P., Tzioumis, A. K., & Markoff, S. 2003, Astronomy and Astrophysics, 400, 1007

Coriat, M., Corbel, S., Buxton, M. M., et al. 2009, Monthly Notices of the Royal Astronomical Society, 400, 123

Coriat, M., Corbel, S., Prat, L., et al. 2011, Monthly Notices of the Royal Astronomical Society, 414, 677

Coriat, M., Fender, R. P., & Dubus, G. 2012, Monthly Notices of the Royal Astronomical Society, 424, 1991

Crummy, J., Fabian, A. C., Gallo, L., & Ross, R. R. 2006, Monthly Notices of the Royal Astronomical Society, 365, 1067

Dauser, T., Garcia, J., Parker, M. L., Fabian, A. C., & Wilms, J. 2014, Monthly Notices of the Royal Astronomical Society, 444, L100

De Marco, B., Zdziarski, A. A., Ponti, G., et al. 2021, Astronomy and Astrophysics, 654, A14

Droulans, R., Belmont, R., Malzac, J., & Jourdain, E. 2010, The Astrophysical Journal, 717, 1022

Du, P. & Wang, J.-M. 2019, The Astrophysical Journal, 886, 42

Dubus, G., Hameury, J. M., & Lasota, J. P. 2001, Astronomy and Astrophysics, 373, 251

Dumont, A. M., Abrassart, A., & Collin, S. 2000, Astronomy and Astrophysics, 357, 823

Dumont, A. M., Collin, S., Paletou, F., et al. 2003, Astronomy and Astrophysics, 407, 13

Dunn, R. J. H., Fender, R. P., Körding, E. G., Belloni, T., & Cabanac, C. 2010, Monthly Notices of the Royal Astronomical Society, 403, 61

Dunn, R. J. H., Fender, R. P., Körding, E. G., Cabanac, C., & Belloni, T. 2008, Monthly Notices of the Royal Astronomical Society, 387, 545

Esin, A. A., McClintock, J. E., & Narayan, R. 1997, The Astrophysical Journal, 489, 865

Espinasse, M. & Fender, R. 2018, Monthly Notices of the Royal Astronomical Society, 473, 4122

Event Horizon Telescope Collaboration, Akiyama, K., Alberdi, A., et al. 2022, The Astrophysical Journal Letters, 930, L12

Event Horizon Telescope Collaboration, Akiyama, K., Alberdi, A., et al. 2019, The Astrophysical Journal Letters, 875, L1

Falcke, H. & Biermann, P. L. 1995, Astronomy and Astrophysics, 293, 665

Fanaroff, B. L. & Riley, J. M. 1974, Monthly Notices of the Royal Astronomical Society, 167, 31P

Fender, R. & Belloni, T. 2012, Science, 337, 540

Fernández-Ontiveros, J. A. & Muñoz-Darias, T. 2021, Monthly Notices of the Royal Astronomical Society, 504, 5726

Ferreira, J. 1997, Astronomy and Astrophysics, 319, 340

Ferreira, J., Marcel, G., Petrucci, P. O., et al. 2022, Astronomy and Astrophysics, 660, A66

Ferreira, J. & Pelletier, G. 1993, Astronomy and Astrophysics, 276, 625

Ferreira, J. & Pelletier, G. 1995, Astronomy and Astrophysics, 295, 807

Ferreira, J., Petrucci, P.-O., Henri, G., Saugé, L., & Pelletier, G. 2006, Astronomy and Astrophysics, 447, 813

Frank, J., King, A., & Raine, D. J. 2002, Accretion Power in Astrophysics, iSBN: 0521620538

Frank, J., King, A., & Raine, D. J. 2002, Accretion Power in Astrophysics: Third Edition

Fürst, F., Nowak, M., Tomsick, J., et al. 2015, The Astrophysical Journal, 808, 122

Gallo, E., Fender, R. P., & Pooley, G. G. 2003, Monthly Notices of the Royal Astronomical Society, 344, 60

Gallo, L. 2018, Sissa Medialab, Trieste TS, Italy, 34

Gandhi, P., Blain, A., Russell, D., et al. 2011, The Astrophysical Journal Letters, 740, L13

García, J., Dauser, T., Lohfink, A., et al. 2014, The Astrophysical Journal, 782, 76

Garcia, J., Dauser, T., Reynolds, C., et al. 2013, The Astrophysical Journal, 768, 146

García, J. A., Kara, E., Walton, D., et al. 2019, The Astrophysical Journal, 871, 88

García, J. A., Steiner, J. F., McClintock, J. E., et al. 2015, The Astrophysical Journal, 813, 84

Genzel, R., Eisenhauer, F., & Gillessen, S. 2010, Reviews of Modern Physics, 82, 3121

Genzel, R., Schödel, R., Ott, T., et al. 2003, Nature, 425, 934

Ghez, A. M., Klein, B. L., Morris, M., & Becklin, E. E. 1998, The Astrophysical Journal, 509, 678

Ghez, A. M., Salim, S., Hornstein, S. D., et al. 2005, The Astrophysical Journal, 620, 744

Ghez, A. M., Salim, S., Weinberg, N. N., et al. 2008, The Astrophysical Journal, 689, 1044

Ghisellini, G. & Celotti, A. 2001, Astronomy and Astrophysics, 379, L1

Gierliński, M. & Done, C. 2004, Monthly Notices of the Royal Astronomical Society, 349, L7

Goodrich, R. W. 1989, The Astrophysical Journal, 342, 224

Gronkiewicz, D. & Różańska, A. 2020, Astronomy and Astrophysics, 633, A35

Hameury, J. M., King, A. R., & Lasota, J. P. 1986, Astronomy and Astrophysics, 162, 71

Hameury, J. M., Lasota, J. P., Knigge, C., & Körding, E. G. 2017, Astronomy and Astrophysics, 600, A95

Harrison, C. 2014, Ph.D. Thesis

Harrison, C. M. 2017, Nature Astronomy, 1, 0165

Heinz, S. & Sunyaev, R. A. 2003, Monthly Notices of the Royal Astronomical Society: Letters, 343, L59

Homan, J., Buxton, M., Markoff, S., et al. 2005, The Astrophysical Journal, 624, 295

Hubeny, I. 1990, The Astrophysical Journal, 351, 632

Hwang, H.-C., Zakamska, N. L., Alexandroff, R. M., et al. 2018, Monthly Notices of the Royal Astronomical Society, 477, 830

Inoue, Y. & Doi, A. 2018, The Astrophysical Journal, 869, 114

Inoue, Y., Khangulyan, D., & Doi, A. 2021, Galaxies, 9, 36

Islam, N. & Zdziarski, A. A. 2018, Monthly Notices of the Royal Astronomical Society, 481, 4513

Jacquemin-Ide, J., Ferreira, J., & Lesur, G. 2019, Monthly Notices of the Royal Astronomical Society, 490, 3112

Jacquemin-Ide, J., Lesur, G., & Ferreira, J. 2021, Astronomy and Astrophysics, 647, A192

Jannaud, T., Zanni, C., & Ferreira, J. 2022, arXiv e-prints, arXiv:2210.14809

Jiang, J., Fabian, A. C., Wang, J., et al. 2019, Monthly Notices of the Royal Astronomical Society, 484, 1972

Jiang, J., Gallo, L. C., Fabian, A. C., Parker, M. L., & Reynolds, C. S. 2020, Monthly Notices of the Royal Astronomical Society, 498, 3888

Jiang, J., Gallo, L. C., Fabian, A. C., Parker, M. L., & Reynolds, C. S. 2020, Monthly Notices of the Royal Astronomical Society, 498, 3888

Jin, C., Done, C., & Ward, M. 2017a, Monthly Notices of the Royal Astronomical Society, 468, 3663

Jin, C., Done, C., Ward, M., & Gardner, E. 2017b, Monthly Notices of the Royal Astronomical Society, 471, 706

Jin, C., Ward, M., & Done, C. 2012, Monthly Notices of the Royal Astronomical Society, 425, 907

Kajava, J. J. E., Motta, S. E., Sanna, A., et al. 2019, Monthly Notices of the Royal Astronomical Society, 488, L18

Kara, E., Steiner, J. F., Fabian, A. C., et al. 2019, Nature, 565, 198

Kawamura, T., Axelsson, M., Done, C., & Takahashi, T. 2022, Monthly Notices of the Royal Astronomical Society, 511, 536

Kawamuro, T., Negoro, H., Yoneyama, T., et al. 2018, The Astronomer's Telegram, 11399, 1

Kerr, R. P. 1963, Physical Review Letters, 11, 237

Koljonen, K., Russell, D., Fernández-Ontiveros, J., et al. 2015, The Astrophysical Journal, 814, 139

Koljonen, K. I. I. & Russell, D. M. 2019, The Astrophysical Journal, 871, 26

Kording, E. G., Fender, R. P., & Migliari, S. 2006, Monthly Notices of the Royal Astronomical Society, 369, 1451

Körding, E. G., Jester, S., & Fender, R. 2006, Monthly Notices of the Royal Astronomical Society, 372, 1366

Krawczynski, H., Muleri, F., Dovčiak, M., et al. 2022, Science, 378, 650

Kubota, A. & Done, C. 2018, Monthly Notices of the Royal Astronomical Society, 480, 1247

Kubota, A. & Done, C. 2019, Monthly Notices of the Royal Astronomical Society, 489, 524

Kylafis, N. D. & Belloni, T. M. 2015, Astronomy and Astrophysics, 574, A133

Laor, A. 1991, The Astrophysical Journal, 376, 90

Laor, A. & Behar, E. 2008, Monthly Notices of the Royal Astronomical Society, 390, 847

Lasota, J. P., Narayan, R., & Yi, I. 1996, Astronomy and Astrophysics, 314, 813

Ledlow, M. J. & Owen, F. N. 1996, , 112, 9

Leipski, C., Falcke, H., Bennert, N., & Hüttemeister, S. 2006, Astronomy and Astrophysics, 455, 161

Lense, J. & Thirring, H. 1918, Physikalische Zeitschrift, 19, 156

Liska, M., Hesp, C., Tchekhovskoy, A., et al. 2018, Monthly Notices of the Royal Astronomical Society, 474, L81

Liska, M., Tchekhovskoy, A., & Quataert, E. 2020, Monthly Notices of the Royal Astronomical Society, 494, 3656

Liu, H., Luo, B., Brandt, W. N., et al. 2021, The Astrophysical Journal, 910, 103

Lusso, E., Comastri, A., Vignali, C., et al. 2010, Astronomy and Astrophysics, 512, A34

Lusso, E. & Risaliti, G. 2016, The Astrophysical Journal, 819, 154

Lusso, E. & Risaliti, G. 2017, Astronomy and Astrophysics, 602, A79

Lusso, E., Risaliti, G., Nardini, E., et al. 2020, Astronomy and Astrophysics, 642, A150

Lynden-Bell, D. 1969, Nature, 223, 690

Magdziarz, P., Blaes, O. M., Zdziarski, A. A., Johnson, W. N., & Smith, D. A. 1998, Monthly Notices of the Royal Astronomical Society, 301, 179

Malzac, J., Kalamkar, M., Vincentelli, F., et al. 2018, Monthly Notices of the Royal Astronomical Society, 480, 2054

Marcel, G. 2018, thèse de doctorat dirigée par Ferreira, Jonathan Astrophysique et milieux dilues Université Grenoble Alpes (ComUE) 2018

Marcel, G., Cangemi, F., Rodriguez, J., et al. 2020, Astronomy and Astrophysics, 640, A18

Marcel, G., Ferreira, J., Clavel, M., et al. 2019, Astronomy and Astrophysics, 626, A115

Marcel, G., Ferreira, J., Petrucci, P. O., et al. 2022, Astronomy and Astrophysics, 659, A194

Marcel, G., Ferreira, J., Petrucci, P.-O., et al. 2018a, Astronomy and Astrophysics, 617, A46

Marcel, G., Ferreira, J., Petrucci, P.-O., et al. 2018b, Astronomy and Astrophysics, 615, A57

Marcel, G. & Neilsen, J. 2021, The Astrophysical Journal, 906, 106

Marino, A., Barnier, S., Petrucci, P. O., et al. 2021, Astronomy and Astrophysics, 656, A63

Marino, A., Malzac, J., Del Santo, M., et al. 2020, Monthly Notices of the Royal Astronomical Society, 498, 3351

Matt, G., Marinucci, A., Guainazzi, M., et al. 2014, Monthly Notices of the Royal Astronomical Society, 439, 3016

McClintock, J. E., Remillard, R. A., Rupen, M. P., et al. 2009, The Astrophysical Journal, 698, 1398

McKinney, J. C. 2005, The Astrophysical Journal Letters, 630, L5

McKinney, J. C., Tchekhovskoy, A., & Blandford, R. D. 2012, Monthly Notices of the Royal Astronomical Society, 423, 3083

McKinney, J. C., Tchekhovskoy, A., & Blandford, R. D. 2012, Monthly Notices of the Royal Astronomical Society, 423, 3083

McLure, R. J. & Dunlop, J. S. 2001, Monthly Notices of the Royal Astronomical Society, 327, 199

Merloni, A., Heinz, S., & di Matteo, T. 2003, Monthly Notices of the Royal Astronomical Society, 345, 1057

Middei, R., Bianchi, S., Cappi, M., et al. 2018, Astronomy and Astrophysics, 615, A163

Middei, R., Bianchi, S., Petrucci, P. O., et al. 2019, Monthly Notices of the Royal Astronomical Society, 483, 4695

Middei, R., Petrucci, P. O., Bianchi, S., et al. 2020, Astronomy and Astrophysics, 640, A99

Middelberg, E., Roy, A. L., Nagar, N. M., et al. 2004, Astronomy and Astrophysics, 417, 925

Miller-Jones, J. C. A., Bahramian, A., Orosz, J. A., et al. 2021, Science, 371, 1046

Mingo, B., Croston, J. H., Hardcastle, M. J., et al. 2019, Monthly Notices of the Royal Astronomical Society, 488, 2701

Mitsuda, K., Inoue, H., Koyama, K., et al. 1984, Publications of the Astronomical Society of Japan, 36, 741

Molla, A. A., Chakrabarti, S. K., Debnath, D., & Mondal, S. 2017, The Astrophysical Journal, 834, 88

Moravec, E., Svoboda, J., Borkar, A., et al. 2022, Astronomy and Astrophysics, 662, A28

Motta, S., Belloni, T., & Homan, J. 2009, Monthly Notices of the Royal Astronomical Society, 400, 1603

Motta, S., Muñoz-Darias, T., Casella, P., Belloni, T., & Homan, J. 2011, Monthly Notices of the Royal Astronomical Society, 418, 2292

Muñoz-Darias, T., Jiménez-Ibarra, F., Panizo-Espinar, G., et al. 2019, The Astrophysical Journal Letters, 879, L4

Mullaney, J. R., Alexander, D. M., Fine, S., et al. 2013, Monthly Notices of the Royal Astronomical Society, 433, 622

Nandi, A., Debnath, D., Mandal, S., & Chakrabarti, S. K. 2012, Astronomy and Astrophysics, 542, A56

Narayan, R., Igumenshchev, I. V., & Abramowicz, M. A. 2003, Publications of the Astronomical Society of Japan, 55, L69

Narayan, R., SÄ dowski, A., Penna, R. F., & Kulkarni, A. K. 2012, Monthly Notices of the Royal Astronomical Society, 426, 3241

Narayan, R. & Yi, I. 1994, The Astrophysical Journal Letters, 428, L13

Narayan, R. & Yi, I. 1995a, The Astrophysical Journal, 444, 231

Narayan, R. & Yi, I. 1995b, The Astrophysical Journal, 452, 710

Nayakshin, S. & Kallman, T. R. 2001, The Astrophysical Journal, 546, 406

Nims, J., Quataert, E., & Faucher-Giguère, C.-A. 2015, Monthly Notices of the Royal Astronomical Society, 447, 3612

Olsson, E., Aalto, S., Thomasson, M., & Beswick, R. 2010, Astronomy and Astrophysics, 513, A11

Orienti, M., D'Ammando, F., Giroletti, M., Giovannini, G., & Panessa, F. 2015, in Advancing Astrophysics with the Square Kilometre Array (AASKA14), 87

Orosz, J. A., McClintock, J. E., Aufdenberg, J. P., et al. 2011, The Astrophysical Journal, 742, 84

Osterbrock, D. & Phillips, M. 1977, Publications of the Astronomical Society of the Pacific, 89, 251

Owen, F. N. & Ledlow, M. J. 1994, in Astronomical Society of the Pacific Conference Series, Vol. 54, The Physics of Active Galaxies, ed. G. V. Bicknell, M. A. Dopita, & P. J. Quinn, 319

Panessa, F., Baldi, R. D., Laor, A., et al. 2019, Nature Astronomy, 3, 387

Parker, M., Tomsick, J., Kennea, J., et al. 2016, The Astrophysical Journal Letters, 821, L6

Péault, M., Malzac, J., Coriat, M., et al. 2019, Monthly Notices of the Royal Astronomical Society, 482, 2447

Petrucci, P.-O., Ferreira, J., Henri, G., Malzac, J., & Foellmi, C. 2010, Astronomy and Astrophysics, 522, A38

Petrucci, P.-O., Ferreira, J., Henri, G., & Pelletier, G. 2008, Monthly Notices of the Royal Astronomical Society: Letters, 385, L88

Petrucci, P. O., Gronkiewicz, D., Rozanska, A., et al. 2020, Astronomy and Astrophysics, 634, A85

Petrucci, P. O., Paltani, S., Malzac, J., et al. 2013, Astronomy and Astrophysics, 549, A73

Petrucci, P.-O., Ursini, F., De Rosa, A., et al. 2018, Astronomy and Astrophysics, 611, A59

Petrucci, P. O., Ursini, F., De Rosa, A., et al. 2018, Astronomy and Astrophysics, 611, A59

Pineau, F.-X., Boch, T., Derrière, S., & Schaaff, A. 2020, in Astronomical Society of the Pacific Conference Series, Vol. 522, Astronomical Data Analysis Software and Systems XXVII, ed. P. Ballester, J. Ibsen, M. Solar, & K. Shortridge, 125

Prat, L., Rodriguez, J., Cadolle Bel, M., et al. 2009, Astronomy and Astrophysics, 494, L21

Remillard, R. A. & McClintock, J. E. 2006, Annual Rev. Astron. Astrophys., 44, 49

Reynolds, S. P. 1982, The Astrophysical Journal, 256, 13

Risaliti, G. & Lusso, E. 2015, The Astrophysical Journal, 815, 33

Risaliti, G. & Lusso, E. 2019, Nature Astronomy, 3, 272

Roy, A. L., Wilson, A. S., Ulvestad, J. S., & Colbert, J. M. 2000, in EVN Symposium 2000, Proceedings of the 5th european VLBI Network Symposium, ed. J. E. Conway, A. G. Polatidis, R. S. Booth, & Y. M. Pihlström, 7

Różańska, A., Dumont, A. M., Czerny, B., & Collin, S. 2002, Monthly Notices of the Royal Astronomical Society, 332, 799

Różańska, A., Malzac, J., Belmont, R., Czerny, B., & Petrucci, P.-O. 2015, Astronomy and Astrophysics, 580, A77

Russell, T. D., Soria, R., Miller-Jones, J. C., et al. 2014, Monthly Notices of the Royal Astronomical Society, 439, 1390

Salgado, M., Bonazzola, S., Gourgoulhon, E., & Haensel, P. 1994, Astronomy and Astrophysics, 291, 155

Sargent, M. T., Schinnerer, E., Murphy, E., et al. 2010, The Astrophysical Journal Supplement, 186, 341

Scepi, N., Lesur, G., Dubus, G., & Jacquemin-Ide, J. 2020, Astronomy and Astrophysics, 641, A133

Schneider, D. P., Richards, G. T., Hall, P. B., et al. 2010, , 139, 2360

Shakura, N. I. & Sunyaev, R. A. 1973, Astronomy and Astrophysics, 24, 337

Shapiro, S. L., Lightman, A. P., & Eardley, D. M. 1976, The Astrophysical Journal, 204, 187

Shen, Y., Richards, G. T., Strauss, M. A., et al. 2011, The Astrophysical Journal Supplement, 194, 45

Skilling, J. 2004, in American Institute of Physics Conference Series, Vol. 735, Bayesian Inference and Maximum Entropy Methods in Science and Engineering: 24th International Workshop on Bayesian Inference and Maximum Entropy Methods in Science and Engineering, ed. R. Fischer, R. Preuss, & U. V. Toussaint, 395–405

Steiner, J. F., García, J. A., Eikmann, W., et al. 2017, The Astrophysical Journal, 836, 119

Steiner, J. F., McClintock, J. E., & Reid, M. J. 2012, The Astrophysical Journal Letters, 745, L7

Stepney, S. & Guilbert, P. W. 1983, Monthly Notices of the Royal Astronomical Society, 204, 1269

Stiele, H., Motta, S., Muñoz-Darias, T., & Belloni, T. M. 2011, Monthly Notices of the Royal Astronomical Society, 418, 1746

Svoboda, J., Guainazzi, M., & Merloni, A. 2017, Astronomy and Astrophysics, 603, A127

Tauris, T. M. & van den Heuvel, E. P. J. 2006, in Compact stellar X-ray sources, Vol. 39, 623–665

Tchekhovskoy, A. & Bromberg, O. 2016, Monthly Notices of the Royal Astronomical Society, 461, L46

Tchekhovskoy, A., Narayan, R., & McKinney, J. C. 2011, Monthly Notices of the Royal Astronomical Society: Letters, 418, L79

Thorne, K. S. & Price, R. H. 1975, The Astrophysical Journal Letters, 195, L101

Tominaga, M., Nakahira, S., Shidatsu, M., et al. 2020, The Astrophysical Journal Letters, 899, L20

Tomsick, J. A., Parker, M. L., García, J. A., et al. 2018, The Astrophysical Journal, 855, 3

Torres, M. A. P., Casares, J., Jiménez-Ibarra, F., et al. 2020, The Astrophysical Journal Letters, 893, L37

Torres, M. A. P., Casares, J., Jiménez-Ibarra, F., et al. 2019, The Astrophysical Journal Letters, 882, L21

Tremou, E., Corbel, S., Fender, R. P., et al. 2020, Monthly Notices of the Royal Astronomical Society, 493, L132

Tucker, M. A., Shappee, B. J., Holoien, T. W. S., et al. 2018, The Astrophysical Journal Letters, 867, L9

Urry, C. M. & Padovani, P. 1995, Publication of the Astronomical Society of the Pacific, 107, 803

Ursini, F., Petrucci, P.-O., Bianchi, S., et al. 2020, Astronomy and Astrophysics, 634, A92

Ursini, F., Petrucci, P. O., Matt, G., et al. 2018, Monthly Notices of the Royal Astronomical Society, 478, 2663

Ursini, F., Petrucci, P. O., Matt, G., et al. 2016, Monthly Notices of the Royal Astronomical Society, 463, 382

Vestergaard, M. & Peterson, B. M. 2006, The Astrophysical Journal, 641, 689

Walter, R. & Fink, H. H. 1993, Astronomy and Astrophysics, 274, 105

Walton, D. J., Nardini, E., Fabian, A. C., Gallo, L. C., & Reis, R. C. 2013, Monthly Notices of the Royal Astronomical Society, 428, 2901

Wang-Ji, J., García, J. A., Steiner, J. F., et al. 2018, The Astrophysical Journal, 855, 61

Webb, N. A., Coriat, M., Traulsen, I., et al. 2020, Astronomy and Astrophysics, 641, A136

Webb, N. A., Coriat, M., Traulsen, I., et al. 2022, VizieR Online Data Catalog, IX/65

Wilms, J., Allen, A., & McCray, R. 2000, The Astrophysical Journal, 542, 914

Xiang, X., Ballantyne, D. R., Bianchi, S., et al. 2022, Monthly Notices of the Royal Astronomical Society, 515, 353

Yatabe, F., Negoro, H., Nakajima, M., et al. 2019, The Astronomer's Telegram, 12425, 1

Yuan, F. & Narayan, R. 2014, Annual Rev. Astron. Astrophys., 52, 529

Zakamska, N. L. & Greene, J. E. 2014, Monthly Notices of the Royal Astronomical Society, 442, 784

Zdziarski, A. A., Dziełak, M. A., De Marco, B., Szanecki, M., & Niedźwiecki, A. 2021, The Astrophysical Journal Letters, 909, L9

Zdziarski, A. A., Gierlinski, M., Mikolajewska, J., et al. 2004, Monthly Notices of the Royal Astronomical Society, 351, 791

Zdziarski, A. A., Ziółkowski, J., & Mikołajewska, J. 2019, Monthly Notices of the Royal Astronomical Society, 488, 1026

Zhang, W., Dovčiak, M., & Bursa, M. 2019, The Astrophysical Journal, 875, 148

Zhao, X., Gou, L., Dong, Y., et al. 2021, The Astrophysical Journal, 908, 117

Zhu, S. F., Brandt, W. N., Luo, B., et al. 2020, Monthly Notices of the Royal Astronomical Society, 496, 245